THE PHYSICAL CHEMISTRY OF CORTICOSTEROID-CYCLODEXTRIN COMPLEXES

S.A. ETEER

PhD

2018

The Physical Chemistry of Corticosteroid-cyclodextrin Complexes

The Host-guest Chemistry of Corticosteroid and Cyclodextrin Systems Elucidated with NMR and Applied to Novel Surface-decorated Surface Enhanced Raman Spectroscopic Probes

Shahrazad Ali ETEER

Submitted for the Degree of Doctor of Philosophy

School of Chemistry and Biosciences
Faculty of Life Sciences
University of Bradford

2018

Abstract

Shahrazad Ali Eteer

The Physical Chemistry of Corticosteroid-cyclodextrin Complexes

The Host-guest Chemistry of Corticosteroid and Cyclodextrin Systems Elucidated with NMR and Applied to Novel Surface-decorated Surface Enhanced Raman Spectroscopic Probes

Keywords: Corticosteroids, HFA, complexation, cyclodextrins, inhalation, pMDI, NMR, SERS, nanoparticles.

Inhaled corticosteroids (ICS) are used to address inflammatory illnesses including asthma and COPD, with delivery commonly achieved using pressurised metered dose inhalers (pMDI). Hydrofluoroalkanes (HFAs) have been introduced as an alternative propellant to chlorofluorocarbons (CFCs) to reduce their environmental impact. However, the thermodynamic properties of HFAs are poorly understood and are different to those of CFCs. It is essential, therefore, to characterise the drugs and excipients used in HFA inhalers in order to obtain a comprehensive understanding of the device performance and the therapeutic efficacy.

This work has developed different analytical methods to study the complexation between ICS and CD which are added to enhance the solubility of inhaled drugs in pMDI propellant systems providing rational control of suspension vs. solution formulations and hence their dose uniformity and stability.

The Nuclear Magnetic Resonance (NMR) method developed has shown weaker complexation between budesonide and the derivatised CDs DIMEB and TRIMEB in organic solvents compared to D_2O with the strength of the complex formed being ranked as D_2O > MeOD > $CDCl_3$ > CD_3CN. The derivatisation of the CD also shows a marked difference in complexation with budesonide with the strength of the association being ranked as DIMEB > *β*CD > TRIMEB. Studies of various ICS compounds with TRIMEB in the fluorinated propellant HPFP showed the association to be greatest in budesonide, followed by beclomethasone dipropionate, momestasone furoate and fluticasone propionate.

Surface-enhanced Raman scattering (SERS) has been used for the detection of corticosteroids in water using thiol functionalised *β*CD as a complementary study to NMR. This has been utilised to evaluate the host-guest complexes formed and provides further insight into the complexation of the compounds by their inclusion into the CD cavity.

The structural data obtained using the NMR and SERS approaches developed have provided a fundamental insight into the physical chemistry of these interactions at a molecular level.

Acknowledgements

I would like to express my sincere thank my supervisors; Professor Ian Scowen, Dr Tasnim Munshi and Dr Richard Telford for their valuable guidance and continued support thorough my work.

Also, Dr Philip Drake for helping me with SERS experiments and the analytical centre staff especially Mr Dennis Farwell, Mr Andrew Healey and Mr Stuart Fox for the training on the use of the instrument and Miss Saiba Halim for their help.

My thanks go to my husband, kids, parents, brothers and sisters for their encouragement and support during this work. My thanks also go for my government for providing me the sponsorship to do this work.

List of Contents

Abstract……..i

Acknowledgements……..……...……..…….ii

Table of Contents..…….. ……..…….iii

List of Figures……..…….……vii

List of Tables……..……..……..xviii

List of Abbreviations and Symbols…..…..…… xxv

1 Introduction 1

1.1 Physiology of the lung, diseases and associated responses 1

1.2 Inhaled corticosteroids (ICS).....4

1.3 Delivery Devices 5

1.3.1 Nebuliser devices 6

1.3.2 Pressurised Metered Dose Inhaler (pMDI) devices 6

1.3.3 Dry Powder Inhaler (DPI) devices 7

1.4 Chlorofluorocarbons (CFC) and Hydrofluoroalkanes (HFA) – used in pMDIs 8

1.5 Characteristics of HFA pMDIs formulations 9

1.5.1 Suspension formulations 11

1.5.2 Solution formulations.....12

1.5.3 Suspension vs solution formulations 14

1.5.4 Cyclodextrins (CDs) as pMDI excipients 15

1.6 Study objectives.....26

1.7 Aims.....27

2 Experimental 29

2.1 Materials 29

2.2 Methods.....29

2.2.1 Determination of host:guest stoichiometry by UV-Vis spectroscopy 29

2.2.2 Determination of host:guest association constants by UV-Vis spectroscopy....31
2.2.3 Determination of host:guest stoichiometry by NMR spectroscopy 33
2.2.4 Determination of host:guest association constants by NMR spectroscopy....35
2.2.5 Preparation of physical mixtures of budesonide and cyclodextrins36
2.2.6 Preparation of inclusion complexes using evaporation methods...36
2.2.7 SERS study....36
2.3 Instrumentation....39
2.3.1 UV-Vis spectroscopy....39
2.3.2 Inductively Coupled Plasma Optical Emission Spectrometry (ICP-OES) analysis of Ag/Au NPs....39
2.3.3 Dynamic Light Scattering (DLS) analysis of Ag/Au NPs....40
2.3.4 Transmission Electron Microscopy (TEM) analysis of Ag/Au NPs 40
2.3.5 NMR spectroscopy....40
2.3.6 FT-IR spectroscopy....41
2.3.7 Raman spectroscopy....41
3 Development of UV-Vis and NMR methods for the study of host:guest complexes using vanillin and *β*CD....42
3.1 Complexation study of vanillin and *β*CD in D_2O by NMR....42
3.2 Complexation study of vanillin and *β*CD in water by UV-Vis spectroscopy....45
3.3 Discussion....49
4 Host:guest Interactions in conventional solvents using UV-Vis and NMR spectroscopy....50
4.1 Complexation study of BUD and *β*CD/TRIMEB by UV-Vis spectroscopy 50
4.1.1 Complexation of BUD and *β*CD in EtOH: H_2O and H_2O....50
4.1.2 Complexation of BUD and TRIMEB in EtOH: H_2O and H_2O....55

4.2 Complexation study of BUD and DIMEB/TRIMEB by NMR 58
4.2.1 Complexation of BUD and DIMEB/TRIMEB in CD_3CN.....58
4.2.2 Complexation of BUD and DIMEB/TRIMEB in $CDCl_3$ 59
4.2.3 Complexation of BUD and DIMEB/TRIMEB in MeOD 61
4.2.4 Complexation of BUD and *β*CD/DIMEB/TRIMEB in D_2O 64
4.3 Analysis of solid complexes of BUD and *β*CD/TRIMEB/DIMEB using vibrational spectroscopy 94
4.3.1 FTIR 94
4.3.2 Raman spectroscopy.....99
4.4 Discussion 102
4.4.1 Complexation studies by UV-Vis spectroscopy 102
4.4.2 Complexation studies by NMR 103
5 Host:guest interactions in HFA solvents using NMR spectroscopy .115
5.1 Assignment of corticosteroids in HPFP.....116
5.2 Complexation study of BUD and TRIMEB 120
5.2.1 (22-*R*)-budesonide (pure enantiomer) with TRIMEB 126
5.3 Complexation study of BDP and TRIMEB.....134
5.4 Complexation study of MOM and TRIMEB 138
5.5 Complexation study of FLU and TRIMEB 142
5.6 Complexation study of BUD and DIMEB.....146
5.7 Complexation study of BDP and DIMEB.....151
5.8 Discussion 156
5.8.1 Comparison between corticosteroids compounds.....156
5.8.2 CD type and its effect on complexation 158
5.8.3 Chiral discrimination of BUD by TRIMEB 159
6 Development of Cyclodextrin-Functionalised Metal Nanoparticles as Receptors for as Surface Enhanced Raman Spectroscopy of Corticosteroids 163
6.1 Characterisation of the Silver and Gold Nanoparticle Formulations...164

6.1.1 Plasmon resonance....164
6.1.2 Particle analysis: Dynamic Light scattering....166
6.1.3 Particle analysis: Transmission Electron Microscopy.....169
6.1.4 Concentrations of Nanoparticles....175
6.2 Raman Spectroscopic Study of Selected Corticosteroids....175
6.2.1 Spectral Region 3200-2800 cm^{-1}....181
6.2.2 Region 1780-1550 cm^{-1}....182
6.2.3 Region 1500-100 cm^{-1}....183
6.3 Raman Spectroscopic Study of *per*-6-thio-β-cyclodextrin (SCD)....184
6.4 Raman Spectroscopic Studies of SCD-Ag-NP and SCD-Au-NP....186
6.5 Raman Spectroscopic Studies of Budesonide with Metal Nanoparticles 187
6.5.1 BUD with Ag-NP....187
6.5.2 BUD with Au-NP....192
6.6 Raman Spectroscopic Studies of Beclometasone Dipropionate with Metal Nanoparticles....194
6.7 Raman Spectroscopic Studies of Fluticasone Propionate and Mometasone Furoate with Metal Nanoparticles....196
7 Conclusion....199
7.1 NMR Studies....199
7.2 SERS Studies....205
7.2.1 Conventional Raman Spectroscopic Studies of Corticosteroids..206
7.2.2 Nanoparticle Synthesis and Characterisation....206
7.2.3 SERS with CSs....206
7.2.4 SERS with SCD-M-NP....207
8 Further work....208
9 References....209
Appendix A1…….. …. ……..…… 222

List of Figures

Figure 1.1: Chemical structure of budesonide (BUD), beclomethasone dipropionate (BDP), beclomethasone (BCL), fluticasone propionate (FLU) and mometasone furoate (MOM). 5
Figure 1.2: Gamma scintographic images of lung (left side) and oropharynx (right side) of beclomethasone dipropionate MDI with a) HFA and b) CFC propellants.[69].....9
Figure 1.3: (a) Chemical structure of *α*, *β* and *γ* CDs (composed of 6, 7 and 8 glucose units respectively) and (b) the condensed cone.....15
Figure 1.4: Chemical structure of (a) *β*CD, (b) DIMEB and (c) TRIMEB 16
Figure 1.5: Schematic diagram of SERS process. (1) metal nanoparticles surrounded by a solvent medium. (2) incident field E_0 excites the nanoparticles at a wavelength λ_0. (3) molecule is located near the nanoparticle surface. (4) the molecule is polarised by the local field that is then scattered E_{scat} at Raman wavelength λ_R (5) the scattered field is then reacted with the nanoparticles producing field Erad through re-radiation process.[158] 23
Figure 3.1: Structure of vanillin 42
Figure 3.2: Partial ^{1}H NMR spectrum of (a) *β*CD (10 mM), (b) 5 mM of *β*CD and 5 mM of vanillin. 43
Figure 3.3: Determination of the stoichiometry of the complex between vanillin and *β*CD by ^{1}H NMR based on H5 proton of *β*CD 44
Figure 3.4: Structure of vanillin 44
Figure 3.5: Reciprocal plot for the determination of association constant between vanillin and *β*CD by ^{1}H NMR. 45
Figure 3.6: Determination of the stoichiometry of the complex between vanillin and *β*CD based on the absorbance at 280 nm using UV-Vis spectroscopy. 46
Figure 3.7: UV spectra of vanillin with *β*CD concentration at 1) 0, 2) 2, 3) 4, 4) 6 and 5) 8 mM.....48
Figure 3.8: Reciprocal plot for the association constant determination between vanillin and *β*CD by UV-Vis spectroscopy (Mean ± SD, n=3).....48
Figure 4.1: UV spectra of budesonide with *β*CD concentration at 1) 0, 2) 2, 3) 4, 4) 6 and 5) 8 mM in EtOH/H_2O (50:50) solvent. 51

Figure 4.2: Reciprocal plot for the determination of association constant between budesonide and *β*CD in EtOH/H_2O (50:50) and H_2O by UV-Vis spectroscopy (Mean ± SD, n=3). 53
Figure 4.3: Determination of the stoichiometry of the complex between budesonide and *β*CD in EtOH/H_2O (50:50) and H_2O based on the absorbance at 246 nm using UV-Vis spectroscopy. 54
Figure 4.4: Reciprocal plot for the determination of association constant between budesonide and TRIMEB in EtOH/H_2O (50:50) and H_2O by UV-Vis spectroscopy (Mean ± SD, n=3). 56
Figure 4.5: Determination of the stoichiometry of the complex between budesonide and TRIMEB in EtOH/H_2O (50:50) and H_2O based on the absorbance at 246 nm using UV-Vis spectroscopy.....58
Figure 4.6: Chemical structure of budesonide.....58
Figure 4.7: Reciprocal plot for the determination of association constant between budesonide and TRIMEB in $CDCl_3$ by ^1H NMR based on the chemical shift of H-C_4 and H-C_{19} at 6.022 and 1.4338 ppm respectively. 60
Figure 4.8: Reciprocal plot for the determination of association constant between budesonide and DIMEB in $CDCl_3$ by ^1H NMR based on the chemical shift of H-C_4 and H-C_{19} at 6.022 and 1.4338 ppm respectively. 61
Figure 4.9: Reciprocal plot for the determination of association constant between budesonide and TRIMEB in MeOD by NMR depending on the chemical shift of H-C_4 and H-C_{19} at 5.9860 and 1.4600 ppm respectively. 62
Figure 4.10: Reciprocal plot for the determination of association constant between budesonide and DIMEB in MeOD by NMR depending on the chemical shift of H-C_4 and H-C_{19} at 5.9860 and 1.4600 ppm respectively. 63
Figure 4.11: ^1H NMR spectra of budesonide in D_2O (a) without and (b) with solvent suppression at 4.67 ppm. 65
Figure 4.12: Calculation of the S/N of budesonide spectra in D_2O for the H-C_{18} peak at 0.75 ppm collected with different scan number at 128, 256 and 2048 scan. 66
Figure 4.13: Calculation of the S/N of budesonide spectra in D_2O for the H-C_4 peak at 5.97 ppm collected with different scan number at 128, 256 and 2048 scan. 67

Figure 4.14: A co-axial NMR tube set up consists of inner tube (upper) inserted in the standard NMR tube (lower) with the addition of sample solution and the reference material added to the inner tube.[178] 68
Figure 4.15: ^{1}H NMR spectra of budesonide and *β*CD in D_2O using $CHCl_3/CD_3CN$ at (a) 10 mg/mL and (b) 100 µg/mL as reference showing that the peak at 8.24 ppm decreased in intensity when the concentration of $CHCl_3$ decreased. 69
Figure 4.16: ^{1}H NMR spectrum of budesonide in D_2O run without co-axial insert with solvent suppression at 4.67 ppm showing that the absence of the peak at 8.24 ppm. 70
Figure 4.17: ^{1}H NMR spectra of D_2O with the addition of only $CHCl_3$ (a) and $CHCl_3/CD_3CN$ (b) in the co-axial insert with solvent suppression at 4.67 ppm showing that the peak of $CHCl_3$ is shifted from 7.07 to 8.24 ppm. 71
Figure 4.18: Budesonide spectra in D_2O collected at 2048 scan showing the calculation of the S/N using different concentrations at 0.02, 0.03 and 0.04 mM. 72
Figure 4.19: ^{1}H NMR spectrum of budesonide in $CDCl_3$ 73
Figure 4.20: ^{1}H NMR spectrum of budesonide in $CDCl_3$ in high field region (0.5-4 ppm).....74
Figure 4.21: ^{1}H NMR spectrum of budesonide in $CDCl_3$ in low field region (4-8 ppm).....74
Figure 4.22: Budesonide chemical shift in $CDCl_3$ (lower) and D_2O (upper) in high field region (0.6-1.7 ppm) showing a little shift when using different solvents. 76
Figure 4.23: Budesonide chemical shift in $CDCl_3$ (lower) and D_2O (upper) in low field region (5.5-8 ppm) showing a little shift when using different solvents. 76
Figure 4.24: Budesonide (0.04 mM) chemical shift in high field region (0.6-1.6 ppm) with the addition of *β*CD at 0, 0.2, 0.4, 1, 1.4 and 2 mM in D_2O.....78
Figure 4.25: Budesonide (0.04 mM) chemical shift in low field region (5.9-7.6 ppm) with the addition of *β*CD at 0, 0.2, 0.4, 1, 1.4 and 2 mM in D_2O.....79
Figure 4.26: Reciprocal plot for the determination of the association constant between budesonide and *β*CD in D_2O by ^{1}H NMR based on the chemical shift of H-C_{19} at 1.2570 ppm (Mean ± SD, n=3). 80

Figure 4.27: Determination of the stoichiometry of the complex between budesonide and βCD in D_2O by ^1H NMR based on the chemical shift of H-C_2 proton of budesonide. 82
Figure 4.28: Budesonide (0.04 mM) chemical shift in high field region (0.6-1.6 ppm) with the addition of TRIMEB at 0, 0.2, 0.4, 1, 1.4 and 2 mM in D_2O. 83
Figure 4.29: Budesonide (0.04 mM) chemical shift in low field region (5.9-7.54 ppm) with the addition of TRIMEB at 0, 0.2, 0.4, 1, 1.4 and 2 mM in D_2O. 84
Figure 4.30: Reciprocal plot for the determination of the association constant between budesonide and TRIMEB in D_2O by ^1H NMR based on the chemical shift differences of H-C_{19} and H-C_4 at 1.2570 and 5.9645 ppm (Mean ± SD, n=3).....86
Figure 4.31: Determination of the stoichiometry of the complex between budesonide and TRIMEB in D_2O by ^1H NMR based on the chemical shift differences of H-C_2 proton of budesonide. 88
Figure 4.32: Budesonide (0.04 mM) chemical shift in high field region (0.6-1.6 ppm) with the addition of DIMEB at 0, 0.2, 0.4, 1, 1.4 and 2 mM in D_2O. 89
Figure 4.33: Budesonide (0.04 mM) chemical shift in low field region (5.8-7.6 ppm) with the addition of DIMEB at 0, 0.2, 0.4, 1, 1.4 and 2 mM in D_2O. 90
Figure 4.34: Reciprocal plot for the determination of the association constant between budesonide and DIMEB in D_2O by ^1H NMR based on the chemical shift of H-C_{19} and H-C_4 at 1.2570 and 5.9645 ppm (Mean ± SD, n=3).....92
Figure 4.35: Determination of the stoichiometry of the complex between budesonide and DIMEB in D_2O by ^1H NMR based on the chemical shift change of H-C_{19} and H-C_4 protons of budesonide. 94
Figure 4.36: IR spectra of pure budesonide, βCD, physical mixture and co-evaporation complex showing a broad band of OH group in the range or 3300-3500 cm^{-1} and other shifts related to the quinone ring of budesonide.....96
Figure 4.37: IR spectra of pure budesonide, βCD, physical mixture and co-evaporation complex showing shifts of the quinone ring of budesonide. 96
Figure 4.38: IR spectra of pure budesonide, TRIMEB, physical mixture and co-evaporation complex showing a broad band of OH group in the range or 3300-3500 cm^{-1} and other shifts related to the quinone ring of budesonide.....97
Figure 4.39: IR spectra of pure budesonide, TRIMEB, physical mixture and co-evaporation complex showing shifts of the quinone ring of budesonide. 97

Figure 4.40: IR spectra of pure budesonide, DIMEB, physical mixture and co-evaporation complex showing a broad band of OH group in the range or 3300-3500 cm^{-1} and other shifts related to the quinone ring of budesonide. 98
Figure 4.41: IR spectra of pure budesonide, DIMEB, physical mixture and co-evaporation complex showing shifts of the quinone ring of budesonide. 99
Figure 4.42: Raman spectra of pure budesonide, pure βCD and 1:1 complex of physical mixture and co-evaporation complex showing shifts in the quinone ring bands. 100
Figure 4.43: Raman spectra of pure budesonide, pure TRIMEB and 1:1 complex of physical mixture and co-evaporation complex showing shifts in the quinone ring bands. 100
Figure 4.44: Raman spectra of pure budesonide, pure DIMEB and 1:1 complex of physical mixture and co-evaporation complex showing shifts in the quinone ring bands. 101
Figure 4.45: BUD chemical shift differences in the high field region complexed with 2 mM βCD, DIMEB and TRIMEB. 106
Figure 4.46: BUD chemical shift differences in the low field region complexed with 2 mM βCD, DIMEB and TRIMEB. 106
Figure 4.47: Chemical structure of (a) budesonide, (b) prednisolone and (c) hydrocortisone 107
Figure 4.48: Inclusion complex of the budesonide and (a) βCD, (b) DIMEB and (c) TRIMEB. The black balls represent the methoxyl groups in the DIMEB and TRIMEB molecules. 113
Figure 5.1: ^{1}H NMR spectra of BUD with solvent suppression at 4.38 and 2.15 ppm in HPFP. 116
Figure 5.2: Chemical shift of (a) BUD, (b) BDP, (c) MOM and (d) FLU in $CDCl_3$ (lower) and HPFP (upper) in high field region showing an upfield chemical shift in HPFP compared to $CDCl_3$. 118
Figure 5.3: Chemical shift of (a) BUD, (b) BDP, (c) MOM and (d) FLU in $CDCl_3$ (lower) and HPFP (upper) in low field region showing an upfield chemical shift in HPFP compared to $CDCl_3$ 119
Figure 5.4: Budesonide (0.0875 mM) chemical shift in high field region (0.1-0.9 ppm) with the addition of TRIMEB at 0, 0.1, 0.2, 0.3, 0.4 and 0.5 mM in HPFP. 121

Figure 5.5: Budesonide (0.0875 mM) chemical shift in low field region (5.1-6.7 ppm) with the addition of TRIMEB at 0, 0.1, 0.2, 0.3, 0.4 and 0.5 mM in HPFP. 122
Figure 5.6: Budesonide (0.0875 mM) chemical shift in high field region (0.1-0.9 ppm) with the addition of TRIMEB at 0, 0.4, 0.8, 1.2, 1.6 and 2 mM in HPFP.124
Figure 5.7: Budesonide (0.0875 mM) chemical shift in low field region (5.1-6.7 ppm) with the addition of TRIMEB at 0, 0.4, 0.8, 1.2, 1.6 and 2 mM in HPFP.125
Figure 5.8: pure *R*-enantiomer of BUD (0.0875 mM) chemical shift in high field region (0.2-0.85 ppm) with the addition of TRIMEB at 0, 0.4, 0.8, 1.2, 1.6 and 2 mM in HPFP. The shifted peak annotated with star was assigned to *R*-enantiomer of BUD. 127
Figure 5.9: Racemic BUD (0.0875 mM) chemical shift in high field region (0.2-0.85 ppm) with the addition of TRIMEB at 0, 0.4, 0.8, 1.2, 1.6 and 2 mM in HPFP. The shifted peak annotated with star was assigned to *R*-enantiomer of BUD whereas the peak at 0.34 ppm (annotated with dot) was assigned to *S*-enantiomer of BUD 128
Figure 5.10: Pure *R*-enantiomer of BUD (0.0875 mM) chemical shift in low field region (5.1-6.7 ppm) with the addition of TRIMEB at 0, 0.4, 0.8, 1.2, 1.6 and 2 mM in HPFP.....129
Figure 5.11: Racemic BUD (0.0875 mM) chemical shift in low field region (5.1-6.7 ppm) with the addition of TRIMEB at 0, 0.4, 0.8, 1.2, 1.6 and 2 mM in HPFP. The peaks annotated with star and dot were related to *R*- and *S*-enantiomer of BUD. 130
Figure 5.12: Reciprocal plot for the determination of association constant between *R*-enantiomer of BUD and TRIMEB in HPFP by ^{1}H NMR depending on the chemical shift differnce of H-C_1 proton at 6.5666 and 6.5491 ppm (Mean ± SD, n=3).....132
Figure 5.13: Reciprocal plot for the determination of association constant between *S*-enantiomer of BUD and TRIMEB in HPFP by ^{1}H NMR depending on the chemical shift differnce of H-C_1 proton at 6.5431 and 6.5600 ppm (Mean ± SD, n=3).....132
Figure 5.14: Determination of the stoichiometry of the complex between budesonide and TRIMEB in HPFP by ^{1}H NMR based on H-C_1 proton of budesonide. 134

Figure 5.15: BDP (0.2 mM) chemical shift in high field region (0.1-1.2 ppm) with the addition of TRIMEB at 0, 0.4, 0.8, 1.2, 1.6 and 2 mM in HPFP. 135
Figure 5.16: BDP (0.2 mM) chemical shift in low field region (5.2-6.7 ppm) with the addition of TRIMEB at 0, 0.4, 0.8, 1.2, 1.6 and 2 mM in HPFP. 136
Figure 5.17: Reciprocal plot for the determination of association constant between BDP and TRIMEB in HPFP by ^{1}H NMR depending on the chemical shift at 1.0206 and 5.2943 ppm (Mean ± SD, n=3). 138
Figure 5.18: MOM (0.02 mM) chemical shift in high field region (0.1-1.2 ppm) with the addition of TRIMEB at 0, 0.4, 0.8, 1.2, 1.6 and 2 mM in HPFP.....139
Figure 5.19: MOM (0.02 mM) chemical shift in low field region (5.2-6.9 ppm) with the addition of TRIMEB at 0, 0.4, 0.8, 1.2, 1.6 and 2 mM in HPFP.....140
Figure 5.20: Reciprocal plot for the determination of association constant between MOM and TRIMEB in HPFP by ^{1}H NMR depending on the chemical shift at 1.0263 ppm (Mean ± SD, n=3).. 142
Figure 5.21: FLU (0.02 mM) chemical shift in high field region (0.1-1.2 ppm) with the addition of TRIMEB at 0, 0.4, 0.8, 1.2, 1.6 and 2 mM in HPFP. 143
Figure 5.22: FLU (0.02 mM) chemical shift in low field region (5.5-6.6 ppm) with the addition of TRIMEB at 0, 0.4, 0.8, 1.2, 1.6 and 2 mM in HPFP. 144
Figure 5.23: Reciprocal plot for the determination of association constant between FLU and TRIMEB in HPFP by ^{1}H NMR depending on the chemical shift at 0.8560 ppm (Mean ± SD, n=3). 145
Figure 5.24: BUD (0.0875 mM) chemical shift in high field region (0.1-0.9 ppm) with the addition of DIMEB at 0, 0.075, 0.15, 0.225, 0.3 and 0.375 mM in HPFP. The peak annotated with star was related to *R*-enantiomer of BUD. 147
Figure 5.25: BUD (0.0875 mM) chemical shift in low field region (5.2-6.7 ppm) with the addition of DIMEB at 0, 0.075, 0.15, 0.225, 0.3 and 0.375 mM in HPFP. 148
Figure 5.26: Reciprocal plot for the determination of association constant between budesonide and DIMEB in HPFP by ^{1}H NMR depending on the chemical shift at 6.5666 ppm (Mean ± SD, n=3). 149
Figure 5.27: Determination of the stoichiometry of the complex between budesonide and DIMEB in HPFP by ^{1}H NMR based on H-C_1 proton of budesonide. 151
Figure 5.28: BDP (0.2 mM) chemical shift in high field region (0.1-1.1 ppm) with the addition of DIMEB at 0, 0.075, 0.15, 0.225, 0.3 and 0.375 mM in HPFP. .152

Figure 5.29: BDP (0.2 mM) chemical shift in low field region (5.2-6.6 ppm) with the addition of DIMEB at 0, 0.075, 0.15, 0.225, 0.3 and 0.375 mM in HPFP. .153
Figure 5.30: Reciprocal plot for the determination of association constant between BDP and TRIMEB in HPFP by ^{1}H NMR depending on the chemical shift at 5.2943 ppm (Mean ± SD, n=3). 154
Figure 5.31: Chemical structure of BUD, BDP, MOM and FLU.....157
Figure 5.32: Chemical structure of (a) prednisolone and (b) 6*α*-methyl prednisolone. 157
Figure 5.33: Chemical shift in high field region (0.2-0.85 ppm) of (a) pure BUD, (b) racemic and (c) pure *R*-enantiomer of BUD (0.0875 mM) with 2 mM TRIMEB in HPFP. The peaks annotated with star and dot were assigned to *R*- and *S*-enantiomer of BUD. 160
Figure 5.34: Chemical shift in low field region (5.1-6.7 ppm) of (a) pure BUD, (b) racemic and (c) pure *R*-enantiomer of BUD (0.0875 mM) with 2 mM TRIMEB in HPFP. The peaks annotated with star and dot were assigned to *R*- and *S*-enantiomer of BUD. 161
Figure 6.1: Schematic view of the design of selective SERS substrates through functionalisation of metal nanoparticle surfaces with per-6-thio-*β*-cyclodextrin. 163
Figure 6.2: The synthesis of per-6-thio-*β*-cyclodextrin.[167] 164
Figure 6.3: UV-Vis absorption spectrum of Ag-NP formulation (λ_{max} = 397 nm). 165
Figure 6.4: UV-Vis absorption spectra of seed (solid line, λ_{max} = 520 nm) and final (dashed line, λ_{max} = 532 nm) Au-NP formulations showing the bathochromic shift of the final formulation consistent with its larger particle size. 165
Figure 6.5: Particle size of (a) uncentrifuged and (b) centrifuged Ag-NPs from DLS. 166
Figure 6.6: Particle size of (a) uncentrifuged Ag-NPs without and with SCD and (b) centrifuged Ag-NPs without and with SCD from DLS. 167
Figure 6.7: Particle size of (a) seed Au-NPs, (b) uncentrifuged and (c) centrifuged final Au-NPs from DLS. 168
Figure 6.8: Particle size of (a) uncentrifuged Au-NPs without and with SCD and (b) centrifuged Au-NPs without and with SCD from DLS. 168

Figure 6.9: TEM images of Ag-NP formulations: (a),(b) two images for the same non-centrifuged sample; (c) the size distribution histogram of non-centrifuged material; (d),(e) two images for the same centrifuged sample showing the agglomeration of particles. 170
Figure 6.10: TEM different images of SCD-Ag-NP prepared with the same sample of (a) non-centrifuged Ag-NP and (b) centrifuged Ag-NP. 171
Figure 6.11: TEM analysis of seed Au-NPs: (a) TEM images showing largely spherical nanoparticles loosely associated in chains; (b) a size distribution histogram 172
Figure 6.12: TEM analysis of final Au-NP formulations: (a) two images of the same non-centrifuged Au NPs solution showing both spherical and ellipsoidal particles; (b) size distribution histogram of particle sizes; (c) two images of the same centrifuged product showing loose associate of spherical and ellipsoidal NPs. 173
Figure 6.13: TEM different images of the same sample of (a) non-centrifuged SCD-Au-NP and (b) centrifuged SCD-Au-NP 174
Figure 6.14: The general ring numbering scheme for the steroid ring framework and the corticosteroids selected for Raman spectroscopy studies.....177
Figure 6.15: Offset Raman Spectra for selected corticosteroids (BUD = budesonide, FLU = fluticasone proprionate, BDP = beclomethasone dipropionate, MOM = mometasone furoate, BCL = beclomethasone). 178
Figure 6.16: Raman spectra of selected corticosteroids (BUD = budesonide, FLU = fluticasone proprionate, BDP = beclomethasone dipropionate, MOM = mometasone furoate} in the region 3200-2700 cm^{-1}. 181
Figure 6.17: Raman spectra of selected corticosteroids (BUD = budesonide, FLU = fluticasone proprionate, BDP = beclomethasone dipropionate, MOM = mometasone furoate} in the region 1800-1500 cm^{-1}. 182
Figure 6.18: Raman spectra of selected corticosteroids (BUD = budesonide, FLU = fluticasone propionate, BDP = beclomethasone dipropionate, MOM = mometasone furoate) in the region 1450-165 cm^{-1}. 183
Figure 6.19: Raman spectrum of SCD collected using 633 nm excitation, 50x objective, 100% laser power, 10 s exposure time: (a) 856 accumulations; (b) 10 accumulations. 184
Figure 6.20: Raman spectrum of metal SCD-M-NP formulations compared to reference spectrum of SCD: (i) the SCD reference spectrum (after background

removal), (ii) uncentrifuged Ag-NP after treatment with SCD, (iii) centrifuged Ag-NP after treatment with SCD, (iv) uncentrifuged Au-NP after treatment with SCD, (v) centrifuged Au-NP after treatment with SCD. 186
Figure 6.21: Raman spectra of budesonide (BUD) after mixing with Ag-NP formulations: (i) BUD reference spectrum (after background removal), (ii) BUD with uncentrifuged Ag-NP (iii) BUD with centrifuged Ag-NP. 188
Figure 6.22: Predicted interaction of Bud with naked Ag NPs.....189
Figure 6.23: Baseline-subtracted Raman spectra of budesonide (BUD) after mixing with Ag-NP formulations (after baseline removal) showing the different enhancements for naked and SCD-functionalised Ag-NP: (i) BUD reference spectrum, (ii) BUD with uncentrifuged Ag-NP (iii) BUD with uncentrifuged Ag-SCD-NP. 190
Figure 6.24: Predicted interaction of BUD with Ag-SCD NPs 191
Figure 6.25: Baseline-subtracted Raman spectra of budesonide (BUD) after mixing with Au-NP formulations (after baseline removal) showing the different enhancements for naked and SCD-functionalised Au-NP: (i) BUD reference spectrum, (ii) BUD with centrifuged Au-NP (iii) BUD with centrifuged SCD-Au-NP. 192
Figure 6.26: Baseline-subtracted Raman spectra of beclomethasone dipropionate (BDP) after mixing with metal-NP formulations (after baseline removal) showing the different enhancements for naked and SCD-functionalised particles: (i) BDP reference spectrum, (ii) BDP with centrifuged Ag-NP (iii) BDP with centrifuged SCD-Ag-NP, (iv) BDP with centrifuged Au-NP, (v) BDP with centrifuged SCD-Au-NP. 194
Figure 6.27: Predicted interaction of BDP with metal NPs in (a) naked metal NP and (b) SCD-functionalised NPs. 195
Figure 6.28: Baseline-subtracted Raman spectra of fluticasone propionate (FLU) after mixing with metal-NP formulations showing the different enhancements for naked and SCD-functionalised particles: (i) FLU reference spectrum, (ii) FLU with Ag-NP (iii) FLU with SCD-Ag-NP, (iv) FLU with Au-NP, (v) FLU with SCD-Au-NP. 197
Figure 6.29: Baseline-subtracted Raman spectra of mometasone furoate (MOM) after mixing with metal-NP formulations showing the different enhancements for naked and SCD-functionalised particles: (i) MOM reference

spectrum, (ii) MOM with Ag-NP (iii) MOM with SCD-Ag-NP, (iv) MOM with Au-NP, (v) MOM with SCD-Au-NP. 197
Figure 7.1: Inclusion complex of the budesonide and (a) βCD, (b) DIMEB and (c) TRIMEB. The black balls represent the methoxyl groups in the DIMEB and TRIMEB molecules. 202

List of Tables

Table 1.1: Physicochemical properties of pMDI propellants[71] 10
Table 2.1: Supplier, purity and the batch information of the materials used in this study 29
Table 2.2: The preparetion of vanillin and *β*CD solutions based on continous variation method and analysed by UV–Vis spectroscopy. 30
Table 2.3: The preparetion of BUD and *β*CD/TRIMEB solutions in EtOH:H_2O (50:50) based on continous variation method and analysed by UV-Vis spectroscopy. 31
Table 2.4: The preparetion of BUD and *β*CD/TRIMEB solutions in H_2O based on continous variation method and analysed by UV-Vis spectroscopy. 31
Table 2.5: The preparetion of vanillin and *β*CD solutions based on continous variation method and analysed by ^{1}H NMR. 33
Table 2.6: The preparetion of BUD and *β*CD/DIMEB/TRIMEB solutions based on continous variation method and analysed by ^{1}H NMR 34
Table 2.7: The preparetion of BUD and DIMEB/TRIMEB solutions based on continous variation method and analysed by ^{1}H NMR. 34
Table 2.8: Different corticosteroids solutions prepared by mixing with Ag or Au NPs and SCD 38
Table 3.1: Results of ^{1}H NMR analysis for the determination of stoichiometry between vanillin and *β*CD 43
Table 3.2: Results of the determination of the association constant between vanillin and *β*CD using ^{1}H NMR 45
Table 3.3: Results of the determination of the stoichiometry between vanillin and *β*CD using UV-Vis spectroscopy. 46
Table 3.4: Results of the determination of the association constant between vanillin and *β*CD added at 0, 2, 4, 6 and 8 mM in H_2O using UV-Vis spectroscopy. 47
Table 3.5: Results of the determination of the association constant between vanillin and *β*CD added at 2, 4, 6 and 8 mM in H_2O using UV-Vis spectroscopy. 48
Table 4.1: Results of the complexation between budesonide and *β*CD added at 0, 2, 4, 6 and 8 mM in EtOH/H_2O (50:50) using UV-Vis spectroscopy. 51

Table 4.2: Results of the stability constant determination between budesonide and βCD added at 2, 4, 6 and 8 mM in EtOH/H_2O (50:50) using UV-Vis spectroscopy. 52
Table 4.3: Results of the complexation between budesonide and βCD added at 0, 2, 3, 4, 5 and 7 mM in H_2O using UV-Vis spectroscopy. 52
Table 4.4: Results of the stability constant determination between budesonide and βCD added at 2, 3, 4, 5 and 7 mM in H_2O using UV-Vis spectroscopy. 52
Table 4.5: Results of the determination of the stoichiometry between budesonide and βCD in EtOH/H_2O (50:50) using UV-Vis spectroscopy. 53
Table 4.6: Results of the determination of the stoichiometry between budesonide and βCD in H_2O using UV-Vis spectroscopy. 54
Table 4.7: Results of the complexation and the stability constant determination between budesonide and TRIMEB added at 0, 0.4, 0.6, 0.8, 1 and 1.4 mM in EtOH/H_2O (50:50) using UV-Vis spectroscopy. 55
Table 4.8: Results of the stability constant determination between budesonide and TRIMEB added at 0.4, 0.6, 0.8, 1 and 1.4 mM in EtOH/H_2O (50:50) using UV-Vis spectroscopy. 55
Table 4.9: Results of the complexation and the stability constant determination between budesonide and TRIMEB added at 0, 0.4, 0.6, 0.8, 1 and 1.4 mM in H_2O using UV-Vis spectroscopy. 55
Table 4.10: Results of the stability constant determination between budesonide and TRIMEB added at 0.4, 0.6, 0.8, 1 and 1.4 mM in H_2O using UV-Vis spectroscopy. 56
Table 4.11: Results of the determination of the stoichiometry between budesonide and TRIMEB in EtOH/H_2O (50:50) using UV-Vis spectroscopy. 57
Table 4.12: Results of the determination of the stoichiometry between budesonide and TRIMEB in H_2O using UV-Vis spectroscopy. 57
Table 4.13: Results of the chemical shift of budesonide and TRIMEB added at 0, 1, 2, 4, 6, and 8 mM in CD_3CN using ^1H NMR. 59
Table 4.14: Results of the chemical shift of budesonide and DIMEB added at 0, 1, 2, 4, 6, and 8 mM in CD_3CN using ^1H NMR. 59
Table 4.15: Results of the chemical shift of budesonide and TRIMEB added at 0, 1, 2, 4, 6, and 8 mM in $CDCl_3$ using ^1H NMR. 59
Table 4.16: Results of the chemical shift of budesonide and DIMEB added at 0, 1, 2, 4, 6, and 8 mM in $CDCl_3$ using ^1H NMR. 60

Table 4.17: The calculated K for the complex formed between budesonide and (TRIMEB, DIMEB) in $CDCl_3$ 61
Table 4.18: results of the chemical shift of budesonide and TRIMEB added at 0, 1, 2, 4, 6, and 8 mM in MeOD using ^1H NMR. 61
Table 4.19: results of the chemical shift of budesonide and DIMEB added at 0, 1, 2, 4, 6, and 8 Mm in MeOD using ^1H NMR. 62
Table 4.20: The calculated K for the complex formed between budesonide and (TRIMEB, DIMEB) in MeOD.....63
Table 4.21: ^1H NMR spectral assignment of the budesonide in $CDCl_3$.[180,181]....75
Table 4.22: Chemical shift of budesonide in D_2O and compared to those in $CDCl_3$ 75
Table 4.23: Results of the chemical shift of budesonide and βCD added at 0, 0.2, 0.4, 1, 1.4 and 2 mM in D_2O using ^1H NMR. 80
Table 4.24: Results of the complexation between budesonide and βCD added at 0.2, 0.4, 1, 1.4 and 2 mM in D_2O using ^1H NMR based on the chemical shift of H-C_{19} at 1.2570 ppm. 80
Table.4.25: Results of the stability constant between budesonide and βCD added at 0.2, 0.4, 1, 1.4 and 2 mM in D_2O using ^1H NMR. 81
Table 4.26: Results of ^1H NMR analysis for the determination of stoichiometry between budesonide and βCD in D_2O based on the chemical shift of H-C_2 proton of budesonide at 6.1931 ppm. 81
Table 4.27: Results of ^1H NMR analysis for the determination of stoichiometry between budesonide and βCD in D_2O based on the chemical shift of H-C_2 proton of budesonide at 6.1744 ppm. 82
Table 4.28: Results of the chemical shift of budesonide and TRIMEB added at 0, 0.2, 0.4, 1, 1.4 and 2 mM in D_2O using ^1H NMR. 85
Table 4.29: Results of the complexation between budesonide and TRIMEB added at 0.2, 0.4, 1, 1.4 and 2 mM in D_2O using ^1H NMR based on the chemical shift differences of H-C_{19} and H-C_4 at 1.2570 and 5.9645 ppm. 85
Table 4.30: Results of the stability constant between budesonide and TRIMEB added at 0.2, 0.4, 1, 1.4 and 2 mM in D_2O using ^1H NMR. 86
Table 4.31: Results of ^1H NMR analysis for the determination of stoichiometry between budesonide and TRIMEB in D_2O based on the chemical shift of H-C_2 proton of budesonide at 6.1931 ppm. 87

Table 4.32: Results of ^{1}H NMR analysis for the determination of stoichiometry between budesonide and TRIMEB in D_2O based on the chemical shift of H-C_2 proton of budesonide at 6.1744 ppm. 87
Table 4.33: Results of the chemical shift of budesonide and DIMEB added at 0, 0.2, 0.4, 1, 1.4 and 2 mM in D_2O using ^{1}H NMR. 91
Table 4.34: Results of the complexation between budesonide and DIMEB added at 0.2, 0.4, 1, 1.4 and 2 mM in D_2O using ^{1}H NMR based on the chemical shift of H-C_{19} and H-C_4 at 1.257 and 5.9645 ppm. 91
Table 4.35: Results of the stability constant between budesonide and DIMEB added at 0.2, 0.4, 1, 1.4 and 2 mM in D_2O using ^{1}H NMR. 92
Table 4.36: Results of ^{1}H NMR analysis for the determination of the stoichiometry between budesonide and DIMEB in D_2O based on the chemical shift of H-C_{19} proton of budesonide at 1.2570 ppm. 93
Table 4.37: Results of ^{1}H NMR analysis for the determination of the stoichiometry between budesonide and TRIMEB in D_2O based on the chemical shift of H-C_4 proton of budesonide at 5.9645 ppm. 93
Table 4.38: IR bands of budesonide.[182,183].....94
Table 4.39: IR bands of *β*CD.[184,185].....95
Table 4.40: Main bands of pure budesonide, pure *β*CD and their complexes (physical mixture and co-evaporation) 95
Table 4.41: Main bands of pure budesonide, pure TRIMEB and their complexes (physical mixture and co-evaporation) 97
Table 4.42: Main bands of pure budesonide, pure DIMEB and their complexes (physical mixture and co-evaporation) 98
Table 4.43: Complex formation of budesonide with *β*CD, DIMEB and TRIMEB in three solvent system; D_2O, MeOD and $CDCl_3$. 103
Table 4.44: Chemical shift displacements of BUD with 2 mM *β*CD, DIMEB and TRIMEB in D_2O related to the chemical shift of free BUD.....105
Table 4.45: The chemical shift difference of budesonide peaks without and with the addition of *β*CD and TRIMEB.....114
Table 5.1: Chemical shift of BUD, BDP, MOM and FLU in HPFP compared to their chemical shift in $CDCl_3$.....117
Table 5.2: Assignment of BUD, BDP, MOM and FLU in HPFP.....117
Table 5.3: Results of the chemical shift of budesonide and TRIMEB added at 0, 0.4, 0.8, 1.2, 1.6 and 2 mM in HPFP using ^{1}H NMR. 131

Table 5.4: Results of the complexation between *R*-enantiomer of budesonide and TRIMEB added at 0.4, 0.8, 1.2, 1.6 and 2 mM in HPFP using ^{1}H NMR depending on the chemical shift differnce of H-C_1 proton 6.5666 and 6.5491 ppm. 131
Table 5.5: Results of the complexation between *S*-enantiomer of budesonide and TRIMEB added at 0.4, 0.8, 1.2, 1.6 and 2 mM in HPFP using ^{1}H NMR depending on the chemical shift differnce of H-C_1 proton at 6.5431 and 6.5600 ppm. 132
Table 5.6: Results of the stability constant between *R* and *S*-enantiomers of budesonide and TRIMEB added at 0, 0.4, 0.8, 1.2, 1.6 and 2 mM in HPFP using ^{1}H NMR. 133
Table 5.7: Results of ^{1}H NMR analysis for the determination of stoichiometry between budesonide and TRIMEB in HPFP based on the chemical shift at H-C_1 proton of budesonide at 6.5666 ppm. 133
Table 5.8: Results of the chemical shift of BDP and TRIMEB added at 0, 0.4, 0.8, 1.2, 1.6 and 2 mM in HPFP using ^{1}H NMR. 137
Table 5.9: Results of the complexation between BDP and TRIMEB added at 0.4, 0.8, 1.2, 1.6 and 2 mM in HPFP using ^{1}H NMR depending on the chemical shift at 1.0206 and 5.2943 ppm. 137
Table 5.10: Results of the stability constant between BDP and TRIMEB added at 0.4, 0.8, 1.2, 1.6 and 2 mM in HPFP using ^{1}H NMR. 138
Table 5.11: Results of the chemical shift of MOM and TRIMEB added at 0, 0.4, 0.8, 1.2, 1.6 and 2 mM in HPFP using ^{1}H NMR. 141
Table 5.12: Results of the complexation between MOM and TRIMEB added at 0.4, 0.8, 1.2, 1.6 and 2 mM in HPFP using ^{1}H NMR depending on the chemical shift at 1.0263 ppm. 141
Table 5.13: Results of the stability constant between MOM and TRIMEB added at (0, 0.4, 0.8, 1.2, 1.6 and 2 mM) in HPFP using ^{1}H NMR. 142
Table 5.14: Results of the chemical shift of FLU and TRIMEB added at 0, 0.4, 0.8, 1.2, 1.6 and 2 mM in HPFP using ^{1}H NMR. 145
Table 5.15: Results of the complexation between FLU and TRIMEB added at 0.4, 0.8, 1.2, 1.6 and 2 mM in HPFP using ^{1}H NMR depending on the chemical shift at 0.8560 ppm. 145
Table 5.16: Results of the stability constant between FLU and TRIMEB added at 0, 0.4, 0.8, 1.2, 1.6 and 2 mM in HPFP using 600 MHz ^{1}H NMR. 146

Table 5.17: Results of the chemical shift of budesonide and DIMEB added at 0, 0.075, 0.15, 0.225, 0.3 and 0.375 mM in HPFP using ^{1}H NMR. 149
Table 5.18: Results of the complexation between budesonide and DIMEB added at 0.075, 0.15, 0.225, 0.3 and 0.375 mM in HPFP using ^{1}H NMR depending on the chemical shift at 6.5666 ppm. 149
Table 5.19: Results of the stability constant between budesonide and DIMEB added at 0, 0.075, 0.15, 0.225, 0.3 and 0.375 mM in HPFP using ^{1}H NMR. ..150
Table 5.20: Results of ^{1}H NMR analysis for the determination of stoichiometry between budesonide and DIMEB in HPFP based on the chemical shift at H-C_1 proton of budesonide at 6.5666 ppm. 150
Table 5.21: Results of ^{1}H NMR analysis for the determination of stoichiometry between budesonide and DIMEB in HPFP based on the chemical shift at H-C_1 proton of budesonide at 6.5600 ppm. 150
Table 5.22: Results of the chemical shift of BDP and DIMEB added at 0, 0.075, 0.15, 0.225, 0.3 and 0.375 mM in HPFP using ^{1}H NMR. 154
Table 5.23: Results of the complexation between BDP and DIMEB added at 0.075, 0.15, 0.225, 0.3 and 0.375 mM in HPFP using ^{1}H NMR depending on the chemical shift at 5.2943 ppm. 154
Table 5.24: Results of the stability constant between BDP and DIMEB added at 0.075, 0.15, 0.225, 0.3 and 0.375 mM in HPFP using ^{1}H NMR. 155
Table 5.25: A summary of the chemical shift displacements (in ppm) for BUD, BDP, MOM and FLU with 2 mM TRIMEB in HPFP related to the chemical shift of the free compounds. 156
Table 5.26: Chemical shift displacements of the BUD and BDP with 0.375 mM DIMEB compared to the chemical shift of the free compound. 158
Table 6.1: Calculation of the % NP yield for prepared Ag and Au-NP.....175
Table 6.2: Assignment of the Raman peaks of the Raman spectra of budesonide (BUD), fluticasone propionate (FLU), beclomethasone dipropionate (BDP) and mometasone furoate (MOM). 179
Table 6.3: Assignment of SCD Raman spectrum on the basis of the *β*CD assignment.....185
Table 7.1: A summary of the chemical shift displacements observed (in ppm) for BUD with 2 mM *β*CD, DIMEB and TRIMEB in D_2O related to the chemical shift of free BUD. 200

Table 7.2: A summary of the chemical shift displacements (in ppm) for BUD, BDP, MOM and FLU with 2 mM TRIMEB in HPFP related to the chemical shift of the free compounds. 202

List of Abbreviations and Symbols

% CV	% Coefficient of Variation
®	Registered Trademark
Å	Angstrom
ADC	Analogue-to-Digital Converter
Ag NPs	Silver nanoparticles
API	Active Pharmaceutical Ingredient
Au NPs	Gold nanoparticles
B_0	Applied Magnetic Field
BCL	Beclometasone
BDP	Beclomethasone dipropionate
BUD	Budesonide
CDs	Cyclodextrins
CF	Cystic Fibrosis
CFC	Chlorofluorocarbon
COPD	Chronic Obstructive Pulmonary Disease
dB	Decibel
DIMEB	Heptakis(2,6-di-O-methyl)-*β*-cyclodextrin
DLS	Dynamic Light Scattering
DPI	Dry Powder Inhaler
DPPC	dipalmitoylphosphatidylcholine
DSC	Differential Scanning Calorimetry
FID	Free Induction Decay
FLU	Fluticasone propionate
GOLD	Global Initiative for Chronic Obstructive Lung Disease
GINA	Global Initiative for Asthma
HFA	Hydrofluoroalkane
HFA 134a	1,1,1,2-tetrafluoroethane
HFA 227	1,1,1,2,3,3,3-heptafluoropropane
HP*β*CD	2-Hydroxypropyl-*β*-cyclodextrin
HPFP	2H,3H-decafluoropentane
ICP-OES	Inductively Coupled Plasma Optical Emission Spectrometry
ICS	Inhaled Corticosteroid

IL-8	Interleukin-8
IPPs	Inhaled Pharmaceutical Products
LSP	Localised surface plasmon
MMAD	Mass Median Aerodynamic Diameter
MOM	Mometasone furoate
PEG	Polyethylene Glycol
PFGs	Pulsed Field Gradients
pMDI	Pressurised Metered Dose Inhaler
SCD	Thiol functionalised *β*CD
SERS	Surface-enhanced Raman scattering
TNF-*α*	Tumor Necrosis Factor-alpha
TRIMEB	Heptakis(2,3,6-tri-O-methyl)-*β*-cyclodextrin
WHO	World Health Organisation

1 Introduction

1.1 Physiology of the lung, diseases and associated responses

Administration of drugs *via* the pulmonary route was originally introduced 400 years ago in the Middle East and India.[1-3] Many drugs are favourably administered *via* the lung due to the advantages of having a large surface area and the existence of the epithelium with a thin membrane together with the low aqueous fluid available at the site of absorption. This enhances the drug absorption process resulting in quick uptake and fast onset of action compared to any other route of administration, with the exception of intravenous injection.[4,5] Another advantage of this route is that the metabolism process decreases as a result of lower metabolising enzymes in the lung compared to the oral delivery route.[4,6,7] Accordingly, the dose of the drug is reduced compared to the oral route, for example the salbutamol dose decreases to half when administered *via* the lung compared to oral administration[3] and as a result, the systematic adverse effects are reduced.[5]

Nowadays, different drugs are formulated to be administered by the pulmonary route to treat pulmonary diseases locally or to address some systematic diseases such as insulin for the treatment of diabetes mellitus and levodopa for Parkinson disease, which are not effective when given by oral administration.[3,8] It has been estimated that the around twenty Active Pharmaceutical Ingredients (APIs) in 65 different medications are administrated through the respiratory system.[2,9] Research published by Ritchie in 2009 shows that 29 out of 81 marketed pulmonary drugs are delivered directly to treat local pulmonary illnesses.[10] Lower doses are administered *via* the pulmonary route to achieve the clinical effect without a reduction in the concentration at the action site such as inhaled corticosteroids and beta 2 agonists or a combination of the two groups which are administered in low doses that in turn reduce the adverse effects and produce rapid onset of action.[3,11] Other examples are antibiotics, which are used to treat infectious diseases such as tuberculosis and cystic fibrosis (CF). In the case of CF, the dose is directly delivered to the infectious site which is the endobronchial space and therefore has the advantage of decreasing both the systemic adverse effects and the toxicity.[12]

Chronic Obstructive Pulmonary Disease (COPD) is a main cause of global mortality and morbidity where many people are affected and die from the disease itself or from the complications.[13,14] It is considered the fourth leading cause of mortality, which is expected to be the third leading cause of mortality by 2020.[14] It has been estimated that around 3 million UK people have COPD with 900,000 diagnosed as affected by COPD. Around 2 million are left without a definite diagnosis and most of these cases are diagnosed at the age of 50.[15] The World Health Organisation (WHO) estimated that the COPD burden is projected to increase and the number of cases affected is estimated to move from twelfth to fifth by 2020.[16] Regarding asthma, around 300 million people are affected by asthma in the world[17-19] with 250,000 mortalities per year.[20]

Limited progress has been made in the development of therapeutic medications to treat COPD, however, a huge advancement in recent years has been achieved to develop medications with a variety of dosage forms to address the symptoms of asthma and this is due to a better understanding of the disease mechanism.[16] The reason behind the difficulty in the development of COPD drugs is the lack of proper models to test COPD drugs which needs long term studies (not less than 3 years) and a high number of patients.[16] Another reason is the unavailability of suitable animal models to test these drugs.[21] Also, a difficulty in determining the suitable markers used to investigate the immediate efficacy of the new therapy. On the other hand, drug development in the treatment of COPD is ongoing with the existence of some drugs in preclinical and clinical stages of assessment.[16]

The global initiative for asthma (GINA) defines asthma as a chronic inflammatory illness, which affects a number of cells and also cellular elements of the airways. It is accompanied by an increase in the hyperresponsiveness of the airways and as a result the patient suffers from recurrent symptoms of wheezing, breathlessness, chest tightness and coughing. It is also associated with obstruction in the air flow which is reversible spontaneously or after receiving therapy.[19,22] Chronic inflammation causes the smooth muscle contraction of the lungs which leads to the narrowing of the airway. This change is associated with the increase in the easinophils and the thickening of the lamina reticularis. In addition, the size of the airway smooth muscle increases along with the number of the mucous glands by time. Other cells have also

been included in the inflammation process such as neutrophils, T lymphocyte and macrophages, with the existence of other immune system compartments such as chemokines, histamine, cytokines and leukotrienes.[23]

The Global Initiative for Chronic Obstructive Lung Disease (GOLD) defines COPD as a persistent airflow limitation accompanied by the chronic inflammatory response of the airways to harmful particles or gases. The airway limitation results from the damage to the parenchyma and the airways, in addition to that caused by smoking.[15] Although it is progressive over time, it is still classified as a preventable and treatable illness. The main inflammatory cells included in COPD patients are neutrophils and macrophages which are estimated to be in higher number compared to patients with chronic bronchitis.[22]

Although the two diseases are classified as chronic inflammatory illnesses causing bronchoconstriction, the main difference between them is the reversibility of the airway obstruction where it is reversible with or without therapy in the case of asthma but not so in COPD. Another difference is the aging of the population where the asthma affects people in their early childhood while COPD generally affects elderly people into and beyond their sixties.[22,24] A study conducted by Keatings *et al*. shows that cytokines, tumor necrosis factor-alpha (TNF-α) and interleukin-8 (IL-8) increases in the case of COPD and that might be responsible for the inflammation.[25]

Current treatments are available to alleviate the episodes by reducing the inflammation and treat asthma, however, these are not effective in the case of COPD.[26] Smoking cessation is a non-pharmacological intervention which is considered effective in the relieving the symptoms and preventing the development of COPD.[27,28] Reducing the exposure to the risk factors could be considered as a part of treatment such as avoiding certain food, drugs (such as aspirin and beta blockers) or any additives that are known to cause episodes of the disease. Also, any triggers which might increase the incidence, such as viral infections and allergens or pollutants.[19] Drug interventions can be used to address both diseases such as theophylline which is effective to treat asthma[29,30] and COPD.[31] Antibiotics have been found to have a beneficial effect in the case of acute exacerbation,[27] however, some studies showed that they are not effective in the prophylaxis or in the treatment of both diseases.[31] It has

been found that the viral infection such as influenza leads to exacerbation in asthmatic patients,[32,33] and therefore, it is recommended to give influenza vaccines to patients who suffer from asthma including children[33,34] or to those with COPD.[35] This vaccine is safe and given to avoid pulmonary infection in the case of both diseases.[35,36] Oligonucleotides are another class of drugs used to address many targets inside the lungs and it is a novel medicine used for the treatment of pulmonary illnesses.[37,38] Recently, it has been reported that dietary antioxidants might be effective in the treatment of asthma and COPD.[39,40] Shaheen *et al*. demonstrated that higher intake of apples and also selenium may protect from asthma attack as a result of the flavonoid effect in the case of apple consumption.[41] Another study suggests that low consumption of vitamin C (as a result of deficient in fruit intake) and manganese is associated with asthma.[42] Other examples of antioxidants include thiol molecules such as glutathione and mucolytic drugs, these target the free radicals and oxidants involved in glutathione biosynthesis, which was further ending with the inhibition of gene expression in the inflammatory process.[40] Tumor necrosis factor (TNF)-*α* is a pleiotropic cytokine which is associated with many inflammatory diseases such as asthma.[43,44] It is showed that TNF-*α* inhibitor therapy enhances the lung function and reduces the exacerbation of asthma[44] and thus it is recommended to start controlled trials of this type of treatment to people with severe exacerbation of COPD.[45]

1.2 Inhaled corticosteroids (ICS)

Inhaled corticosteroids (ICS) are commonly used to address many inflammatory illnesses including asthma.[46] It has been recommended to be used as first line therapy to treat persistent asthma in all ages[47] and are effective in relieving the symptoms of asthma in all cases of different ages.[48] Recent research showed that ICS is effective in the control of the inflammation in asthma, however, little response or sometimes non in case of COPD.[49] This might be due to the differences in the inflammatory process between the two diseases in which a good response was achieved in asthma while very poor in COPD.[48] Their mechanism of action is firstly by diffusing the cell membrane and binding to the cytoplasmic glucocorticoid receptors. This results in the activation of different processes that ends with the suppression of the inflammatory cells such as T-lymphocytes, easinophils and mast cells.[49] It has been found the administration

of systematic corticosteroids for acute asthma in emergency departments decreases patient admission to hospital.[50] The most commonly used ICS are budesonide (BUD), beclomethasone dipropionate (BDP), beclomethasone (BCL), fluticasone propionate (FLU), mometasone furoate (MOM) (Figure 1.1), prednisolone and triamcinolone acetonide. This group of drugs have high molecular weight and are classified as lipophilic[51] with low water solubility.[52]

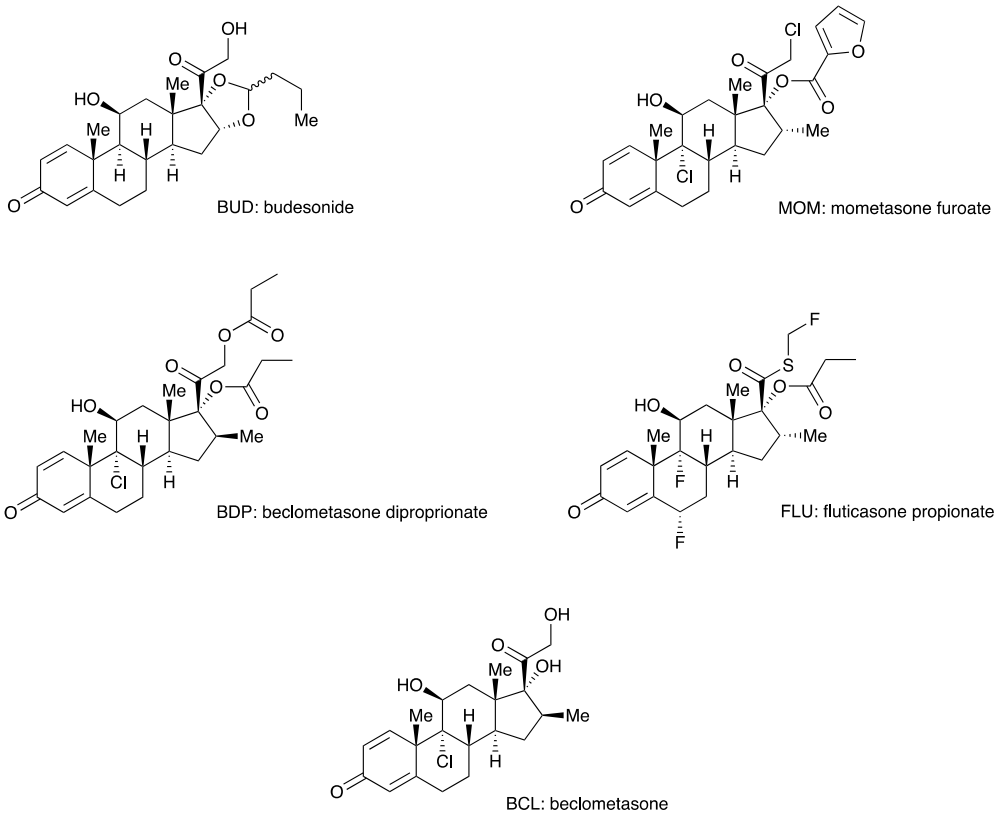

Figure 1.1: Chemical structure of budesonide (BUD), beclomethasone dipropionate (BDP), beclomethasone (BCL), fluticasone propionate (FLU) and mometasone furoate (MOM).

1.3 Delivery Devices

Three primary devices are commonly used to deliver APIs to the lungs; nebulisers, dry powder inhalers (DPIs) and pressurised metered dose inhalers (pMDIs). Nebulisers work by producing an inhalable aerosol of the API from a solution using compressed air. DPIs rely on the inhalation of a dry powdered blend of the API and a carrier particle (usually a sugar such as lactose). The particle size of the API is the key to the efficacy of the drug and needs to be controlled effectively. pMDIs are slightly different in their design, and produce the inhaled particles on actuation of the device. They consist of a pressurised canister containing the API and a propellant (volatile solvent) held as a liquid

under pressure. Once actuated, the liquid is delivered through the mouthpiece of the device producing the solid material *in-situ*, which is subsequently breathed in by the user. Depending on whether the API is held as a suspension in the canister, or is fully dissolved as a solution will play a key role in the products performance.[53]

1.3.1 Nebuliser devices

The nebulizer uses the compressed air to generate droplets from solutions or suspensions, which are then inhaled to the lung by normal breathing process.[5] There are two types of nebulisers namely pneumatic nebuliser and the ultrasonic nebuliser. In the first type, the compressed gas is forced through hole called venturi. Increase in the gas velocity leads to formation of a negative pressure that draws liquid up the tube. The liquid is then broken into small droplets by the effect of surface tension that in turn is inhaled by the patient *via* the mouthpiece during inspiration. The nebuliser system also continues to form droplets during expiration and is then exhaled outside body.[54] In the ultrasonic nebuliser, high frequency sound waves are produced and then passed over the drug surface liquid which are then broken to form an aerosol.[5] The most important point concerning the ultrasonic device is the size of the respirable droplets which is the range of 1-5 µm that is able to reach lower airways and better therapy. The other advantage of using the nebulizer is the simplicity of use[55] and therefore, it can be used for young or very ill patients since no propellant is included in the formula so it is easy to use and it can be used to deliver large drug doses. In contrast, it is considered to be less portable compared to the DPI and pMDI as it needs compressed air for operation. Also, it takes longer time to achieve the therapy and is more expensive in terms of more equipment is needed compared to the DPI and pMDI.[5,53]

1.3.2 Pressurised Metered Dose Inhaler (pMDI) devices

Pressurised Metered Dose Inhaler (pMDI) is another device used to deliver COPD and asthmatic drugs. It was developed in the mid-20th century at Riker Laboratories[56,57] and a new device introduced to the market was Medihaler Epi® in 1956.[58] The device is formulated as a solution or suspension where the API is dissolved or suspended in the volatile propellant respectively. Some other additives are added in the case of suspension based formulation such as the

surfactant to increase the stability and the solvent to solubilise the API in the propellant.[59]

The device has many advantages including the availability in a multi-dose unit, portability, ease of use, convenience and it is relatively inexpense.[5,57,60] Also, it does not need high inspiratory flow, which is needed by DPI, to ensure good lung deposition; therefore, it is preferable to those with low lung efficiency. The main drawbacks of pMDI include; (i) the cold-Freon effect which results from the effect of a cold propellant that reaches the back of the throat, and (ii) higher drug deposition in the oropharynx resulting in the appearance of both local and systemic side effects. This latter issue has been addressed by recent re-formulation of pMDI as discussed in Section 1.4.[57]

1.3.3 Dry Powder Inhaler (DPI) devices

Dry Powder Inhalers (DPIs) were introduced to the market in 1967[61] as an alternative to pMDIs to decrease the ozone-depleting effect of CFC which is a propellant that exists in pMDI and also to deliver molecules of high molecular weight.[62] They consist of the drug mixed with a carrier powder commonly lactose preserved in separate gelatin capsule. Each capsule contains a single dose which is positioned in the inhaler at the administration time and punctured to release the drug. This protects the drug from moisture and thus the powder maintains its flowability to be perfectly deposited at the site of action.[61] These devices needs strong inspiration to deliver the drug to the lung and therefore no coordination of actuation is needed and therefore better lung deposition.[55,62] The device has some disadvantages as it needs time to load the inhaler with the capsule every time and different brands of DPIs have different operation instructions.[55] Some considerations are taken into account when dealing with the device as it needs to be kept dry as exposure to the air or exhalation through the mouthpiece results in clumping of the powder and restricts its flowability so it decreases the fine particles fraction on actuation.[63,64] However, DPIs are still considered to be efficient in drug delivery to the lung and are easy to use.[62] There are three types of DPI devices (i) unit dose where the inhaler is loaded by individual capsules before use,[55] (ii) multi-unit dose by using sealed blisters of individual capsules that are loaded into the inhaler before actuation, and (iii) multi-dose reservoir which contains a bulky API and individual doses are released upon actuation.[61,65] Examples of ADI of the three mentioned types

include; Rotahaler® (GSK), Diskus, also known as Accuhaler (GSK), and Turbuhaler (AstraZeneca) respectively.[61] The DPI is principally designed by blending the drug with a carrier molecule, then by active or passive dispersion, the particles enter the body followed by separation of the drug particles from the carrier particles which are then ready for the deposition either in the oropharynx or deeply in the lung depending on their size.[62]

1.4 Chlorofluorocarbons (CFC) and Hydrofluoroalkanes (HFA) – used in pMDIs

All pMDIs prescribed before 1995 were mainly composed of CFC propellant. However, the Montreal Protocol banned the use of CFCs in 1987 as they caused damage to the ozone layer that was important to prevent the harmful sun ultraviolet radiation from reaching the earth. Therefore, the use of more environmentally friendly substances such as HFA propellants and alternative devices (DPI) could be considered a better solution to replace the CFC based formulations.[5,56] The switching to HFAs was not a simple process, and the issues encountered during the formulation needed to be addressed; *e.g.* the surfactants in CFC formulations were insoluble and device seals were incompatible with HFAs. Also, because of the difference in the thermodynamic properties of HFAs, designing a special actuator is essential to obtain the ideal particle size of APIs.[66] In 1995, both 1,1,1,2-tetrafluoroethane (HFA 134a) and 1,1,1,2,3,3,3-heptafluoropropane (HFA 227) propellants were officially approved by European Union to be efficient and safe for use in pMDIs.[67,68] It appears to be generally accepted that the switching to HFA results in the production of more environmently friendly formulations of very fine particles that are deposited more successfully in the lung with reduced deposition in the oropharynx, and hence provide a more efficacious therapy with less local/systemic adverse effects compared to the CFC inhalers. Figure 1.2 shows the lung scintographic images of beclomethasone deposition from CFC and HFA pMDI devices which clearly indicates the increased lung deposition with an associated decrease in oropharyngeal deposition from HFA formulations compared to the CFC devices.[69]

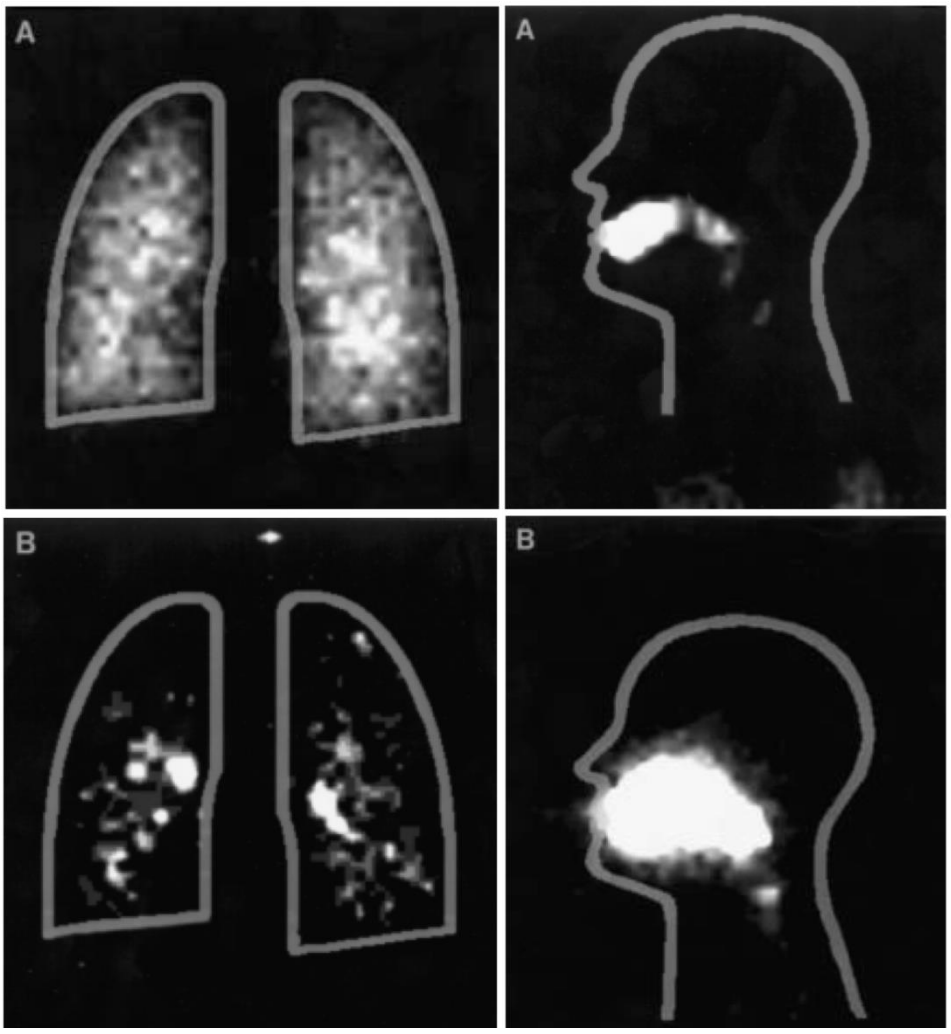

Figure 1.2: Gamma scintographic images of lung (left side) and oropharynx (right side) of beclomethasone dipropionate MDI with a) HFA and b) CFC propellants.[69]

The reformulation of pMDI products in HFA has led to an improvement in lung therapy due to lower initial spray velocity, initial droplet size and its evaporation which is different to those of CFC products.[70]

1.5 Characteristics of HFA pMDIs formulations

Many factors affect the performance of pMDI products such as (i) device design in terms of metering valve, nozzle diameter and (ii) the formulation namely; propellant volatility, vapour pressure, and its solubilising ability for the API in addition to the excipients.[57] The propellant should be nontoxic and non-flammable and compatible with other excipients. It should also have definite density and boiling point and its vapour pressure remains constant over product's shelf-life.[57] It is noted that the thermodynamic properties of both types of HFA (HFA 134a and HFA 227) were similar to CFC 12. However, no HFA propellant is comparable to trichlorofluoromethane and

dichlorotetrafluoroethane (CFC 11 and CFC 114), which were used to modify the vapour pressure in CFC system by reducing CFC 12 vapour pressure. The physical properties of each propellant (Table) can be related to its chemical structure and physicochemical behaviour[71]. Excipients are needed with lower volatility for modification of vapour pressure of the new type of HFA.[57,72] The addition of non-volatile solvents such as polyethylene glycol and glycerol decreases the vapour pressure of propellant and thus modify its volatility.[73] The addition of glycerol leads to production of larger particles with sizes similar to those of CFC particles so that the deposition and the absorption in the lung are comparable to those of CFC formulation. Examples of HFA formulation include the availability of BDP and budesonide as Modulite® which has characteristics that resemble the CFC based formulation.[74,75]

Table 1.1: Physicochemical properties of pMDI propellants[71]

Property	CFC 11	CFC 12	CFC 114	HFA 134a	HFA 227
Boiling point (°C)	24	-30	4	-26	-16
Vapor pressure (kPa)	89	566	182	572	390
Enthalpy vap. (kJ/mol)	25.1	17.2	22.1	18.6	19.6
Dielectric constant	2.3	2.1	2.2	9.5	4.1
Dipole moment	0.45	0.51	0.58	2.1	1.2
Induced polarisation ($m^3\ mol^{-2} \times 10^5$)	2.8	2.3	3.2	6.1	6.1
Solubility parameter (Hildabrand units)	7.5	6.1	6.4	6.6	6.2
Kauri-Butanol value	60	18	12	9	13
Log *P* (oct/water)	2.0	2.2	2.8	1.1	2.1
Water solubility (ppm)	130	120	110	2200	610
Density (g/cm^3)	1.49	1.33	1.47	1.23	1.42
Viscosity (mPa.s)	0.43	0.20	0.30	0.21	0.27
Surface tension (mN/m^2)	18	9	11	8	7

The main problem associated with the formulation of HFA preparations is the solubility of API and excipients in HFA. Therefore, it is considered a critical issue that should be taken into account during the design of new formulations. The solubility is the ability of a solute to dissolve in a solvent until the solution reaches saturation at which point no increase in the concentration of solute is observed and the solution is in equilibrium at specific temperature and pressure.[76] It is predicted that around 70% of new drugs are poorly soluble in

water with nearly 40% of marketed oral drugs being practically insoluble in water (< 100 μg/mL)[77] and this is attributed to the chemistry of these drugs which are considered either weakly basic or acidic, so this contributes to give poor aqueous solubility properties.[76] The solubility of drug compounds in HFAs is also poorly understood, and methods to determine these values are needed.

1.5.1 Suspension formulations

Preparing the drugs using excipients and/or co-solvents, forming salts / co-crystals or using more advanced strategies such as delivering as pro-drugs can provide other possible mechanisms for improving solubility.[78] Alternatively, the drug compounds can be prepared as suspensions in the case of pMDI products.[79] A study conducted by Seville *et al*. prepared salbutamol as a pro-drug with complete miscibility in HFA 134a compared to the lower solubility of salbutamol, which is released as a result from the metabolism of pro-drug by esterase to generate salbutamol.[80] Drugs in pMDIs can be formulated as either suspension or solution preparations. Suspensions are generally prepared by micronising the particles of the APIs (commonly in a fluid or jet mill) to form smaller particles of 1-5 µm in size.[57,76] The reformulation of APIs as a suspension is the common approach given the poor solubility of most inhaled drugs in HFAs.[81] The advantages of this kind of formulation is its relative simplicity and minimal requirements for the inclusion of potentially toxic excipients in the product.[82]

Many problems affect the stability of the suspension preparations which include: (i) creaming where the suspended drug is lighter in density than the HFA propellant so the particles separate and forms a layer on the surface of the propellant on standing,[83] (ii) sedimentation where the drug particle is higher in density than the propellant and (iii) flocculation where there is difference in the hydrophobicity and hydrophilicity of the drug and propellant which causes the drug to deposit on the container wall. All these issues can lead to inhomogeneity in the dose emitted from the canister.[82]

Ostwald ripening is another major influence on suspension stability; this phenomenon causes suspended particles to increases in size over time through mass transfer from the smaller particles in the suspension. This occurs through two principal mechanisms: (i) the smaller particles are deposited on the surface

of larger particles at the saturation point which leads to the increase the size of the suspended particles (ii) at high concentrations of suspended particles, the small particles tend to cluster and deposit on the surface of the bigger particles.[84,85] This phenomenon causes formation of a supersaturated solution regarding the large particles that ends with crystallisation and the growth of the larger particles.[86]

Adequate use of the device with proper shaking before the actuation is important for dose uniformity.[83,87] Many drug companies have offered some ways to tackle the problem of suspension instability by adding excipients such as surfactants. It has been reported that the conventional surfactants used in CFC (sorbitan trioleate, oleic acid and lecithin) are not soluble in HFA and therefore do not disperse appropriately to be adsorbed on the drug particles surface.[88] Other substituted surfactants such as Span 85 and dipalmitoylphosphatidylcholine (DPPC) have been used to stabilise the HFA formulation of nanoparticles, although they have so far proved inadequate to confer suspension stability over the shelf-life. This is due to the different physico-chemical characteristics of HFAs as solvents, compared to CFC that influences properties critical to stabilisation of nanoparticle dispersion such as zeta potential and related surface characteristics.[89] Some novel stabilisers based on essential oils such as cineole, cinnamaldehyde, and citral, have been studied and it is reported that citral and cineole have an advantage for stabilisation of insulin in HFA 134a propellant.[90] Dickinson *et al*. found that lecithin based nanoparticles can form homogenous suspension by being dispersed in HFA propellant in the presence of 5% *n*-hexane,[91] however, no long-term storage stability studies were reported. Research by Tan *et al*. showed that thymopentin nanoparticles formed a stable suspension in HFA 134a using cineole and/or *n*-heptane as a stabiliser.[89] Some products formulated as suspension formulations in HFA are available such as Ventolin® which is a combination of albuterol and HFA 134a. Other two component products are Advair®/Flovent®; suspensions of fluticasone propionate in HFA 134a.

1.5.2 Solution formulations

In solution formulations, the drug is entirely dissolved in HFA propellant and this methodology produces preparations with the advantages of forming a

homogenous uniform product with efficient reproducible dose delivered to the lung compared to suspension formulation.[82,92] Also, the formulation is considered to be stable and does not suffer from suspension associated issues described earlier (*e.g.* creaming, flocculation and sedimentation) and with deposition of the drug on the device's surfaces. The solution preparation has some drawbacks such as the drug can be lost into the valve elastic components, and this is a considerable problem especially for low drug concentration. Also, when ethanol is added in excess amount as a co-solvent to increase the solute's solubility, it is noticed that the vapour pressure might decrease below that required for efficient atomisation. In addition, toxicological studies are needed for alternative solvents to ethanol that can be used instead.[82] Drugs should be soluble in the propellant to some extent to ensure good delivery and absorption to get better clinical efficacy.

It is a difficult issue to formulate drugs with poor solubility since more adaption is needed, however several approaches to tackle the solubility problems have been explored.[76] The addition of excipients is not only to enhance the solubility but also for better and more stable formulations during the storage period. Excipients are added to (i) control the bitter taste using flavouring agents, for example saccharin or menthol (ii) increase stability using antioxidants like ascorbic acid (iii) increase APIs solubility using co-solvents (the most common, ethanol) or surfactants in the propellant and (iv) modify aerosol size, stabilise the particles and also lubricate the valve using surfactants such as oleic acid.[93]

Products of three components have also been marketed by using ethanol as a co-solvent to overcome the problem of solubility and enable their formulation as solution. Examples include; QVAR® / ALVESCO/ AEROSPAN® which is a solution of BDP, ciclesonide and flunisolide respectively in HFA 134a/ethanol mixture. Formulations with additional stabilising excipients include ATROVENT® which is ipratropium bromide in solution of HFA 134a with water, anhydrous citric acid and ethanol.[93] Zhu *et al*. studied the effect of ethanol on the particle properties for this formulation and they found that the increase in ethanol concentration causes a decrease in the fine particle fraction and an increase in the mass median aerodynamic diameter and noted that the resulting particles could be classed within two morphologies.[94] Evans *et al*. studied the possibility of forming a stable solution by using soya lecithin and water to form

micelles in CFC based formulation.[95] Saleem and Smyth reported that the particle size increases with an increasing in co-solvent and surfactants concentration.[96] However, the co-solvent caused a decrease in fine particles level. Recently, the water solubility and thus the dissolution of the compounds has been increased by addition of cyclodextrins (CDs).[97]

1.5.3 Suspension vs solution formulations

Generally, the main key difference between suspension and solution formulations is the dose actuated from the container (dose uniformity). Suspension preparation emitted particles are usually delivered in various sizes compared to the original particles in the formulation.[98] The particle size generally depends on the initial actuated droplet size and the amount of non-volatile materials in the preparation. The efficacy of the inhaler depends on the particle size distribution, the concentration of the drug in the inhaler, the number and the size of the delivered drug particles. These factors were studied by Stein who was trying to develop an equation for the determination the number of the particles in the MDI inhaler, concluding that the number is highly reliant on the mass median aerodynamic diameter (MMAD) of the particles and to a lesser extent on their mass in the entire inhaler. Also, it is found that solution preparation emitted a higher mass of drug particles as each actuated droplet has more drug compared to the suspension where many of the emitted droplets do not contain drug particles.[99] Stein *et al*. developed a model for prediction of the aerodynamic particle size distribution from a suspension pMDI inhaler. They found good agreement in the results obtained with this model to those from a cascade impactor experiment which indicated the accurate estimation of particle size distribution acquired from suspension pMDI.[100] Recently Ivey *et al*. developed an equation to determine the mass median aerodynamic diameter of the emitted aerosol from both HFA 134a and 227 solution MDIs, with various amounts of ethanol with a given propellant pressure and its surface tension. It is considered accurate in the determination of MMAD in comparison with results reported in the literature.[101]

Stein and Myrdal studied the residual particle size distribution of solution MDIs on actuation by theoretical and experimental examination based on the determination of aerodynamic size distribution. Their residual size distribution is dependent on the propellant type and its pressure, ethanol and non-volatile

excipients (if present) concentrations, the diameter of actuator orifice and valve size.[102] Solution pMDIs generate particles in the inhaler upon actuation, as soon as it is atomised. The droplets go through quick evaporation of propellant and other volatile excipients (if present) to form particles that are spherical and smaller in size containing the drug and any other non-volatile excipients present in the preparation. Their size is dependent on the initial size of the droplet, as the drug forms solubilised homogenous solutions and therefore, small droplets lead to a formation of small particles and vice versa. However, in the case of suspensions the droplets atomised have different diameters depending on the device and the formulation with some of them containing no drug and others with one, two or more drug particles which tend to diverge from the spherical shape compared to solution based formulations.[100]

If we can develop additional strategies to formulate inhaled drugs as solutions in HFAs we can potentially obtain more stable and efficacious medications. In addition to the co-solvent approaches that have been used to good effect, excipients such as cyclodextrins (which have been commonly applied in oral dosage forms to increase the solubility of drugs) show promise in HFA based media to increase the solubility of inhaled drugs to a level where solutions are produced at a therapeutically relevant dose level.

1.5.4 Cyclodextrins (CDs) as pMDI excipients

Cyclodextrins (CDs) are molecules that consist of 6, 7 or 8 glucose units linked with *α*-1,4 bonds to form *α*, *β* or *γ* CD respectively to form condensed cone-like structure (Figure 1.3).[103,104]

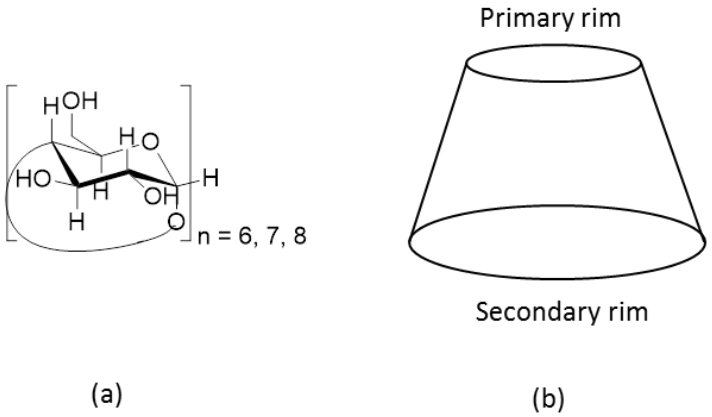

Figure 1.3: (a) Chemical structure of *α*, *β* and *γ* CDs (composed of 6, 7 and 8 glucose units respectively) and (b) the condensed cone.

When the glucose units are connected together, the structure is firm, while it still has some flexibility provided by *α*-1,4 bonds. This flexibility orientates the protons of methine group of both C3 and C5 and the two protons of methylene group of C6 in addition to the lone pairs of the oxygen atoms of the C4 (included in the *α*-1,4 bonds) towards the interior surface of the CD cavity (Figure 1.4, a).[105] The ethereal oxygen of glucose residues and skeletal carbons that compose the inner CD cavity are responsible for giving it the hydrophobic character.[106] This allows the CDs to form inclusion complexes with different hydrophobic molecules entirely or partially by hydrophobic interaction with van der Waals forces, compared to the external surface of CDs which are considered hydrophilic with the presence of hydroxyl group.[104,107,108] The rim of the CD are knowns as primary and secondary rims, according to the number of the hydroxyl groups, where the primary rim has a single hydroxyl group of C6 while the secondary one has two hydroxyl groups of C2 and C3. Accordingly, the primary rim becomes narrower while the secondary is wider and gives a truncated cone structure to the CD instead of cylinder, because of the natural arrangement of the glucose units.[109] To improve the solubility, and increase the CD capacity to form inclusion complex, chemical modifications of the primary and secondary hydroxyl groups are made by substituting with ethyl, methyl, hydroxyethyl, sulfobutyl or hydroxypropyl groups. Methylated derivatives of CD include heptakis(2,6-di-O-methyl)-*β*-cyclodextrin (DIMEB) (Figure 1.4, b) and heptakis (2,3,6-tri-O-methyl)-*β*-cyclodextrin (TRIMEB) (Figure 1.4, c) where the hydroxyl groups at C6, C3 and C2 in *β*CD are methylated to obtain TRIMEB whereas the methylation of hydroxyl groups at only C6 and C2 produces DIMEB. The physical and chemical properties of methylated derivatives are relatively altered compared to those of *β*CD. The water solubility of DIMEB and TRIMEB are 57 and 31 g/100 mL respectively which has been improved compared to 1.85 g/100 mL for the parent *β*CD.[110]

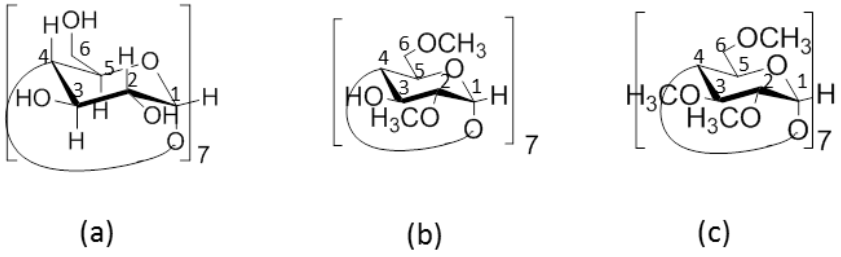

Figure 1.4: Chemical structure of (a) *β*CD, (b) DIMEB and (c) TRIMEB

Recently, the use of CDs in the pharmaceutical industry has been adopted to overcome some solubility and dissolution problems. Different approaches have been taken in order to tackle the solubility issue which include the use of salt formation, surfactants, pH alteration of the medium or the use of co-solvents.[106] The use of CDs has been recently adopted to enhance the solubility, dissolution, bioavailability, physical and chemical stability and other applications in the pharmaceutical industry.[111] The way of increasing the solubility by using CD is by forming the inclusion complex with incorporation of the hydrophobic part of the guest into the cavity, while the hydroxyl groups of the CD external surface gives the hydrophilicity of the resulting complex. The hiding of the hydrophobic part of the guest which is responsible for its poor solubility leads to an overall enhancement of its water solubility.[112] Different range of the drugs have been prepared as inclusion complexes to enhance their water solubility, such as non-steroidal anti-inflammatory drugs (piroxicam[113] and indomethacin[114]), griseofulvin,[115] antidiabetic agents (gliclazide[116] and tolbutamide[117]) and steroids.[118] The CDs also can be added in order to decrease or even to avoid the irritation of eye and gastrointestinal tract (flufenamic acid,[119] thalidomide[120] and naproxen[121]) or to overcome the unpleasant taste or odour (naproxen, ibuprofen and bile acids).[122]

The inclusion complex can be formed between the CDs and the guest molecules in water[107] and also in many polar organic solvents.[123,124] However, it has been reported that the formation of the inclusion complex in nonpolar solvent is difficult.[125] Many studies were conducted to probe the effect of the addition of CDs on the solubility and stability of formulations in HFA propellants used in pMDI preparations. Williams *et al*. studied the stability of the HFA-aspirin formulation by the addition of 2-Hydroxypropyl-*β*-cyclodextrin (HP*β*CD).[126] Likewise, Steckel *et al*. studied the effect of HP*β*CD to stabilise HFA-budesonide formulations in the presence of ethanol and polyethylene glycol (PEG) 300. They found a formation of a stable suspension with no agglomeration over the storage period of 3 months. Importantly, without adding HP*β*CD, a supersaturated solution was formed and the material recrystallized on the inner surface of the container. However, they did not examine the effect of the co-solvent and CD on the solubility of budesonide and their effect on aerosol performance.[127]

The most significant feature of CDs is their capability to form the inclusion complex either in solution or in the solid state. In the case of solid state, the guest molecule can either be encapsulated or weakly interact with the surface of CD, while in solution state the equilibrium occurs between non-complexed and complexed molecule. Accordingly, the change in the physicochemical properties of both host and guest molecules occur and can be determined by various techniques.[108,128] In aqueous solution, the apolar cavity of the cyclodextrin is occupied by the water molecules which can form a less favoured system in terms of energy because of the polar-apolar interaction. Therefore, the high enthalpy water can be readily displaced by suitable guest molecules (that have a lower polarity than water) to achieve apolar–apolar association; this is considered the driving force for the complex formation. This leads to a reduction of the ring strain of the CD as it is in the more favourable and stable low energy state.[129]

1.5.4.1 Binding forces involved in complexation formation

The equilibrium exists between the associated molecules (H.G) and their dissociated forms of CD (H) and guest (G) entities, and can be expressed by the stability constant, Ka.

$$H+G \leftrightarrows H{\cdot}G \qquad \textbf{Equation 1.1}$$

$$Ka = \frac{[H{\cdot}G]}{[H][G]} \qquad \textbf{Equation 1.2}$$

It is used as an indicator to assess the stability of the inclusion complex between the guest and the host and its value is directly proportional to the stability of the formed complex. There are two main factors affecting the formation of the inclusion complex, the first one is the size of the CD and the guest molecule as well as the guest structure, as if the guest is not of suitable size; it will not enter the CD cavity. The second factor is the ability of the three components; guest, CD and solvent to thermodynamically interact to form a more favourable driving force that causes the guest to enter into the CD cavity.[106] As the CD is a neutral molecule, therefore, the main forces involved in the complex formation are; hydrophobic interaction, hydrogen bonding and van der Waals interactions.

Hydrophobic interactions arises from the repulsive force between the apolar CD cavity and the water inside the CD cavity which has a high enthalpy in one side, and between the apolar guest and the vehicle water on the other side.[129] Accordingly, the high enthalpy polar water molecules in the apolar CD cavity would be displaced by the hydrophobic guest, as well as the number of hydrogen bonds increases as the displaced water comes out to the external media. This leads to the decrease in the repulsive force between the guest and the bulk water on one hand, and an increase in the apolar–apolar (hydrophobic) interaction between the guest and the apolar CD cavity on the other hand. These interactions cause increase in free water molecules which ultimately leads to a positive change in entropy and to a lesser extent in the enthalpy.[130]

Van der Waals interactions can occur due to the polarity of the molecules like dipole-dipole and dipole induced polar interaction. Conversely, this can also take place between apolar parts of the molecules and this is called London dispersion. The former interaction is weak with water and it is indirectly proportion to the permittivity of the medium and such interaction becomes stronger in presence of CD particularly in CD cavity and this is due to its small permittivity. Apolar interaction on the other hand happens when the molecules are near each other and are separated by a small distance and its affected by the steric hindrance of the molecules. Once again, van der Waals interaction also causes change in the thermodynamic state of the system and when it is minor compared to the hydrophobic interaction this leads to positive values of entropy and enthalpy. Conversely, if van der Waals forces are more predominant than hydrophobic interaction then this results in both entropy and enthalpy values are less than zero.[131-133]

Hydrogen bonding can be formed between the primary and secondary hydroxyl groups of the CD with the guest molecule. Also, the bonding can be formed between the two hydroxyl groups of the CD.[134] All the above bond act together to form the inclusion complex between the CD and the guest.

The thermodynamic parameters such as the enthalpy change (ΔH°), the entropy change (ΔS°) and the free energy change (ΔG°) can be used to as a confirmation for the complexation driving forces. The van't Hoff equations are used to calculate ΔS° and ΔH° as follows:

$$\ln K = -\frac{\Delta H^\circ}{RT} + \frac{\Delta S^\circ}{R}$$ **Equation 1.3**

$$\Delta G^\circ = -RT \ln K$$ **Equation 1.4**

If the ΔH° and ΔS° are positive, this indicates that the interaction between the CD and the guest is an entropy-driven process and the hydrophobic interaction is the main force included in the complexation. However, if the ΔH° and ΔS° are negative, this implies an enthalpy-driven process and both hydrogen bonding and van der Waals interactions are the main forces for complexation.[135] The positive entropy arises from the flexibility of guest molecule upon complexation, the liberation of water from the cavity and desolvation from the hydrophilic parts of both guest and the host. The negative enthalpy results from the suitable matching in term of shape and size between the CD and the guest whereas the negative entropy is attributable to the reduction in the conformational and translational freedoms of both guest and the CD after complexation.[136]

1.5.4.2 Inclusion complex characterisation

There are numerous techniques used for the characterisation of the inclusion complex. For example, high performance liquid chromatography (HPLC),[137] powder *X*-ray diffraction (PXRD),[108] circular dichroism,[138] thermogravimetric analysis (TGA),[139] differential scanning calorimetry (DSC),[140] FT-Raman spectroscopy,[141] Fourier Transform Infrared Spectroscopy (FTIR),[108] UV-Vis spectroscopy[142] and Nuclear Magnetic Resonance (NMR).[117] The two last instrumental techniques have been used in this thesis to study the complexation in solution form.

The inclusion complex is characterised by measuring the stoichiometry and the stability constant of the systems under study. A continuous variation method or so-called Job's plot is used to determine the stoichiometry of the complex where the change in the specific properties such as the chemical shift and absorbance is evaluated as an indication for the complexation.[143] The setup of the method is based on the preparation of two equimolar solutions of both host and guest. Then different mixtures of both host and guest are made by taking different ratios from them and mixing to the standard volume with the total of the concentration of both components remaining constant.[144] The stoichiometry is

then determined by measuring either the chemical shift in the case of NMR or the change in the absorbance at a certain wavelength by UV spectroscopy. The Hildebrand-Benesi method is a very common means to study the inclusion complex between the host and the guest,[135] and depends on the measurements of the chemical shift changes as a function of concentration (NMR titration). The method is performed by adding a constant volume of the guest to different ratios from the CD solution to form different solutions which are then analysed by NMR. The CD concentrations are plotted versus the change in chemical shift, and the stability constant is calculated from the slope and the intercept of the obtained graphs using Hildebrand-Benesi Equation:

$$\frac{1}{\Delta\delta_{obs}} = \frac{1}{[CD]K\,\Delta\delta_{max}} + \frac{1}{\Delta\delta_{max}} \qquad \textbf{Equation 1.5}$$

Where; $\Delta\delta_{obs}$ is the change in the chemical shift of the proton of the complexed guest, $\Delta\delta_{max}$ is the chemical shift difference between the complex and free guest. The [CD] and K are the concentration of CD and association constant respectively.[143]

Ultraviolet-Visible (UV-Vis) spectroscopy can also be used in the same manner by measuring the change in the absorbance of the guest as a function of concentration and the stability constant is measured using the following equation:

$$\frac{1}{\Delta A} = \frac{1}{\Delta\varepsilon\,[G]_0 K[CD]} + \frac{1}{\Delta\varepsilon\,[G]_0} \qquad \textbf{Equation 1.6}$$

Where; ΔA and $\Delta\varepsilon$ are the absorbance and the molar absorptivity difference between the free and complexed guest. $[G]_0$ is the initial guest concentration, K is the apparent formation and [CD] is the CD concentration.[135]

1.5.4.3 Nuclear Magnetic Resonance (NMR)

NMR is one of the techniques that has been used widely in this area of study.[104,145-147] It is considered the most valuable technique for obtaining information on complex formation; the inclusion complex causes a change in the chemical shift of the protons of both the host and guest molecules. Due to the fact that the exchange between the free and complex guest or host is fast compared with the NMR time scale, it is expected that the peaks in the NMR

spectrum observed are a weighted average of the chemical shifts of both the free and the complexed molecule.[148,149] The extent of the shift is related to the proton position in the molecule, cavity size of CD and also the ratio between the guest and CD.[104,147] The chemical shift change of both the CD and the guest molecule has been attributed to the environment change from the polar aqueous medium to the apolar CD cavity and to the shielding effect arising from the cavity. The greater chemical shift change is an indication of the stronger interaction between the guest and the CD.[150] NMR is therefore considered the most favourable technique to study complex formation since the ^{1}H NMR titration experiments confirm the complex formation. The information about the mode, the deepness of guest penetration in the CD cavity, the stability and the stoichiometry of the complex can all be obtained from the NMR titration data.[104,151] In addition, advanced two-dimensional techniques such as rotational overhauser effect spectroscopy (ROESY) can be used to assign the change in the shift of the protons of the complex structure.[104]

1.5.4.4 Ultraviolet-Visible (UV-Vis) Spectroscopy

Ultraviolet-Visible (UV-Vis) spectroscopy is one of the techniques used to identify the complexation by measuring the change in the absorption spectrum of the guest molecule which results from the change in the solvent environment before and after the addition of the host molecule.[108,152] When the cyclodextrin is added, some changes are observed in terms of the intensity and position of the absorption spectrum of the molecule.[153] As the molecule is inserted into the CD cavity, it is transferred from the aqueous environment to the apolar CD cavity. This results in the change of the molar extinction coefficient (Δε) of the chromophore of the molecule[154] due to the perturbation of the chromophore electrons of the guest molecules.[155] Also, the UV maximum is shifted and the fluorescence is enhanced for the fluorescence molecule as a result of the change in the surrounding medium.[129] Another explanation of the change in the UV-Vis spectrum is replacement of the solvation shell around the guest completely or partially by the CD molecule which creates a new solute environment for the interactions.[153]

1.5.4.5 Surface-enhanced Raman Scattering (SERS)

Raman spectroscopy can be used as a fingerprint for the identification of a molecule; however, this technique has low sensitivity compared to fluorescence

or infrared absorption[156] therefore, signal enhancement is sometimes necessary in order to detect low concentration molecules by this technique. It can be seen that (P) is the magnitude of the dipole moment resulting from the Raman scattering of the light, is directly proportional to the magnitude of the electric field (E) used for the excitement of the molecules. Their relation can be expressed in the equation $P = \alpha E$, where α is the molecule polarizability. If the electric field is enhanced, it leads to the enhancement of the Raman scattering and the signal, this enhancement can result from the excitation of localised surface plasmon (LSP). This induces the enhancement of the electric field at the nanoparticle which enhances the Raman signal of the molecule located closer to the nanoparticle surface.[157] The SERS effect results from the electromagnetic interaction between the metal nanoparticles and the adsorbate by involving of two processes as shown in Figure 1.5. The first process comes from the interaction between the incident beam and the nanoparticle which causes an enhancement of the local incident field E_0 at a wavelength λ_0. The second one (re-radiation of the Raman signal) is resulted from the interaction of the Raman signal scattered by adsorbate and the nanoparticle which then induces the Raman signal enhancement at a wavelength λ_R (Raman scattering enhancement).[158]

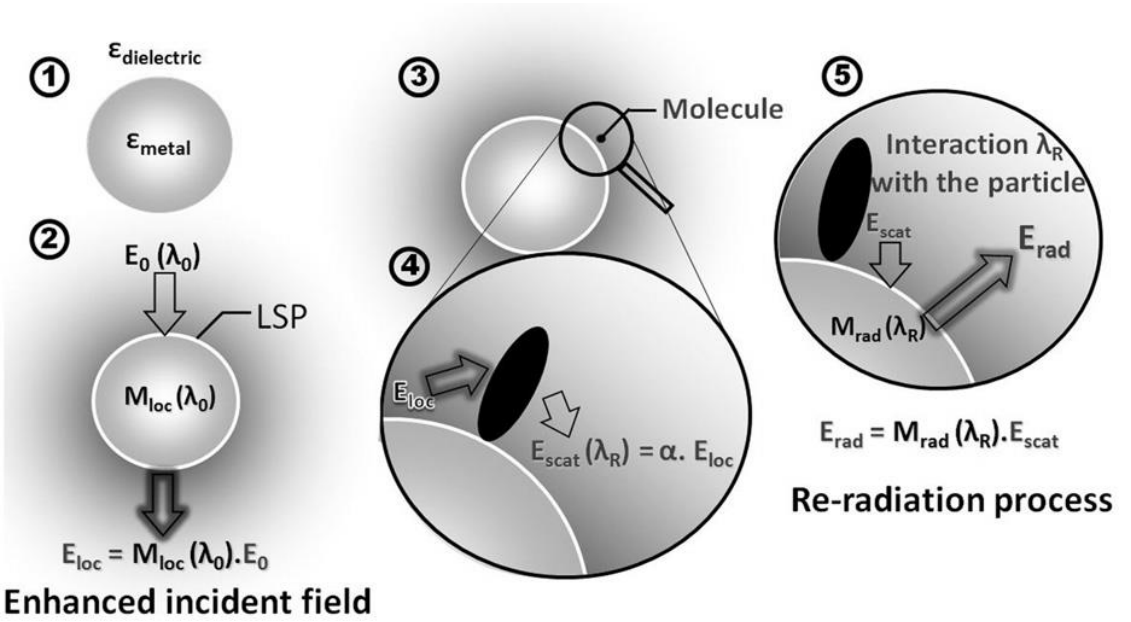

Figure 1.5: Schematic diagram of SERS process. (1) metal nanoparticles surrounded by a solvent medium. (2) incident field E_0 excites the nanoparticles at a wavelength λ_0. (3) molecule is located near the nanoparticle surface. (4) the molecule is polarised by the local field that is then scattered E_{scat} at Raman wavelength λ_R (5) the scattered field is then reacted with the nanoparticles producing field E_{rad} through re-radiation process.[158]

The incident field, E_0, causes the excitation to the metallic nanoparticle that leads to the enhancement of the local field at the particle vicinity. This local enhancement can be expressed by the following equation:

$$E_{Loc} = M_{loc}(\lambda_0)E_0 \qquad \textbf{Equation 1.7}$$

The M_{loc} is local enhancement factor of the excited field at wavelength λ_0. Then the enhanced local field excites the molecule near the nanoparticle, then, the excited molecule scatters a Raman signal in all directions at a shifted wavelength λ_R and this can be explained as:

$$E_{scat} = \alpha E_{Loc} = \alpha\, M_{loc}(\lambda_0)E_0 \qquad \textbf{Equation 1.8}$$

Where α is the molecule polarisability. The scattered field then interacts with the nanoparticle, which subsequently enhances the Raman scattering by the re-radiation process which can be expressed by the following equation:

$$E_{rad} = M_{rad}(\lambda_R)E_{scat} = M_{rad}(\lambda_R)\alpha E_{Loc} = \alpha M_{loc}(\lambda_0)M_{rad}(\lambda_R)E_0 \qquad \textbf{Equation 1.9}$$

As a result of two enhancement processes, the Raman signal scattered by molecule has two enhancement factors at the excitation, λ_0, and the Raman wavelengths, λ_R. Accordingly, The SERS intensity is then calculated as:

$$I_{SERS} = M^2_{loc}(\lambda_0)M^2_{rad}(\lambda_R)I_0 = GI_0 \qquad \textbf{Equation 1.10}$$

Where; I_0 is the Raman signal intensity of the molecule without the nanoparticle. Without enhancement, the enhancement factor can be defined as:

$$G(\lambda_0, \lambda_R)\ M^2_{loc}(\lambda_0)M^2_{rad}(\lambda_R) \qquad \textbf{Equation 1.11}$$

Because of the Raman shift is low, it is found that the λ_0 and λ_R are nearly close and consequently their factors are likely to be approximately equal as $M^2_{loc} \approx M^2_{rad}$ and then $G \approx M^4_{loc}$. Accordingly, the SERS intensity can be estimated as:

$$I_{SERS} \approx M^4_{loc}(\lambda_0)\cdot I_0. \qquad \textbf{Equation 1.12}$$

Thus the Raman enhancement is high as it is proportional to the fourth power of the electromagnetic field enhancement by the nanoparticle.[158] The effect of the SERS is local, as the LSP decay length is about a few tens of nanometers

(between 15 and 20 nm).[159,160] The decay length depends on the size and geometry of the nanostructure. For example, nanotriangles with height and width in the range of 30-35 and 70-100 nm respectively, the decay length is in the direct proportional to the nanotriangles width, whereas it inversely proportional to their height. On the other hand, as the Raman signal has been estimated as the fourth power of the electromagnetic field enhancement near the nanoparticle, the Raman enhancement length is more restricted than the field decay length. Dieringer *et al*. have estimated the relation between the SERS and the distance from the surface by the following equation:

$$I_{SERS} = (1 + r/a)^{-10} \qquad \textbf{Equation 1.13}$$

Where; r, is the distance between the adsorbate and the surface of the particle and, a, is the mean size of the field enhancement at the particle surface.[161] As a result, the SERS intensity decreases and is approximately nil in the range of nanometers distance from the nanoparticle surface.

Lastly, it has been proved that the Raman enhancement depends on the position of the LSP resonance, that in turn can be modified by controlling the geometrical and optical properties of the nanoparticles.[158]

SERS can be used in different fields such as biochemistry, polymer, material science and electrochemistry. It is used for the identification and also for structural prediction of the chemicals. Due to the fact that this technique is highly selective and sensitive, it can be used as a biosensor for the detection of diseases such as Alzheimer's disease, cancers and Parkinson's disease.[162]

1.5.4.6 Solid state studies

Different methods have been reported to prepare the inclusion complex in the solid state such as physical blending, kneading, co-precipitation, solution/solvent evaporation and co-grinding methods.[163] The prepared system is then characterised by a range of techniques such as PXRD, Fourier transform-infrared (FT-IR) spectroscopy,[108,140] Raman spectroscopy[141] and differential scanning calorimetry (DSC).[140] All these methods are important as additional tools to study the inclusion complex formation between the guest compounds and CDs in addition to the NMR and UV-Vis spectroscopy, which both can give information regarding the complexation in aqueous solution.

1.6 Study objectives

It is essential to characterise and study the drugs and excipients in HFA inhalers in order to get a comprehensive understanding of the device performance and hence the therapy. Many studies have been conducted after the banning of CFCs and approval of HFA propellants (see Section 1.3), where both *in vitro* and *in vivo* studies have been undertaken to assess the effectiveness of HFA based therapies compared to CFC.[69] As the driving force that is responsible for the formation of the inclusion complex is van der Waals or hydrophobic interactions between the host and the guest, the use of nonpolar solvents can act as strong competitors for the occupation of the CD cavity. Few studies have been carried out to probe the complexation and physical chemistry of host guest complexes in nonpolar solvents; a study by Menger and Dulany has assessed p-nitrophenol and heptakis (3-O-butyl-2,6-di-O-methyl)-*β*-cyclodextrin in heptane and acetonitrile showing a complexation only in the former solvent.[164] Another study performed by Uccello-Barretta on 1,1,1,3,3-pentafluoro-2-(fluoromethoxy)-3-methoxypropane and heptakis(2,3-di-O-acetyl-6-O-tert-butyldimethylsilyl)-*β*-cyclodextrin in deuterated cyclohexane showing the interaction between both compounds and in this case the derivatised cyclodextrin is used as a chiral selector for the enantiodiscrimination.[165] Notably, we are unaware of any other systematic studies of the physical chemistry of host guest complexes in the HFAs used in pMDI inhalers at this time.

This work aims to develop methods using various analytical techniques to study the physicochemical properties of the active ingredients after the addition of the CDs and probe the host guest interactions. The drugs are studied in the presence of different types of CDs in a range of solvents of differing polarity; water, organic solvents and HFA. As stated in Section 1.5.4, the inclusion of the guest API into the CD cavity causes a change in the physicochemical properties of both the host and guest molecules. This is dependent on the strength of the interaction force between them in solution which is commonly expressed as the stability or equilibrium constant, K_a. UV-Vis and NMR studies will be carried out to investigate the complex formation in solution in terms of (i) stoichiometry and (ii) the stability constant. The ICS compound, budesonide will be used as a model to develop appropriate methods to investigate host guest complexes

established with beta cyclodextrin (βCD), and two derivatised βCDs, DIMEB and TRIMEB. The initial studies will be carried out in water (and D_2O in the case of NMR) for ease of manipulation and to establish reliable methods.

These methods will be developed further to allow the study of the budesonide complexes in the non-polar HFA solvents discussed earlier. The volatility of these systems makes analysis very challenging, and significant thought has to be given to their manipulation in the laboratory and within analytical instrumentation. Methods will be developed using HPFP (2H,3H-decafluoropentane) as a model for HFA 134a and 227 based on work published by Rogueda[166] that concludes the properties of HPFP were similar to those of HFA 134a and HFA 227 propellants. This assists the studies since HPFP is a volatile liquid at standard temperature and pressure (STP), whereas HFA 134 a and HFA 227 are both gases. It is, however, an objective of the development to produce methods that are easy to transfer to the study of the gaseous propellants using pressurised NMR.

More conventional solid state studies will underpin the solution work to further our understanding of the complexation occurring, primarily using vibrational spectroscopy to characterise isolated host guest complexes. Solid mixtures of budesonide and βCD, DIMEB or TRIMEB will be prepared in a ratio depending on the stoichiometry results obtained from NMR and UV-Vis spectroscopy techniques. The prepared mixtures will be studied by Raman and FT-IR spectroscopy to give additional information about complexation by comparing the obtained spectra to the original of the guest and CDs.

As the ICS are poorly soluble and weak Raman signals are obtained from solution, SERS techniques will be used to selectively enhance these signals. Silver and gold functionalised thiolated βCD will be used to attempt to exploit the SERS effect observed with multiple ICS compounds and further our understanding of the interactions with the CD systems.

1.7 Aims

The aim of this work is to develop novel analytical methods to interrogate the physical chemistry of HFA-based formulations. This requires development of structural analytical methods to study the product and characterise the interplay between the API and the formulation excipients. It covers both solution and

solid state studies to allow a better understanding of the behaviour and the stability of the ingredients in the device. The approach has been extended to investigate the interaction with solubilising excipients based on CDs. This will be a platform to help develop the formulation of inhaled drugs in HFA propellants, which in turn allows us to produce more effective systems in terms of better solubility and stability. The specific aims of this work can be summarised as follows:

- Development of UV-Vis and NMR methods to study corticosteroids in the presence of *β*CD, TRIMEB and DIMEB in solvents of different polarity (including volatile HFAs) utilising budesonide as a model steroid compound.
- Solid state studies to further investigate the complexation between budesonide and *β*CD, TRIMEB and DIMEB using vibrational spectroscopic techniques (Raman and FT-IR).
- Assess the complexation of different ICS compounds including (i) budesonide (ii) beclomethasone dipropionate, (iii) beclomethasone, (iv) fluticasone propionate and (v) mometasone furoate in the presence of TRIMEB and DIMEB in HFA by NMR spectroscopy.
- Development of SERS approaches to further interrogate the complexation between ICS and bespoke thiolated *β*CD.

2 Experimental

2.1 Materials

The materials were used as supplied and without further purification (Table 2.1.)

Table 2.1: Supplier, purity and the batch information of the materials used in this study

material	supplier	batch No. (purity)
Beclomethasone	Jai Radhe	BMD-N-006-09
Beclomethasone dipropionate	Jai Radhe	BMD-N-004-09
Budesonide	Sigma-Aldrich	100 %
(22R)-Budesonide	Clearsynth	98.49 %
Fluticasone propionate	Jai Radhe	408901-FP
Mometasone furoate	Jai Radhe	APL/72/C-09
*β*CD	SAFC	STBB6461
DIMEB	Sigma-Aldrich	98 %
TRIMEB	Sigma-Aldrich	98 %
Vanillin	Sigma-Aldrich	STBC7969V (99%)
Deuterium oxide (D_2O)	Sigma-Aldrich	99.9 %
Deuterated chloroform ($CDCl_3$)	CIL	99.8 %
Deuterated acetonitrile (CD_3CN)	CIL	99.8 %
Deuterated methanol (MeOD)	CIL	99.8 %
EtOH (analytical grade)	Fisher chemical	99.5 %
$CHCl_3$ (HPLC grade)	Fisher chemical	99.8 %
HPFP	Apollo Scientific	98 %
Triphenylphosphine	Maybridge	21792
Dimethylformamide	Sigma-Aldrich	STBD6091V (99.8 %)
Iodine	Origin uncertain	
Sodium methoxide in methanol	Sigma-Aldrich	STBD7353V (25 %)
Thiourea	Sigma-Aldrich	SZBE2950V (99 %)
Sodium hydroxide	Sigma-Aldrich	SZBE1620V (98 %)
Silver nitrate	ACROS	A0341730 (99.8 %)
Potassium chloride	AnalaR	1318220 (99.8 %)
Sodium borohydride	Sigma-Aldrich	STBD3364V (98 %)
Hydrogen tetrachloroaurate	Sigma-Aldrich	MKBS1011V
Trisodium citrate	Sigma-Aldrich	BCBL0853V (99 %)

2.2 Methods

2.2.1 Determination of host:guest stoichiometry by UV-Vis spectroscopy

The solutions were prepared based on continuous variation method (Job's plot) where an equal molar concentration of both compounds (guest) and cyclodextrin (host) were prepared, then different ratios of both components

were taken to form different solutions of equal volumes but the sum of the concentration of both components in each solution is constant and the solutions were then analysed by UV-Vis spectroscopy. The stoichiometry was determined by measuring the change in the absorbance at a certain wavelength by UV spectroscopy.

2.2.1.1 Vanillin and βCD in H_2O

The solutions were prepared based on continuous variation method as shown in Table 2.2 where both vanillin and *β*CD are prepared in original concentration of 5 mM in water. Then different ratios were taken from both solutions to form different solutions of constant concentration at 0.05 mM with constant volume at 10 mL. All solutions were then analysed using Varian CARY 50 Probe UV-Visible spectroscopy at λ_{max} at 280 nm.

Table 2.2: The preparetion of vanillin and *β*CD solutions based on continous variation method and analysed by UV–Vis spectroscopy.

[*β*CD]*10^{-2} (mM)	r	Volume (mL)	[van]*10^{-2} (mM)	r	Volume (mL)
0	0	0	5	1	10
0.5	0.1	1	4.5	0.9	9
1	0.2	2	4	0.8	8
1.5	0.3	3	3.5	0.7	7
2	0.4	4	3	0.6	6
2.5	0.5	5	2.5	0.5	5
3	0.6	6	2	0.4	4
3.5	0.7	7	1.5	0.3	3
4	0.8	8	1	0.2	2
4.5	0.9	9	0.5	0.1	1
5	1	10	0	0	0

2.2.1.2 BUD and βCD/TRIMEB in EtOH:H_2O and H_2O

The solutions were prepared based on continuous variation method as shown in Table 2.3 where both budesonide and *β*CD/TRIMEB are prepared in original concentration of 0.04 mM in EtOH:H_2O (50:50). Then different ratios were taken from both solutions to form different solutions of constant concentration at 0.04 mM with constant volume at 10 mL. In the case of studying their complex in water, both components were prepared as stock solution of 0.05 mM in water. Then the same procedure was followed as in the case of using mixture of

EtOH:H_2O (Table 2.4). All solutions were then analysed using Varian CARY 50 Probe UV-Visible spectroscopy.

Table 2.3: The preparetion of BUD and *β*CD/TRIMEB solutions in EtOH:H_2O (50:50) based on continous variation method and analysed by UV-Vis spectroscopy.

[*β*CD/TRIMEB]*10^{-2} (mM)	r	Volume (mL)	[BUD]*10^{-2} (mM)	r	Volume (mL)
0	0	0	4	1	10
0.4	0.1	1	3.6	0.9	9
0.8	0.2	2	3.2	0.8	8
1.2	0.3	3	2.8	0.7	7
1.6	0.4	4	2.4	0.6	6
2	0.5	5	2	0.5	5
2.4	0.6	6	1.6	0.4	4
2.8	0.7	7	1.2	0.3	3
3	0.8	8	0.8	0.2	2
3.6	0.9	9	0.4	0.1	1
4	1	10	0	0	0

Table 2.4: The preparetion of BUD and *β*CD/TRIMEB solutions in H_2O based on continous variation method and analysed by UV-Vis spectroscopy.

[*β*CD/TRIMEB]*10^{-2} (mM)	r	Volume (mL)	[BUD]*10^{-2} (mM)	r	Volume (mL)
0	0	0	5	1	10
0.5	0.1	1	4.5	0.9	9
1	0.2	2	4	0.8	8
1.5	0.3	3	3.5	0.7	7
2	0.4	4	3	0.6	6
2.5	0.5	5	2.5	0.5	5
3	0.6	6	2	0.4	4
3.5	0.7	7	1.5	0.3	3
4	0.8	8	1	0.2	2
4.5	0.9	9	0.5	0.1	1
5	1	10	0	0	0

2.2.2 Determination of host:guest association constants by UV-Vis spectroscopy

The tested compound was held at constant concentration and different increasing concentrations of the CD were added to form different solutions which were then analysed by UV-Vis spectroscopy. The CD concentrations were plotted versus the change in the absorbance and the stability constant was calculated from the slope and the intercept of the obtained graphs.

2.2.2.1 Vanillin and βCD in H_2O

The vanillin solution was prepared at concentration of 1 mM in water. Then serial dilutions from *β*CD were then taken to form 2, 4, 6 and 8 mM solutions with the addition of fixed amount (0.5 mL) of vanillin from the stock solution and completed the volume with solvent to the 10 mL mark. All solutions were then taken for the analysis at λ_{max} at 280 nm.

2.2.2.2 BUD and βCD in EtOH:H_2O and H_2O

The budesonide and *β*CD was studied in a 50:50 mixture of ethanol and water (EtOH:H_2O), as the complex is not formed in the presence of only ethanol. The experiment was carried out by preparing a 0.4 mM budesonide and 10 mM *β*CD in ethanol/water solution. Then serial dilutions from *β*CD were then taken to form 2, 4, 6 and 8 mM solutions with the addition of fixed amount (1 mL) of budesonide from the stock solution and completed the volume with solvent to the 10 mL mark. The solutions were analysed with UV at λ_{max} at 246 nm using a mixture of EtOH:H_2O (50:50) as a blank. To study the complex formation in water, a solution of 0.05 mM of budesonide and solution of 10 mM *β*CD were prepared in water. Then serial dilutions from *β*CD were made to form 2, 3, 4, 5 and 7 mM with the addition of fixed amount (1 mL) of budesonide from the stock solution (0.05 mM) and completed the volume with solvent to the 5 mL mark. All solutions were then measured with UV-Vis spectroscopy at 246 nm using water as a blank.

2.2.2.3 BUD and TRIMEB in EtOH:H_2O and H_2O

The experiment was done by preparation of 0.4 mM of budesonide and 2 mM TRIMEB in EtOH:H_2O 50:50 solution. Then serial dilutions from TRIMEB were made to form 0.4, 0.6, 0.8, 1 and 1.4 mM with the addition of fixed amount (0.5 mL) of budesonide from the stock solution and completed the volume with solvent to the 5 mL mark. All solutions were then measured with UV at 246 nm using a mixture of EtOH:H_2O (50:50) as a blank. To study the complex formation in water, a solution of 0.05 mM of budesonide and solution of 2 mM TRIMEB were prepared in water. Then serial dilutions from TRIMEB were made to form 0.4, 0.6, 0.8, 1 and 1.4 mM with the addition of fixed amount (1 mL) of budesonide from the stock solution (0.05 mM) and completed the volume with solvent to the 5 mL mark. All solutions were then measured by UV-Vis spectroscopy at 246 nm using water as a blank.

2.2.3 Determination of host:guest stoichiometry by NMR spectroscopy

An equal molar concentration of both compounds (guest) and cyclodextrin (host) were prepared, then different ratios of both components were taken to form different solutions of equal volumes but the sum of the concentration of both components in each solution is constant and the solutions were then analysed by NMR spectroscopy. The stoichiometry was determined by measuring the chemical shift differences of the guest molecule protons.

2.2.3.1 Vanillin and βCD in D_2O

The solutions were prepared according to continuous variation methods where both vanillin and *β*CD original concentrations equal to 10 mM in D_2O and different ratios were taken from both stock solutions to give different solutions of the same concentrations at 10 mM with constant volume at 1 mL (Table 2.5). The solution was then added to the standard NMR tube and then inserted into the Bruker 400 MHz NMR spectroscopy.

Table 2.5: The preparetion of vanillin and *β*CD solutions based on continous variation method and analysed by ^{1}H NMR.

[*β*CD] (mM)	r	Volume (mL)	[van] (mM)	r	Volume (mL)
0	0	0	10	1	1
1	0.1	0.1	9	0.9	0.9
2	0.2	0.2	8	0.8	0.8
3	0.3	0.3	7	0.7	0.7
4	0.4	0.4	6	0.6	0.6
5	0.5	0.5	5	0.5	0.5
6	0.6	0.6	4	0.4	0.4
7	0.7	0.7	3	0.3	0.3
8	0.8	0.8	2	0.2	0.2
9	0.9	0.9	1	0.1	0.1
10	1	1	0	0	0

2.2.3.2 BUD and βCD/DIMEB/TRIMEB in D_2O

The stoichiometry was studied by preparing equimolar concentration of both budesonide and either *β*CD, DIMEB or TRIMEB at 0.05 mM in D_2O. Then, different ratios were taken from both solutions to form different solutions at constant concentration of 0.05 mM with constant volume at 1 mL (Table 2.6). The solution was added to the standard NMR tube while the reference solution ($CHCl_3$ in CD_3CN) was added to the inside capillary tube. The co-axial tube was then inserted into the JEOL 600 MHz NMR spectroscopy for analysis.

Table 2.6: The preparetion of BUD and *β*CD/DIMEB/TRIMEB solutions based on continous variation method and analysed by ^{1}H NMR

[*β*CD/DIMEB/TRIMEB] (mM)	r	Volume (mL)	[BUD] (mM)	r	Volume (mL)
0	0	0	0.05	1	1
0.005	0.1	0.1	0.045	0.9	0.9
0.01	0.2	0.2	0.04	0.8	0.8
0.015	0.3	0.3	0.035	0.7	0.7
0.02	0.4	0.4	0.03	0.6	0.6
0.025	0.5	0.5	0.025	0.5	0.5
0.03	0.6	0.6	0.02	0.4	0.4
0.035	0.7	0.7	0.015	0.3	0.3
0.04	0.8	0.8	0.01	0.2	0.2
0.045	0.9	0.9	0.005	0.1	0.1
0.05	1	1	0	0	0

2.2.3.3 BUD and DIMEB/TRIMEB in HPFP

The stoichiometry was studied by preparing equimolar concentration of both budesonide and either of DIMEB or TRIMEB at 0.175 mM in HPFP. Then, different ratios were taken from both solutions to form different solutions at constant concentration of 0.175 mM with constant volume at 0.5 mL (Table 2.7). The solution was added to the standard NMR tube while the reference solution ($CHCl_3$ in CD_3CN) was added to the inside capillary tube. The co-axial tube was then inserted into the JEOL 600 MHz NMR spectroscopy for analysis.

Table 2.7: The preparetion of BUD and DIMEB/TRIMEB solutions based on continous variation method and analysed by ^{1}H NMR.

[DIMEB/TRIMEB] (mM)	r	Volume (mL)	[BUD] (mM)	r	Volume (mL)
0	0	0	0.175	1	0.5
0.0175	0.1	0.05	0.1575	0.9	0.45
0.035	0.2	0.1	0.14	0.8	0.4
0.0525	0.3	0.15	0.1225	0.7	0.35
0.07	0.4	0.2	0.105	0.6	0.3
0.0875	0.5	0.25	0.0875	0.5	0.25
0.105	0.6	0.3	0.07	0.4	0.2
0.1225	0.7	0.35	0.0525	0.3	0.15
0.14	0.8	0.4	0.035	0.2	0.1
0.1575	0.9	0.45	0.0175	0.1	0.05
0.175	1	0.5	0	0	0

2.2.4 Determination of host:guest association constants by NMR spectroscopy

The tested compound was held at constant concentration and different increasing concentrations of the CD were added to form different solutions which were then analysed by NMR spectroscopy. The CD concentrations were plotted versus the change in the chemical shift and the stability constant was calculated from the slope and the intercept of the obtained graphs.

2.2.4.1 Vanillin and βCD in D_2O

The vanillin concentration was held at 8 mM in D_2O with adding *β*CD at 0, 12, 14, 15 and 16 mM in D_2O. The solution was then placed in the standard NMR tube and then inserted into the Bruker 400 MHz NMR spectroscopy.

2.2.4.2 BUD and DIMEB/TRIMEB in CD_3CN, $CDCl_3$ and MeOD

This is done by preparing 10 mM budesonide solution and 10 mM of DIMEB separately in CD_3CN, Then fixed volume of budesonide was taken, which was equal to 2 mM and added to the DIMEB in increasing amount at (1, 2, 4, 6 and 8 mM) to form different solutions of fixed budesonide concentration. The solution was placed in the standard NMR and then inserted into the JEOL 600 MHz NMR spectroscopy for analysis. The same experiment was repeated using $CDCl_3$ and MeOD as solvent. The same procedure was followed using TRIMEB instead of DIMEB.

2.2.4.3 BUD and βCD/DIMEB/TRIMEB in D_2O

The calculation of stability constant was carried out by preparing 0.05 mM budesonide solution and 10 mM solution of either *β*CD, DIMEB or TRIMEB in D_2O. Then 0.8 mL of budesonide was taken (equivalent to 0.04 mM) with adding different volumes of either; *β*CD, DIMEB or TRIMEB solution to give concentration of 0.2, 0.4, 1, 1.4 and 2 mM. All the solutions were made up to 1 mL with D_2O. The solution was then added to the standard NMR tube while the reference solution ($CHCl_3$ in CD_3CN) was added to the inside capillary tube. The co-axial tube was then inserted into the JEOL 600 MHz NMR spectroscopy for analysis.

2.2.4.4 (BUD/BDP/MOM/FLU) and TRIMEB/DIMEB in HPFP

The calculation of stability constant was carried out by preparing 0.175, 0.4, 0.04 and 0.04 mM solutions of BUD, BDP, MOM and FLU respectively and 1

mM and 0.75 mM solution of TRIMEB and DIMEB in HPFP respectively. Then 0.5 mL of either; BUD, BDP, MOM or FLU was taken (equivalent to 0.0875, 0.2, 0.02 and 0.02 mM respectively) with adding different volumes of TRIMEB solution to give concentration of 0.1, 0.2, 0.3, 0.4 and 0.5 mM. For the experiments using the high concentration of TRIMEB, the same procedure followed with the addition of different volumes of TRIMEB solution (4 mM) to give concentration of 0.4, 0.8, 1.2, 1.6 and 2 mM. A 0.5 mL of either BUD or BDP was added to the DIMEB solution with adding different volumes to give concentration of 0.075, 0.15, 0.225, 0.3 and 0.375 mM. All the solutions were made up to 1 mL with HPFP. The solution was then added to the standard NMR tube while the reference solution ($CHCl_3$ in CD_3CN) was added to the inside capillary tube. The co-axial tube was then inserted into the JEOL 600 MHz NMR spectroscopy for analysis.

2.2.5 Preparation of physical mixtures of budesonide and cyclodextrins

A physical mixture of budesonide and CDs are prepared by mixing them by trituration using a mortar and pestle and the solid mixtures are then stored in a closed vial.[163]

2.2.6 Preparation of inclusion complexes using evaporation methods

The complex is prepared by dissolving 1 mole of CD in water (1 mL) and 1 mole of budesonide in ethanol (1 mL). Then, the aqueous solution of CD is added to the ethanolic solution of budesonide. The resultant solution is then stirred for 24 hours followed by vacuum evaporation and the dried mass is stored in a closed vial.[163]

2.2.7 SERS study

2.2.7.1 Synthesis of thiol functionalised βCD (SCD)

The compound was initially synthesised by dissolving triphenylphosphine (10.10 g, 38.5 mmol) in dry dimethylformamide (DMF, 40 mL) followed by careful addition of iodine (10.15 g, 39.85 mmol) with vigorous stirring. Then oven dried *β*CD (2.70 g, 2.35 mmol) was added to the resulted dark brown solution and left overnight with stirring at 70 °C under nitrogen. The DMF was then removed under reduced pressure to leave a brown oil. Sodium methoxide in methanol (3 M) was added to alter the pH from 1 to 9 and the solution was then allowed to stand at room temperature for 30 minutes. Then, the mixture was poured into

methanol (200 mL) to form a precipitate which was then filtered and washed thoroughly with methanol and finally purified by Soxhlet extraction with methanol. The product (per-6-iodo-*β*CD) was then dried in the oven to reach a constant weight; yield 2.80 g (61.8%).[167]

Per-6-iodo-*β*CD (0.97 g, 0.5 mmol) was dissolved in dry DMF (10 mL) followed by the slow addition of thiourea (0.30 g, 4.0 mmol). The resulted mixture was left overnight with stirring at 70 °C under nitrogen. The DMF was then removed under reduced pressure to produce a yellow oil. Water (50 mL) and sodium hydroxide (0.26 g) were then added and the mixture was heated to a gentle reflux under nitrogen for 1 hour. The formed suspension was then acidified with HCl (2 M, 2 mL) and the resulting precipitate was then collected by vacuum filtration and washed thoroughly with water. The product (per-6-thio-*β*CD) was then was dried in the oven to reach a constant weight; yield 0.497 g (51 %).

Per-6-thio-*β*CD (0.10 g) was suspended in 10 mL water and 0.23 g of sodium hydroxide was added and stirred for 30 min. The excess NaOH was then neutralized with 1 M HCl by measuring the pH of the solution. The sodium salt of per-thio-*β*CD was then recovered by freeze-drying.[167]

per-6-iodo-*β*CD

NMR δ/ppm: 3.3 (21H, H2, H4, H6a, m), 3.6 (14H, H3, H5, m), 3.8 (14H, H7, H6b, d), 5 (7H, Ha, s), 5.9 (7H, OH-3, s), 6.1 (7H, OH-2, d).

IR ῡ/cm^{-1}: 585 (C-I, ms), 1036 (C-O, vs), 1326/1368/1413 (CH_2 *bend*, mw), 2913 (C-H *stretch*, w), 3325 (OH *hydrogen bonded*, m br).

per-6-thio-*β*CD

NMR δ/ppm: 2.1 (7H, SH, t), 2.5 (solvent, s), 3.2 (14H, H7, H6b, m), 3.7 (14H, H3, H5, m), 5 (7H, H1, s), 5.9 (14H, H3, OH-2, m).

IR ῡ/cm^{-1}: 1012 (C-O, vs), 1363 (CH_2 *bend*, m br.), 2554 (S-H, w), 2916 (CH *stretch*, m), 3317 (O-H *hydrogen bonded*, m br).

2.2.7.2 Silver nanoparticles preparation (Ag NPs)

Silver nitrate (10 mL, 1 mM) was added dropwise to chilled sodium borohydride (30 mL, 2 mM). The mixture was stirred vigorously with the addition of silver

nitrate, the stirring was then stopped and potassium chloride (20 µL) was then added. The yellowish resulting solution was then wrapped with foil and kept away from the natural light.[168]

2.2.7.3 Gold nanoparticles preparation (Au NPs)

Small seed Au-NPs were synthesised by citrate reduction. 1% solution of trisodium citrate was prepared by dissolving 50 mg in 5 mL of distilled water which was then added to a refluxing solution of hydrogen tetrachloroaurate ($HAuCl_4$ (20 mg) in distilled water (50 mL). The colour of the resulting solution was changed through the reaction to deep red colour. The heat was removed after the solution was refluxed for 30 minutes.[169] Final Au-NPs were synthesised from the seed solution with citrate reduction. Hydrogen tetrachloroaurate (0.5 mL, 11 mM) was added to distilled water (32 mL) and the solution brought to reflux. The prepared seed Au-NPs solution (0.3 mL) was added followed closely by 1% solution of trisodium citrate (0.17 mL). The heat was removed after 10 minutes and the solution was allowed to cool with stirring.[169]

2.2.7.4 Corticosteroids (CSs) solution

Aqueous solution of each of corticosteroids (BUD, BDP, FLU and MOM) was prepared in the concentration near their solubility in water (0.05, 0.003, 0.001 and 0.0015 mM respectively). 1 mL of each solution was then mixed with 0.5 mL of the prepared Ag or Au-NPs and 0.5 mL of water (S1). Another solution prepared by mixing 0.5 mL of the prepared Ag or Au-NPs with 0.5 mL of SCD solution (0.125 mM) and the resulting solution was added to 1 mL of corticosteroid solution (S2). Both prepared solutions had the same Ag or Au NPs concentration and the same corticosteroid concentration with the second contains SCD. Blank solution was prepared by mixing 1 mL of corticosteroid solution with 1 mL of water to produce the same concentration of the compound as the above prepared solutions (S3). All the prepared solutions are presented in Table 2.8.

Table 2.8: Different corticosteroids solutions prepared by mixing with Ag or Au NPs and SCD.

S1	S2	S3
1 mL of CS solution 0.5 mL of Ag or Au-NPs 0.5 mL of water	1 mL of CS solution 0.5 mL of Ag or Au-NPs 0.5 mL of SCD	1 mL of CS solution 1 mL of water ///

The prepared Ag-NPs were centrifuged by placing in a 1.5 mL centrifuged tube for 30 min at 3000 g, 1.25 mL of supernatant was removed and the NPs were resuspended in water to 1.5 mL [170]. The Au-NPs were centrifuged by placing in a 1.5 mL centrifuged tube for 20 min at 7000 g, 1.25 mL of supernatant was removed and the NPs were resuspended in water to 1.5 mL [171]. Then both centrifuged solutions of Ag and Au-NPs were mixed with the corticosteroid solution and the same procedure was followed as in the case of uncentrifuged solutions. All the solutions were analysed by Raman spectroscopy.

2.3 Instrumentation

2.3.1 UV-Vis spectroscopy

2.3.1.1 UV-Vis analysis of the complexation

The samples are analysed in a glass cuvette and positioned in the Varian CARY 50 Probe UV-Visible spectroscopy using Cary WinUv software. The blank was also run between samples, which was the solvent being used for the preparation.

2.3.1.2 UV-Vis analysis of Ag/Au NPs

The Au and Ag NPs solutions were analysed in a glass cuvette and positioned in the Varian CARY 50 Probe UV-Visible spectroscopy using Cary WinUv software. The blank was also run which was the solvent being used for the preparation (water). The absorption spectra for both Au and Ag-NPs solutions were recorded in the range of 300-900 nm.

2.3.2 Inductively Coupled Plasma Optical Emission Spectrometry (ICP-OES) analysis of Ag/Au NPs

The Ag and Au-NPs were prepared according to the method specified in the section 2.2.7.2 and 2.2.7.3. Equal volumes of the uncentrifuged Ag-NPs solution and nitric acid (69 %) were mixed. Similarly, equal volumes of the centrifuged Ag-NPs solution and nitric acid (69 %) were mixed and then both uncentrifuged and centrifuged solutions were taken for the analysis. The addition of the nitric acid is to dissolve the Ag-NPs and convert them back to the silver nitrate.[172] Both uncentrifuged and centrifuged Au-NPs solutions were taken directly for the analysis. The test samples were prepared for analysis by ICP-OES (Thermo Fisher iCAP 6500 Duo ICP-OES) by diluting 0.1 mL in 2 mL

of nitric acid with 25 µL of Rhodium (internal standard). The samples were then made up to the volume 25 mL with deionised water. Clear solutions, free from particulates were generated that were taken for the analysis.

2.3.3 Dynamic Light Scattering (DLS) analysis of Ag/Au NPs

DLS measurements were performed at 25° C using a Malvern ZS ZEN 3600 system (Malvern instruments GmbH, UK) equipped with a red laser (633 nm). The Au and Ag-NPs solutions were put in the cuvette that was then positioned in the instrument where the laser light was directed and focused on the cuvette. The measurements were performed with 3 runs of 10 measurements. The signals were collected by a photodiode detector and processed by Malvern Zetasizer nanoapplication software.

2.3.4 Transmission Electron Microscopy (TEM) analysis of Ag/Au NPs

Transmission electron microscopy (TEM) measurements were performed at an acceleration voltage of 80 kV. A drop of Au and Ag-NPs solutions were placed onto carbon coated 200 mesh copper grids and allowed to dry overnight prior to the measurements. Mean particle sizes were determined on the basis of the TEM images taken by measuring 100 particles per sample.

2.3.5 NMR spectroscopy

For studying the complex formation in different solvents, the prepared solution of the molecule and CD in the desired solvent is transferred to a 5 mm NMR tube which was then inserted into the JEOL 600 MHz NMR spectroscopy. A co-axial NMR tube setup (Wilmad Labglass, NJ, USA) was prepared by inserting a co-axial capillary tube within the standard 5 mm NMR tube for the purpose of adding a physically isolated reference material. The studied solution was added to the standard NMR tube while the reference solution ($CHCl_3$ in CD_3CN) was added to the inside capillary tube. The co-axial tube was then inserted into the JEOL 600 MHz NMR spectroscopy. The sample was locked and shimmed using PFGs (D_2O) and a standard ^1H NMR spectrum collected. Further ^1H experiment was performed using a presaturation method by suppressed solvent at 4.67 ppm (D_2O) and at 2.80 ppm (CH_3CN residual) using different attenuation at (30,40), (40,40), (50,40), (30,50), (40,50), (50,50), (60,50), (44,50), (46,50), (45,50) dB. The experiment was repeated with an attenuation value of (45,50) dB at 4.67 ppm (D_2O) and at 2.80 ppm (CH_3CN residual) respectively and the

spectra were obtained using 2048 scans. The study of the complexation in HPFP was performed by suppression of HPFP signal at 4.38 ppm and residual CH_3CN signal at 2.15 ppm using a power of 45 and 50 dB respectively with long acquisition times (2048 scans). The study of the pure *R*-enantiomer of BUD was performed on 400 MHz NMR using the same pre-saturation suppression parameters used for the racemic mixture and the spectra were collected with equivalent acquisition times (2048 scans). NMR spectra were acquired over a 10 ppm spectral width using 65 K data points, giving a spectral resolution of 0.00015 ppm. These acquisition parameters allowed us to extract chemical shift values for the titration experiments with accuracy to the 4^{th} decimal place and track the small displacements observed in the experiments.

2.3.6 FT-IR spectroscopy

Samples of physical mixtures and complexes of budesonide and (*β*CD, TRIMEB and DIMEB) were prepared as potassium bromide (KBr) discs by taking about 2 mg of sample in an agate mortar and pestle and about 350 mg of KBr and grind them into a fine powder. The resultant powder was then pressed to form KBr disc using a SpecAc hydraulic press and die set under 10 tonne pressure. The disc was then transferred to be analysed by the Digilab UMA 400 FT-IR using a transmission mode with 64 scans and 2 cm^{-1} spectral resolution in the range of 400-4000 cm^{-1} with an acquisition of a background spectrum that was subtracted from the sample spectra using the Digilab software.

2.3.7 Raman spectroscopy

Samples of physical mixtures and complexes of budesonide and (*β*CD, TRIMEB and DIMEB) were put on aluminium slides for Raman analysis using 50x objective lens of the Renishaw InVia Raman microscope which was calibrated prior starting work using the internal silicon reference for wavenumber shift with manual adjustment to 520.0 cm^{-1}. Spectra were collected over the range 100-3200 cm^{-1} using 785 nm high powered diode laser at 100% power with 10 seconds exposure time and 10 accumulations.

SERS studies were performed using foil covered glass slides, placing a drop of the sample on the slide and using the 20x lens to collect the spectrum. The analysis was performed using 100 % laser power and 10 s exposure time with 1 accumulation. Raw data were pre-processed with Bruker OPUS 7.5 before

plotting with Origin 2018. Baselines were corrected with concave rubber band method over 64 baseline points and 10 iterations; spectra were normalised in the range 3200-300 cm^{-1} before plotting.

3 Development of UV-Vis and NMR methods for the study of host:guest complexes using vanillin and *β*CD

NMR spectroscopy is one of the techniques that has been extensively used for this purpose, as part of method development, it is valuable to repeat some published work to ensure the reproducibility of the methods and results obtained from the analytical instrumentation. Also, to understand the determination of the stoichiometry and the apparent stability, as they both depend on the chemical shift differences between the pure and the complex compound with CD. Vanillin has been studied by NMR for complexation with CD and was chosen as a representative model for the method development.[173] It has a simple structure (Figure 3.1) and has a large chemical shift difference between its free and complexed forms so that it is easier to understand the determination of the stability constant. Vanillin was also examined by UV-Vis spectroscopy as another method to study the complexation.

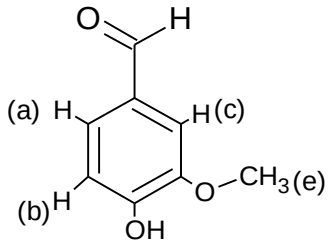

Figure 3.1: Structure of vanillin

3.1 Complexation study of vanillin and *β*CD in D_2O by NMR

The stoichiometry was determined using continuous variation method as described in Section 2.2.3.1. The results are presented in Table 3.1 where the chemical shift was recorded in Hz (very small shift were observed in the case of taking shift at ppm) taking 4.75 ppm for the residual water as reference. The calculation was based on the shift occurred at H5 proton of *β*CD (the same proton was taken in the literature) which had a considerable shift compared to the other hydrogens (Figure 3.2). The chemical shift difference between pure

vanillin and complex vanillin ($\Delta\delta_{obs}$) was calculated by taking the difference between pure vanillin (in the absence of *β*CD, δ_{free}) and complex vanillin (in the presence of *β*CD, $\delta_{complex}$).

Table 3.1: Results of ^{1}H NMR analysis for the determination of stoichiometry between vanillin and *β*CD

[*β*CD] (mM)	R	$\delta_{complex}$ (Hz)	$\Delta\delta_{obs}$ (δ_{free} - $\delta_{complex}$) Hz	$\Delta\delta$[*β*CD]
0	0	0	0	0
1	0.1	1495.9	42.4	42.4
2	0.2	1501	37.3	74.6
3	0.3	1505.5	32.8	98.4
4	0.4	1509.5	28.8	115.2
5	0.5	1513.6	24.7	123.5
6	0.6	1519.1	19.2	115.2
7	0.7	1526.2	12.1	84.7
8	0.8	1530.8	7.5	60
9	0.9	1534.3	4	36
10	1	1538.3	0	0

δ_{free} = 1538.3 Hz

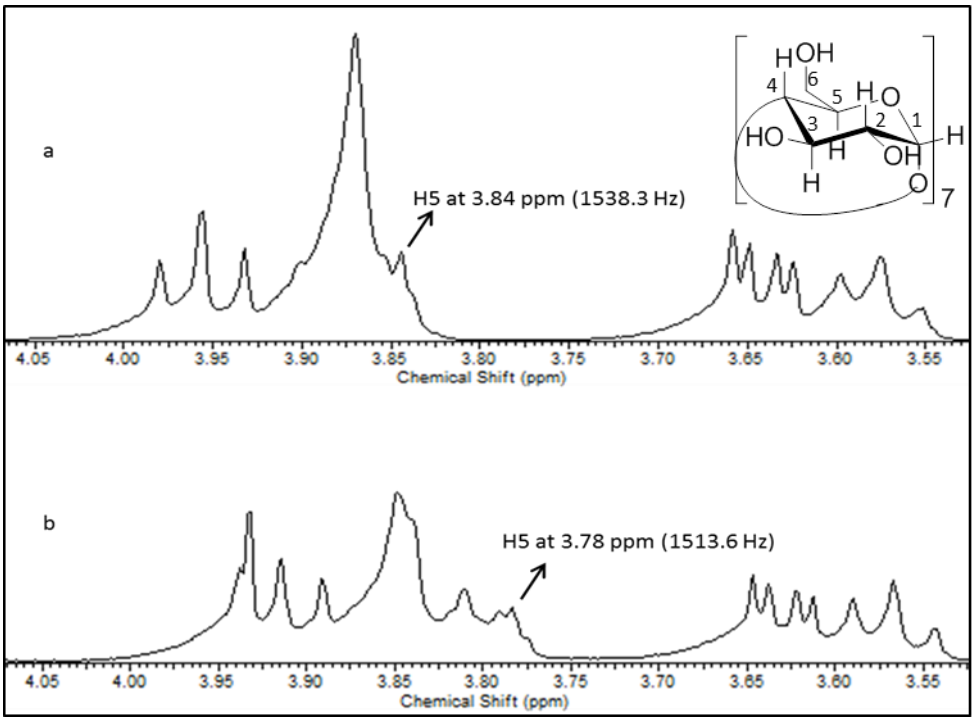

Figure 3.2: Partial ^{1}H NMR spectrum of (a) *β*CD (10 mM), (b) 5 mM of *β*CD and 5 mM of vanillin.

The stoichiometry was determined by plotting r which was the ratio of [*β*CD]/[van]+[*β*CD] versus Δδ * [*β*CD] (Figure 3.3) which clearly showed that the highest value of r was at 0.5, indicating the stoichiometry ratio of the complex was 1:1 and was consistent with those reported by Pirnau *et al*.[173]

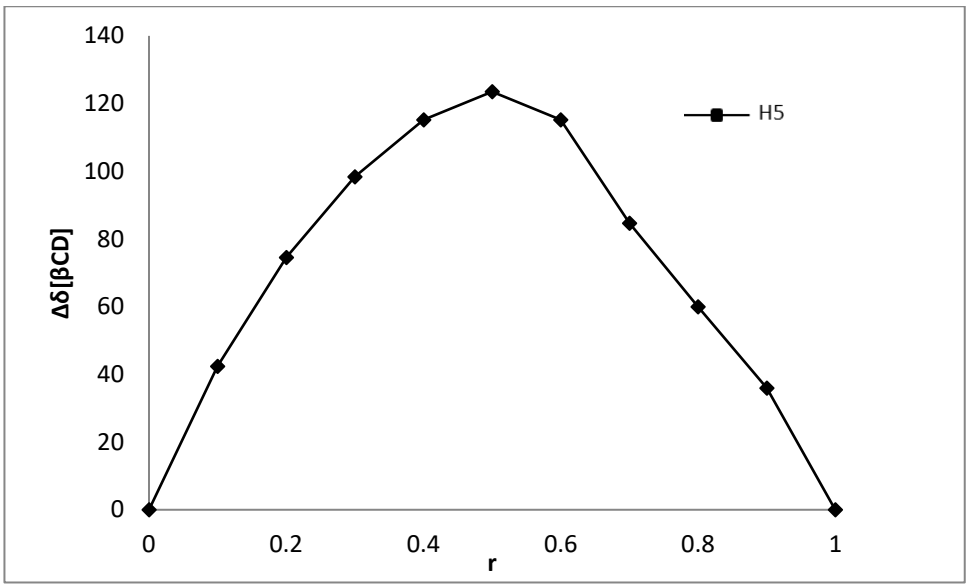

Figure 3.3: Determination of the stoichiometry of the complex between vanillin and *β*CD by ^{1}H NMR based on H5 proton of *β*CD

The stability constant was determined by keeping the vanillin concentration constant while increasing the concentration of *β*CD to form different solutions of constant vanillin concentration with different concentrations of *β*CD (Section 2.2.4.1). The stability constant of the complex was calculated according to Hildebrand-Benesi Equation:[174]

$$\frac{1}{\Delta\delta_{obs}} = \frac{1}{[CD]K\,\Delta\delta_{max}} + \frac{1}{\Delta\delta_{max}}$$ **Equation 3.1**

Where $\Delta\delta_{obs}$ is the difference in the chemical shift between free vanillin and the observed value for a given ratio, and $\Delta\delta_{max}$ is the chemical shift difference between free vanillin and the pure complex. The [CD] and K are the concentration of *β*CD and association constant respectively. The stability constant was determined depending on the shift at Hb proton of vanillin (Figure 3.4). The results are presented in Table 3.2.

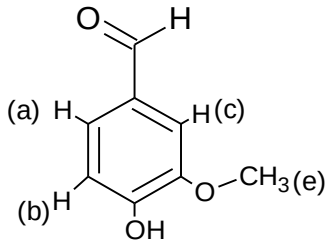

Figure 3.4: Structure of vanillin

Table 3.2: Results of the determination of the association constant between vanillin and *β*CD using ^{1}H NMR

*β*CD (mM)	1/*β*CD (mM^{-1})	Exp. 1 (δ_{free} = 2805.5 Hz)			Exp. 2 (δ_{free} = 2809.1 Hz)		
		$\delta_{complex}$	$\Delta\delta_{obs}$	$1/\Delta\delta_{obs}$	$\delta_{complex}$	$\Delta\delta_{obs}$	$1/\Delta\delta_{obs}$
12	0.083	2818.2	12.7	**0.079**	2820.2	11.1	**0.090**
14	0.071	2821.0	15.5	**0.065**	2822.8	13.7	**0.073**
15	0.067	2822.7	17.2	**0.058**	2824.7	15.6	**0.064**
16	0.063	2824.9	19.4	**0.052**	2826.3	17.2	**0.058**

$\Delta\delta_{obs}$ ($\delta_{complex}$ - δ_{free})

The stability constant can be calculated from the slope and the intercept of the straight line equation of the NMR titration (Figures 3.5).

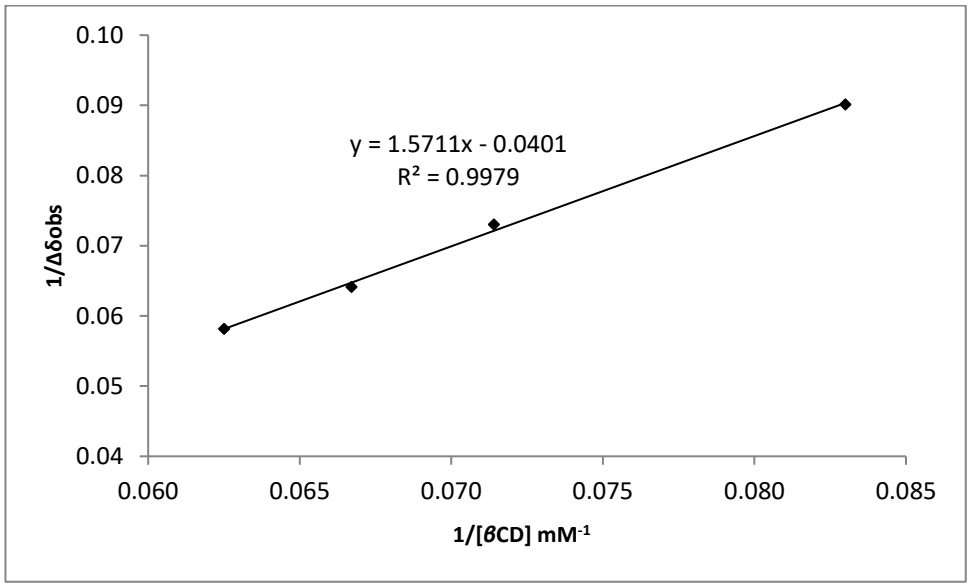

Figure 3.5: Reciprocal plot for the determination of association constant between vanillin and *β*CD by ^{1}H NMR.

A good linear relationship was obtained from the two experiments which indicated the stoichiometry of the complex was 1:1 and the mean stability constant was 24 M^{-1}.

3.2 Complexation study of vanillin and *β*CD in water by UV-Vis spectroscopy

The vanillin solution without the *β*CD (at 0.05 mM) was first run in the scan range of 200-350 nm to determine the λ_{max} of vanillin in the presence of water as a solvent and peaks were found at 230, 280 and 310 nm. The λ_{max} at 280 nm was chosen for the analysis of vanillin in this study. The solutions were prepared based on continuous variation method (Section 2.2.1.1) and their

absorbance were measured at 280 nm. The absorbance (A) was calculated by taking the differences in the absorbance between free vanillin (without *β*CD) A_0, and absorbance of each solution of *β*CD-complexed vanillin ($A_{measured}$), and the results are presented in Table 3.3.

Table 3.3: Results of the determination of the stoichiometry between vanillin and *β*CD using UV-Vis spectroscopy.

Vanillin [van]*10^{-2} (mM)	r	$A_{measured}$	A	A[van]
5	1	0.52	0	0
4.5	0.9	0.449	0.071	0.320
4	0.8	0.39	0.13	0.520
3.5	0.7	0.335	0.185	0.648
3	0.6	0.284	0.236	0.708
2.5	0.5	0.228	0.292	0.730
2	0.4	0.189	0.331	0.662
1.5	0.3	0.147	0.373	0.560
1	0.2	0.09	0.43	0.430
0.5	0.1	0.051	0.469	0.235
0	0	0	0	0

$A_0 = 0.520$

The stoichiometry was determined by plotting r which was the ratio of [van]/[van]+[*β*CD] versus A* [van] (Figure 3.6) and it has been found that the maximum r was 0.5 which revealed 1:1 stoichiometry ratio of the complexation.

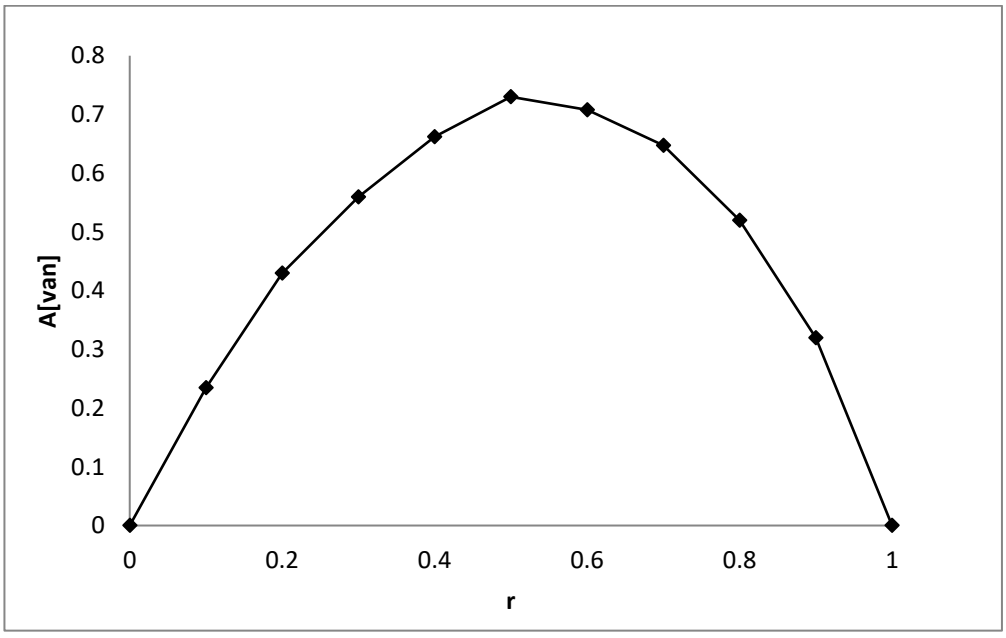

Figure 3.6: Determination of the stoichiometry of the complex between vanillin and *β*CD based on the absorbance at 280 nm using UV-Vis spectroscopy.

To determine the association constant, the vanillin concentration was kept constant at 0.05 mM and βCD was added at 2, 4, 6 and 8 mM as described in Section 2.2.2.1. The experiment was repeated three times and the results are presented in the Table 3.4.

Table 3.4: Results of the determination of the association constant between vanillin and βCD added at 0, 2, 4, 6 and 8 mM in H_2O using UV-Vis spectroscopy.

βCD (mM)	Absorbance at 280 nm			Mean	SD	% CV
	1	2	3			
0	0.477	0.476	0.480	**0.478**	**0.002**	**0.436**
2	0.500	0.504	0.508	**0.504**	**0.004**	**0.794**
4	0.513	0.520	0.524	**0.519**	**0.006**	**1.073**
6	0.521	0.530	0.534	**0.528**	**0.007**	**1.260**
8	0.529	0.538	0.543	**0.537**	**0.007**	**1.322**

The stability constant of the complex formed between vanillin and βCD was determined by plotting 1/ [βCD] versus 1/A according to Hildebrand-Benesi Equation [175]:

$$\frac{1}{\Delta A} = \frac{1}{\Delta\varepsilon\,[G]_0 K[CD]} + \frac{1}{\Delta\varepsilon\,[G]_0}$$ **Equation 3.2**

Where; ΔA is the absorbance difference between the absorbance of free vanillin A_0 and complex vanillin ($A_{measured}$). $[G]_0$ and K are the initial vanillin concentration and stability constant while Δε is the molar absorptivity difference between the free and complex vanillin and [CD] is the βCD concentration. It can be seen clearly the absorbance of vanillin was increased as the concentration of βCD was increased (hyperchromic effect) with small hypsochromic shift to the maximum at 280 nm (Figure 3.7).

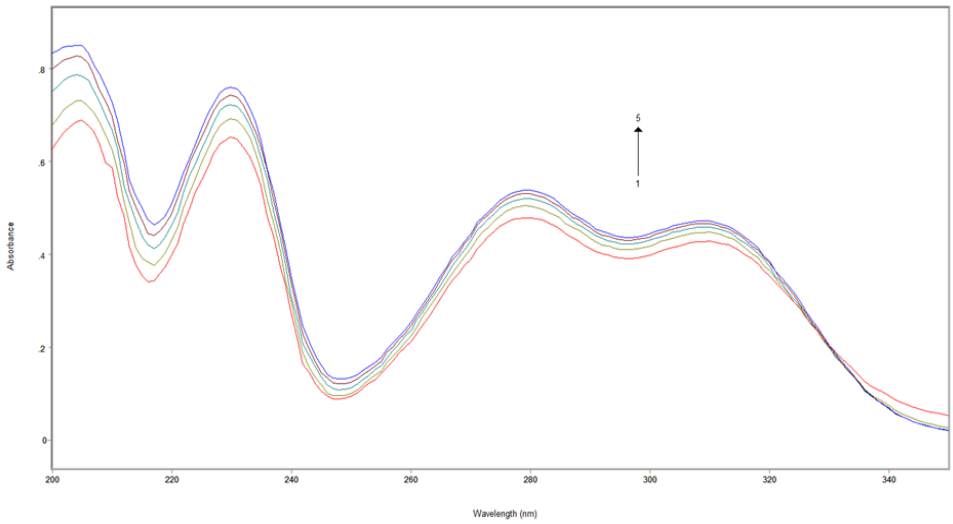

Figure 3.7: UV spectra of vanillin with *β*CD concentration at 1) 0, 2) 2, 3) 4, 4) 6 and 5) 8 mM

The results for the three experiments are shown in Table 3.5 and the reciprocal plot to determine the stability constant is shown in Figure 3.8.

Table 3.5: Results of the determination of the association constant between vanillin and *β*CD added at 2, 4, 6 and 8 mM in H_2O using UV-Vis spectroscopy.

1/CD mM^{-1}	Exp. 1 (A_0 = 0.477)			Exp. 2 (A_0 = 0.476)			Exp. 3 (A_0 = 0.480)			Mean
	A*	A	1/A	A*	A	1/A	A*	A	1/A	
0.5	0.5	0.023	**43.5**	0.504	0.028	**35.7**	0.508	0.028	**35.7**	38.3
0.25	0.513	0.036	**27.8**	0.52	0.044	**22.7**	0.524	0.044	**22.7**	24.4
0.17	0.521	0.044	**22.7**	0.53	0.054	**18.5**	0.534	0.054	**18.5**	19.9
0.13	0.529	0.052	**19.2**	0.538	0.062	**16.1**	0.543	0.063	**15.9**	17.1

$A^* = A_{measured}$, $A = A^* - A_0$

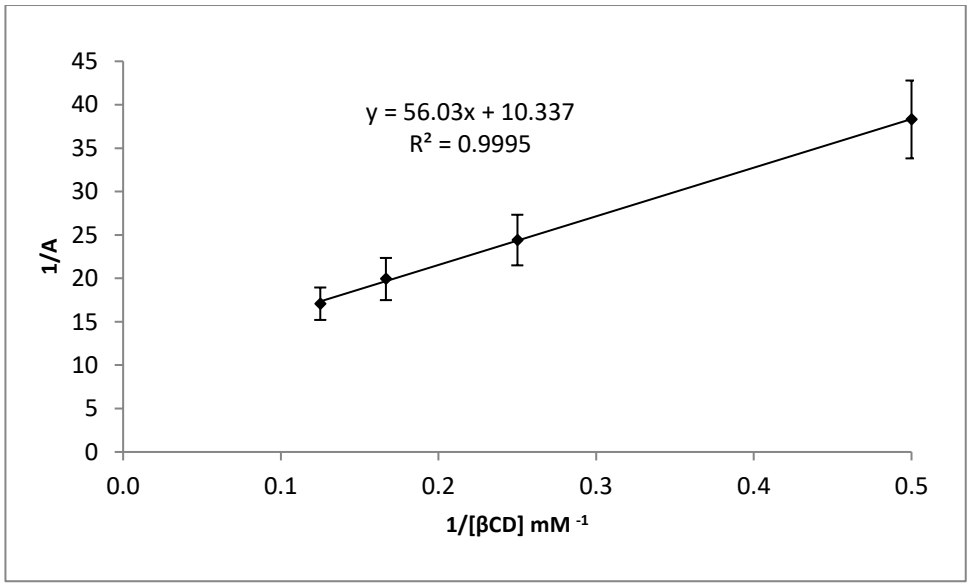

Figure 3.8: Reciprocal plot for the association constant determination between vanillin and *β*CD by UV-Vis spectroscopy (Mean ± SD, n=3).

A good linear relationship was obtained which demonstrated that the stoichiometry of the complex formed between vanillin and *β*CD is 1:1. The mean K value was calculated from the slope and the intercept as mentioned above and was found to be 184 M^{-1}.

3.3 Discussion

The method of continuous variation applied to study the stoichiometry and the titration method to calculate the stability constant based on Hildebrand-Benesi equation showed good results from both techniques used. This indicated that both methods can be applied as an additional approach to study the inclusion complex between budesonide and other corticosteroids with cyclodextrins.

4 Host:guest Interactions in conventional solvents using UV-Vis and NMR spectroscopy

The main aim of this work is to study complexation of corticosteroids and CDs in HFA based solvent systems. Our first step, has been to study the complexation of BUD (as a representative model to the other corticosteroids) in conventional solvents using UV-Vis methods and in deuterated solvents using NMR methods to obtain comprehensive data on the complexation of BUD in three derivatised CDs in a range of different solvent systems. The three solvents were chosen to investigate the effect of differing solvent polarity on the complexation. $CDCl_3$ is used as a relatively non-polar solvent, with CD_3CN and MeOD being polar aprotic and protic solvents respectively. The complexation of BUD was also studied in D_2O to investigate the behaviour in polar solvents, though significant challenges with this system were encountered with the limited solubility of BUD in D_2O, and these method development challenges are also discussed in this Chapter.

4.1 Complexation study of BUD and *β*CD/TRIMEB by UV-Vis spectroscopy

The complexation of BUD and *β*CD/TRIMEB was investigated in a mixture of EtOH/H_2O and in water alone. BUD solution in water was prepared at a concentration near the previously determined solubility (23.5 µg/mL).[52] The study relies on the addition of different concentrations of cyclodextrins to a fixed concentration of budesonide followed by the determination of the absorbances of each solution (at a fixed wavelength) and compared to that of the original budesonide solution (without the addition of cyclodextrins). The complex formation was confirmed by the existence of either a hyperchromic or bathochromic shift at λ_{max} of budesonide.

4.1.1 Complexation of BUD and *β*CD in EtOH: H_2O and H_2O

The complexation between BUD and *β*CD was investigated in 50:50 mixture of EtOH/H_2O and in water by preparing different solutions as described in Section 2.2.2.2. The BUD solution without *β*CD (at 0.04 mM) was first run in the scan range 200-350 nm to determine its λ_{max} which was found at 246 nm in EtOH/H_2O and in water. All solutions were measured at 246 nm.

The results showed that BUD had a hyperchromic shift as its absorbance was increased with the increasing *β*CD concentration. No significant appearance of either hypsochromic or bathochromic shifts to the maximum at 246 nm (Figure 4.1). The change in the absorption spectrum of the guest molecule as its chromophore was transferred from a polar medium (EtOH/H_2O) to a non-polar CD cavity is a result of the inclusion complex forming in solution. This caused disconcertion of guest electronic energy levels as a result of the interaction of guest with the host molecule directly or by elimination of water molecules or both together.[128]

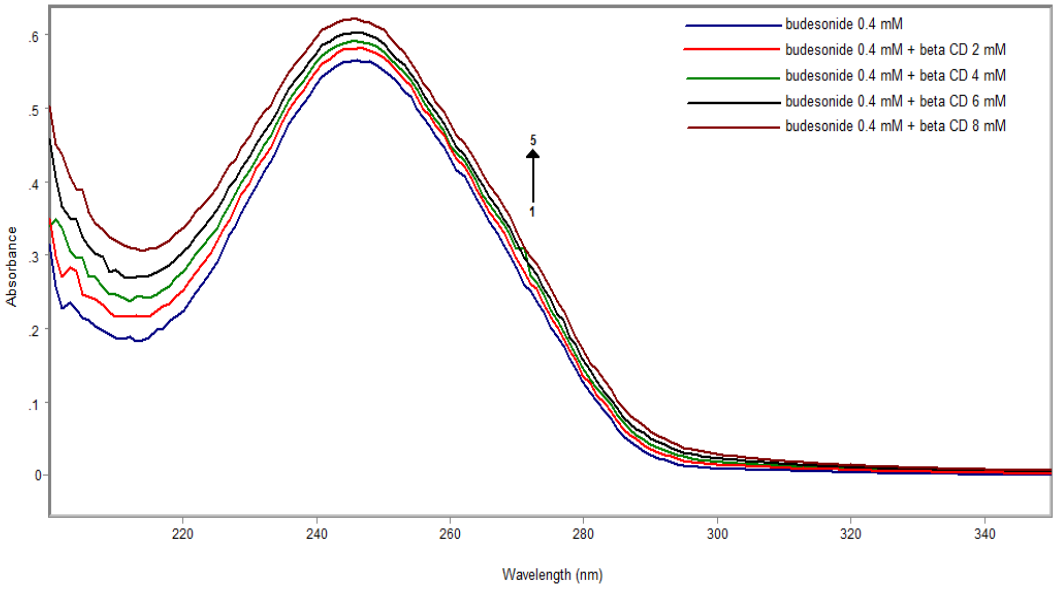

Figure 4.1: UV spectra of budesonide with *β*CD concentration at 1) 0, 2) 2, 3) 4, 4) 6 and 5) 8 mM in EtOH/H_2O (50:50) solvent.

The results and the calculation of the stability constant of the complexation in (EtOH:H_2O) and in water are presented in Tables 4.1/4.2 and 4.3/4.4 respectively with the reciprocal plots are shown in Figure 4.2.

Table 4.1: Results of the complexation between budesonide and *β*CD added at 0, 2, 4, 6 and 8 mM in EtOH/H_2O (50:50) using UV-Vis spectroscopy.

CD (mM)	Absorbance at 246 nm			Mean	SD	% CV
	1	2	3			
0	0.573	0.568	0.575	**0.572**	**0.004**	**0.630**
2	0.583	0.579	0.586	**0.583**	**0.004**	**0.603**
4	0.597	0.600	0.603	**0.600**	**0.003**	**0.5**
6	0.618	0.625	0.627	**0.623**	**0.005**	**0.758**
8	0.64	0.635	0.655	**0.643**	**0.01**	**1.618**

Table 4.2: Results of the stability constant determination between budesonide and *β*CD added at 2, 4, 6 and 8 mM in EtOH/H_2O (50:50) using UV-Vis spectroscopy.

1/CD mM^{-1}	Exp. 1 (A_0 = 0.573)			Exp. 2 (A_0 = 0.568)			Exp. 3 (A_0 = 0.575)			Mean
	A*	A	1/A	A*	A	1/A	A*	A	1/A	
0.5	0.583	0.01	**100**	0.579	0.011	**90.9**	0.586	0.011	**90.9**	**93.9**
0.25	0.597	0.024	**41.8**	0.600	0.032	**31.3**	0.603	0.028	**35.7**	**36.2**
0.17	0.618	0.045	**22.2**	0.625	0.057	**17.5**	0.627	0.052	**19.2**	**19.7**
0.13	0.64	0.067	**14.9**	0.635	0.067	**14.9**	0.655	0.08	**12.5**	**14.1**

$A^* = A_{measured}$, $A = A^* - A_0$

Table 4.3: Results of the complexation between budesonide and *β*CD added at 0, 2, 3, 4, 5 and 7 mM in H_2O using UV-Vis spectroscopy.

CD (mM)	Absorbance at 246 nm			Mean	SD	% CV
	1	2	3			
0	0.141	0.146	0.138	**0.142**	**0.004**	**2.853**
2	0.147	0.152	0.144	**0.148**	**0.004**	**2.737**
3	0.151	0.156	0.148	**0.152**	**0.004**	**2.665**
4	0.156	0.162	0.154	**0.157**	**0.004**	**2.646**
5	0.165	0.17	0.163	**0.166**	**0.004**	**2.172**
7	0.192	0.197	0.187	**0.192**	**0.005**	**2.604**

Table 4.4: Results of the stability constant determination between budesonide and *β*CD added at 2, 3, 4, 5 and 7 mM in H_2O using UV-Vis spectroscopy.

1/CD mM^{-1}	Exp. 1 (A_0 = 0.141)			Exp. 2 (A_0 = 0.146)			Exp. 3 (A_0 = 0.138)			Mean
	A*	A	1/A	A*	A	1/A	A*	A	1/A	
0.50	0.147	0.006	**167**	0.152	0.006	**167**	0.144	0.006	**167**	**167**
0.33	0.151	0.01	**100**	0.156	0.01	**100**	0.148	0.01	**100**	**100**
0.25	0.156	0.015	**66.7**	0.162	0.016	**62.5**	0.154	0.016	**62.5**	**63.9**
0.20	0.165	0.024	**41.7**	0.17	0.024	**41.7**	0.163	0.025	**40**	**41.1**
0.14	0.192	0.051	**19.6**	0.197	0.051	**19.6**	0.187	0.049	**20.4**	**19.9**

$A^* = A_{measured}$, $A = A^* - A_0$

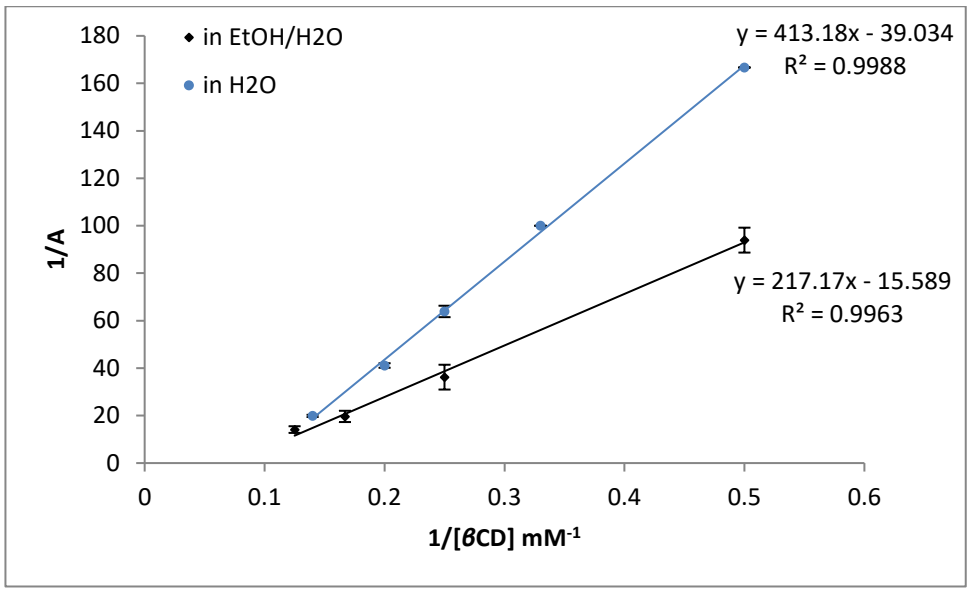

Figure 4.2: Reciprocal plot for the determination of association constant between budesonide and *β*CD in EtOH/H_2O (50:50) and H_2O by UV-Vis spectroscopy (Mean ± SD, n=3).

It can be seen from the plots that a good linear relationship was obtained which indicated that the stoichiometry of the complex formed between budesonide and *β*CD was 1:1. The mean K values of the complexation in EtOH/H_2O and in water were calculated from the slope and the intercept and they were found to be 72 and 94 M^{-1} respectively. The stoichiometry of the complex in EtOH/H_2O and in water was confirmed by the continuous variation method where both BUD and *β*CD are prepared as stock solutions. Then different ratios were taken from both solutions to form different solutions of constant concentration with constant volume (see Section 2.2.1.2). The results are presented in Tables 4.5 and 4.6.

Table 4.5: Results of the determination of the stoichiometry between budesonide and *β*CD in EtOH/H_2O (50:50) using UV-Vis spectroscopy.

[BUD]*10^{-2} (mM)	r	$A_{measured}$	A ($A_{measured}$ - A_0)	A[BUD]
4	1	0.586	0	0
3.6	0.9	0.517	0.069	0.248
3.2	0.8	0.46	0.126	0.403
2.8	0.7	0.403	0.183	0.512
2.4	0.6	0.341	0.245	0.588
2	0.5	0.287	0.299	0.598
1.6	0.4	0.232	0.354	0.566
1.2	0.3	0.174	0.412	0.494
0.8	0.2	0.117	0.469	0.375
0.4	0.1	0.067	0.519	0.208
0	0	0	0	0

A_0 = 0.586

Table 4.6: Results of the determination of the stoichiometry between budesonide and *β*CD in H_2O using UV-Vis spectroscopy.

[BUD]*10^{-2} (mM)	r	$A_{measured}$	A ($A_{measured}$ - A_0)	A[BUD]
5	1	0.901	0	0
4.5	0.9	0.772	0.129	0.581
4	0.8	0.67	0.231	0.924
3.5	0.7	0.575	0.326	1.141
3	0.6	0.48	0.421	1.263
2.5	0.5	0.37	0.531	1.328
2	0.4	0.302	0.599	1.198
1.5	0.3	0.243	0.658	0.987
1	0.2	0.158	0.743	0.743
0.5	0.1	0.076	0.825	0.413
0	0	0	0	0

A_0 = 0.901

The stoichiometry was determined by plotting r which is the ratio of [BUD]/[BUD]+[*β*CD] versus A* [BUD] (Figure 4.3), and it has been found that the highest r value was 0.5 which corresponds to 1:1 stoichiometric ratio of the complex in both co-solvent system and in water.

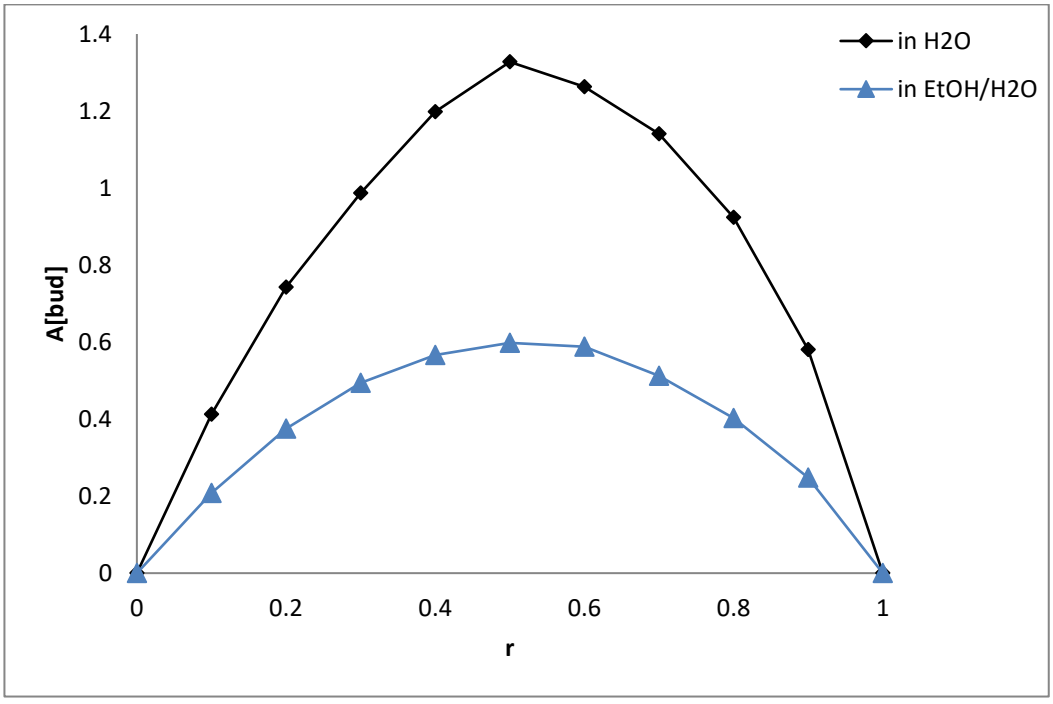

Figure 4.3: Determination of the stoichiometry of the complex between budesonide and *β*CD in EtOH/H_2O (50:50) and H_2O based on the absorbance at 246 nm using UV-Vis spectroscopy.

4.1.2 Complexation of BUD and TRIMEB in EtOH: H_2O and H_2O

The complexation between BUD and TRIMEB was studied in 50:50 (EtOH:H_2O) and in water where the prepared solutions (see Section 2.2.2.3) were measured at 246 nm. The results of the triplicate experiments and the calculation of the stability constant in (EtOH:H_2O) and in water are presented in Tables 4.7/4.8 and 4.9/4.10 respectively with the reciprocal plots being shown in Figure 4.4.

Table 4.7: Results of the complexation and the stability constant determination between budesonide and TRIMEB added at 0, 0.4, 0.6, 0.8, 1 and 1.4 mM in EtOH/H_2O (50:50) using UV-Vis spectroscopy.

CD (mM)	Absorbance at 246 nm			Mean	SD	% CV
	1	2	3			
0	0.577	0.571	0.576	**0.575**	**0.003**	**0.559**
0.4	0.589	0.584	0.587	**0.587**	**0.003**	**0.429**
0.6	0.595	0.59	0.591	**0.592**	**0.003**	**0.447**
0.8	0.601	0.596	0.595	**0.597**	**0.003**	**0.538**
1	0.606	0.601	0.6	**0.602**	**0.003**	**0.534**
1.4	0.613	0.613	0.612	**0.613**	**0.001**	**0.094**

Table 4.8: Results of the stability constant determination between budesonide and TRIMEB added at 0.4, 0.6, 0.8, 1 and 1.4 mM in EtOH/H_2O (50:50) using UV-Vis spectroscopy.

1/CD mM^{-1}	Exp. 1 (A_0 = 0.577)			Exp. 2 (A_0 = 0.571)			Exp. 3 (A_0 = 0.576)			Mean
	A*	A	1/A	A*	A	1/A	A*	A	1/A	
2.5	0.589	0.012	**83.3**	0.584	0.013	**76.9**	0.587	0.011	**90.9**	**83.7**
1.7	0.595	0.018	**55.6**	0.59	0.019	**52.6**	0.591	0.015	**66.7**	**58.3**
1.3	0.601	0.024	**41.7**	0.596	0.025	**40.0**	0.595	0.019	**52.6**	**44.8**
1	0.606	0.029	**34.5**	0.601	0.03	**33.3**	0.6	0.024	**41.7**	**36.5**
0.7	0.613	0.036	**27.8**	0.613	0.042	**23.8**	0.612	0.036	**27.8**	**26.5**

$A^* = A_{measured}$, $A = A^* - A_0$

Table 4.9: Results of the complexation and the stability constant determination between budesonide and TRIMEB added at 0, 0.4, 0.6, 0.8, 1 and 1.4 mM in H_2O using UV-Vis spectroscopy.

CD (mM)	Absorbance at 246 nm			Mean	SD	% CV
	1	2	3			
0	0.178	0.172	0.169	**0.173**	**0.005**	**2.649**
0.4	0.2	0.194	0.191	**0.195**	**0.005**	**2.350**
0.6	0.213	0.208	0.204	**0.208**	**0.005**	**2.164**
0.8	0.226	0.221	0.218	**0.222**	**0.004**	**1.823**
1	0.241	0.235	0.233	**0.236**	**0.004**	**1.762**
1.4	0.278	0.27	0.266	**0.271**	**0.006**	**2.252**

Table 4.10: Results of the stability constant determination between budesonide and TRIMEB added at 0.4, 0.6, 0.8, 1 and 1.4 mM in H_2O using UV-Vis spectroscopy.

1/CD mM^{-1}	Exp. 1 (A_0 = 0.178)			Exp. 2 (A_0 = 0.172)			Exp. 3 (A_0 = 0.169)			Mean
	A*	A	1/A	A*	A	1/A	A*	A	1/A	
2.5	0.2	0.022	**45.5**	0.194	0.022	**45.5**	0.191	0.022	**45.5**	**45.5**
1.7	0.213	0.035	**28.6**	0.208	0.036	**27.8**	0.204	0.035	**28.6**	**28.3**
1.3	0.226	0.048	**20.8**	0.221	0.049	**20.4**	0.218	0.049	**20.4**	**20.6**
1	0.241	0.063	**15.9**	0.235	0.063	**15.9**	0.233	0.064	**15.6**	**15.8**
0.7	0.278	0.1	**10**	0.27	0.098	**10.2**	0.266	0.097	**10.3**	**10.2**

$A^* = A_{measured}$, $A = A^* - A_0$

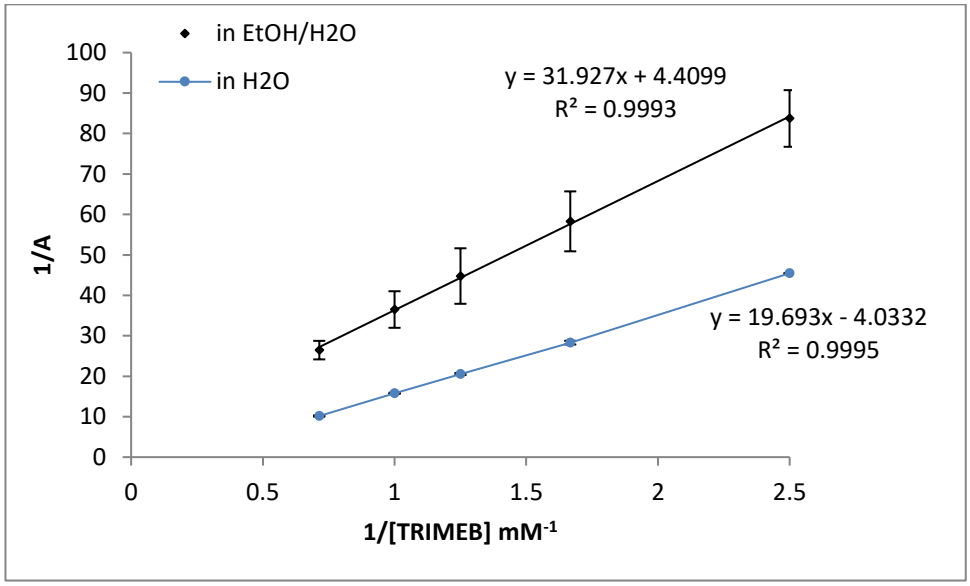

Figure 4.4: Reciprocal plot for the determination of association constant between budesonide and TRIMEB in EtOH/H_2O (50:50) and H_2O by UV-Vis spectroscopy (Mean ± SD, n=3).

The reciprocal plots showed a good linear relationship indicating that the inclusion complex formed had a stoichiometry of 1:1 in both solvent systems. The mean K values were calculated from the slope and the intercept and they were found to be 138 and 205 M^{-1} in EtOH/H_2O and in water respectively. The stoichiometry of the complex in EtOH/H_2O and in water was verified by Job's plot of continuous variation method (Section 2.2.1.2) as shown in Tables 4.11 and 4.12 respectively.

Table 4.11: Results of the determination of the stoichiometry between budesonide and TRIMEB in EtOH/H_2O (50:50) using UV-Vis spectroscopy.

[BUD]*10^{-2} (mM)	r	$A_{measured}$	A ($A_{measured}$ - A_0)	A[BUD]
4	1	0.568	0	0
3.6	0.9	0.527	0.041	0.148
3.2	0.8	0.467	0.101	0.323
2.8	0.7	0.402	0.166	0.465
2.4	0.6	0.337	0.231	0.554
2	0.5	0.27	0.298	0.596
1.6	0.4	0.227	0.341	0.546
1.2	0.3	0.183	0.385	0.462
0.8	0.2	0.129	0.439	0.351
0.4	0.1	0.07	0.498	0.199
0	0	0	0	0

A_0 = 0.568

Table 4.12: Results of the determination of the stoichiometry between budesonide and TRIMEB in H_2O using UV-Vis spectroscopy.

[BUD]*10^{-2} (mM)	r	$A_{measured}$	A ($A_{measured}$ - A_0)	A[BUD]
5	1	0.835	0	0
4.5	0.9	0.74	0.095	0.428
4	0.8	0.657	0.178	0.712
3.5	0.7	0.585	0.25	0.875
3	0.6	0.506	0.329	0.987
2.5	0.5	0.415	0.42	1.050
2	0.4	0.345	0.49	0.980
1.5	0.3	0.253	0.582	0.873
1	0.2	0.166	0.669	0.669
0.5	0.1	0.092	0.743	0.372
0	0	0	0	0

A_0 = 0.835

The Job's plots showed the maximum value of r was 0.5 which indicated the inclusion complex had stoichiometric ratio of 1:1 in both in water and in EtOH/H_2O solvent system (Figure 4.5).

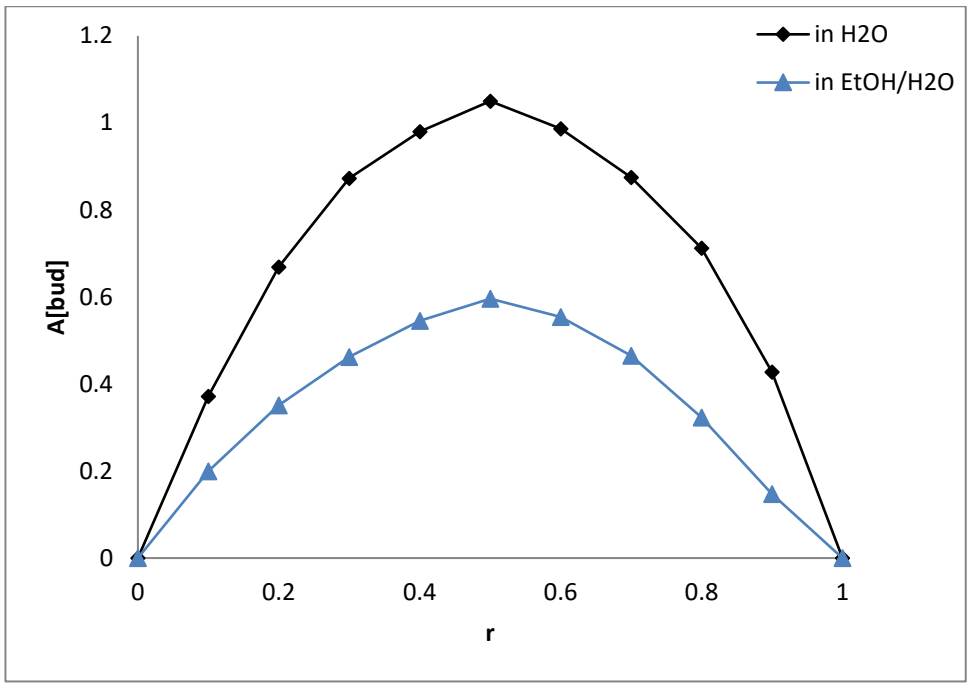

Figure 4.5: Determination of the stoichiometry of the complex between budesonide and TRIMEB in EtOH/H_2O (50:50) and H_2O based on the absorbance at 246 nm using UV-Vis spectroscopy.

4.2 Complexation study of BUD and DIMEB/TRIMEB by NMR

The complexation between BUD and DIMEB/TRIMEB was investigated in the three solvents; CD_3CN, $CDCl_3$ and MeOD using 600 MHz NMR (Section 2.2.4.2). The studies of the complexation with *β*CD in organic solvents were not assessed because of its insolubility in many organic solvents.

4.2.1 Complexation of BUD and DIMEB/TRIMEB in CD_3CN

It was found that there was no chemical shift differences observed for BUD (Figure 4.6) with TRIMEB and DIMEB using CD_3CN as solvent indicating no complex formed (Tables 4.13 and 4.14).

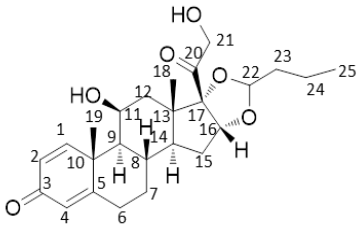

Figure 4.6: Chemical structure of budesonide

Table 4.13: Results of the chemical shift of budesonide and TRIMEB added at 0, 1, 2, 4, 6, and 8 mM in CD_3CN using ^1H NMR.

Proton position	TRIMEB concentration (mM)					
	0	1	2	4	6	8
	Chemical shift (ppm)					
H-C_{18}	0.8848	0.8852	0.8848	0.8848	0.8847	0.8843
H-C_{19}	1.3898	1.3902	1.3898	1.3898	1.3992	1.3894
H-C_4	5.8968	5.8961	5.8957	5.8963	5.8962	5.8964
H-C_2	6.1491	6.1509	6.1505	6.1505	6.1510	6.1512
H-C_1	7.2695	7.2709	7.2700	7.2700	7.2705	7.2695

Table 4.14: Results of the chemical shift of budesonide and DIMEB added at 0, 1, 2, 4, 6, and 8 mM in CD_3CN using ^1H NMR.

Proton position	DIMEB concentration (mM)					
	0	1	2	4	6	8
	Chemical shift (ppm)					
H-C_{18}	0.8848	0.8854	0.8859	0.8861	0.8870	0.8871
H-C_{19}	1.3898	1.3909	1.3911	1.3921	1.3927	1.3935
H-C_4	5.8968	5.8962	5.897	5.8997	5.9014	5.9015
H-C_2	6.1491	6.1499	6.1496	6.1499	6.1499	6.1494
H-C_1	7.2695	7.2700	7.2702	7.2705	7.2705	7.2717

4.2.2 Complexation of BUD and DIMEB/TRIMEB in $CDCl_3$

The same experiments were repeated for BUD with both DIMEB and TRIMEB in $CDCl_3$. The results showed fewer chemical shift differences for BUD (Figure 4.6) with TRIMEB (Table 4.15) compared to that with DIMEB (Table 4.16).

Table 4.15: Results of the chemical shift of budesonide and TRIMEB added at 0, 1, 2, 4, 6, and 8 mM in $CDCl_3$ using ^1H NMR.

Proton position	TRIMEB concentration (mM)					
	0	1	2	4	6	8
	Chemical shift (ppm)					
H-C_{18}	0.9808	0.9804	0.9799	0.9784	0.9773	0.9766
H-C_{19}	1.4338	1.4334	1.4328	1.4315	1.4307	1.4295
H-C_4	6.0220	6.0217	6.0213	6.0204	6.0196	6.0179
H-C_2	6.2833	6.2851	6.2846	6.2833	6.2824	6.2813
H-C_1	7.2304	7.2271	7.2260	7.2258	7.2249	7.2238

Table 4.16: Results of the chemical shift of budesonide and DIMEB added at 0, 1, 2, 4, 6, and 8 mM in $CDCl_3$ using ^1H NMR.

Proton position	DIMEB concentration (mM)					
	0	1	2	4	6	8
	Chemical shift (ppm)					
H-C_{18}	0.9808	0.9804	0.9799	0.9787	0.9770	0.975
H-C_{19}	1.4338	1.4334	1.4328	1.4316	1.4305	1.4285
H-C_4	6.0220	6.0217	6.0214	6.0203	6.0186	6.0167
H-C_2	6.2833	6.2847	6.2840	6.2828	6.2811	6.2796
H-C_1	7.2304	7.2267	7.2265	7.2265	7.2248	7.2249

The K values were determined from the reciprocal plots between BUD and TRIMEB/DIMEB as shown in Figures 4.7 and 4.8 respectively based on the chemical shift differences of protons (H-C_{19} and H-C_4). The values were found to be 64 and 73 M^{-1} with TRIMEB and DIMEB respectively (Table 4.17).

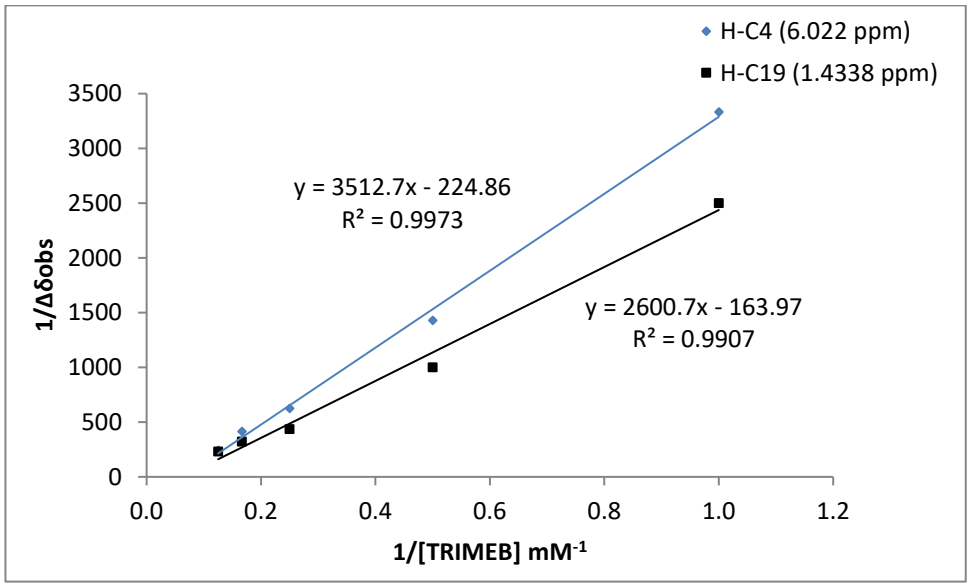

Figure 4.7: Reciprocal plot for the determination of association constant between budesonide and TRIMEB in $CDCl_3$ by ^1H NMR based on the chemical shift of H-C_4 and H-C_{19} at 6.022 and 1.4338 ppm respectively.

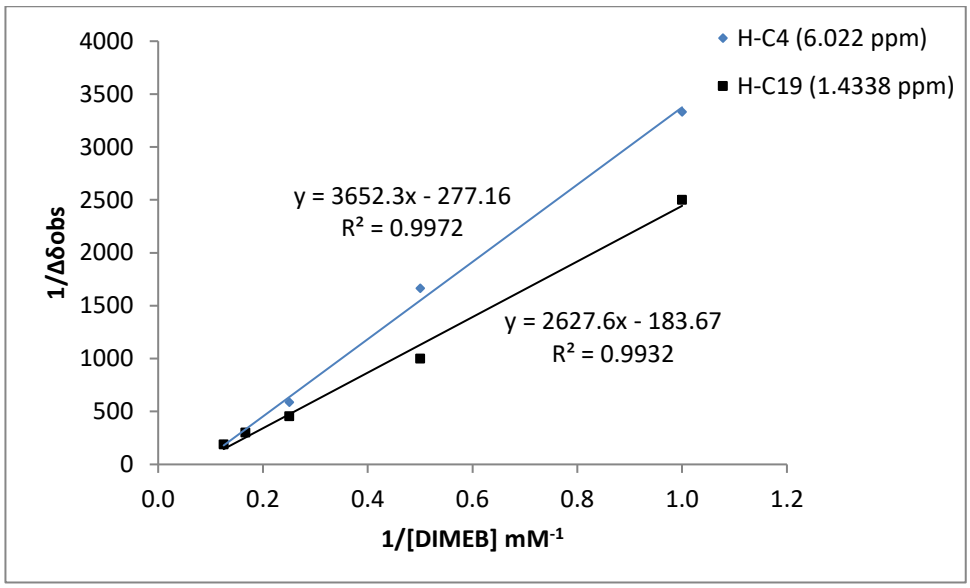

Figure 4.8: Reciprocal plot for the determination of association constant between budesonide and DIMEB in $CDCl_3$ by ^1H NMR based on the chemical shift of H-C_4 and H-C_{19} at 6.022 and 1.4338 ppm respectively.

Table 4.17: The calculated K for the complex formed between budesonide and (TRIMEB, DIMEB) in $CDCl_3$

Host	Stability constant, K (M^{-1})	
	H-C_{19}	H-C_4
TRIMEB	63	64
DIMEB	70	75

4.2.3 Complexation of BUD and DIMEB/TRIMEB in MeOD

The complexation between BUD and TRIMEB/DIMEB was also investigated in MeOD and the results showed fewer chemical shifts differences for BUD (Figure 4.6) with TRIMEB (Table 4.18) compared to that with DIMEB (Table 4.19).

Table 4.18: results of the chemical shift of budesonide and TRIMEB added at 0, 1, 2, 4, 6, and 8 mM in MeOD using ^1H NMR.

Proton position	TRIMEB concentration (mM)					
	0	1	2	4	6	8
	Chemical shift (ppm)					
H-C_{18}	0.9493	0.9499	0.9508	0.9536	0.9558	0.9564
H-C_{19}	1.4600	1.4621	1.4637	1.4670	1.4687	1.4706
H-C_4	5.9860	5.9885	5.9908	5.9940	5.9963	5.9988
H-C_2	6.2408	6.2410	6.2416	6.2454	6.2471	6.2496
H-C_1	7.4204	7.4206	7.4218	7.4238	7.4255	7.4263

Table 4.19: results of the chemical shift of budesonide and DIMEB added at 0, 1, 2, 4, 6, and 8 Mm in MeOD using ^{1}H NMR.

Proton position	DIMEB concentration (mM)					
	0	1	2	4	6	8
	Chemical shift (ppm)					
H-C_{18}	0.9493	0.9523	0.9550	0.9573	0.9615	0.9643
H-C_{19}	1.4600	1.4645	1.4689	1.4733	1.4775	1.4802
H-C_4	5.9860	5.9899	5.9925	5.9969	6.0020	6.0067
H-C_2	6.2408	6.2415	6.2414	6.2420	6.2439	6.2455
H-C_1	7.4204	7.4223	7.4244	7.4256	7.4281	7.4302

The K values were determined from the reciprocal plots between BUD and TRIMEB/DIMEB as shown in Figures 4.9 and 4.10 respectively based on the chemical shift differences at H-C_{19} and H-C_4 protons which were found to be 91 and 116 M^{-1} with TRIMEB and DIMEB respectively (Table 4.20).

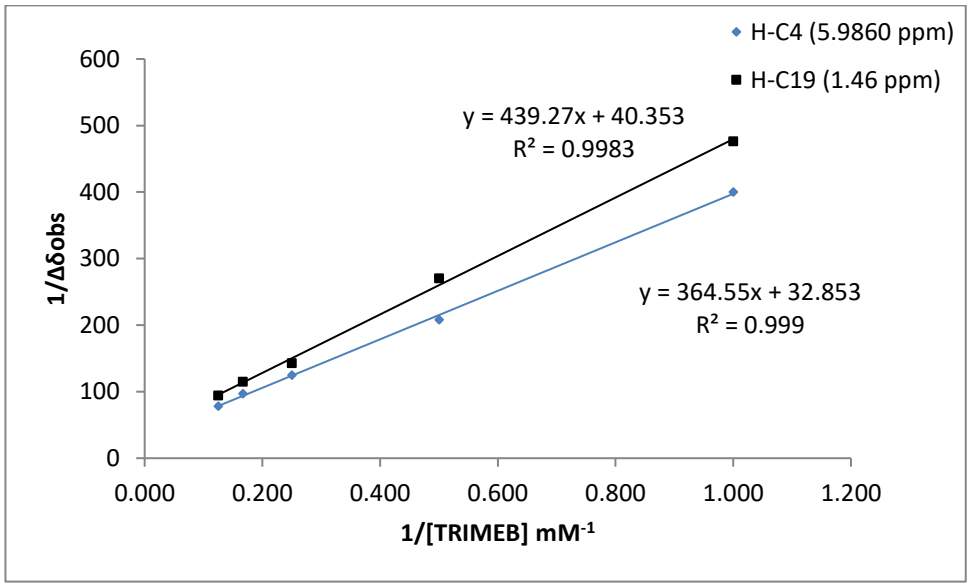

Figure 4.9: Reciprocal plot for the determination of association constant between budesonide and TRIMEB in MeOD by NMR depending on the chemical shift of H-C_4 and H-C_{19} at 5.9860 and 1.4600 ppm respectively.

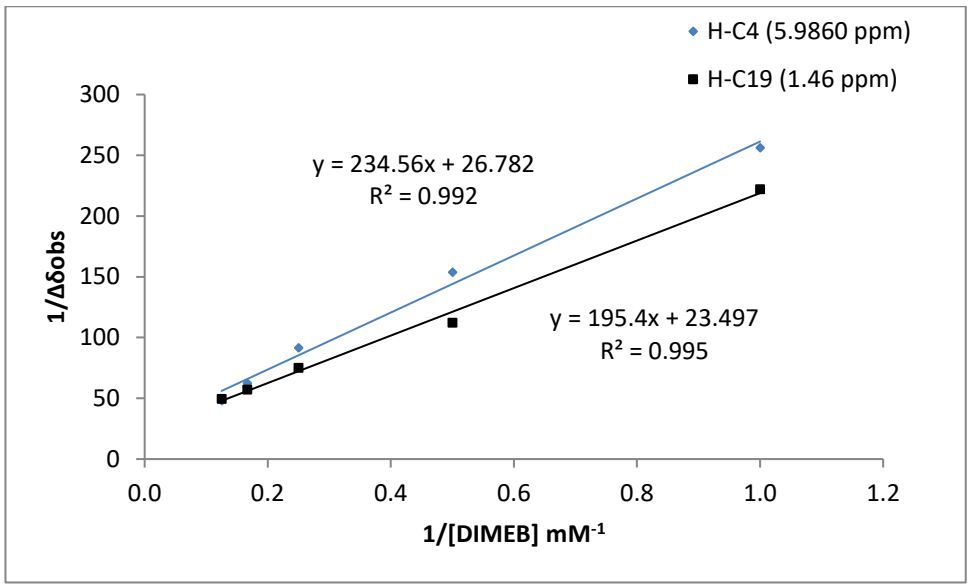

Figure 4.10: Reciprocal plot for the determination of association constant between budesonide and DIMEB in MeOD by NMR depending on the chemical shift of H-C_4 and H-C_{19} at 5.9860 and 1.4600 ppm respectively.

Table 4.20: The calculated K for the complex formed between budesonide and (TRIMEB, DIMEB) in MeOD

Host	Stability constant, K (M^{-1})	
	H-C_{19}	H-C_4
TRIMEB	92	90
DIMEB	118	114

4.2.4 Complexation of BUD and *β*CD/DIMEB/TRIMEB in D_2O

The study of the complexation between BUD and the three types of CD; *β*CD, TRIMEB and DIMEB was investigated in D_2O. First, BUD was prepared at a concentration near the previously determined solubility in D_2O (23.5 µg/mL) [52]. The solution was prepared at 21.5 µg/mL, which is equivalent to 0.05 mM. The solution was analysed by 600 MHz NMR and the spectrum showed that BUD signals were masked by a large signal of D_2O (Figure 4.11, a) which was *ca.* three orders of magnitude larger than the BUD signals. This difference in resonance intensity hindered the detection of BUD signals. During acquisition of the Free Induction Decay (FID) signal, the analogue-to-digital converter (ADC) limits the dynamic range of both the spectral width and the amplitude of the measured resonances. This process is responsible for translating the electrical signals of NMR into a dual number which is proportional to the signal magnitude in terms of bits. The ratio between the largest and smallest bits is defined as the dynamic range of ADC i.e. it is the ability for the NMR to detect small signals in the presence of largest ones.[176,177] In the case of detecting BUD in D_2O, the receiver gain is restricted by the D_2O signal because the ADC limits exceed by D_2O signal as the receiver gain increases. Most instruments use 16-bit ADC which gives a dynamic range of 65536 to 1 and in this case if it is assumed that the D_2O signal fills the ADC, then the smallest signal that can be detected takes a value of 1. Therefore, any signal less than 1 is not detected. Multiple methods are used in order to decrease the D_2O signal intensity and consequently the dynamic range of NMR signals will be within the dynamic range of ADC and receiver. One such method is presaturation of the solvent resonance, which serves to decrease its magnitude before the NMR signals reach the receiver. This is carried out by giving irradiation with low power at the solvent frequency for the purpose of saturating the solvent protons. Then, a pulse with high power is applied for the excitation of the sample nuclei to get the FID. At the time of applying the high power pulse, there is no difference in the population of the solvent protons (i.e. no magnetisation), hence no FID signal is produced.[177] In this study, the suppression method was applied by presaturating the D_2O signal at 4.67 ppm, using a power of 40 dB with scan numbers of 128, 256 and 2048 scans. It has been shown that suppression of the D_2O signal with 2048 scans produced a spectrum with BUD peaks of acceptable S:N (Figure 4.11, b).

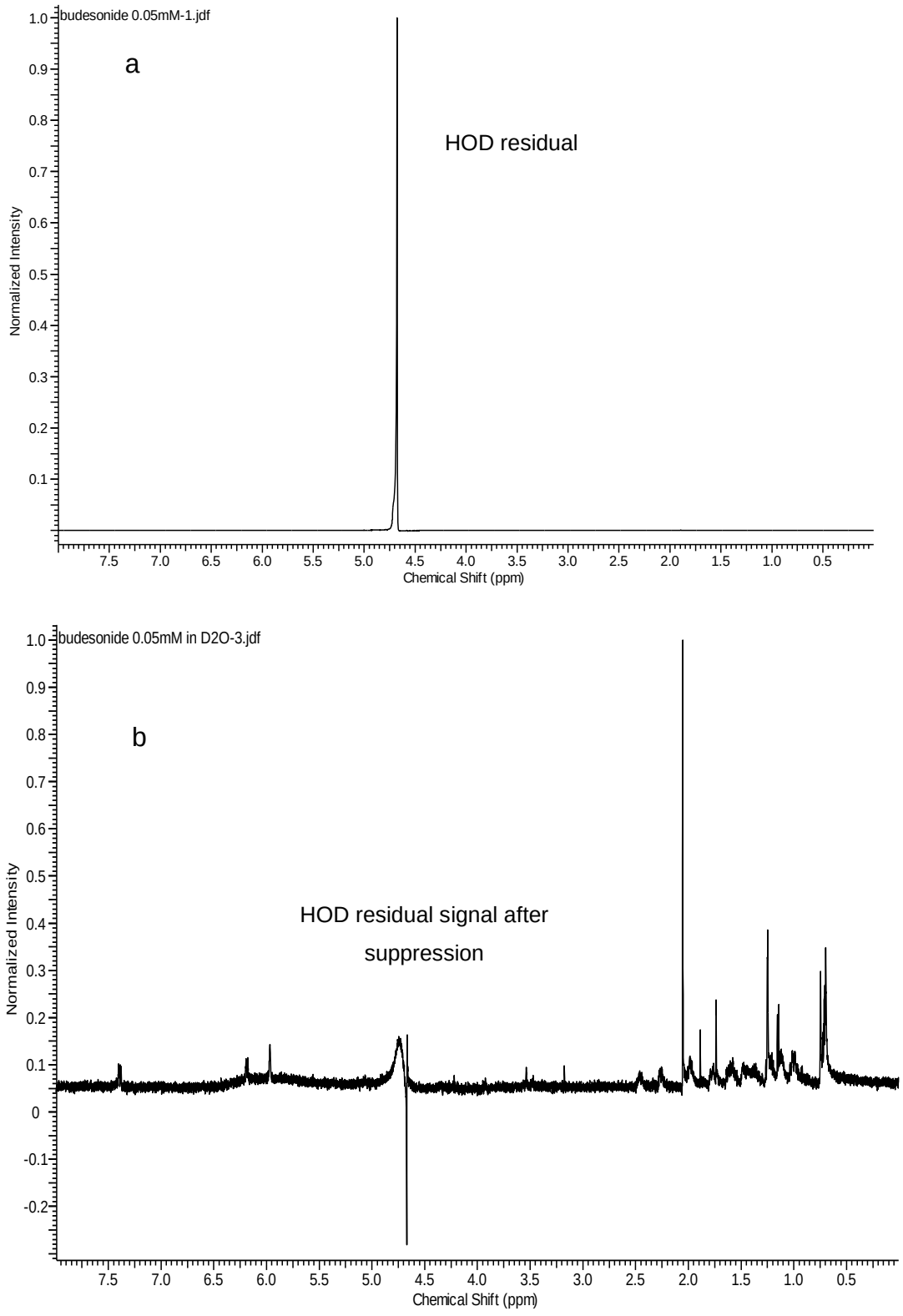

Figure 4.11: ^{1}H NMR spectra of budesonide in D_2O (a) without and (b) with solvent suppression at 4.67 ppm.

Increasing the acquisition times is a process in the NMR spectrometer which can be used to increase the signal to noise ratio by repeating acquisition and collecting the recorded FID. The signal intensity adds coherently as the number of scans increase. However, the noise is likely to cancel as it adds according to

the square root of the scan number ($\sqrt{SN}$). Thus, the signal to noise ratio (S/N) is proportional to the scan number divided by the square root as follows:

$$\frac{S}{N} \propto \frac{SN}{\sqrt{SN}} = \sqrt{SN} \qquad \textbf{Equation 4.1}$$

The effect of the acquisition times on budesonide system (D_2O) was investigated by increasing the scan number and calculating the S/N of the peak H-C_{18} (Figure 4.12) and H-C_4 (Figure 4.13) at 0.75 and 5.97 ppm respectively. As anticipated, increasing the scan number led to the increase in the S/N values observed following the $\sqrt{SN}$ relationship (Equation 4.1).

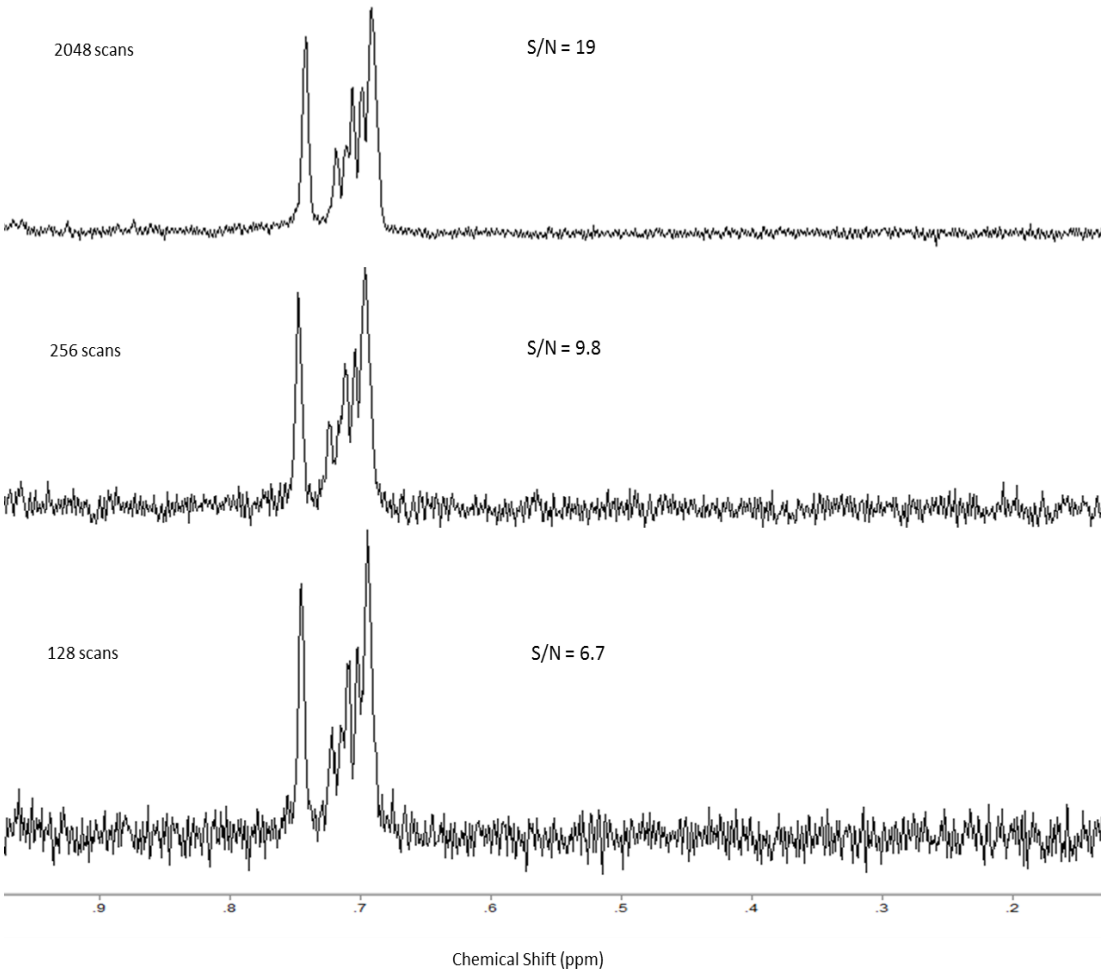

Figure 4.12: Calculation of the S/N of budesonide spectra in D_2O for the H-C_{18} peak at 0.75 ppm collected with different scan number at 128, 256 and 2048 scan.

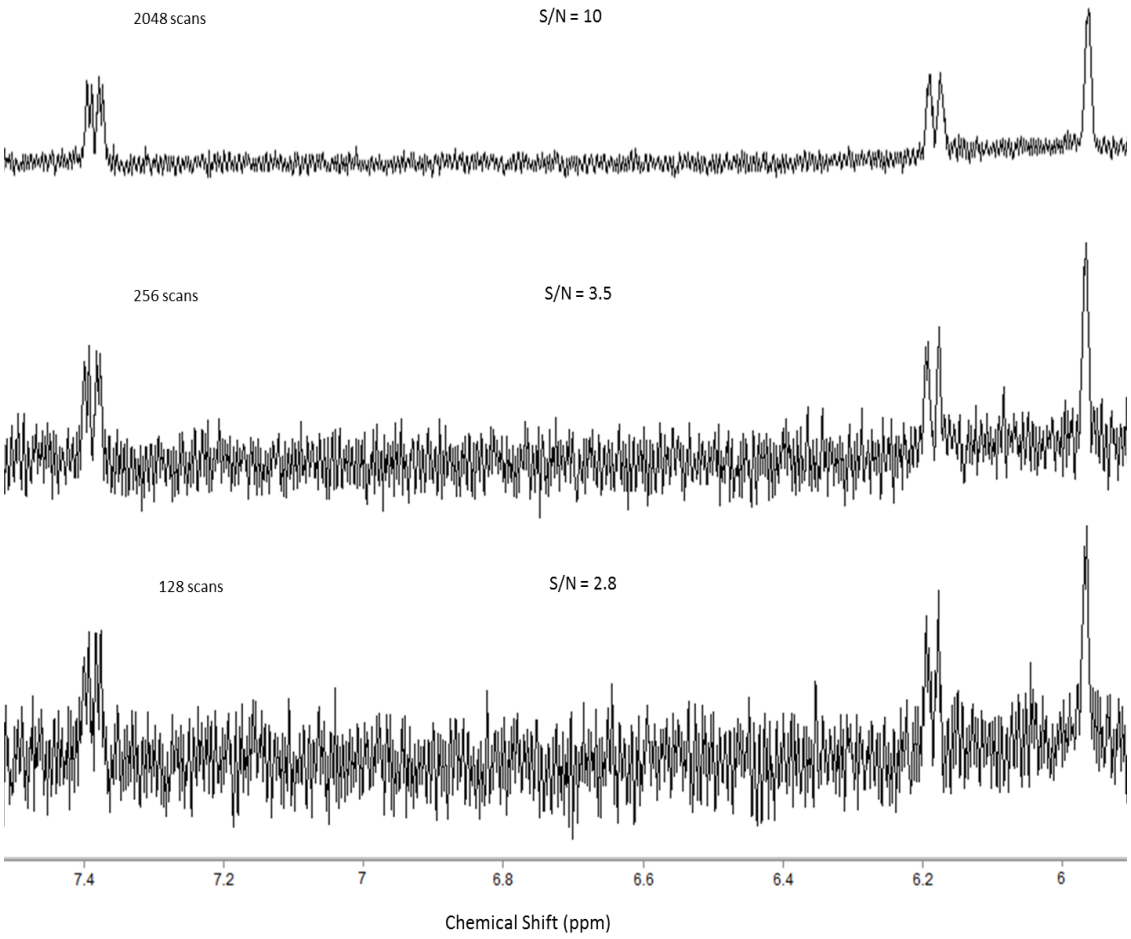

Figure 4.13: Calculation of the S/N of budesonide spectra in D_2O for the H-C_4 peak at 5.97 ppm collected with different scan number at 128, 256 and 2048 scan.

It is important to reference the chemical shift of all the peaks in the NMR spectrum by relating them to an internal reference (tetramethylsilane, TMS (0 ppm) or residual solvent resonance). In this case, the HOD signal (residual solvent) at 4.67 ppm was altered too dramatically by the applied suppression and therefore it cannot be used for this purpose. Alternatively, the addition of the internal standard can be used for this referencing purpose, but addition to the analytical solution needed to be avoided so as not to change the solvent properties of the complexation medium. It should therefore be physically separated from the other components. A co-axial NMR tube set up (Figure 4.14) is commonly used for this purpose, where a small NMR tube with the capillary end (co-axial insert) is inserted in the standard NMR tube. The sample solution is added to the standard tube while the internal standard is added to the co-axial tube so that it would be physically separated from the sample solution by a

glass capillary. The advantage of this system is allowing the addition of a reference NMR material in a sensible way for a calibration purpose.

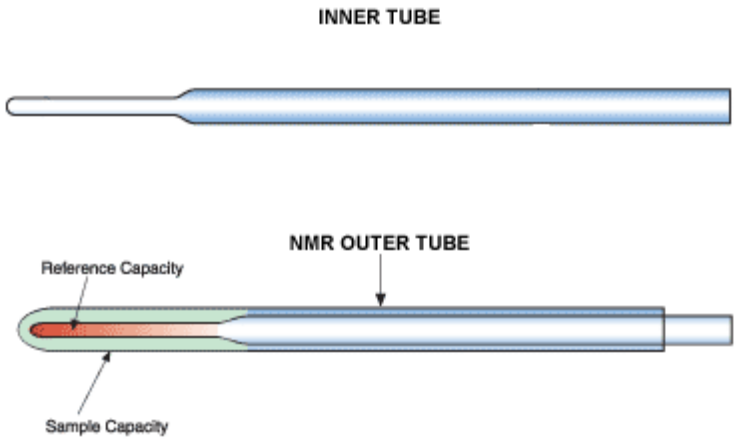

Figure 4.14: A co-axial NMR tube set up consists of inner tube (upper) inserted in the standard NMR tube (lower) with the addition of sample solution and the reference material added to the inner tube.[178]

The internal standard used in this work was a mixture of ($CHCl_3$ / CD_3CN) based on the previous study conducted by Telford[179] where $CHCl_3$ was chosen because it has singlet sharp peak and its chemical shift position is away from the other budesonide and cyclodextrin signals so that it can be used as a reference for chemical shift referencing and quantitative work as necessary. The experiment was set up by preparing solutions of budesonide and *β*CD in D_2O and adding to the standard NMR tube of the co-axial tube system as mentioned above with the addition of ($CHCl_3$ / CD_3CN) in the concentration of 10 mg/mL in the inner tube. It was found that a large peak at 8.24 ppm (Figure 4.15, a) was different to the normal $CHCl_3$ resonance which was usually located at 7.24 ppm. In order to investigate the relation of this peak to $CHCl_3$, the concentration was reduced to 100 µg/mL. It was found that the peak was reduced in intensity proportionally to the decrease in the concentration (Figure 4.15, b) which suggested the relation of this peak to the $CHCl_3$.

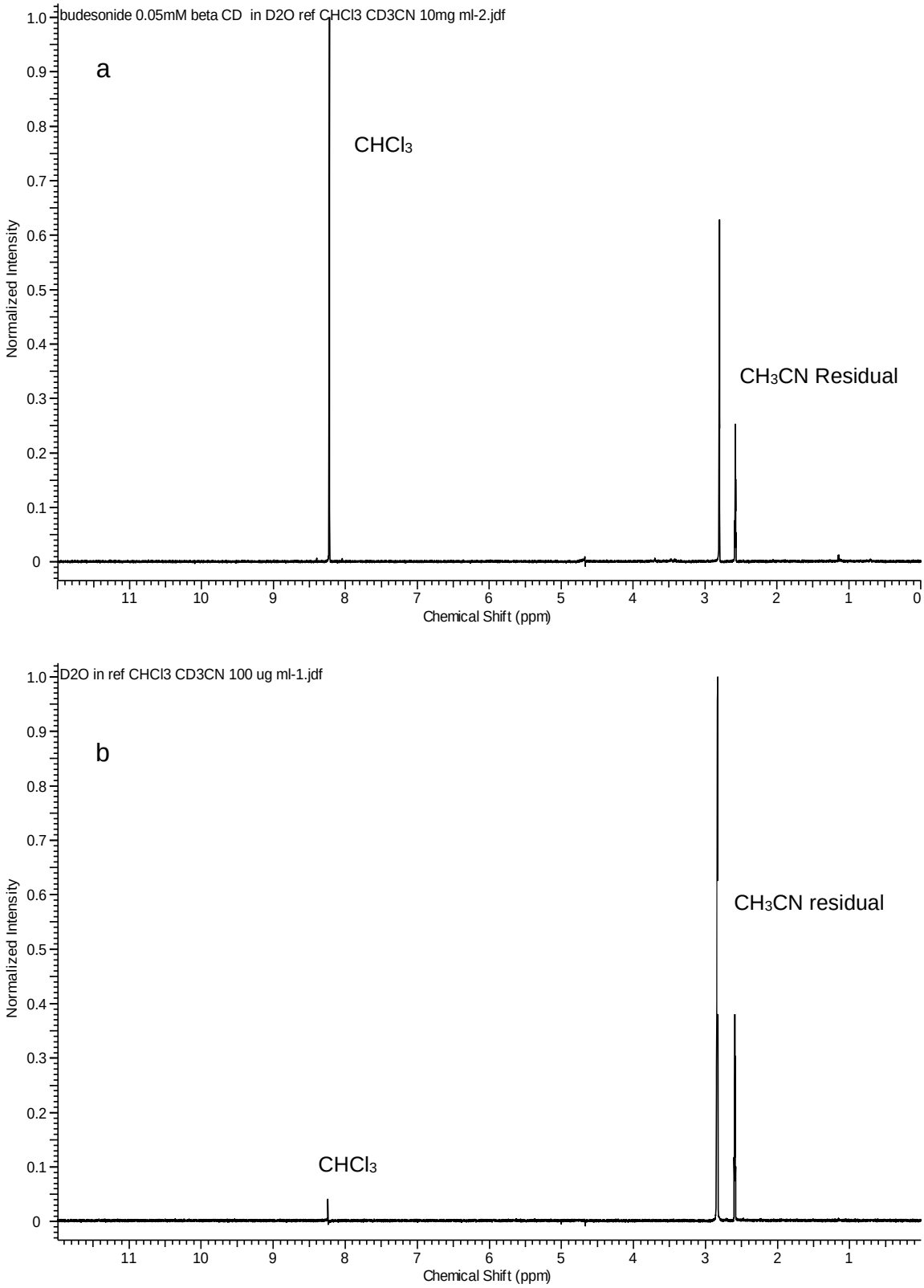

Figure 4.15: ^{1}H NMR spectra of budesonide and *β*CD in D_2O using $CHCl_3/CD_3CN$ at (a) 10 mg/mL and (b) 100 µg/mL as reference showing that the peak at 8.24 ppm decreased in intensity when the concentration of $CHCl_3$ decreased.

Then, the sample solution of budesonide and *β*CD in D_2O (in NMR tube) was run without a co-axial insert tube and the result showed the absence of the peak

at 8.24 ppm which confirmed the relation of this peak to the $CHCl_3$ and not to the sample components (Figure 4.16).

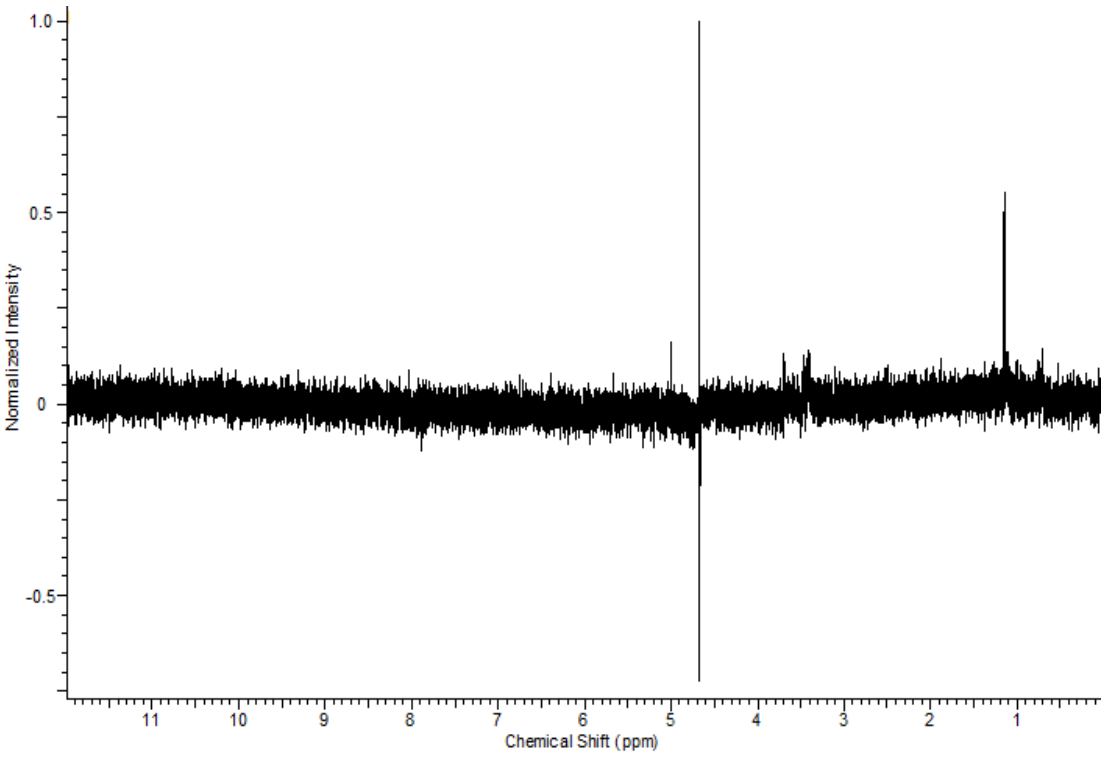

Figure 4.16: ^{1}H NMR spectrum of budesonide in D_2O run without co-axial insert with solvent suppression at 4.67 ppm showing that the absence of the peak at 8.24 ppm.

Finally, the spectrum of D_2O solvent (positioned in NMR tube of the co-axial system) with the co-axial inner tube containing only $CHCl_3$ was compared to the spectrum of D_2O with ($CHCl_3$ / CD_3CN) in the co-axial tube. It has been shown that one peak appeared at 7.07 ppm in the first spectrum (Figure 4.17, a) and was shifted to 8.24 ppm in the second spectrum with the presence of CD_3CN (Figure 4.17, b). It has been reported that the residual peaks of both solvents in the co-solvent system have different chemical shifts compared to either of these two alone.[177] Accordingly, the peak at 7.07 ppm for the $CHCl_3$ was shifted to 8.24 ppm because of the presence CD_3CN in the system. This $CHCl_3$ resonance at 8.24 ppm is used as a reference in the further experiments for the assignment of both host and the guest peaks in the same solvent system.

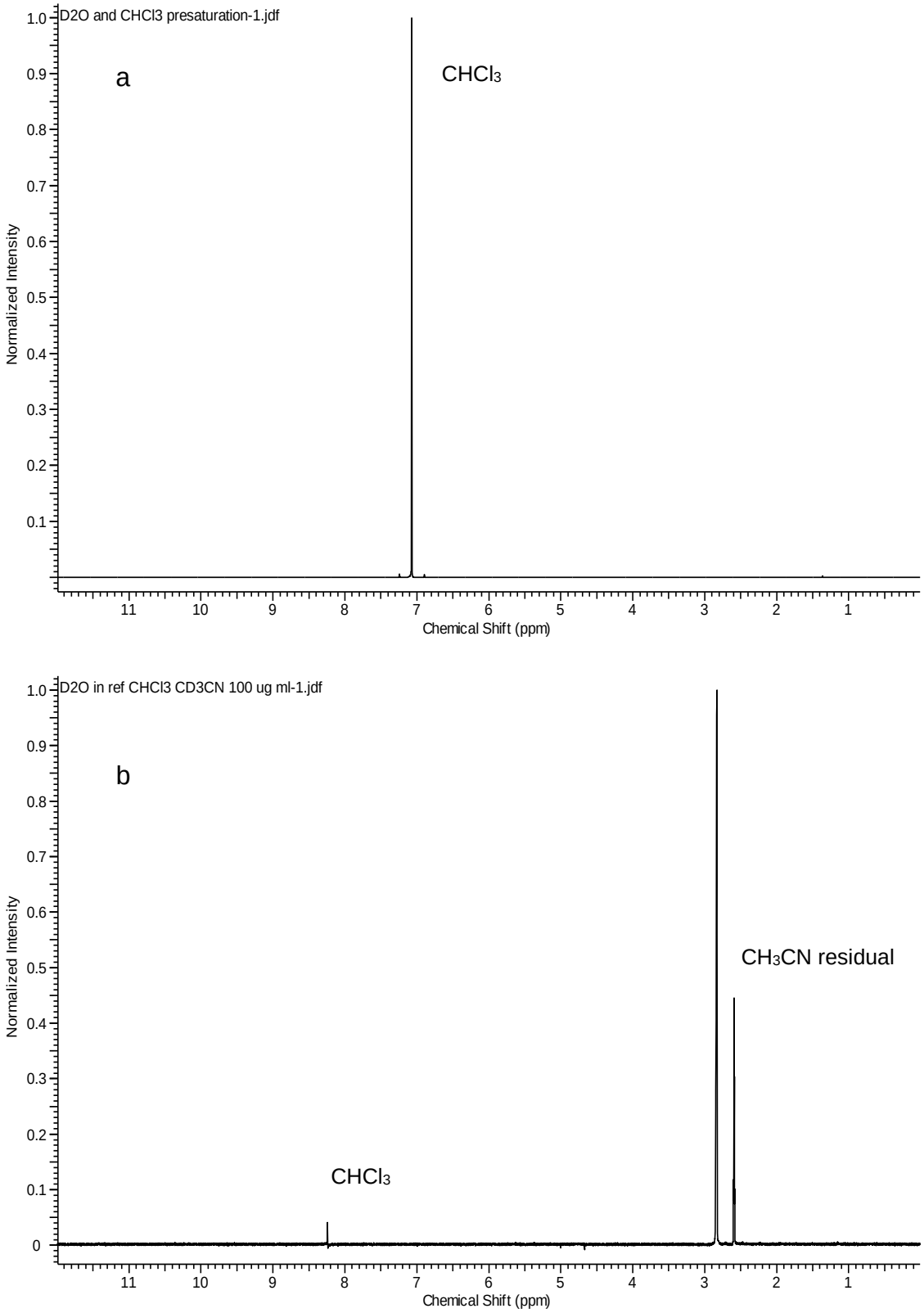

Figure 4.17: ^{1}H NMR spectra of D_2O with the addition of only $CHCl_3$ (a) and $CHCl_3/CD_3CN$ (b) in the co-axial insert with solvent suppression at 4.67 ppm showing that the peak of $CHCl_3$ is shifted from 7.07 to 8.24 ppm.

It has been found another intense peak was appeared in the spectrum at 2.80 ppm which was related to the CH_3CN residual. Suppression of this peak alongside with D_2O peak might enhance the BUD spectrum. Therefore, the

method was developed using two suppressions at 4.67 ppm (D_2O) and at 2.80 ppm (CH_3CN residual) with different attenuations at (30,40), (40,40), (50,40), (30,50), (40,50), (50,50), (60,50), (44,50),(46,50), (45,50) dB. The suppression with 45 dB at 4.67 ppm and 50 dB at 2.8 ppm was the best and chosen for the further experiments. To enhance the sensitivity, different parameters are used for this purpose. It is clearly that the sensitivity can be improved by increasing the magnetic field (B_0) which increases the difference in the population between α and β states and therefore, the sample magnetisation at the equilibrium increases with an increase in the FID signal. The largest NMR magnetic field available at the University of Bradford is 600 MHz and it is used in this work for a better sensitivity. The method has been further developed by using different concentrations of BUD (0.01, 0.02, 0.03 and 0.04 mM). The S/N ratio was calculated for H-C_1, H-C_2 and H-C_4 resonances and the spectrum with 0.04 mM produced a better S/N ratio with a reasonable intensity of the BUD signals together with the decrease in the noise intensity (Figure 4.18).

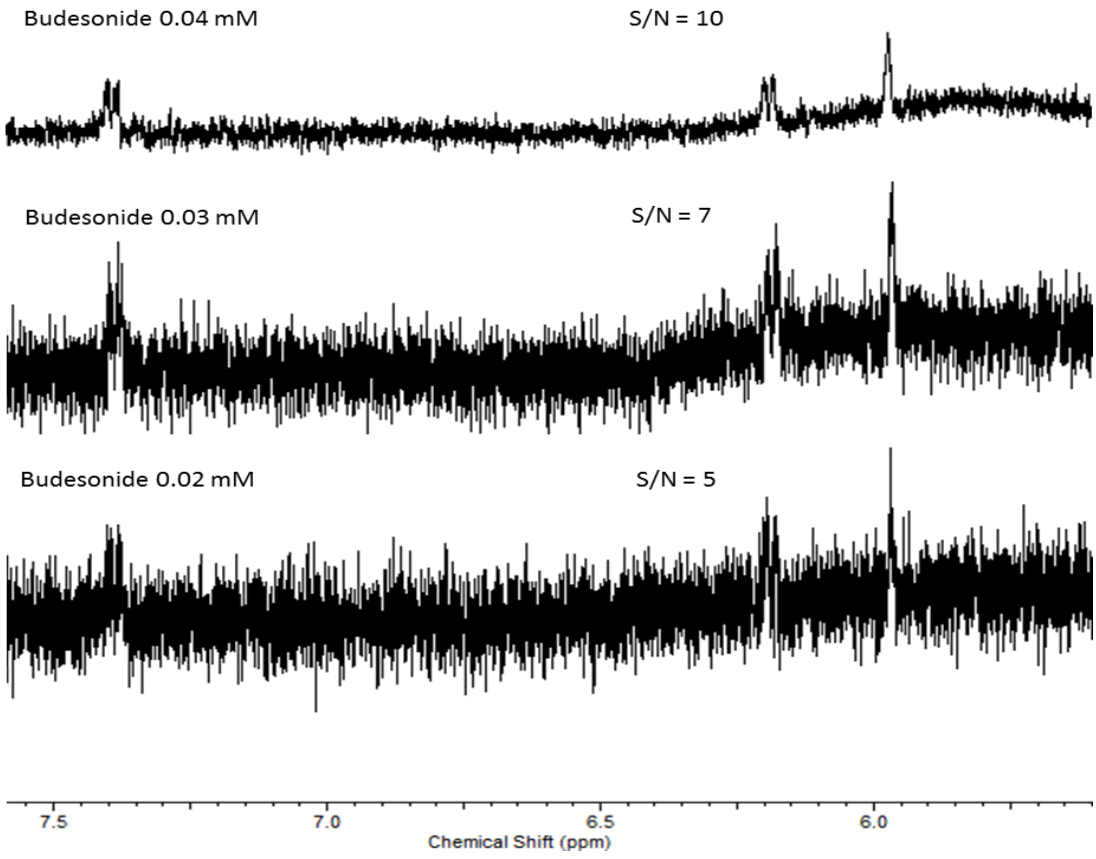

Figure 4.18: Budesonide spectra in D_2O collected at 2048 scan showing the calculation of the S/N using different concentrations at 0.02, 0.03 and 0.04 mM.

The study of the inclusion formation between BUD and *β*CD was performed with the solvent suppressions at 4.67 ppm (45 dB) and 2.80 ppm (50 dB) with the internal standard of $CHCl_3$ in CD_3CN (100 µg/mL) and long acquisition times (2048 scans).

The assignment of BUD in D_2O was made based on its assignment in $CDCl_3$ (Figure 4.19), where small shift occurs for all the peaks in two different solvents ($CDCl_3$ and D_2O). BUD was analysed in $CDCl_3$ by NMR and its assignment are shown in Table 4.21.[180,181] Figures 4.20 and 4.21 showed spectral expansion of the budesonide spectrum in the high and low field regions respectively.

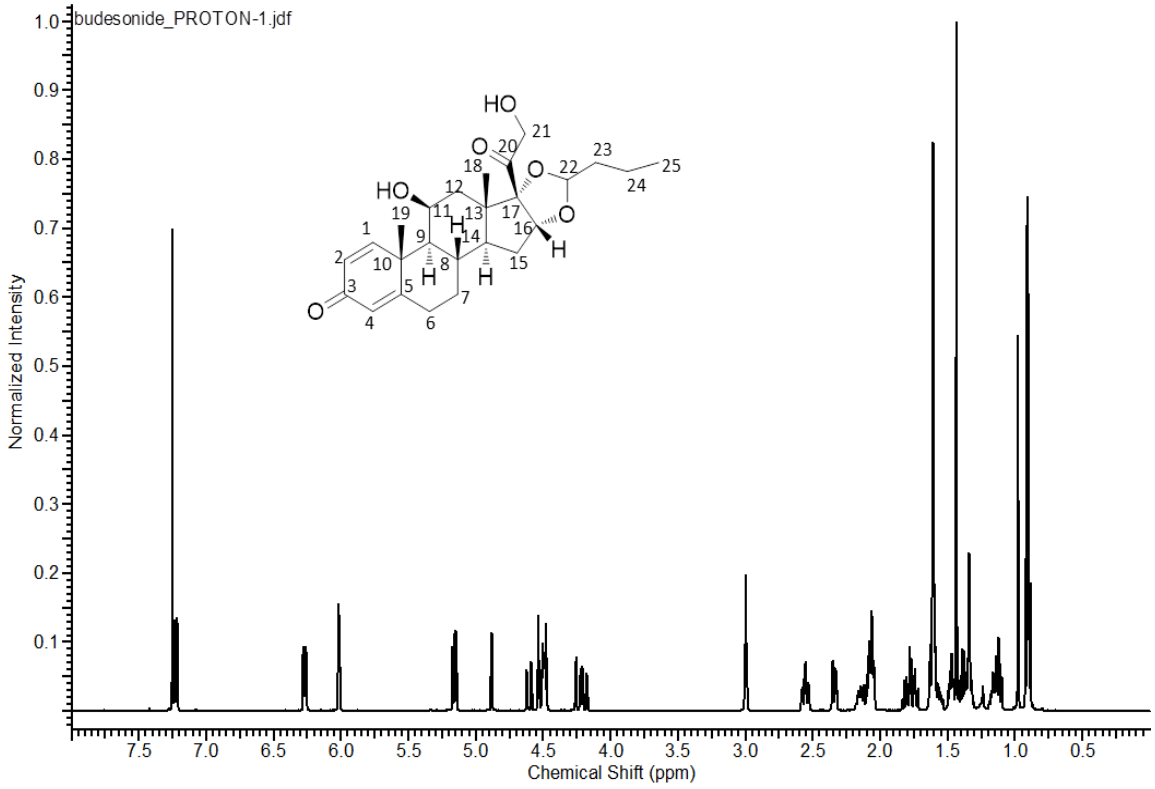

Figure 4.19: ^{1}H NMR spectrum of budesonide in $CDCl_3$

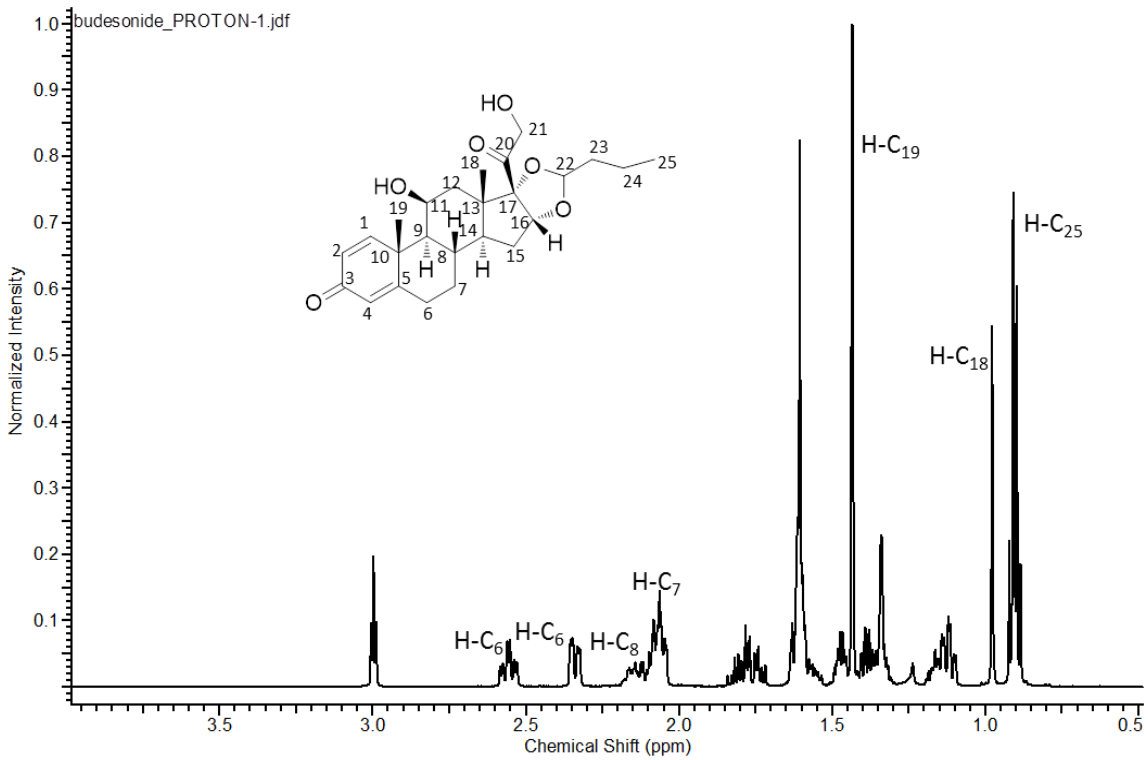

Figure 4.20: ^{1}H NMR spectrum of budesonide in $CDCl_3$ in high field region (0.5-4 ppm)

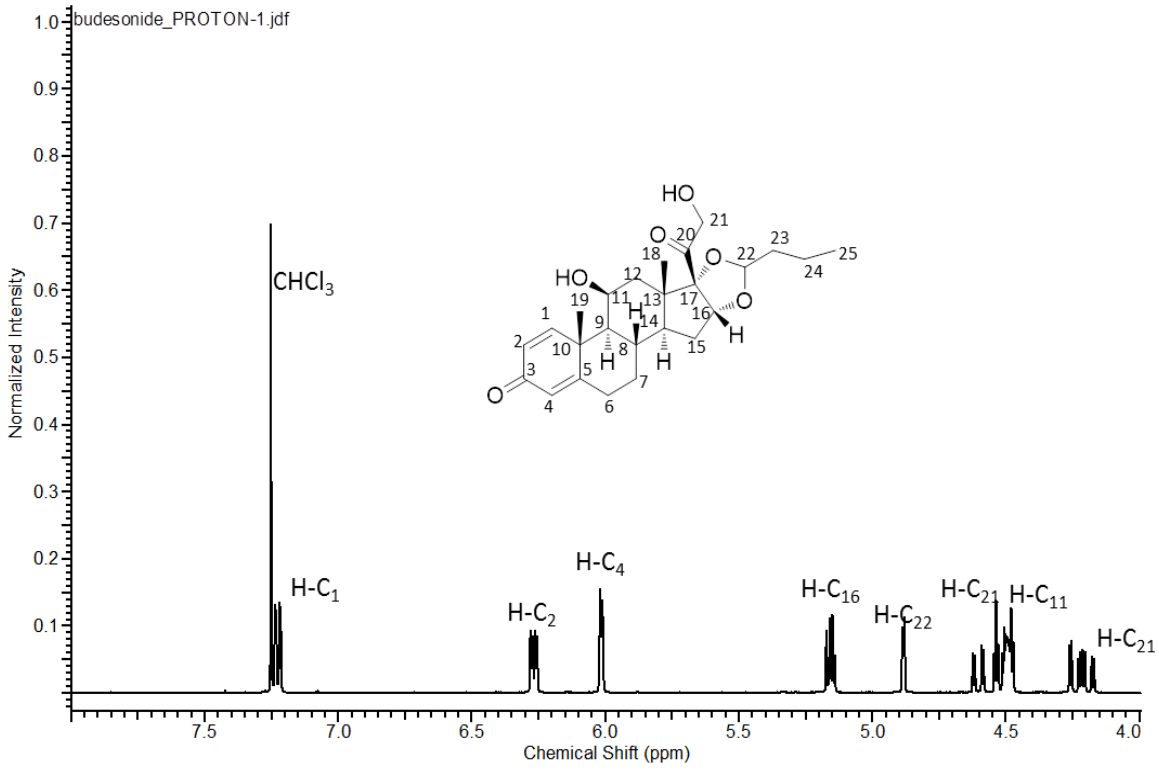

Figure 4.21: ^{1}H NMR spectrum of budesonide in $CDCl_3$ in low field region (4-8 ppm)

Table 4.21: ^{1}H NMR spectral assignment of the budesonide in $CDCl_3$.[180,181]

Proton position	Chemical shift (ppm)	Spin-Spin Coupling Data
C1	7.23	(dd, J=10.3, 2.7 Hz)
C2	6.27	(ddd, J=10, 4.8, 1.7 Hz)
C4	6.01	(m)
C6	2.34	(m)
C7	1.15	(m)
C8	2.16	(m)
C9	1.12	(dd, J=3.0, 4.5 Hz)
C11	4.49	(m)
C16	4.88	(*R*) (d, J=4.8 Hz)
	5.16	(*S*) (m)
C18	0.98	(s)
C19	1.44	(d, J=1.4 Hz)
C21	4.49	(*R*) (m),
	4.60	(*S*) (dd, J=19.9, 4.8 Hz),
	4.25	(*R*) (dd, J=10, 5.2 Hz)
	4.22	(*S*) (dd, J=10, 5.2 Hz)
C22	4.55	(*R*) (t, J=4.2 Hz)
	5.15	(*S*) (t, J=4.6 Hz)
C25	0.91	(t, J=7.3 Hz)

Budesonide spectrum is assigned relative to residual chloroform at 7.25 ppm. Multiplicity given with the abbreviations: s (singlet), d (doublet), t (triplet), dd (doublet of doublets), ddd (doublet of doublets of doublets), m (multiplet).(*R*) and (*S*) are epimers of budesonide

The peaks at 4-5 ppm in the NMR spectrum of BUD were affected by presaturation of D_2O at 4.67 ppm and hence, were difficult to assign. The other peaks were assigned as shown in Table 4.22 where a consistent upfield shift occurred for the peaks in D_2O when compared to those in $CDCl_3$ as shown in Figures 4.22 and 4.23.

Table 4.22: Chemical shift of budesonide in D_2O and compared to those in $CDCl_3$

Carbon number	Chemical shift (ppm)		Chemical shift difference
	$CDCl_3$	D_2O	
1	7.22	7.39	0.17
2	6.27	6.18	0.09
4	6.02	5.96	0.06
18	0.99	0.75	0.24
19	1.45	1.24	0.21
25	0.91	0.69	0.22

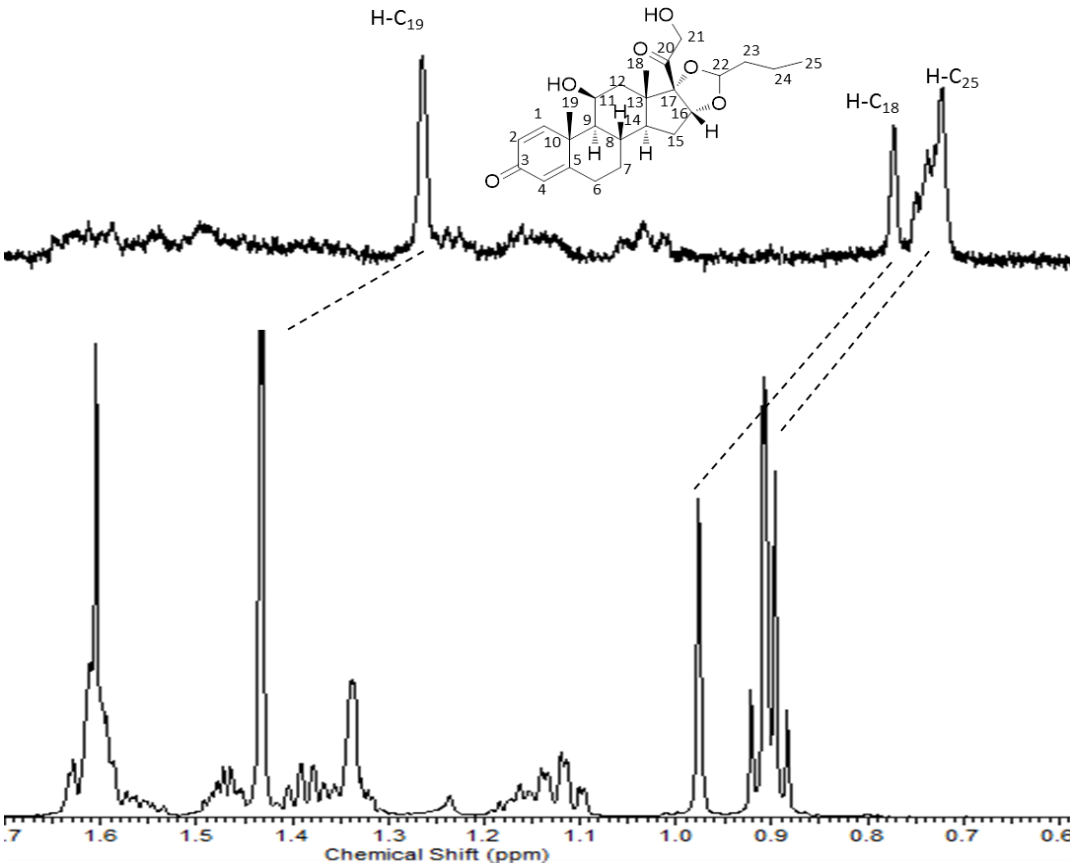

Figure 4.22: Budesonide chemical shift in $CDCl_3$ (lower) and D_2O (upper) in high field region (0.6-1.7 ppm) showing a little shift when using different solvents.

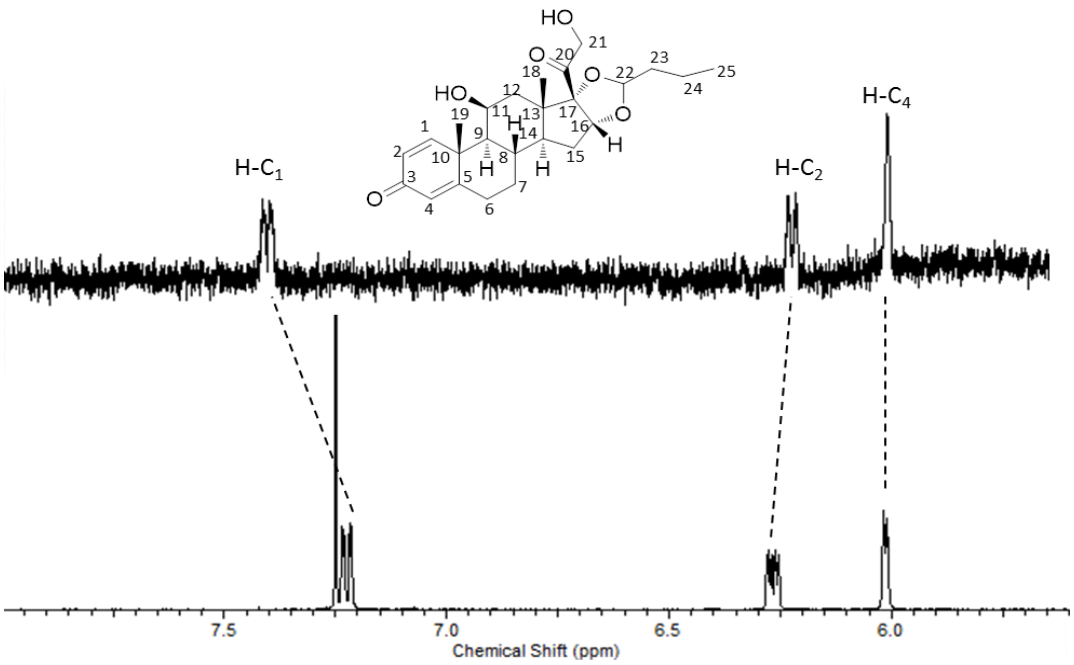

Figure 4.23: Budesonide chemical shift in $CDCl_3$ (lower) and D_2O (upper) in low field region (5.5-8 ppm) showing a little shift when using different solvents.

4.2.4.1 Budesonide and βCD

The complexation of BUD and *β*CD in D_2O was investigated by recording the chemical shift values of BUD peaks (referenced to $CHCl_3$ from the co-axial insert) for the all five different solutions prepared with increasing CD concentration (Section 2.2.4.3) relative to BUD peaks from a pure BUD solution without *β*CD addition.

It has been noticed two peaks were observed at approximately 0.72 and 0.77 ppm at 0.2 mM *β*CD concentration. Both peaks were then slightly downfield shifted with the increasing *β*CD concentration which both could be assigned to the H-C_{18} peak of *R*- and *S*-enantiomers of BUD. However, no observable change was noted for H-C_{25} peak although its multiplicity changed as the *β*CD concentration was increased. The H-C_{19} proton of BUD at 1.25 ppm had remarkable downfield shift and was split into two distinctive peaks as the concentration of *β*CD was increased which both of them could be related to the both enantiomers of BUD. However, it was difficult to assign and match both shifted peaks of the H-C_{18} and H-C_{19} protons to the *R*- and *S*-enantiomers of BUD unless performing an additional experiment with the pure enantiomer and comparing to those of the racemic mixture. The spectra of the complexed BUD in the high field region are shown in Figure 4.24.

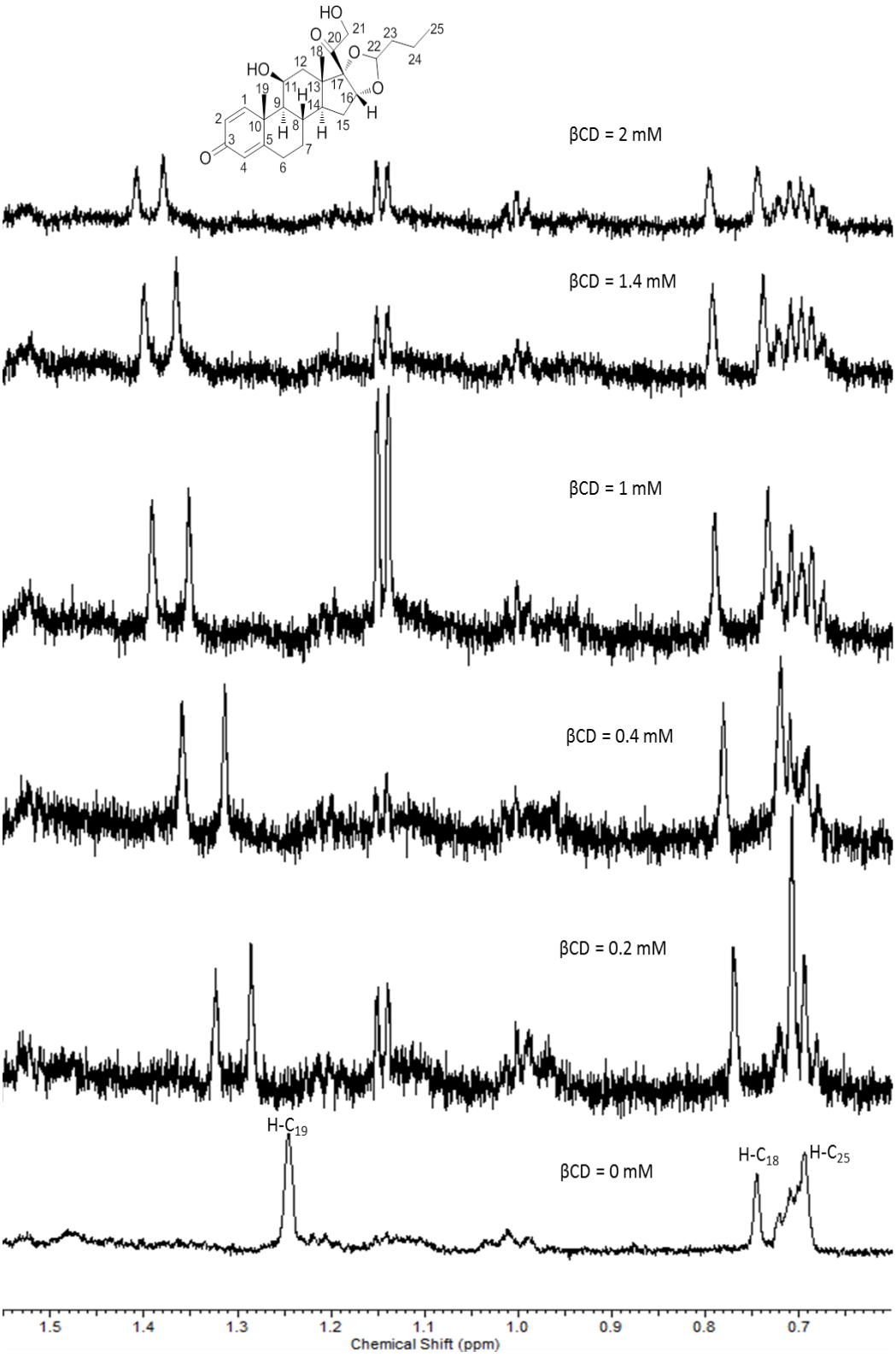

Figure 4.24: Budesonide (0.04 mM) chemical shift in high field region (0.6-1.6 ppm) with the addition of *β*CD at 0, 0.2, 0.4, 1, 1.4 and 2 mM in D_2O.

In the low field region, small downfield shift was observed with H-C_1 proton of the quinone ring, whereas upfield shift was noted for the other protons of the quinone ring (H-C_2 and H-C_4). The doublet H-C_2 peak was split into three peaks with increasing CD concentration. The H-C_4 singlet peak was split into two

distinctive peaks with increasing the *β*CD concentration, and both peaks could be assigned to the both *R*- and *S*-enantiomers of BUD (Figure 4.25).

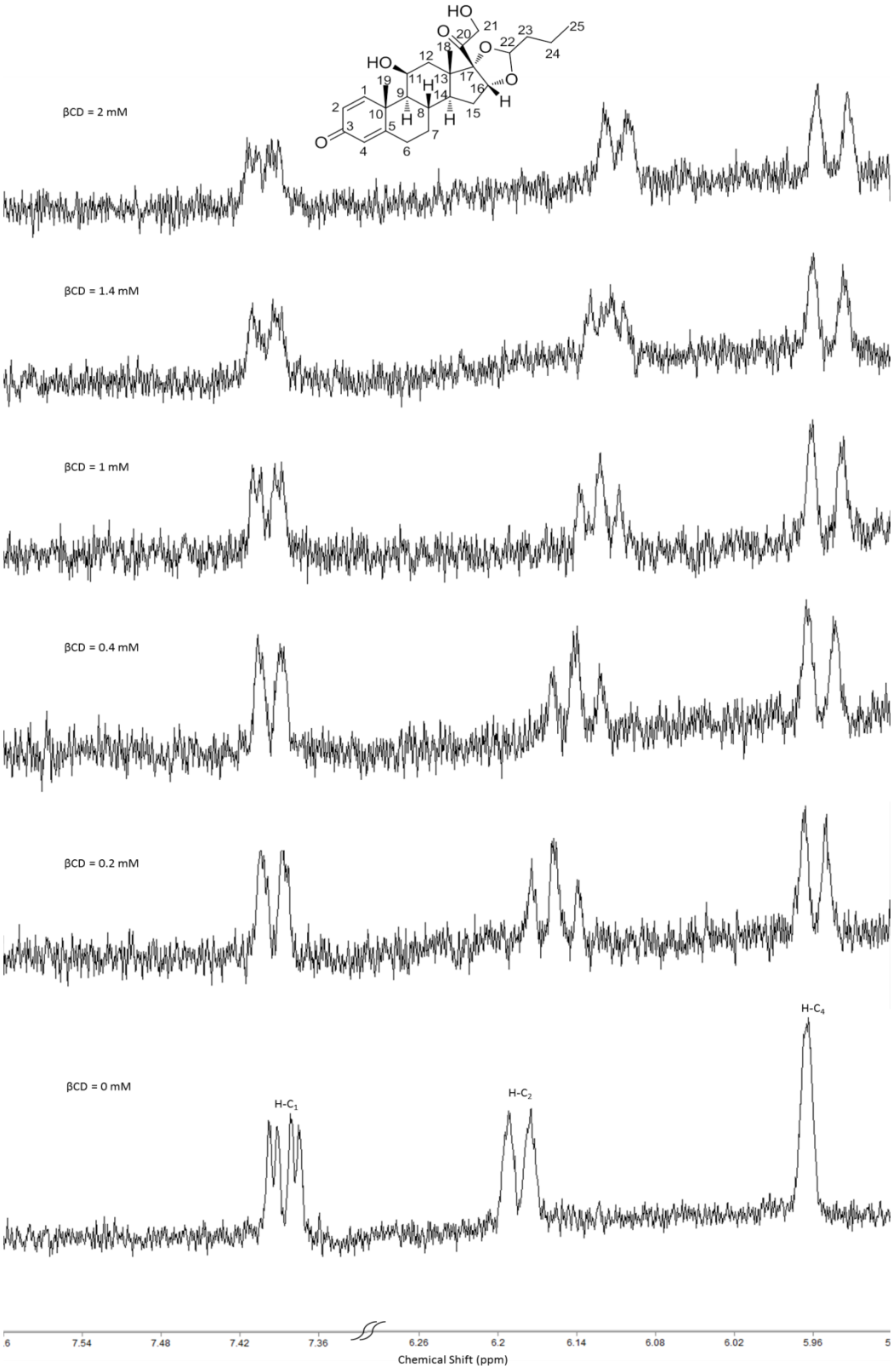

Figure 4.25: Budesonide (0.04 mM) chemical shift in low field region (5.9-7.6 ppm) with the addition of *β*CD at 0, 0.2, 0.4, 1, 1.4 and 2 mM in D_2O.

The chemical shift differences of H-C_{19} proton at 1.2570 ppm (Table 4.23) were used to determine the K as shown in Table 4.24, with the Hildebrand-Benesi plot being shown in Figure 4.26.

Table 4.23: Results of the chemical shift of budesonide and *β*CD added at 0, 0.2, 0.4, 1, 1.4 and 2 mM in D_2O using ^1H NMR.

Experiment number	Proton position (ppm)	*β*CD concentration (mM)					
		0	0.2	0.4	1	1.4	2
		Chemical shift (ppm)					
1	H-C_{19}	1.2570	1.2905	1.3150	1.3530	1.3660	1.3853
2			1.2903	1.3139	1.3542	1.3686	1.3793
3			1.2906	1.3170	1.3558	1.3678	1.3790
Mean			1.2905	1.3153	1.3543	1.3675	1.3812
SD			0.0002	0.0016	0.0014	0.0013	0.0036
% CV			0.0118	0.1195	0.1037	0.0974	0.2573

Table 4.24: Results of the complexation between budesonide and *β*CD added at 0.2, 0.4, 1, 1.4 and 2 mM in D_2O using ^1H NMR based on the chemical shift of H-C_{19} at 1.2570 ppm.

*β*CD (mM)	1/*β*CD (mM^{-1})	$1/\Delta\delta_{obs}$ (1.2570 ppm)			
		1	2	3	Mean
0.2	5	29.9	30	29.8	29.9
0.4	2.5	17.2	17.6	16.7	17.2
1	1	10.4	10.3	10.1	10.3
1.4	0.7	9.2	8.9	9	9.1
2	0.5	7.8	8.2	8.2	8.1

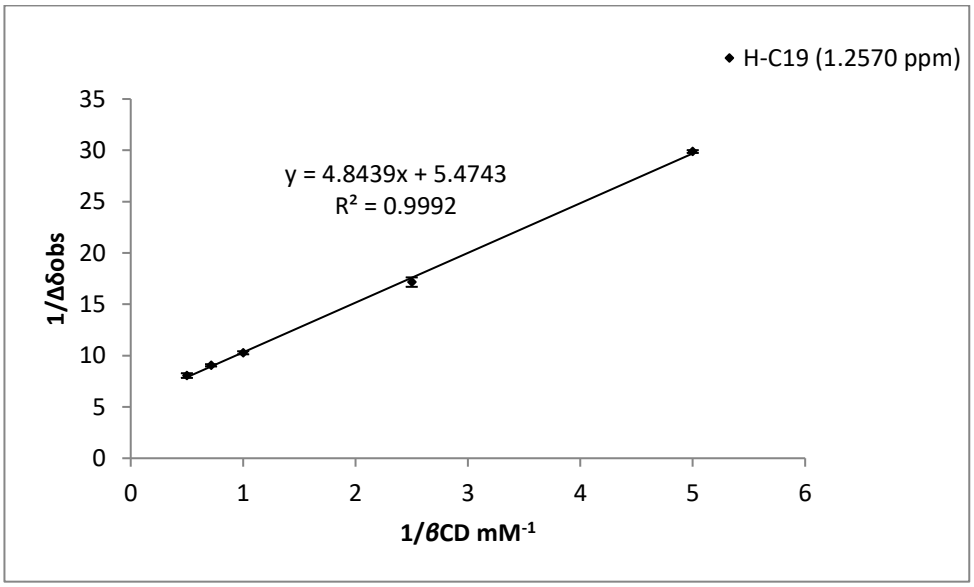

Figure 4.26: Reciprocal plot for the determination of the association constant between budesonide and *β*CD in D_2O by ^1H NMR based on the chemical shift of H-C_{19} at 1.2570 ppm (Mean ± SD, n=3).

The reciprocal plots of $1/\Delta\delta_{obs}$ versus 1/[βCD] showed a good linearity which indicated a stoichiometry of the complexation was 1:1. The mean K value was found to be 1129 M^{-1} according to the chemical shift changes of H-C_{19} proton (Table 4.25).

Table.4.25: Results of the stability constant between budesonide and βCD added at 0.2, 0.4, 1, 1.4 and 2 mM in D_2O using ^1H NMR.

Proton NO.	Chemical shift (ppm)	Stability constant, K (M^{-1})				SD	% CV
		1	2	3	Mean		
H-C_{19}	1.2570	1129	1127	1129	**1129**	2.5	0.2

The stoichiometry 1:1 of the complex was verified by continuous variation method (Section 2.2.3.2). The calculation was based on the chemical shift differences of the H-C_2 proton of BUD at (6.1931 and 6.1744 ppm). The chemical shift difference between free and complexed budesonide ($\Delta\delta_{obs}$) was calculated by taking the difference between chemical shift of free budesonide (in the absence of βCD, δ_{free}) and chemical shift of complexed budesonide (in the presence of βCD, $\delta_{complex}$). The stoichiometry was then determined as shown in Tables 4.26 and 4.27.

Table 4.26: Results of ^1H NMR analysis for the determination of stoichiometry between budesonide and βCD in D_2O based on the chemical shift of H-C_2 proton of budesonide at 6.1931 ppm.

[BUD] (mM)	r	$\delta_{complex}$ (ppm)	$\Delta\delta_{obs}$ (ppm)	$\Delta\delta$[BUD]	$\Delta\delta$[BUD]*10^4
0.05	1	6.1931	0	0	0
0.045	0.9	6.1906	0.0025	11.3×10^{-5}	1.13
0.04	0.8	6.1889	0.0042	16.8×10^{-5}	1.68
0.035	0.7	6.1874	0.0057	19.9×10^{-5}	1.99
0.03	0.6	6.1854	0.0077	23.1×10^{-5}	2.31
0.025	0.5	6.1834	0.0097	24.3×10^{-5}	2.43
0.02	0.4	6.1824	0.0107	21.4×10^{-5}	2.14
0.015	0.3	6.1809	0.0122	18.3×10^{-5}	1.83
0.01	0.2	6.1789	0.0142	14.2×10^{-5}	1.42
0	0	0	0	0	0

δ_{free} = 6.1931 ppm

Table 4.27: Results of ^{1}H NMR analysis for the determination of stoichiometry between budesonide and *β*CD in D_2O based on the chemical shift of H-C_2 proton of budesonide at 6.1744 ppm.

[BUD] (mM)	r	$\delta_{complex}$ (ppm)	$\Delta\delta_{obs}$ (ppm)	$\Delta\delta$[BUD]	$\Delta\delta$[BUD]*10^4
0.05	1	6.1744	0	0	0
0.045	0.9	6.1715	0.0029	13.1 x 10^{-5}	1.31
0.04	0.8	6.1695	0.0049	19.6 x 10^{-5}	1.96
0.035	0.7	6.1675	0.0069	24.2 x 10^{-5}	2.42
0.03	0.6	6.165	0.0094	28.2 x 10^{-5}	2.82
0.025	0.5	6.1625	0.0119	29.8 x 10^{-5}	2.98
0.02	0.4	6.1611	0.0133	26.6 x 10^{-5}	2.66
0.015	0.3	6.1596	0.0148	22.2 x 10^{-5}	2.22
0.01	0.2	6.1568	0.0176	17.6 x 10^{-5}	1.76
0	0	0	0	0	0

δ_{free} = 6.1744 ppm

The stoichiometry was determined by plotting r, which was the ratio of [BUD]/[BUD]+[*β*CD] versus Δδ[BUD] (Figure 4.27). The results showed the maximum value of r was 0.5 which demonstrated that the stoichiometry was 1:1 for the complex.

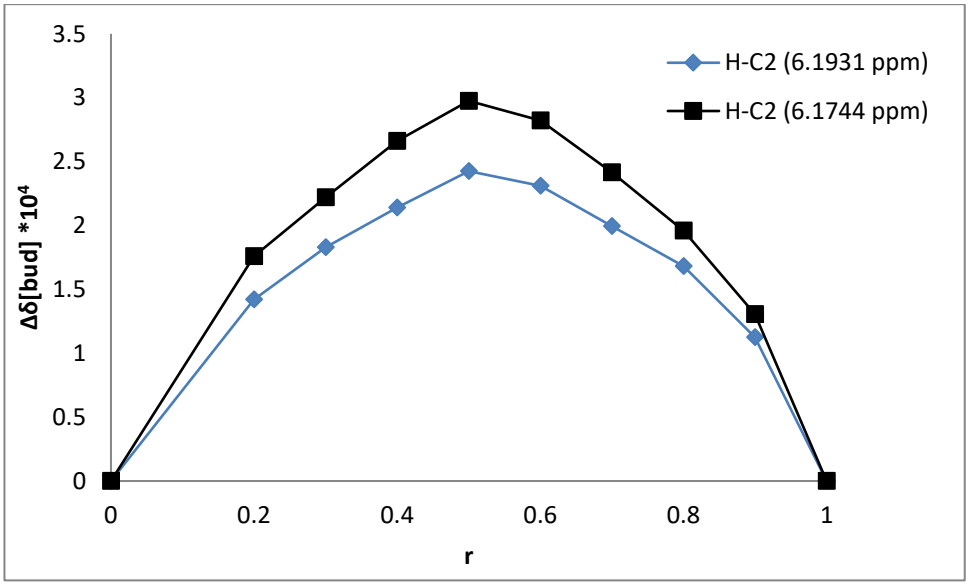

Figure 4.27: Determination of the stoichiometry of the complex between budesonide and *β*CD in D_2O by ^{1}H NMR based on the chemical shift of H-C_2 proton of budesonide.

4.2.4.2 Budesonide and TRIMEB

The complexation between BUD and TRIMEB was investigated in D_2O as described in Section 2.2.4.3. The results showed downfield changes occurred for the H-C_{19} peak at 1.2570 ppm with a partial split at higher TRIMEB

concentration (1.6 and 2 mM). No shift was observed for both H-C_{18} and H-C_{25} protons (Figure 4.28).

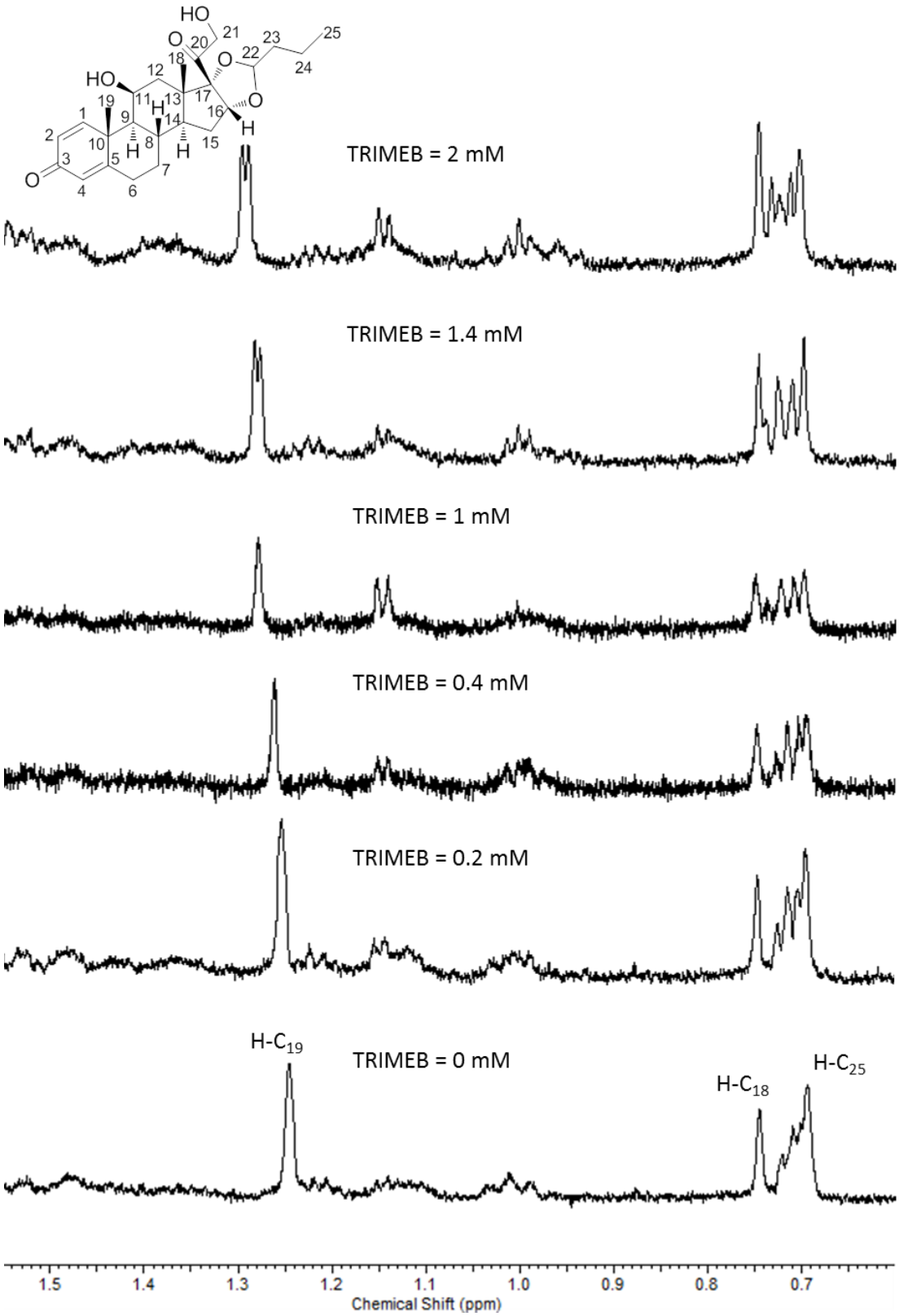

Figure 4.28: Budesonide (0.04 mM) chemical shift in high field region (0.6-1.6 ppm) with the addition of TRIMEB at 0, 0.2, 0.4, 1, 1.4 and 2 mM in D_2O.

The H-C_4 proton of the quinone ring at 5.9645 ppm was observed as a singlet peak with slight upfield shift, and minor shift was noted for the H-C_1 proton of the quinone ring. However, small shift was observed for the doublet H-C_2 proton which was then split into three peaks with increasing TRIMEB concentration (Figure 4.29).

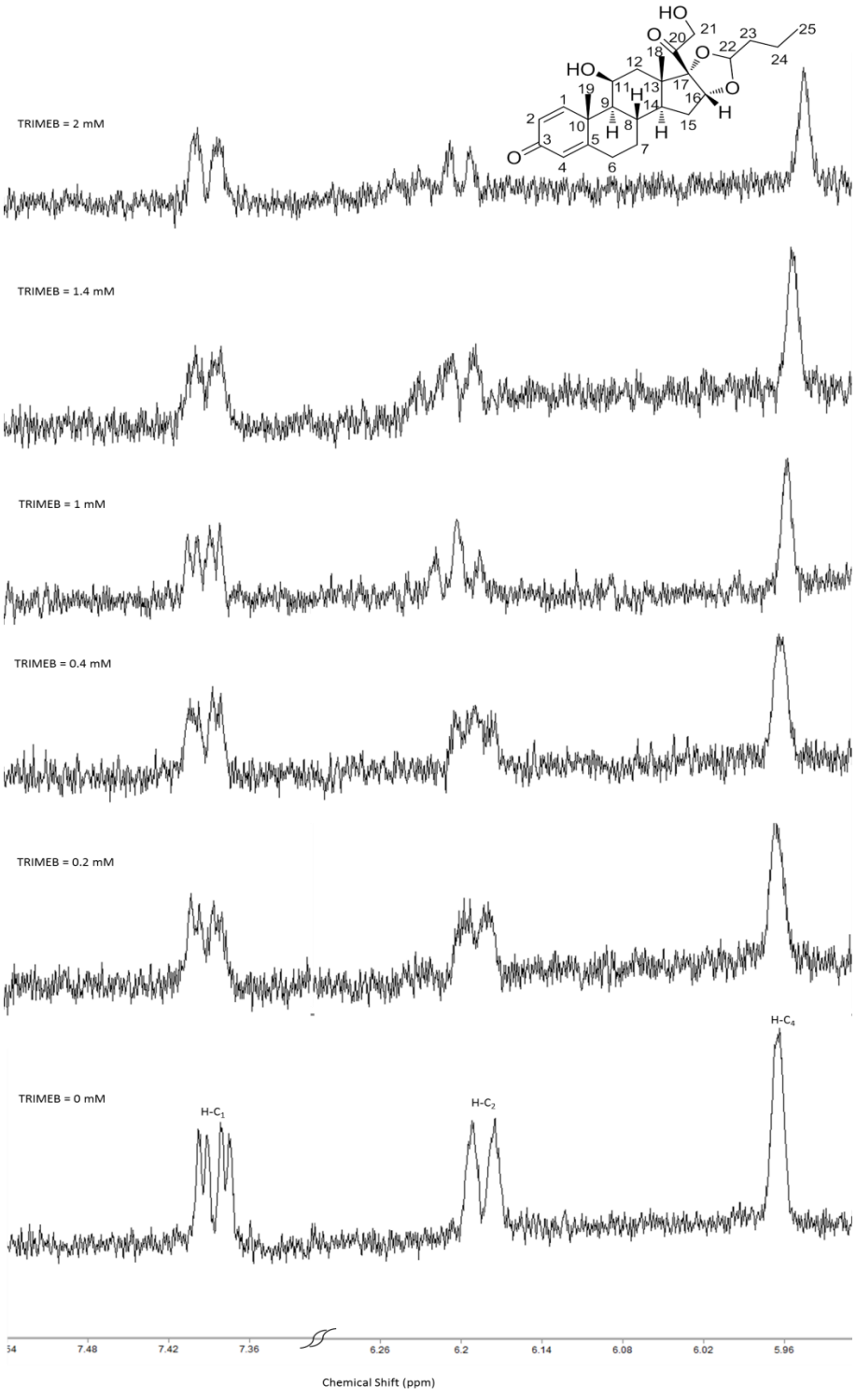

Figure 4.29: Budesonide (0.04 mM) chemical shift in low field region (5.9-7.54 ppm) with the addition of TRIMEB at 0, 0.2, 0.4, 1, 1.4 and 2 mM in D_2O.

The stability constant was calculated based on the chemical shift differences of H-C_{19} and H-C_4 at 1.2570 and 5.9645 ppm respectively. The results are presented in Table 4.28.

Table 4.28: Results of the chemical shift of budesonide and TRIMEB added at 0, 0.2, 0.4, 1, 1.4 and 2 mM in D_2O using ^1H NMR.

Experiment number	Proton position (ppm)	TRIMEB concentration (mM)					
		0	0.2	0.4	1	1.4	2
		Chemical shift (ppm)					
1			1.2588	1.2613	1.2752	1.2836	1.2941
2	H-C_{19}	1.2570	1.2589	1.2614	1.2784	1.2838	1.2961
3			1.2589	1.2615	1.2769	1.2851	1.2954
	Mean		**1.2589**	**1.2614**	**1.2768**	**1.2842**	**1.2952**
	SD		**0.0001**	**0.0001**	**0.0016**	**0.0008**	**0.0010**
	% CV		**0.0046**	**0.0079**	**0.1254**	**0.0634**	**0.0784**
1			5.9636	5.9625	5.9555	5.9500	5.9415
2	H-C_4	5.9645	5.9637	5.9626	5.9574	5.9512	5.9439
3			5.9637	5.9626	5.9573	5.9508	5.9440
	Mean		**5.9637**	**5.9626**	**5.9569**	**5.9504**	**5.9437**
	SD		**0.0001**	**0.0001**	**0.0009**	**0.0012**	**0.0010**
	% CV		**0.0010**	**0.0010**	**0.0150**	**0.0204**	**0.0175**

The data and the reciprocal plots used to determine the stability constant are shown in Table 4.29 and Figure 4.30.

Table 4.29: Results of the complexation between budesonide and TRIMEB added at 0.2, 0.4, 1, 1.4 and 2 mM in D_2O using ^1H NMR based on the chemical shift differences of H-C_{19} and H-C_4 at 1.2570 and 5.9645 ppm.

TRIMEB (mM)	1/TRIMEB (mM^{-1})	$1/\Delta\delta_{obs}$ (1.2570 ppm)				$1/\Delta\delta_{obs}$ (5.9645 ppm)			
		1	2	3	Mean	1	2	3	Mean
0.2	5	555	526	526	**536**	1111	1250	1250	**1204**
0.4	2.5	233	227	222	**227**	500	526.3	526.3	**517.5**
1	1	54.9	46.7	50.3	**50.6**	1111	140.9	138.9	**130.3**
1.4	0.7	37.6	37.3	35.6	**36.8**	68.9	75.2	73	**72.4**
2	0.5	26.9	25.6	26	**26.2**	43	48.5	48.8	**46.9**

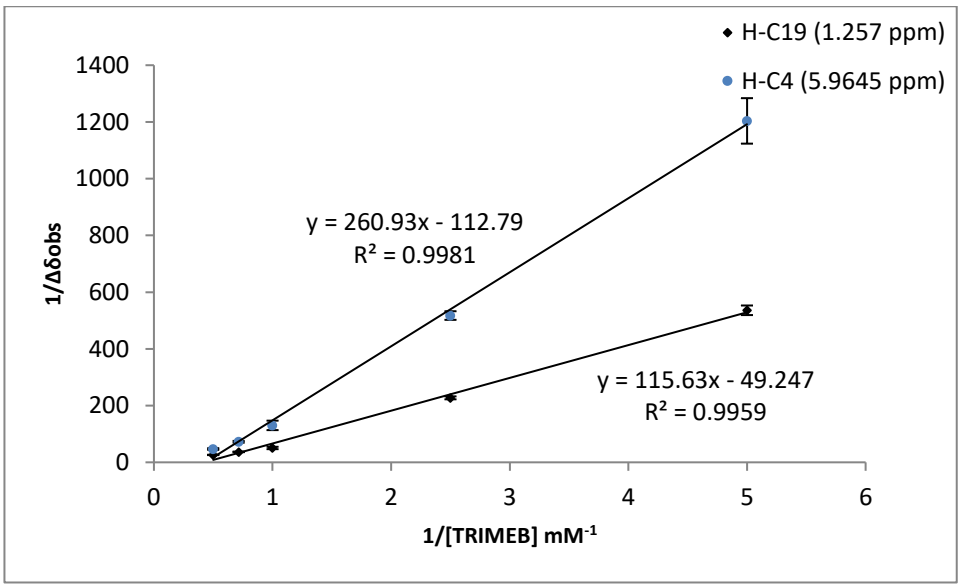

Figure 4.30: Reciprocal plot for the determination of the association constant between budesonide and TRIMEB in D_2O by ^1H NMR based on the chemical shift differences of H-C_{19} and H-C_4 at 1.2570 and 5.9645 ppm (Mean ± SD, n=3).

The reciprocal plot showed a linear relationship which suggested 1:1 stoichiometric ratio of the complex. The mean K values were 429 M^{-1} for the values obtained from two H-C_{19} and H-C_4 protons (Table 4.30).

Table 4.30: Results of the stability constant between budesonide and TRIMEB added at 0.2, 0.4, 1, 1.4 and 2 mM in D_2O using ^1H NMR.

Proton NO.	Chemical shift (ppm)	Stability constant, K (M^{-1})				SD	% CV
		1	2	3	Mean		
H-C_{19}	1.257	425	426	426	**426**	0.6	0.1
H-C_4	5.9645	427	432	437	**432**	5	1.2

The stoichiometry was confirmed by continuous variation method as described in Section 2.2.3.2 and the calculation was based on the chemical shift changes of the H-C_2 proton of BUD at 6.1931 and 6.1744 ppm. The results are presented in Tables 4.31 and 4.32.

Table 4.31: Results of ^{1}H NMR analysis for the determination of stoichiometry between budesonide and TRIMEB in D_2O based on the chemical shift of H-C_2 proton of budesonide at 6.1931 ppm.

[BUD] (mM)	r	$\delta_{complex}$ (ppm)	$\Delta\delta_{obs}$ (ppm)	$\Delta\delta$[BUD]	$\Delta\delta$[BUD]*10^4
0.05	1	6.1931	0	0	0
0.045	0.9	6.1912	0.0019	8.6×10^{-5}	0.86
0.04	0.8	6.1901	0.003	12×10^{-5}	1.2
0.035	0.7	6.189	0.0041	14.4×10^{-5}	1.44
0.03	0.6	6.1874	0.0057	17.1×10^{-5}	1.71
0.025	0.5	6.1855	0.0076	19×10^{-5}	1.9
0.02	0.4	6.1846	0.0085	17×10^{-5}	1.7
0.015	0.3	6.1834	0.0097	14.6×10^{-5}	1.46
0.01	0.2	6.1829	0.0102	10.2×10^{-5}	1.02
0	0	0	0	0	0

δ_{free} = 6.1931 ppm

Table 4.32: Results of ^{1}H NMR analysis for the determination of stoichiometry between budesonide and TRIMEB in D_2O based on the chemical shift of H-C_2 proton of budesonide at 6.1744 ppm.

[BUD] (mM)	r	$\delta_{complex}$ (ppm)	$\Delta\delta_{obs}$ (ppm)	$\Delta\delta$[BUD]	$\Delta\delta$[BUD]*10^4
0.05	1	6.1744	0	0	0
0.045	0.9	6.1722	0.0022	9.9×10^{-5}	0.99
0.04	0.8	6.171	0.0034	13.6×10^{-5}	1.36
0.035	0.7	6.1695	0.0049	17.2×10^{-5}	1.72
0.03	0.6	6.1675	0.0069	20.7×10^{-5}	2.07
0.025	0.5	6.1657	0.0087	21.8×10^{-5}	2.18
0.02	0.4	6.1648	0.0096	19.2×10^{-5}	1.92
0.015	0.3	6.1636	0.0108	16.2×10^{-5}	1.62
0.01	0.2	6.1629	0.0115	11.5×10^{-5}	1.15
0	0	0	0	0	0

δ_{free} = 6.1744 ppm

The plot shown in Figure 4.31 demonstrated that the inclusion complex had 1:1 stoichiometry since the highest value of r was at 0.5.

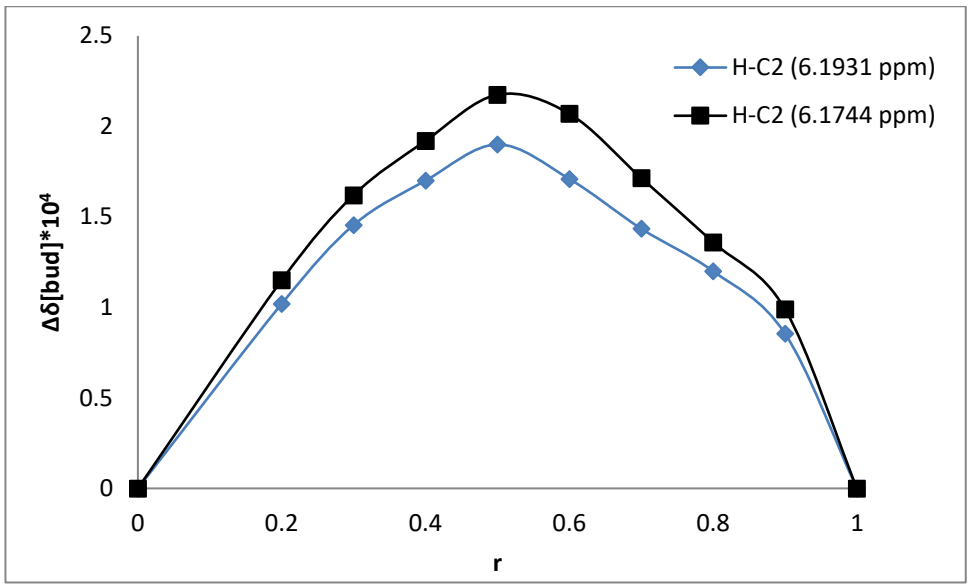

Figure 4.31: Determination of the stoichiometry of the complex between budesonide and TRIMEB in D_2O by ^1H NMR based on the chemical shift differences of H-C_2 proton of budesonide.

4.2.4.3 Budesonide and DIMEB

The inclusion complex between BUD and DIMEB was investigated in D_2O according to method specified in Section 2.2.4.3. The results showed two peaks were observed at approximately 0.72 and 0.77 ppm at 0.2 mM DIMEB concentration which were then slightly downfield shifted with the increasing DIMEB concentration. Both peaks could be assigned to the H-C_{18} peak of *R*- and *S*-enantiomers of BUD. However, no change was observed for H-C_{25} proton although its multiplicity changed as the DIMEB concentration was increased. The H-C_{19} resonance was observed with downfield shift that showed a fully split initially into two distinctive peaks and were then partially split at 1.4 and 2 mM DIMEB concentration. These two peaks could be assigned to the *R*- and *S*-enantiomers of BUD. However, it was hard to assign and relate both shifted peaks for each of the H-C_{18} and H-C_{19} protons to the *R*- and *S*-enantiomers of BUD without performing an additional experiment with the pure enantiomer and comparing to those of the racemic mixture. The spectra of the complexed BUD in the high field region are shown in (Figure 4.32).

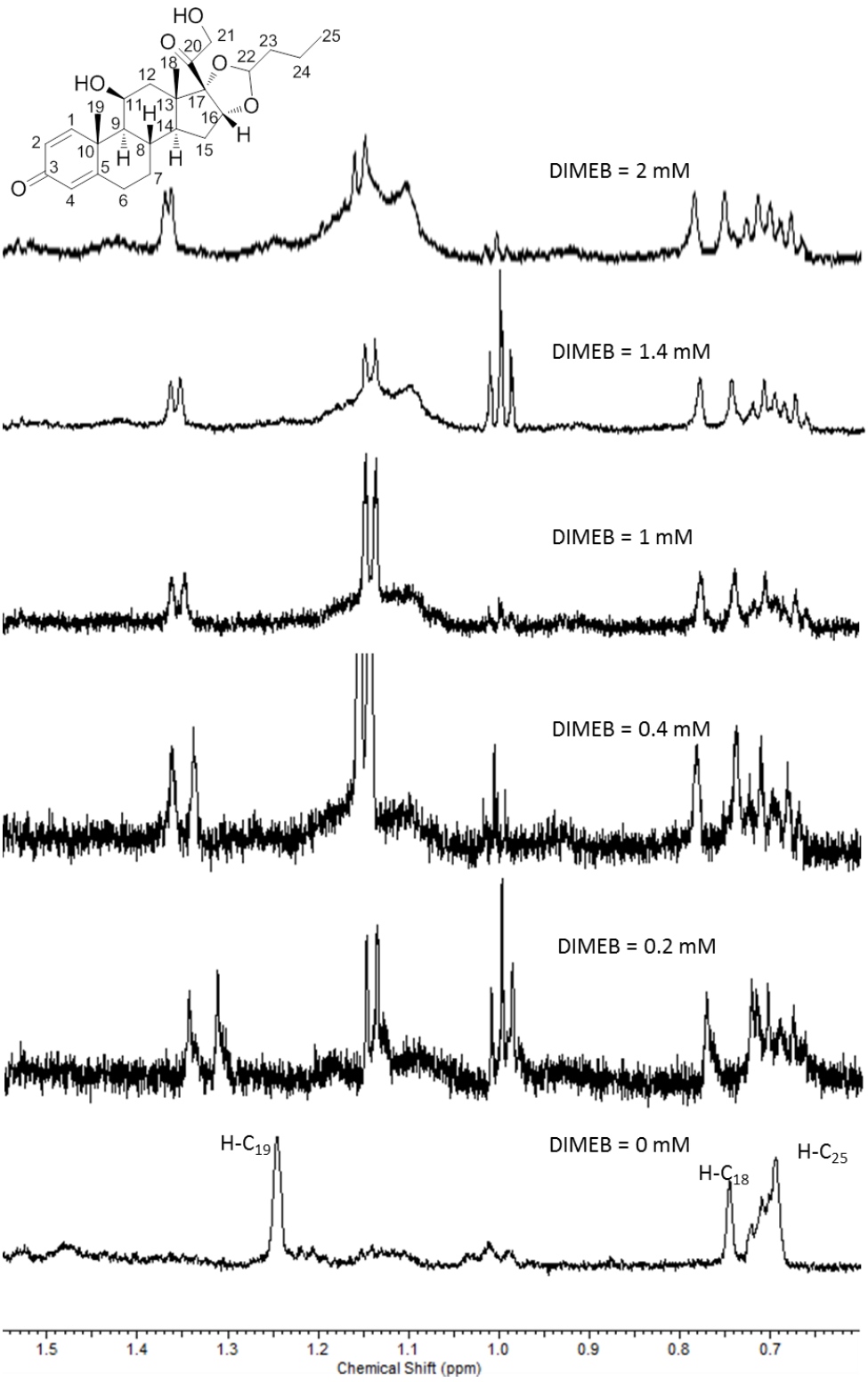

Figure 4.32: Budesonide (0.04 mM) chemical shift in high field region (0.6-1.6 ppm) with the addition of DIMEB at 0, 0.2, 0.4, 1, 1.4 and 2 mM in D_2O.

In the low field region, upfield shifts were observed for all of the quinone ring protons. The H-C_4 singlet peak was split into two distinctive peaks with increasing the DIMEB concentration, and both peaks could be assigned to the both *R*- and *S*-enantiomers of BUD. The doublet H-C_2 peak was split into four

peaks whereas the distinct multiplicity change was observed for H-C_1 proton (*J*-coupling constants increase with increasing DIMEB concentration. The spectra of the complexed BUD in the low field region are shown in Figure 4.33.

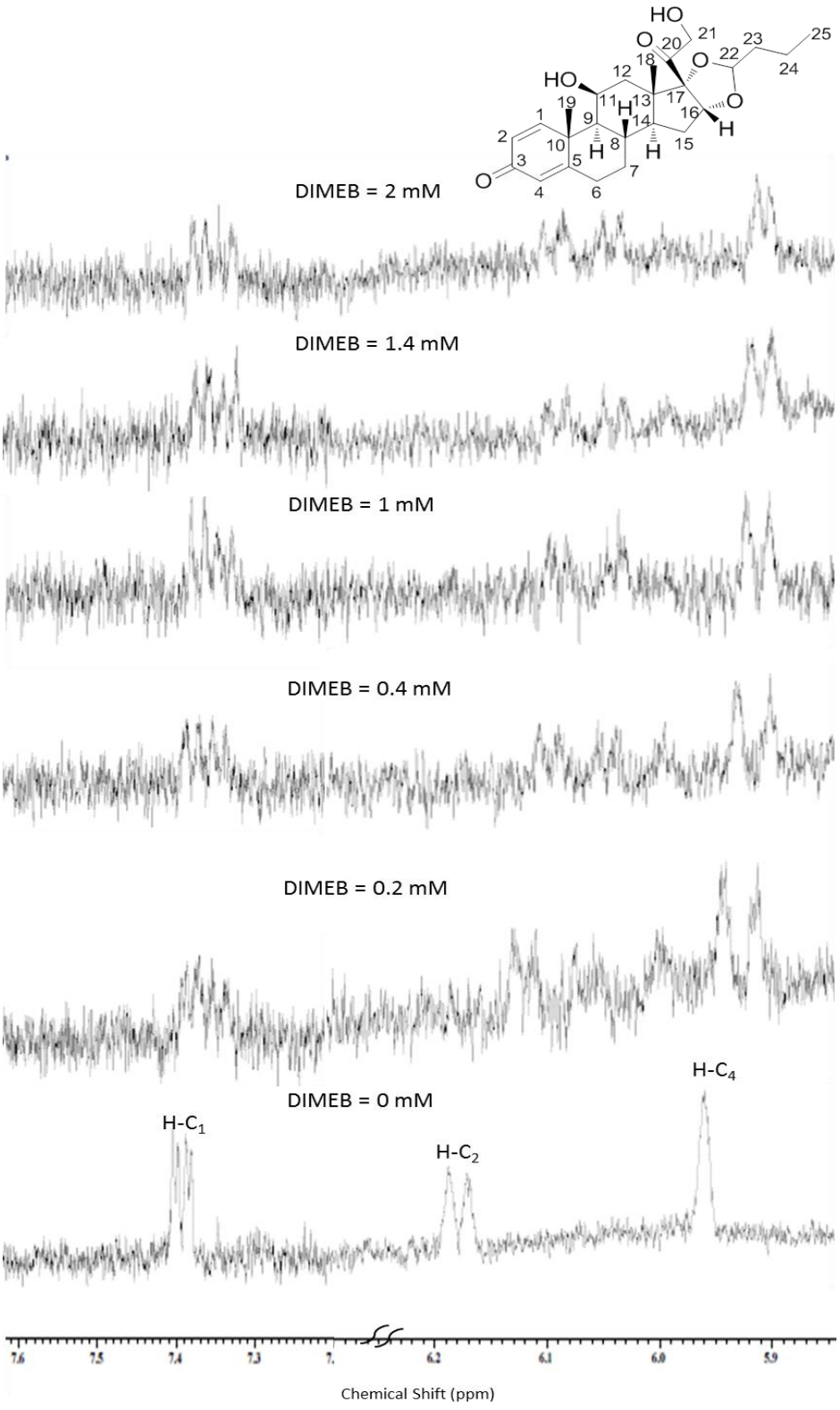

Figure 4.33: Budesonide (0.04 mM) chemical shift in low field region (5.8-7.6 ppm) with the addition of DIMEB at 0, 0.2, 0.4, 1, 1.4 and 2 mM in D_2O.

The K value was calculated based on the chemical shift displacements of H-C_{19} and H-C_4 protons at 1.257 and 5.9645 ppm respectively. The results are presented in Table 4.33.

Table 4.33: Results of the chemical shift of budesonide and DIMEB added at 0, 0.2, 0.4, 1, 1.4 and 2 mM in D_2O using ^1H NMR.

Exp. number	Proton position (ppm)	DIMEB concentration (mM)					
		0	0.2	0.4	1	1.4	2
		Chemical shift (ppm)					
1			1.3124	1.3356	1.3536	1.3576	1.3635
2	H-C_{19}	1.2570	1.3121	1.3333	1.3515	1.3539	1.3674
3			1.3129	1.3346	1.3501	1.3577	1.3693
	Mean		**1.3125**	**1.3345**	**1.3517**	**1.3564**	**1.3667**
	SD		**0.0004**	**0.0012**	**0.0018**	**0.0022**	**0.0030**
	% CV		**0.0308**	**0.0864**	**0.1303**	**0.1597**	**0.2163**
1			5.9422	5.9352	5.9276	5.9231	5.9209
2	H-C_4	5.9645	5.9413	5.9340	5.9264	5.9210	5.9193
3			5.9409	5.9330	5.9247	5.9220	5.9177
	Mean		**5.9415**	**5.9341**	**5.9262**	**5.9220**	**5.9193**
	SD		**0.0007**	**0.0011**	**0.0015**	**0.0011**	**0.0016**
	% CV		**0.0112**	**0.0186**	**0.0246**	**0.0177**	**0.0270**

The data and the reciprocal plot used to calculate the stability constant are presented in Table 4.34 and shown in Figure 4.34.

Table 4.34: Results of the complexation between budesonide and DIMEB added at 0.2, 0.4, 1, 1.4 and 2 mM in D_2O using ^1H NMR based on the chemical shift of H-C_{19} and H-C_4 at 1.257 and 5.9645 ppm.

DIMEB (mM)	DIMEB (mM^{-1})	$1/\Delta\delta_{obs}$ (1.2570 ppm)				$1/\Delta\delta_{obs}$ (5.9645 ppm)			
		1	2	3	Mean	1	2	3	Mean
0.2	5	18.1	18.2	17.9	**18.1**	44.8	43.1	42.4	**43.4**
0.4	2.5	12.7	13.1	12.9	**12.9**	34.1	32.8	31.8	**32.9**
1	1	10.4	10.6	10.7	**10.6**	27.1	26.3	25.1	**26.2**
1.4	0.7	9.9	10.3	9.9	**10.1**	24.2	22.9	23.5	**23.6**
2	0.5	9.4	9.1	8.9	**9.1**	22.9	22.1	21.4	**22.1**

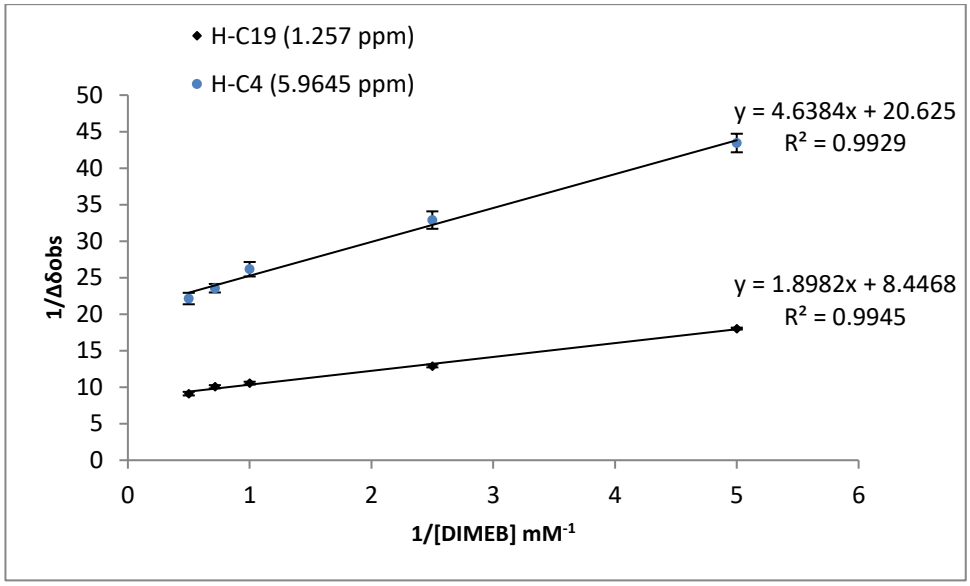

Figure 4.34: Reciprocal plot for the determination of the association constant between budesonide and DIMEB in D_2O by ^1H NMR based on the chemical shift of H-C_{19} and H-C_4 at 1.2570 and 5.9645 ppm (Mean ± SD, n=3).

The reciprocal plot showed a linear relationship indicating that the ratio of the stoichiometry of the complex was 1:1. The mean K value was found to be 4446 M^{-1} based on the H-C_{19} and H-C_4 protons (Table 4.35).

Table 4.35: Results of the stability constant between budesonide and DIMEB added at 0.2, 0.4, 1, 1.4 and 2 mM in D_2O using ^1H NMR.

Proton NO.	Chemical shift (ppm)	Stability constant, K (M^{-1})				SD	% CV
		1	2	3	Mean		
H-C_{19}	1.2570	4444	4440	4449	**4444**	4.5	0.1
H-C_4	5.9645	4446	4449	4445	**4447**	2.1	0.05

The stoichiometry of 1:1 was verified by continuous variation method and the solutions were prepared according to the method specified in Section 2.2.3.2. The calculation was based on the chemical shift changes observed at H-C_{19} and H-C_4 protons of budesonide at 1.2570 and 5.9645 ppm respectively. The stoichiometry was then determined as shown in Tables 4.36 and 4.37.

Table 4.36: Results of ^{1}H NMR analysis for the determination of the stoichiometry between budesonide and DIMEB in D_2O based on the chemical shift of H-C_{19} proton of budesonide at 1.2570 ppm.

[BUD] (mM)	r	$\delta_{complex}$ (ppm)	$\Delta\delta_{obs}$ (ppm)	$\Delta\delta$[BUD]	$\Delta\delta$[BUD]*10^4
0.05	1	1.2570	0	0	0
0.045	0.9	1.2655	0.0085	38.3 x 10^{-5}	3.83
0.04	0.8	1.2760	0.0190	76 x 10^{-5}	7.6
0.035	0.7	1.2840	0.0270	94.5 x 10^{-5}	9.45
0.03	0.6	1.2919	0.0349	104.7 x 10^{-5}	10.47
0.025	0.5	1.3007	0.0437	109.3 x 10^{-5}	10.93
0.02	0.4	1.3076	0.0506	101.2 x 10^{-5}	10.12
0.015	0.3	1.3134	0.0564	84.6 x 10^{-5}	8.46
0.01	0.2	1.3243	0.0673	67.3 x 10^{-5}	6.73
0	0	0	0	0	0

δ_{free} = 1.2570 ppm

Table 4.37: Results of ^{1}H NMR analysis for the determination of the stoichiometry between budesonide and TRIMEB in D_2O based on the chemical shift of H-C_4 proton of budesonide at 5.9645 ppm.

[BUD] (mM)	r	$\delta_{complex}$ (ppm)	$\Delta\delta_{obs}$ (ppm)	$\Delta\delta$[BUD]	$\Delta\delta$[BUD]*10^4
0.05	1	5.9645	0	0	0
0.045	0.9	5.9585	0.006	27 x 10^{-5}	2.7
0.04	0.8	5.9534	0.0111	44.4 x 10^{-5}	4.44
0.035	0.7	5.9482	0.0163	57.1 x 10^{-5}	5.71
0.03	0.6	5.9422	0.0223	66.9 x 10^{-5}	6.69
0.025	0.5	5.936	0.0285	71.3 x 10^{-5}	7.13
0.02	0.4	5.9329	0.0316	63.2 x 10^{-5}	6.32
0.015	0.3	5.9307	0.0338	50.7 x 10^{-5}	5.07
0.01	0.2	5.9299	0.0346	34.6 x 10^{-5}	3.46
0	0	0	0	0	0

δ_{free} = 5.9645 ppm

The Job's plot showed the highest value of r was at 0.5 demonstrating the stoichiometry of the complex was 1:1 (Figure 4.35).

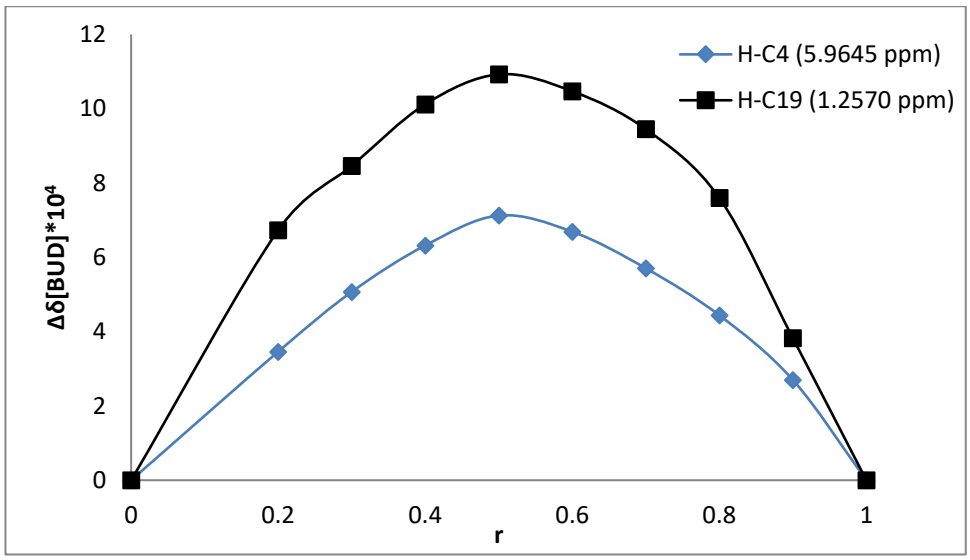

Figure 4.35: Determination of the stoichiometry of the complex between budesonide and DIMEB in D_2O by ^1H NMR based on the chemical shift change of H-C_{19} and H-C_4 protons of budesonide.

4.3 Analysis of solid complexes of BUD and *β*CD/TRIMEB/DIMEB using vibrational spectroscopy

4.3.1 FTIR

4.3.1.1 BUD and βCD complex

The physical mixture and co-evaporation complex prepared from BUD and *β*CD were analysed by IR. The assignment of IR peaks of BUD was consistent to those reported by Raval *et al*.[182] and Gangurde *et al*.[183] The peak at 3480 cm^{-1} was related to the stretching of the OH group. The band at 1721 cm^{-1} was due to the stretching of the C=O ketone group whereas the bands at 1603 cm^{-1} was ascribed to the stretching of C=O ring. The bands at 1667 and 1441 cm^{-1} were related to the stretching of C=C and C-C ring respectively. The stretching of C-O was observed at 1092 cm^{-1} whereas the stretching of C-C was observed at 937 cm^{-1}. The assignment of IR spectrum of BUD is presented in Table 4.38.

Table 4.38: IR bands of budesonide.[182,183]

Wavenumbers (cm^{-1})	Assignment
3480	OH
2957	aliphatic C-H
1721	stretching of C=O ketone
1667	stretching of C=C
1603	stretching of C=O ring
1441	stretching of C-C ring
1092	stretching of C-O group
937	stretching of C-C

The assignment of *β*CD IR peaks is illustrated in Table 4.39 and is consistent to those reported by Roik and Belyakova[184] and Rabadiya *et al*.[185]

Table 4.39: IR bands of *β*CD.[184,185]

Wavenumbers (cm^{-1})	Functional group
3399	stretching of OH
2924	stretching of C-H in (CH/CH_2 groups)
1260-1000	stretching of C-O
1158	stretching of C-C
1030	bending vibration of OH

It has been noticed that the OH bands of both BUD and *β*CD in the complex spectrum were broader compared to the BUD and *β*CD alone. The band at 1667 cm^{-1} which was related to stretching of C=C was slightly shifted to 1666 cm^{-1} and split in the case of physical mixture, while the other band at 1603 cm^{-1} was considerably decreased in intensity. Also, there was a shift in the band at 1721 cm^{-1} that was related to frequency of the C=O ketone and became broader in the case of co-evaporation complex (Figures 4.36 and 4.37). These changes in the bands of the quinone ring suggested that this part was responsible for the complex by entering into the *β*CD cavity. The main bands shift for BUD, *β*CD and their complexes are illustrated in Table 4.40.

Table 4.40: Main bands of pure budesonide, pure *β*CD and their complexes (physical mixture and co-evaporation)

Wavenumbers (cm^{-1})			
BUD	***β*CD**	**Physical mixture**	**Co-evaporation**
3480	−	(3407) Broad band	(3430) Broad band
−	3399		
−	2924	2932	2925
1721	−	1720	1717
1667	−	1666	1666
1603	−	1603 (Decreased in intensity)	
−	1158	1157	1158
−	1030	1029	1030

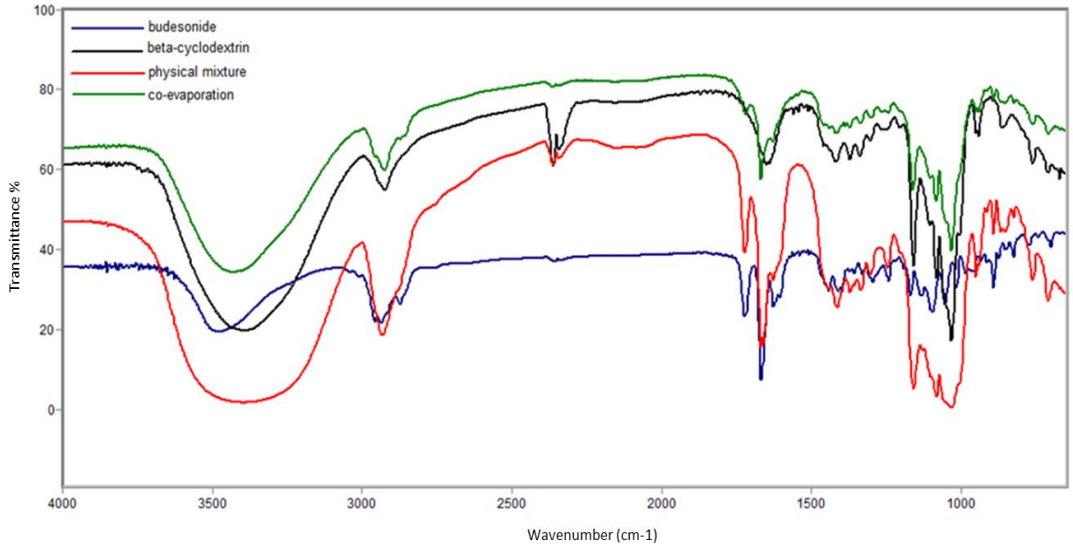

Figure 4.36: IR spectra of pure budesonide, *β*CD, physical mixture and co-evaporation complex showing a broad band of OH group in the range or 3300-3500 cm^{-1} and other shifts related to the quinone ring of budesonide.

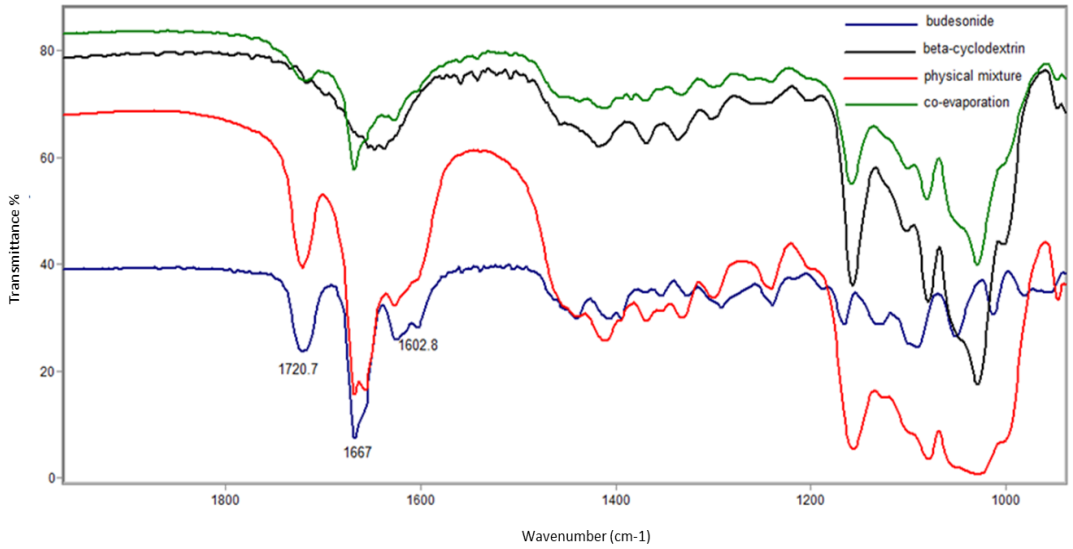

Figure 4.37: IR spectra of pure budesonide, *β*CD, physical mixture and co-evaporation complex showing shifts of the quinone ring of budesonide.

4.3.1.2 BUD and TRIMEB complex

The physical mixture and co-evaporation complex prepared from BUD and TRIMEB were analysed by IR spectroscopy. The same results were obtained with TRIMEB as with *β*CD, where the main changes were with the OH group (Figure 4.38) and quinone ring (Figure 4.39). The main bands shift for BUD, TRIMEB and their complexes are presented in Table 4.41.

Table 4.41: Main bands of pure budesonide, pure TRIMEB and their complexes (physical mixture and co-evaporation)

Wavenumbers (cm^{-1})			
BUD	**TRIMEB**	**Physical mixture**	**Co-evaporation**
3480	–	(3468) Broad peak	(3430) Broad peak
–	3445		
–	2930	2928	2929
1721	–	1718	1717
1667	–	1667	1666
1603	–	1603 (Decreased in intensity)	
–	1162	1163	1163
–	1041	1038	1038

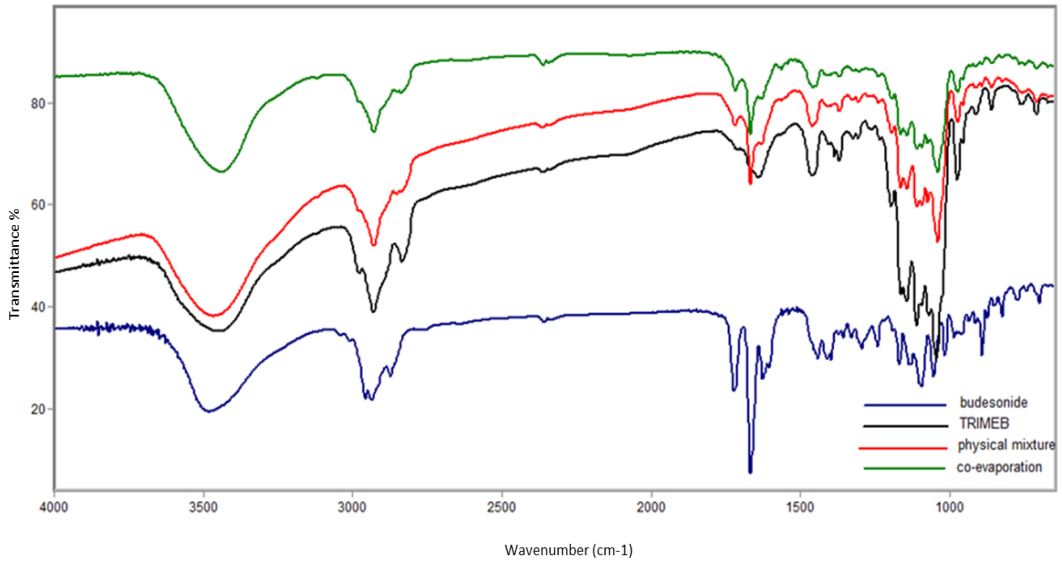

Figure 4.38: IR spectra of pure budesonide, TRIMEB, physical mixture and co-evaporation complex showing a broad band of OH group in the range or 3300-3500 cm^{-1} and other shifts related to the quinone ring of budesonide.

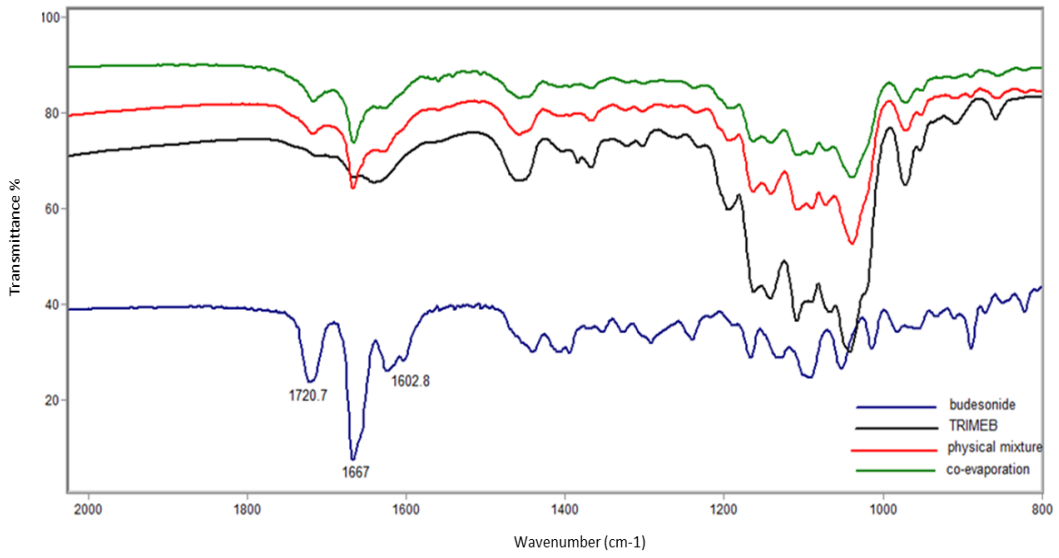

Figure 4.39: IR spectra of pure budesonide, TRIMEB, physical mixture and co-evaporation complex showing shifts of the quinone ring of budesonide.

4.3.1.3 BUD and DIMEB complex

The main band affected in the complexation with DIMEB were the OH group (Figure 4.40) and quinone ring (Figure 4.41). The main bands shift for BUD, DIMEB and their complexes are presented in Table 4.42.

Table 4.42: Main bands of pure budesonide, pure DIMEB and their complexes (physical mixture and co-evaporation)

Wavenumbers (cm^{-1})			
BUD	**DIMEB**	**Physical mixture**	**Co-evaporation**
3480	–	(3408) Broad peak	(3402) Broad peak
–	3404		
–	2926	2929	2927
1721	–	1719	1717
1667	–	1667	1661
1603	–	1603 (Decreased in intensity)	
–	1156	1156	1154
–	1045	1047	1043

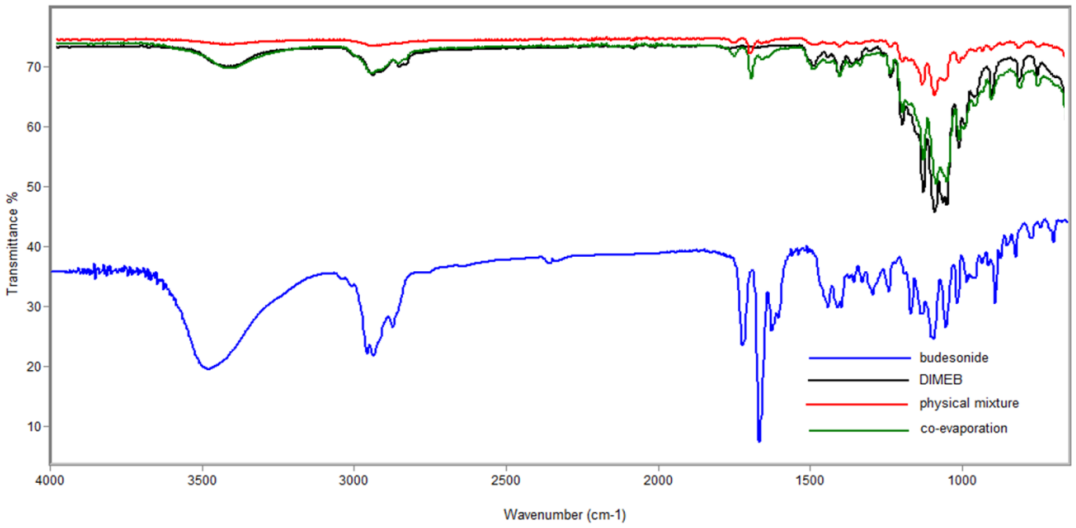

Figure 4.40: IR spectra of pure budesonide, DIMEB, physical mixture and co-evaporation complex showing a broad band of OH group in the range or 3300-3500 cm^{-1} and other shifts related to the quinone ring of budesonide.

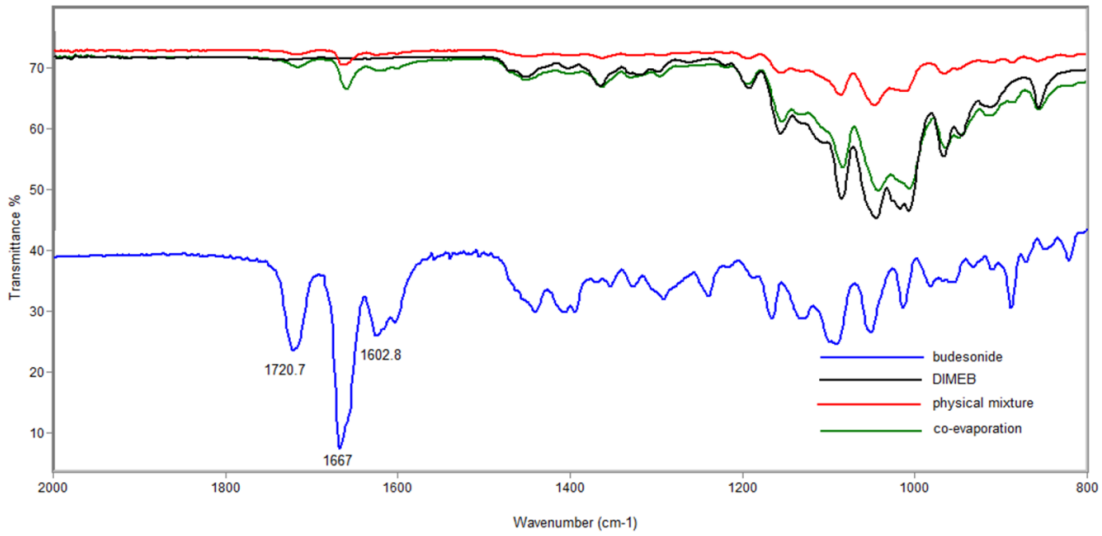

Figure 4.41: IR spectra of pure budesonide, DIMEB, physical mixture and co-evaporation complex showing shifts of the quinone ring of budesonide.

4.3.2 Raman spectroscopy

4.3.2.1 BUD and βCD complex

The Raman spectrum of budesonide has been assigned with refer to the literature, the main peaks at 1714 cm^{-1} and 1657 cm^{-1} were corresponded to the frequency of C=O and C=C of quinone ring respectively.[186] The other two peaks at 1627 cm^{-1} and 1603 cm^{-1} correspond to the frequency of C=C stretching of the ring.[186] It has been noticed that there was no obvious shift at 1657 cm^{-1} of both complexes prepared between budesonide and *β*CD (physical mixture and co-evaporation complex). However, the band at 1603 cm^{-1} became broader and decreased in intensity in the physical mixture compared to the budesonide spectrum with a considerable reduction in the case of co-evaporation of budesonide and *β*CD. On the other hand, considerable reduction in the intensity of the band at 1627 cm^{-1} was observed for the two complexes prepared. There was also a change in the shape and also a reduction in intensity of band at 1714 cm^{-1}. Generally, these bands mentioned earlier were related to the quinone ring and these changes suggested that this part of budesonide formed the complex with *β*CD (Figure 4.42).

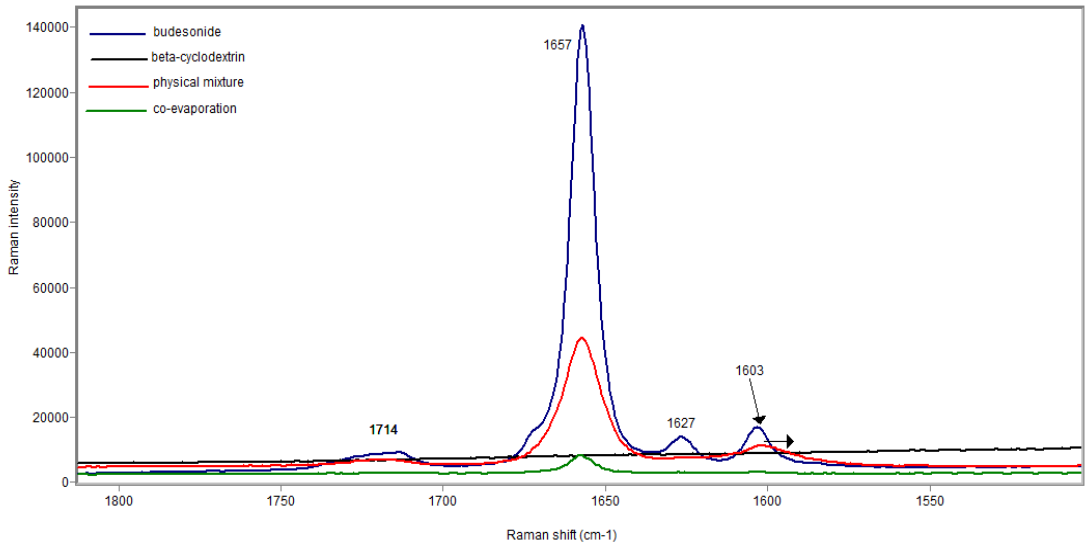

Figure 4.42: Raman spectra of pure budesonide, pure *β*CD and 1:1 complex of physical mixture and co-evaporation complex showing shifts in the quinone ring bands.

4.3.2.2 BUD and TRIMEB complex

The results showed that the band at 1657 cm^{-1} was observed at a higher wavenumber at 1665 cm^{-1} with the co-evaporation of BUD and TRIMEB. For the other bands at 1714, 1627 and 1603 cm^{-1}, the same results were obtained as those with *β*CD which suggests that the quinone ring is engaged in a more significant interaction with the host (TRIMEB) (Figure 4.43).

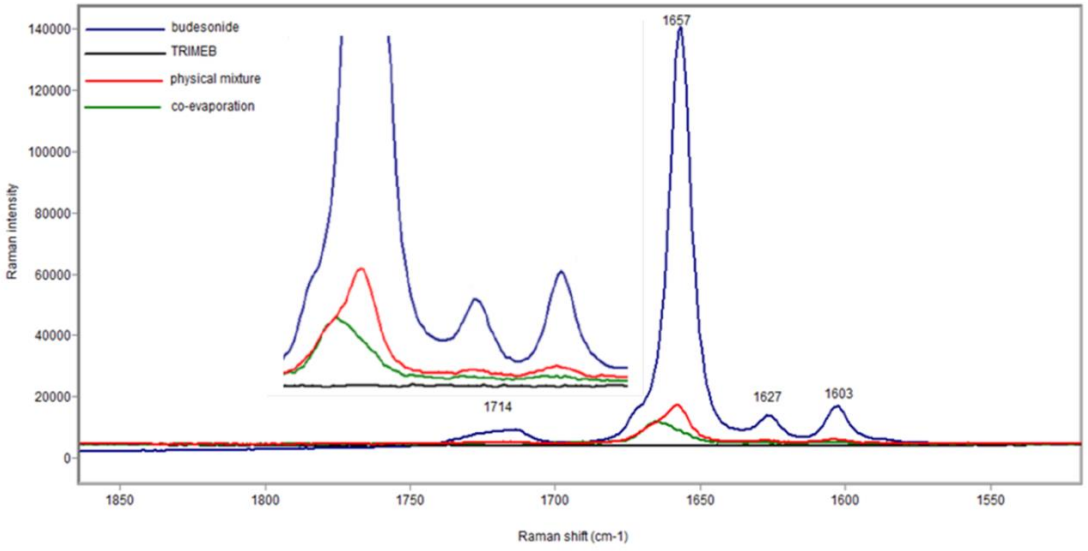

Figure 4.43: Raman spectra of pure budesonide, pure TRIMEB and 1:1 complex of physical mixture and co-evaporation complex showing shifts in the quinone ring bands.

4.3.2.3 BUD and DIMEB complex

In the case of DIMEB, the band at 1657 cm^{-1} was observed at higher frequency shift at 1660 cm^{-1} in the complex of co-evaporation method and at 1665 cm^{-1} in the complex of physical mixture. The same results obtained with other bands at 1714, 1627 and 1603 cm^{-1} as those with *β*CD and TRIMEB which suggests that the quinone ring is involved in the interaction with the DIMEB (Figure 4.44).

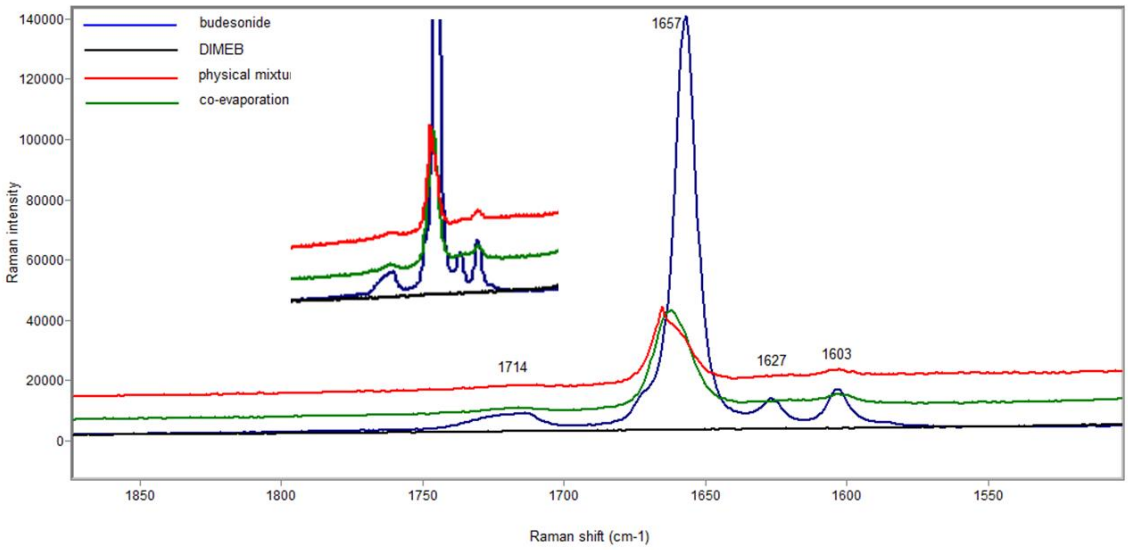

Figure 4.44: Raman spectra of pure budesonide, pure DIMEB and 1:1 complex of physical mixture and co-evaporation complex showing shifts in the quinone ring bands.

4.4 Discussion

4.4.1 Complexation studies by UV-Vis spectroscopy

The results obtained from UV technique showed a higher complexation in H_2O compared to co-solvent of EtOH/H_2O mixture with both *β*CD and TRIMEB where the obtained K values were found to be 94 and 72 M^{-1} in the case *β*CD compared to 205 and 138 M^{-1} for TRIMEB in H_2O and EtOH/H_2O mixture respectively. This might be related to the BUD solubility as it is soluble in ethanol and insoluble in water, since generally as the solubility of the guest molecule in the solvent increases, less complexation occurs with the host making BUD complexation higher in H_2O compared to the EtOH/H_2O mixture. The reciprocal plot of the titration experiments of BUD with both *β*CD and TRIMEB in H_2O and EtOH/H_2O mixture showed a good linearity indicating that the stoichiometry of the complex was 1:1. The stoichiometry was further confirmed by Job's plot of continuous variation method.

The influence of co-solvent on the complexation between CD and the guest is a controversial topic. It has been found that the co-solvent has an ability to dissolve the guest molecule, before entering the CD's cavity and thus facilitates the complex formation. Also, the co-solvent system can dissolve the excess guest molecules that do not enter into the CD's cavity.[187] In contrast, some reports showed that the co-solvent system has a destabilisation effect on the CD involved complexation.[188] This was explained by two mechanisms; firstly, the co-solvent can affect the bulk solvent polarity where it can reduce the polarity of the system at a particular co-solvent concentration to an extent which favours the desolvation of the guest molecule.[189] Secondly, the co-solvent may compete with the guest molecule by entering and occupying the CDs cavity.[190-192] Okubo *et al*. studied the effect of a mixed solvent of ethanol and water on the complexation between the surfactant hexadecyl trimethyl ammonium bromide (C_{16}TAB) and *β*CD. They found that the value of K decreases as the proportion of ethanol increases, with the reported K values of 2000 and 450 M^{-1} for 1 M and 4 M ethanol concentrations respectively. The obtained results were attributed to the stabilisation of the surfactant tail by the organic solvent, which subsequently led to weakening of the hydrophobic interaction between surfactant and the CD.[193] A similar finding was reported on the effect of isopropanol and water mixtures on the complexation between dodecyl trimethyl

ammonium bromide (C_{12}TAB) and *β*CD.[194] The greater complexation observed with water in this work compared to the co-solvent with ethanol is attributed to the fact that the co-solvent system reduces the water solvation (reduces the polarity outside the CD cavity) and thus allows the ethanol to access the BUD molecule. This results in the preference for BUD to be located partially outside the CD cavity and thus a weak complexation occurs. By contrast, in aqueous solution, water inside the CD cavity has a reduced polarity compared to the bulk solvent i.e. outside of the CD cavity. Hence, the non-polar BUD is driven to associate with the cavity of the CD molecule and complexation occurs.

4.4.2 Complexation studies by NMR

4.4.2.1 Effect of solvent

The influence of the solvent type on the complex formation between BUD and three different types of CDs (*β*CD, DIMEB and TRIMEB) was investigated in this work using the NMR titration method. The obtained results showed weaker inclusion complex between BUD and *β*CD, DIMEB/TRIMEB in the organic solvents (CD_3CN, MeOD and $CDCl_3$) compared to D_2O as illustrated in Table 4.43. The reciprocal plot of the titration experiments used to study the complexation of BUD with *β*CD, DIMEB and TRIMEB in D_2O showed good linearity demonstrating that the complex had a stoichiometry of 1:1. The continuous variation method confirmed the stoichiometry to be 1:1 of the inclusion complex since the plot showed a maximum at r = 0.5.

Table 4.43: Complex formation of budesonide with *β*CD, DIMEB and TRIMEB in three solvent system; D_2O, MeOD and $CDCl_3$.

CD type	Association constant, Ka (M^{-1})			
	D_2O	CD_3CN	MeOD	$CDCl_3$
*β*CD	1129	not assessed due to insolubility		
DIMEB	4446	No complex formed	116	73
TRIMEB	429	No complex formed	91	64

The strength of the complex formed among the solvents assessed can be ranked as follows: D_2O > MeOD > $CDCl_3$ > CD_3CN. The results showed that no complexation occurred with CD_3CN and this was consistent with results obtained by Menger and Dulany where no binding was formed between *p*-nitrophenol (guest) and peralkylated CD (host) in acetonitrile.[164] They stated that the acetonitrile displays a polarity similar to that of the CD cavity; hence

there is no drive for complexation.[164] The complexation observed in water was the strongest of all the solvents assessed, and these results are in agreement with those from other studies. For example, Siegel and Breslow reported that the binding constant between anisole and *β*CD in water is two orders of magnitude bigger than that in DMSO.[123] Similarly, Smithrud and Diederich studied the binding affinity of a cyclophane receptor for pyrene in different solvents. They found that the binding constant was decreased in the following order: water > ethanol > acetone > carbon disulphide.[195] Despite the fact that D_2O showed stronger complexation in comparison to the organic solvents in this work and also with some other studies, however, this cannot be obeyed as a general rule since on the other hand, some studies showed stronger complexation with organic solvents than water. For instance, Menger and Dulany found the binding of *p*-nitrophenol with peralkylated CD is stronger in heptane compared to that in water with both *β*CD and *α*CD.[164] Nakai *et al*. found that *p*-nitrophenol transferred from the aqueous phase to the $CDCl_3$ phase by addition of methyl *β*CD to the organic solvent.[196] The contradictory results were explained based on the polarity of the host, guest, and solvent rather than anticipating that complex formation was based on the solvent type solely. It has been found that when both guest and host are nonpolar, the binding is controlled by the dispersion forces between guest and host as well as the desolvation of cohesive and polar solvent molecules.[197] It was concluded that binding occurs when there is a difference in the polarity of the cavity and the solvent system outside the cavity.[164] The binding of a nonpolar guest is preferred in a polar solvent such as water[195] while a polar guest is most favourable in a less polar solvent.[198] The previous examples of anisole and cyclophane (non-polar guests) formed stronger complexation in the presence of water because the CD cavity is less polar than the medium. However, *p*-nitrophenol (has some hydrophilic character) formed stronger complexation in the organic solvent (heptane) as the CD cavity is more polar compared to the medium.

In this study, BUD as a nonpolar guest preferred the CD cavity of less polarity in the presence of water, which is as a result a stronger complexation in the aqueous solvent formed compared to MeOD and $CDCl_3$. In the latter two solvents, BUD cannot form strong complexation as in water because the CD

cavity is more polar than the organic solvents in which it is soluble,[199] which provides the ideal environment for BUD to favour solvation, hence reducing the driving force of BUD to enter the DIMEB and TRIMEB cavity. Also, such solvents might compete with BUD for occupying the DIMEB and TRIMEB cavity, which ultimately decreases its binding and the complexation. This might explain the higher complexation between BUD and CDs in water compared to the utilised organic solvents.

4.4.2.2 CD type and its effect on complexation

The effect of CDs type on the complexation with BUD was studied utilising three different types of CDs; (i) *β*CD, (ii) DIMEB and (iii) TRIMEB and the results were summarised in Table 4.44 and Figures 4.45 and 4.46.

Table 4.44: Chemical shift displacements of BUD with 2 mM *β*CD, DIMEB and TRIMEB in D_2O related to the chemical shift of free BUD.

CD type	Chemical shift displacements (ppm)				
	H-C_1	**H-C_2**	**H-C_4**	**H-C_{18}**	**H-C_{19}**
*β*CD	D* (0.01)	U** (0.07)	U** (0.03)	D* (0.05)	D** (0.12, 0.16)
DIMEB	U** (0.06)	U** (0.11)	U** (0.06)	D* (0.03)	D** (0.11)
TRIMEB	NS	D* (0.01)	U* (0.02)	NS	D* (0.04)

D* = small downfield, D** = large downfield, U* = small upfield, U** = large upfield, NS = no significant shift

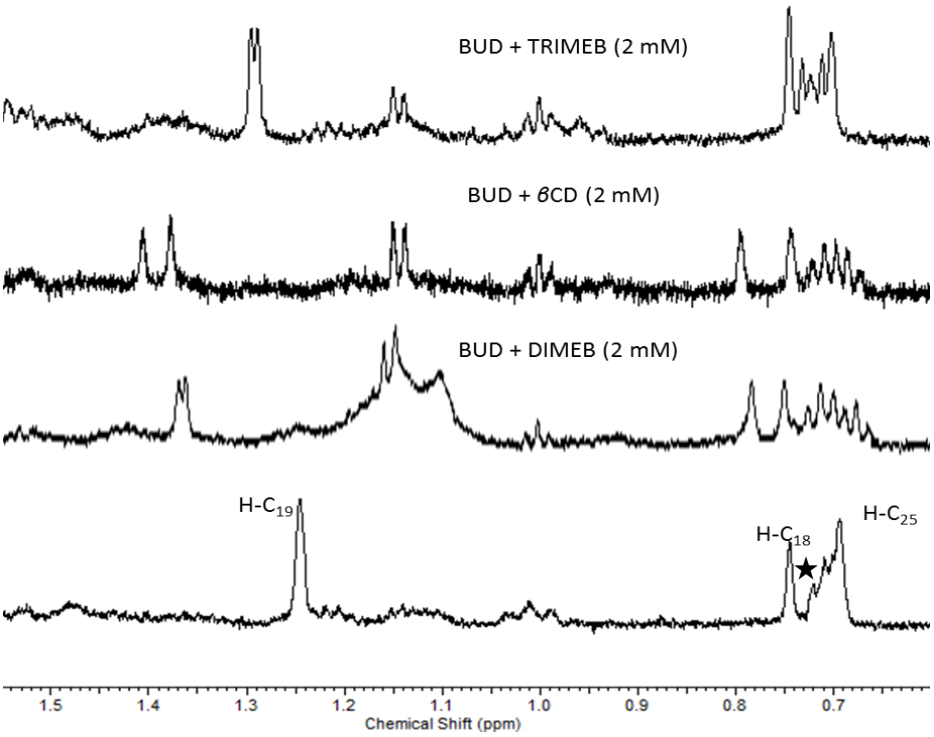

Figure 4.45: BUD chemical shift differences in the high field region complexed with 2 mM *β*CD, DIMEB and TRIMEB.

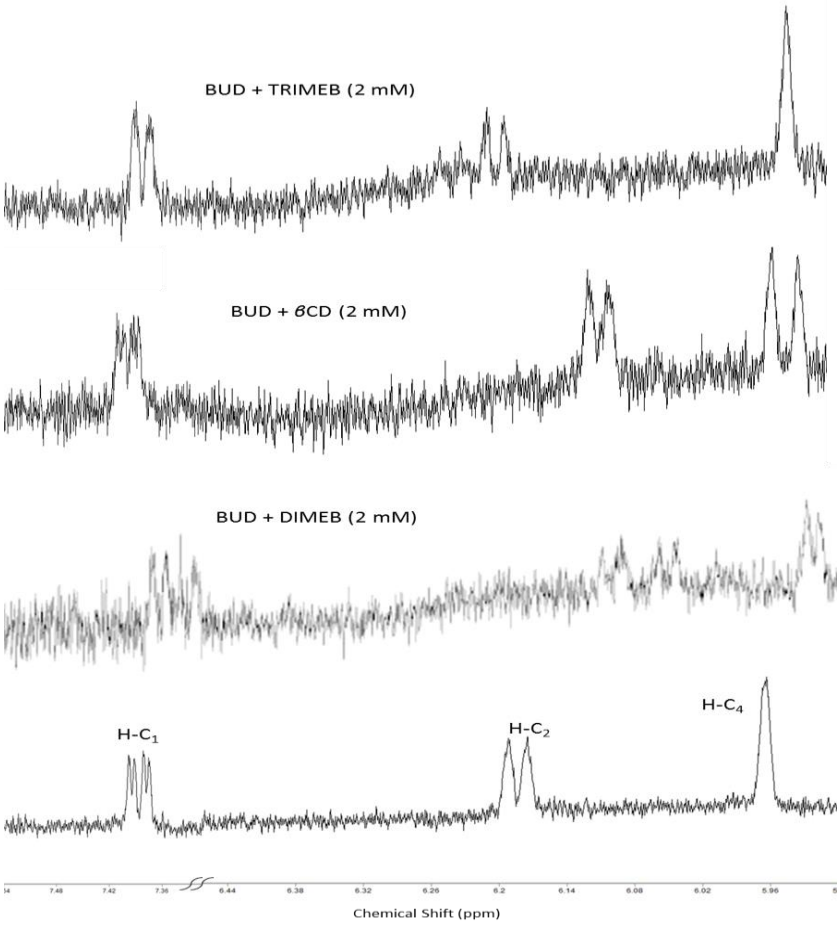

Figure 4.46: BUD chemical shift differences in the low field region complexed with 2 mM *β*CD, DIMEB and TRIMEB.

Veiga *et al*. studied the complexation between tolbutamide and *β*CD which they found a pronounced shift difference for the aromatic protons. They suggested that the positive sign for one proton was an indication for its closeness to oxygen atom in the CD cavity, while the negative sign for the another proton suggested that it is located at a large distance from the oxygen compared to the hydrogen atom.[200] Ribeiro *et al*. also studied the complexation between vinpocetine and *β*CD and sulfobutyl ether *β*CD. They found upfield shifts for the aromatic protons and suggested that this part is involved in the complexation with the CD.[201] Another study was carried out on chloramphenicol and DIMEB which showed both upfield and downfield shifts occurred for the phenyl moiety suggested that this part entered into the DIMEB cavity.[155] The results obtained were in agreement to those obtained by Larsen *et al*. who studied the complex formation between *β*CD and prednisolone (Figure 4.47, b) whose structure is related to budesonide (Figure 4.47, a). They found that the prednisolone forms a complex by entering into *β*CD cavity from the wider rim with the quinone ring being considered the main site responsible for the complex formation through accessing deeply into the cavity.[202] Also, another study conducted by Uekama *et al*. showed that the quinone ring of the hydrocortisone (Figure 4.47, c) was able to enter further into the *β*CD and *γ*CD cavities and thus it was responsible for the complex formation.[203]

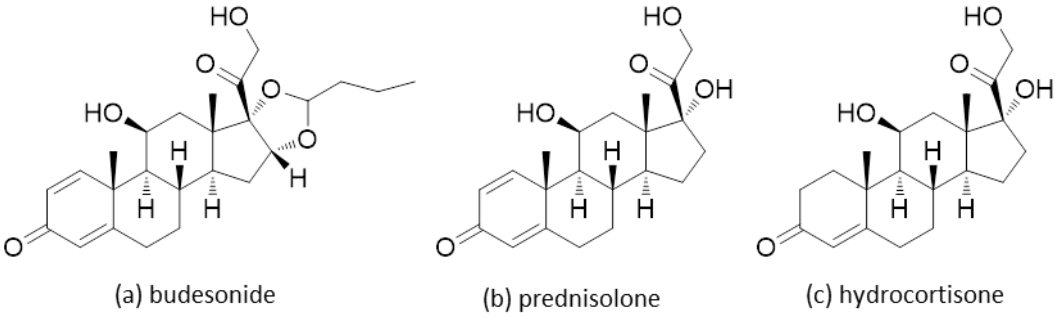

Figure 4.47: Chemical structure of (a) budesonide, (b) prednisolone and (c) hydrocortisone

It has been reported that the intramolecular bonds between the secondary hydroxyl groups of the C2 and C3 of *β*CD at the wider rim are responsible for its rigid structure.[105] The methylation of the OH group of *β*CD at C2 and C6 leads to the improvement of the complexation efficiency of DIMEB.[204] Green and Guillory found strong complexation occurred between chlorambucil and DIMEB compared to that obtained with *β*CD, indicating that the main driving

force for the complexation was not related to the formation of the hydrogen bonds between chlorambucil and DIMEB as fewer free hydroxyl groups (compared to *β*CD) are available to form new hydrogen bonds. They suggested that the methylation of the hydroxyl groups led to the expanding of the DIMEB cavity which enhanced the guest binding by hydrophobic interaction.[205] On the other hand, in the case of TRIMEB, the secondary hydroxyl groups of C2 and C3 are replaced by methyl groups making them unable to form hydrogen bonds. This resulted in the enlargement of the surface area inside the cavity as well as increasing its height by 2 Å, which in turn makes it suitable for accommodation of a large molecule. The DIMEB showed a stronger complex compared to TRIMEB, which might be due to the rounded shape of DIMEB resulting from the formation of the intramolecular hydrogen bonds between C2 and C3, which affords more space in the cavity for the guest to enter deeply compared to that of the TRIMEB.[206] Also, it has been shown that the methylation of the primary OH groups leads to the improvement in the binding constant whereas the secondary OH group methylation decreases the binding. On the other hand, substitution at the primary position does not decrease the rigidity of the cavity and this the reason behind increasing of the binding constant when the substitution happens at the primary position.[207] The substitution of the secondary OH groups (at C2 and C3) by methyl groups results in TRIMEB unable to form hydrogen bonds which resulted in the flexibility and loss of the conformational stabilisation of the cavity that leads to a weak complex formation. The methylation of one secondary OH group at C2 in DIMEB and the presence of a free OH group at C3 gives rigidity to the DIMEB by forming intramolecular hydrogen bonds, which can form a stronger complex with the guest compared to TRIMEB. However, the substituted methyl groups cause a steric hindrance in the cavity which lead to weaker complex.[208] Bardelang *et al*. found that the stability constant of the complex between nitroxide derivative compound and DIMEB is 150 times greater than that with TRIMEB, they explained that the free hydroxyl group at C3 in the DIMEB led to the easy access to its cavity by the guest compared to TRIMEB.[209]

The K values obtained for BUD with CDs can be ordered as following DIMEB > *β*CD > TRIMEB where the values were 4446, 1129, and 429 M^{-1} respectively, which supported the NMR results, where larger chemical shift differences were

observed with both DIMEB and *β*CD compared to TRIMEB. These results were consistent to those obtained by Iijima and Karube who investigated the interaction of the acid azo dyes with *β*CD, DIMEB and TRIMEB by UV spectroscopy. They found the K values at 25°C were 1000, 4350 and 600 M^{-1} and at 35°C were 740, 3980 and 450 M^{-1} for *β*CD, DIMEB and TRIMEB respectively i.e DIMEB > *β*CD > TRIMEB. They assumed that the binding constant was increased with dimethyl derivatised CD compared to the parent CD due to hydrophobic interaction. By contrast, the additional substitution of the methyl group (TRIMEB) decreases the binding constant due to steric hindrance of the dye molecule (guest).[210] Another study performed by Letort *et al*. showed that the parent *β*CD had less hydrolysis inhibition effect on fenitrothion (organophosphorus pesticide) compared to the methylated *β*CDs (TRIMEB and DIMEB). The methyl groups can cause the extension of the cavity size of TRIMEB and DIMEB which in turn allows fenitrothion to enter deeply into the cavity. In addition, the phosphate moiety of the fenitrothion can be protected from external nucleophilic attack by the methyl groups of the methylated *β*CDs which prevented the entry of hydroxide ions.[211] The results performed by Uekama *et al*. on hydrocortisone showed that it forms a more loosely held complex with *γ*CD compared to *β*CD,[203] this is due to the structure of both CDs, where the *γ*CD has a cavity volume of 427 Å with an external and internal diameter of 17.5 and 7.5-8.3 Å respectively, compared to *β*CD with the cavity size of 262 Å and with an external and internal diameter 15.4 and 6-6.5 Å respectively.[212] Therefore, the hydrocortisone forms a strong complex with *β*CD compared to a weaker complex with *γ*CD with a larger cavity. Also, another study performed on prednisolone found a higher association constant with *β*CD compared to *γ*CD whereas 6*α*-methyl prednisolone forms a higher association constant with *γ*CD compared to *β*CD. It was suggested that the bulky molecule of 6*α*-methyl prednisolone with the addition of methyl group required a large cavity to form complex and *γ*CD is more favourable for the complexation than *β*CD (methyl group prevents it from penetrating further inside the cavity). On the other hand, prednisolone alone prefers *β*CD to form a strong complex than *γ*CD since the *β*CD cavity is suitable in size to form an inclusion complex with prednisolone compared to the larger cavity size of *γ*CD.[203] Accordingly, the enlargement of the CD cavity is not always associated with strong complexation and the two mentioned examples support this statement, where the 6*α*-methyl

prednisolone with the bulky structure prefers the larger cavity of γCD whereas prednisolone prefers βCD with smaller cavity for the complex formation.[202]

In this study, the chemical shift differences of the complexed BUD protons with the three types of CDs (βCD, DIMEB and TRIMEB), was related to the change in the microenvironment of the BUD protons in the presence of CDs. All of the three CD types caused chemical shift changes for the quinone ring protons and H-C_{19} which confirmed the entrance of the BUD to their cavities with the quinone ring part. By contrast, the chemical shift change of H-C_{18} of BUD was observed with both βCD and DIMEB but not TRIMEB, indicating the deeper entrance of BUD into βCD and DIMEB cavities compared to TRIMEB. The upfield shifts of the quinone ring protons of BUD (H-C_1, H-C_2 and H-C_4) with βCD and DIMEB, with the exception of H-C_1 proton with βCD could be ascribed to the conformational changes resulting from the complexation and from the shielding effect of the CD hydrophobic cavity. This effect was induced by the oxygen atoms located on the inner surface of the CD cavity and thus could suggest that these protons were located closer to the oxygen atom in the CD cavity.[155,201,213] This indicated that this part of BUD (quinone ring) was involved in the complexation with the βCD and DIMEB by entering into their cavities. By contrast, Both H-C_{18} and H-C_{19} protons of BUD with both types of CDs (βCD and DIMEB) and H-C_1 proton with βCD were observed with downfield shift, and different explanations had been given to clarify this shift difference. One of the reasons behind this change was the structure rearrangement and conformational changes of guest (BUD) molecule after the complexation.[200] Also, it could be related to the change in the local polarity[214] or a deshielding effect resulting from van der Waals interaction with the carbohydrate chains.[213] Another explanation was owing to the interaction of theses protons (H-C_{18} and H-C_{19}) with the hydrophilic external part of the βCD and DIMED.[201] Alternatively, it could be suggested that these protons were located at large distance from the oxygen compared to the hydrogen atom.

According to these views, it could be suggested that H-C_{18} and H-C_{19} protons interacted with the outside surface of βCD and DIMED, but near their wider rim in which they were situated, far from the oxygen atom located inside the CDs cavities. The extent of the chemical shift difference was largely observed with H-C_{19} than H-C_{18} suggested the closer of the former proton to the wider rim of

the both CDs cavities whereas the later was situated away from the rim but still be affected by the CD environment. The downfield shift of H-C_1 proton with *β*CD suggested the presence of this proton near the cavity rim compared to DIMEB, where this proton was observed with upfield shift that in turn indicated its entrance into the DIMEB cavity. This explained the high K value of DIMEB compared with *β*CD as BUD was more deeply entered into the DIMEB cavity.

The complexation with TRIMEB showed an upfield shift for only H-C_4 of the quinone ring whereas a small downfield shift of the H-C_2 proton. Also, the H-C_{19} proton was observed with a small downfield shift and no change was noted for H-C_{18} proton. This suggested that the quinone ring entered the TRIMEB cavity partially where the H-C_4 proton was situated at a distance not closer to the oxygen atoms inside the cavity. This explained the small shift changes for this proton compared to the complexation with *β*CD and DIMED where the H-C_4 proton was located closer to the oxygen atom inside the CD cavity and hence a larger shift change was observed. The other protons with downfield shifts (H-C_2 and H-C_{19}) were located outside the cavity and the shift differences could be attributed to their interaction with the hydrophilic external part of the TRIMEB. However, no shift was observed for H-C_{18} suggesting that this proton was far from the TRIMEB cavity.

To summarise, BUD interacted with DIMEB, where the quinone ring totally entered into its cavity whereas it partially entered into the *β*CD cavity (H-C_1 of BUD observed with downfield shift), leaving both H-C_{19} and H-C_{18} (with downfield shift) outside with the former located near the wider rim whereas the later was situated a large distance from both CDs cavities. Concerning the complexation with TRIMEB, BUD was situated in a position where only H-C_4 proton of the quinone ring (experienced upfield shift) entered the TRIMEB cavity leaving the other H-C_1 and H-C_2 protons of the quinone ring altogether with H-C_{19} proton (with downfield shift) outside the cavity. The chemical shift difference of H-C_2 proton was larger due to its closeness to the methoxyl oxygen atoms of TRIMEB (at C2 and C3) compared to the H-C_{19} proton. As the quinone ring partially entered the cavity, therefore, the BUD molecule would be situated outside the cavity and hence the H-C_{18} was located at a larger distance from the cavity compared to the same proton in the complexation with *β*CD and DIMED. The cavity dimensions of *β*CD and DIMED are suitable for BUD to enter deeply

compared to a larger cavity of TRIMEB. In addition, intramolecular hydrogen bonds are responsible for giving a rigid structure for βCD and DIMEB cavities that formed a higher binding constant and a firm complex compared to the flexible TRIMEB cavity.

One can conclude that, the extent of the chemical shift difference was dependent on the strength of the interaction between the quinone protons and the CD cavity. The closer distance between the CD and the guest (BUD), a stronger host-guest complex formed and hence a larger chemical shift differences was observed. Consequently, the BUD fitted the cavity size of DIMEB and βCD and therefore, their cavities are suitable to accommodate the BUD molecule compared to the TRIMEB cavity. The relatively higher K values for complexation of BUD with DIMEB and βCD indicated a more stable host-guest complex formation by the presence of a better geometric fitting compared to TRIMEB. The highest stability was obtained with DIMEB, indicating that it has the most suitable size to fit and accommodate the BUD into its cavity. This has led us to propose the host-guest model for BUD in each of the three CDs shown in Figure 4.48.

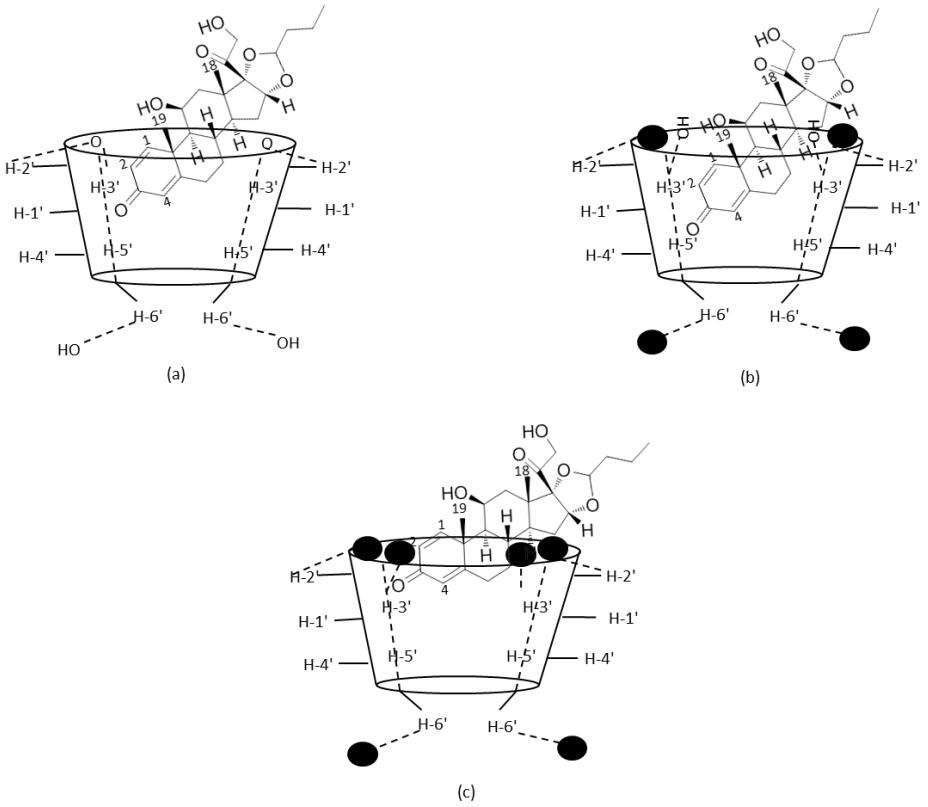

Figure 4.48: Inclusion complex of the budesonide and (a) *β*CD, (b) DIMEB and (c) TRIMEB. The black balls represent the methoxyl groups in the DIMEB and TRIMEB molecules.

The K values obtained from the NMR method for the complex formed were considerably higher compared to those obtained from the UV method for both *β*CD and TRIMEB. This was in agreement to the study conducted by Lee *et al*. which found higher K value from NMR at 295 M^{-1} compared to that obtained from UV studies at 125 M^{-1} for 6-Hydroxyquinoline in DIMEB. This difference was owing to the difference in the principle of both techniques used.[174] Also, another study conducted by Mic *et al*. to study the complex formation between benzocaine and *β*CD by NMR which found the K value (1227.7 M^{-1}) was higher[215] compared to other spectroscopic methods which the K value was equal to 549 M^{-1}.[216]

However, in this study conflicting results were obtained where the K value obtained with *β*CD was higher compared to the TRIMEB (1129 and 429 M^{-1}) from NMR whereas a lower value for *β*CD versus TRIMEB (94 and 205 M^{-1}) from the UV method. It is well known that the UV method is considered sensitive and works well for compounds with reasonable solubility levels. However, the UV results have some uncertainty as the absorbance values of the samples studied in this work were very low (around 0.1 AU). Determination

of subtle increases in absorbance is very difficult to perform with high degrees of accuracy and precision and leads to significant errors. This can be enhanced by the increasing the budesonide concentration, though this is limited by the insoluble character of BUD in water (23 µg/mL). Though NMR is inherently far less sensitive than UV, determining the chemical shift value of the resonances in question can be done accurately and precisely, even for signals with very poor S:N. Some studies of compounds that are structurally related to the budesonide supported our NMR findings, where the complex showing greatest association was *β*CD compared to TRIMEB. In addition, NMR is considered a more useful technique than spectroscopic approaches as the measured chemical shift change provides structural information on the host-guest complex allows us to propose structural models of their interaction in addition to providing the means to calculate the association constants. This information is very difficult to extract from spectroscopic titrations.[151] In this study, it is clearly shown that the shifts observed with *β*CD were considerably higher compared to those of TRIMEB (Table 4.45).

Table 4.45: The chemical shift difference of budesonide peaks without and with the addition of *β*CD and TRIMEB

Proton position	Chemical shift, δ (ppm)				
	BUD (δ_{free})	BUD/*β*CD ($\delta_{complex}$)	Δδ	BUD/TRIMEB ($\delta_{complex}$)	Δδ
H-C_{19}	1.2570	1.3812	-0.1242	1.2952	-0.0382
H-C_4	5.9645	5.9347	0.0298	5.9456	0.0189
H-C_2	6.1744	6.1024	0.072	6.2310	-0.0566
H-C_2	6.1931	6.1192	0.0739	6.2481	-0.055

$\Delta\delta = \delta_{free} - \delta_{complex}$

In conclusion, data generated with solid state techniques (vibrational spectroscopy and solution based measurements using both UV and NMR have allowed us to determine stability constants and complexation models for the systems under study. NMR has the additional advantage of probing the structure of the complexes formed using the relative displacements of the assigned chemical shifts for both the host and guest molecules, and provides a powerful means to study the systems in isolation. Furthermore, it allows us to study complexes in solvents that are volatile in nature and have not been studied in this way before. The development of methods associated with these systems is the focus of Chapter 5.

5 Host:guest interactions in HFA solvents using NMR spectroscopy

The method developed for budesonide in D_2O (Chapter 4.2.4) was used to study the complexation of corticosteroids; (i) BUD, (ii) BDP, (iii) FLU and (iv) MOM and with cyclodextrins in fluorinated solvent. The volatility of the HFAs solvents makes the analysis challenging in terms of their manipulation during sample preparation and with the instrumentation. Therefore, methods were developed using HPFP as a model to the fluorinated solvent (HFA 134a and 227) based on the study performed by Rogueda that concludes both of HFA 134a and 227 propellants have similar properties to that of HPFP.[166] This assists the studies as HPFP is a volatile liquid compared to both HFA 134a and 227 which are gases at STP. The developed method can be applied to study the volatile propellants using pressurised NMR. When the prepared samples were analysed a large resonance from HPFP was observed in the form of a complex multiplet, resulting from the *J*-coupling observed between protons and fluorines in the molecule. This brings about a large dynamic range mismatch in the same way as the residual water resonance in the experiments performed in D_2O discussed previously (Section 4.2.4). Therefore, a presaturation method similar to that developed in the experiments performed on BUD in D_2O was applied with some modifications in terms of the position of the suppressed peak and the concentration of both the host and the guest. Before starting the study, the solubility of all CDs (*β*CD, TRIMEB and DIMEB) which were used to study the complex formation was determined in HPFP by NMR. The solubility of the TRIMEB and DIMEB were determined and found to be around 6 and 1 mg/mL respectively. However, the solubility of *β*CD in HPFP was below the limit of NMR detection (their peaks were not observed in the spectrum) and it was, therefore, not studied as a complexation agent in HPFP.

During the experimentation performed on BUD in HPFP, it was noted that some of the NMR resonances changed chemical shift positions and multiplicity when complexed with the derivatised CDs, whereas some remained unaffected. These changes were investigated further using a chirally pure form of BUD ((22-*R*)-budesonide) to make a true assignment (Section 5.2.1).

5.1 Assignment of corticosteroids in HPFP

Solutions of the four corticosteroids under investigation (BUD, BDP, MOM and FLU) were prepared at 75.3, 208, 20.8 and 20 µg/mL, equivalent to 0.175, 0.4, 0.04 and 0.04 mM respectively. These concentrations were chosen to be slightly lower than the previously determined solubility values for each in HPFP.[179] BUD was used as a model to study the complexation in HPFP based on the developed method used to study its complexation in D_2O (Chapter 4.2.4). The same co-axial NMR tube with the internal standard of $CHCl_3$ in CD_3CN (100 µg/mL) was used. NMR spectra of BUD in HPFP showed the multiplet of HPFP at 4.38 ppm with another intense peak related to the CH_3CN residual being observed at 2.15 ppm. In this system, two resonances required suppression to obtain the levels of sensitivity required for routine observation of the analyte signals. A dual suppression method was developed to suppress both peaks at 4.38 ppm (HPFP) and at 2.15 ppm simultaneously (CH_3CN residual) using separate attenuations of (30,40), (40,40), (50,40), (30,50), (40,50), (50,50), (60,50), (44,50), (46,50), (45,50). The most suitable combination to maximise the suppression, and hence the S:N of the analyte peaks, was 45 and 50 dB respectively. This method was used in concert with extended acquisition times (2048 scans). A representative spectrum of BUD in HPFP acquired using this approach is shown as Figure 5.1. This method was used to study the other corticosteroids complexation with TRIMEB and DIMEB in HPFP with the exception of BDP which was analysed with a reduced scan number (1024 scans) due to the increased solubility of BDP in HPFP relative to BUD (Section 2.2.4.4).

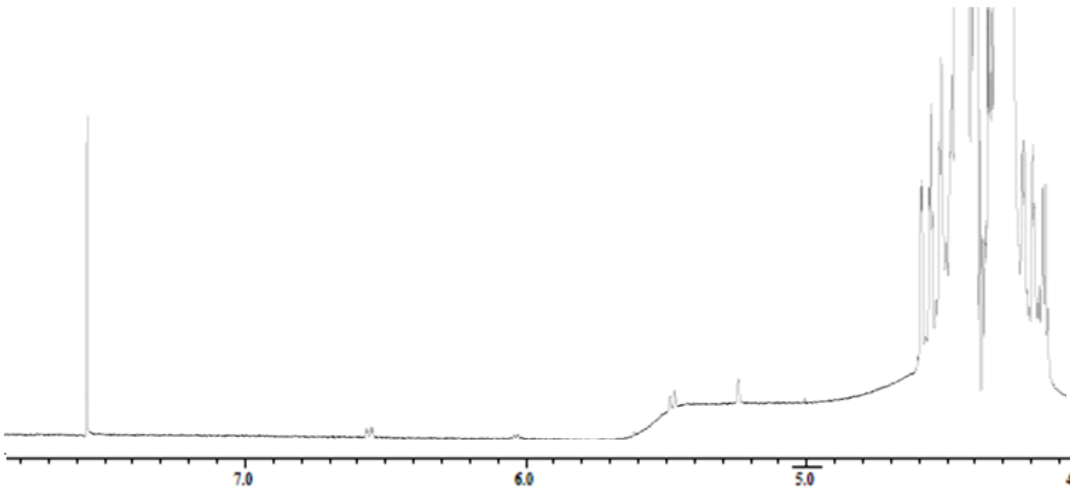

Figure 5.1: ^{1}H NMR spectra of BUD with solvent suppression at 4.38 and 2.15 ppm in HPFP.

The assignment of BUD, BDP, MOM and FLU in HPFP was made based on their assignment in $CDCl_3$,[180,217-219] as it was expected that only small shifts would occur for the peaks in two different solvents ($CDCl_3$ to HPFP). The peaks at 4-5 ppm were affected by the presaturation of HPFP at 4.38 ppm and were therefore difficult to assign. The other peak assignments are presented in Tables 5.1 and 5.2, and show a relatively consistent upfield shift in HPFP when compared to $CDCl_3$ (Figures 5.2 and 5.3).

Table 5.1: Chemical shift of BUD, BDP, MOM and FLU in HPFP compared to their chemical shift in $CDCl_3$

Carbon No.	δ BUD (ppm)		δ BDP (ppm)		δ MOM (ppm)		δ FLU (ppm)	
	$CDCl_3$	HPFP	$CDCl_3$	HPFP	$CDCl_3$	HPFP	$CDCl_3$	HPFP
1	7.23	6.55	7.18	6.51	7.19	6.47	7.15	6.42
2	6.27	5.47	6.34	5.52	6.37	5.53	6.46	5.56
4	6.01	5.24	6.09	5.29	6.13	5.32	6.40	5.64
16	–	–	1.34	0.64	0.99	0.27	1.07	0.32
17	–	–	1.16	0.48	–	–	–	–
18	0.98	0.33	0.99	0.36	1.15	0.48	1.16	0.44
19	1.44	0.80	1.65	1.02	1.68	1.02	1.55	0.85
21	–	–	1.16	0.48	–	–	–	–
25	0.91	0.26	–	–	–	–	–	–
F3	–	–	–	–	7.25	6.61	–	–
F4	–	–	–	–	6.54	5.79	–	–
F5	–	–	–	–	7.63	6.84	–	–

Table 5.2: Assignment of BUD, BDP, MOM and FLU in HPFP.

Carbon No.	Chemical shift (ppm)			
	BUD	BDP	MOM	FLU
1	6.55 (dd)	6.51(d)	6.47 (s)	6.42 (d)
2	5.47 (d)	5.52 (d)	5.53 (d)	5.56 (d)
4	5.24 (s)	5.29 (s)	5.32 (s)	5.64 (s)
Me-16	–	0.64 (d)	0.27 (d)	0.32 (d)
17 Me propionate	–	0.48 (dt)	/	/
Me-18	0.33 (s)	0.36 (s)	0.48 (s)	0.44 (t)
Me-19	0.80 (s)	1.02 (s)	1.02 (s)	0.85 (s)
21 Me propionate	–	0.48 (dt)	–	–
25	0.26 (t)	–	–	–
F3	–	–	6.61 (s)	–
F4	–	–	5.79 (s)	–
F5	–	–	6.84 (s)	–

Spectra are assigned referenced to $CHCl_3$ from the co-axial insert. Multiplicity given with the abbreviations: s (singlet), d (doublet), t (triplet), dd (doublet of triplets), dd (doublet of doublets).

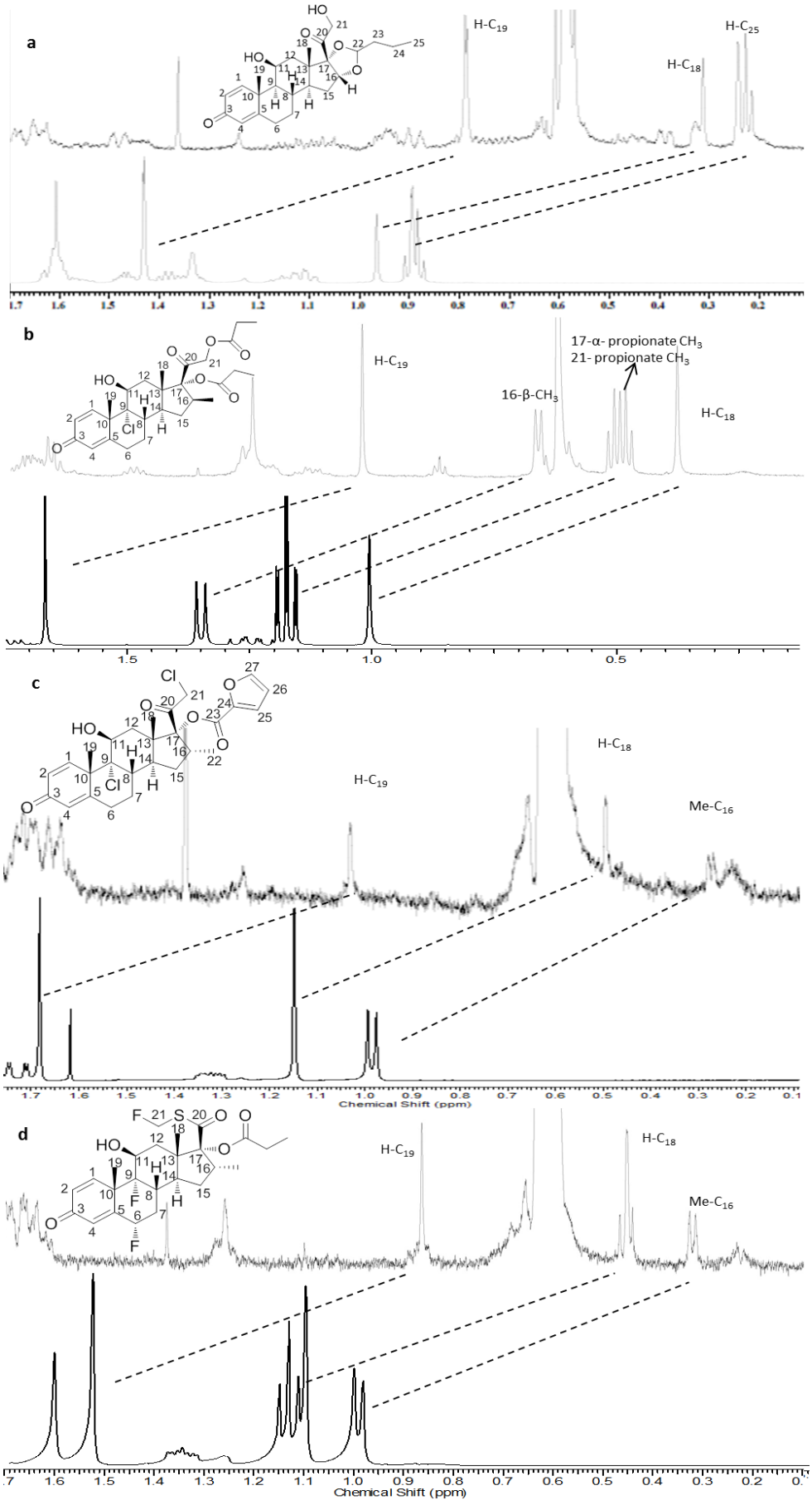

Figure 5.2: Chemical shift of (a) BUD, (b) BDP, (c) MOM and (d) FLU in $CDCl_3$ (lower) and HPFP (upper) in high field region showing an upfield chemical shift in HPFP compared to $CDCl_3$.

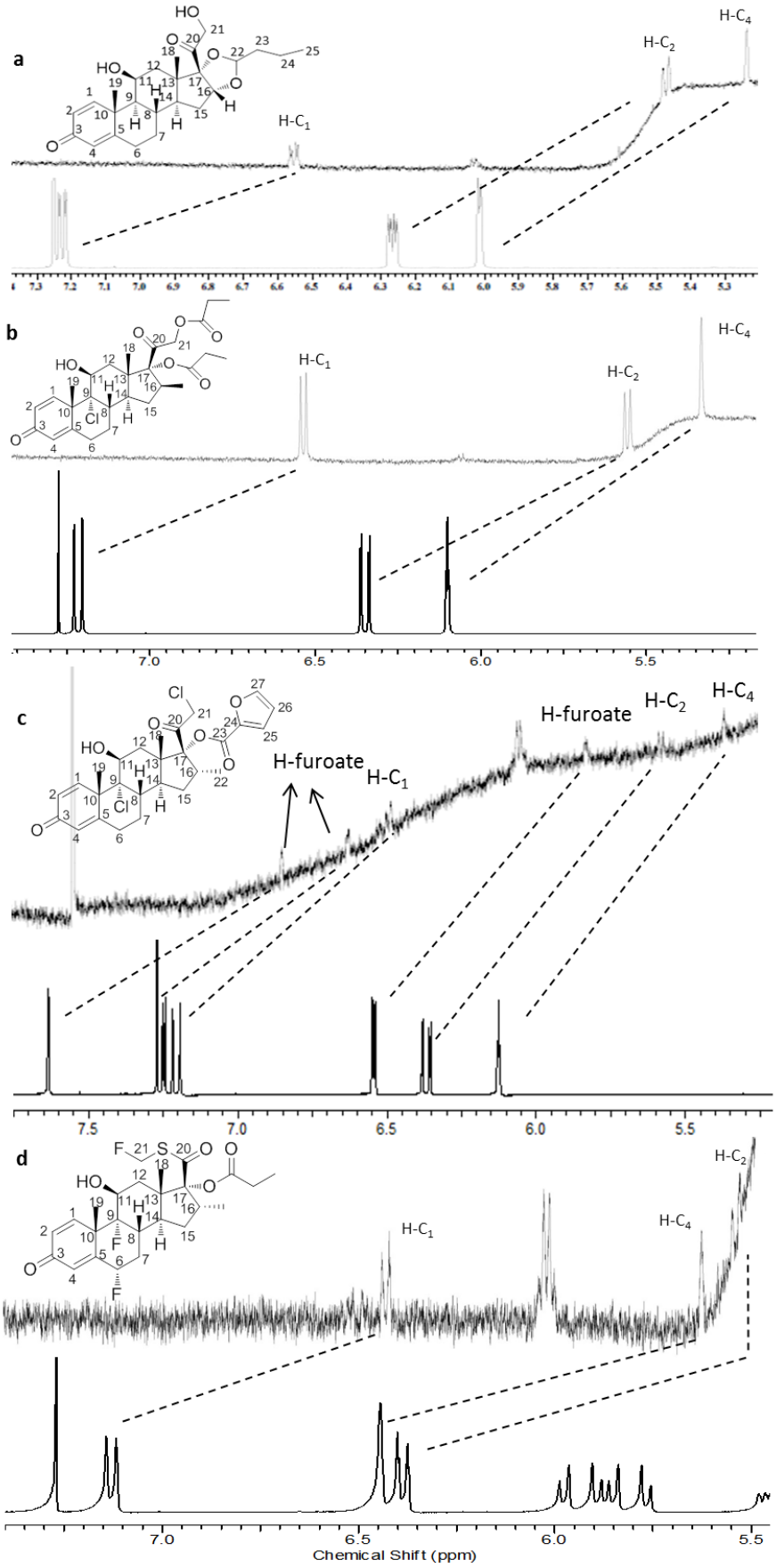

Figure 5.3: Chemical shift of (a) BUD, (b) BDP, (c) MOM and (d) FLU in $CDCl_3$ (lower) and HPFP (upper) in low field region showing an upfield chemical shift in HPFP compared to $CDCl_3$.

The stability constant was determined by recording the chemical shift values of each of the corticosteroids peaks (referenced to $CHCl_3$ from the co-axial insert) for all five different solutions prepared with increasing CD concentrations (Section 2.2.4.4) and calculating their displacement relative to compound peaks from a pure solution without CD addition.

5.2 Complexation study of BUD and TRIMEB

The complexation of BUD and TRIMEB was investigated in HPFP and the results showed very minor shifts occurred for H-C_{18} and H-C_{19} peaks at 0.3354 and 0.7992 ppm chemical shift respectively. The H-C_{25} peak did not shift, though its multiplicity changed as the TRIMEB concentration was increased. An additional peak appeared at 0.2889 ppm chemical shift in the spectrum of the complexed BUD which was then shifted downfield with the increasing TRIMEB concentration until it merged with the H-C_{18} at around 0.34 ppm at higher TRIMEB concentration (at 0.4 and 0.5 mM). The spectra of the complexed BUD in the high field region are shown in Figure 5.4.

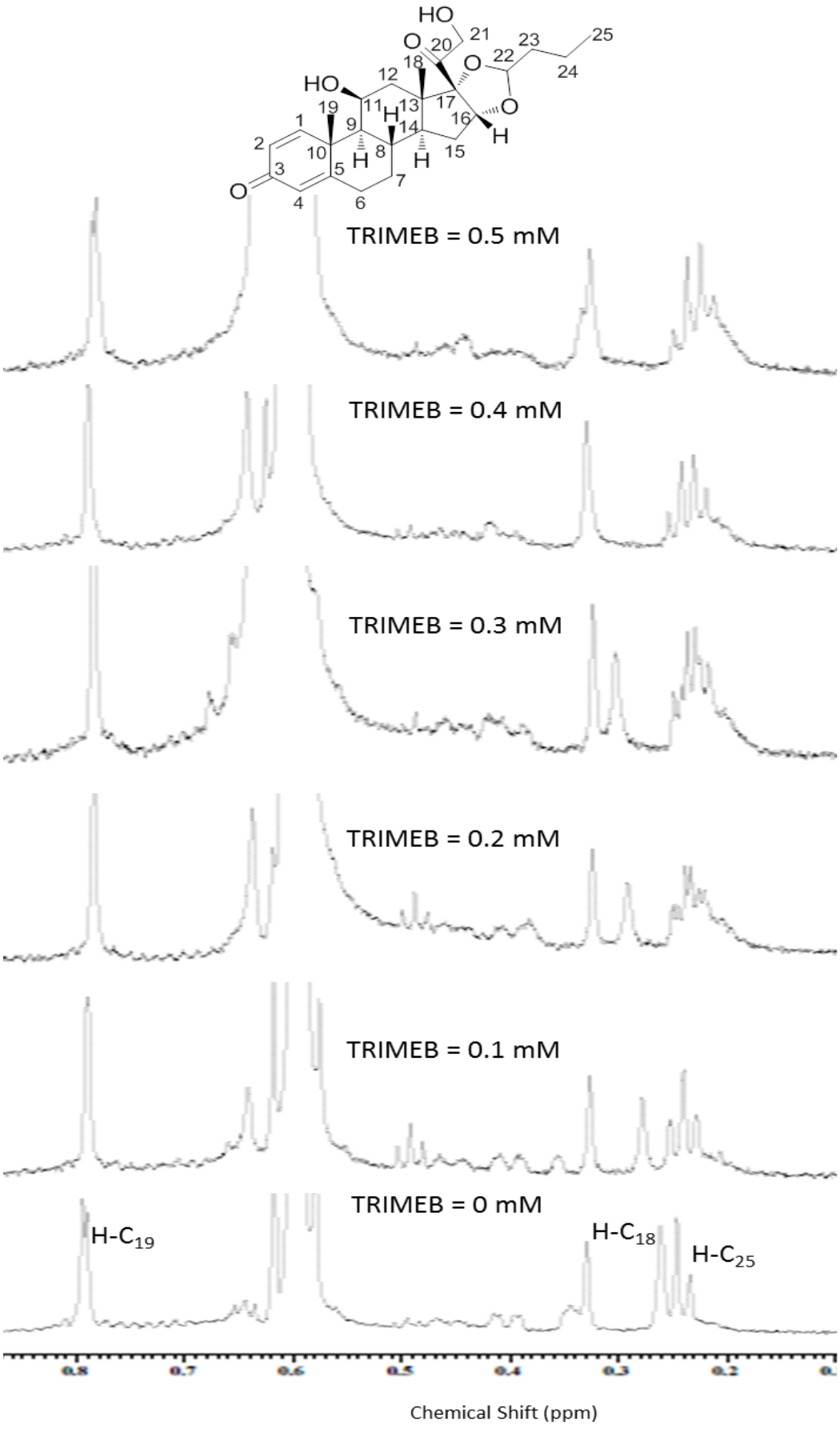

Figure 5.4: Budesonide (0.0875 mM) chemical shift in high field region (0.1-0.9 ppm) with the addition of TRIMEB at 0, 0.1, 0.2, 0.3, 0.4 and 0.5 mM in HPFP.

In addition, a downfield shift was observed for the H-C_1 proton of the quinone ring, and a distinct multiplicity change was noted (*J*-coupling constants increase with increasing CD concentration). A very small upfield shift occurred for H-C_4, and no observable shift was noted for the H-C_2 of the quinone ring (Figure 5.5).

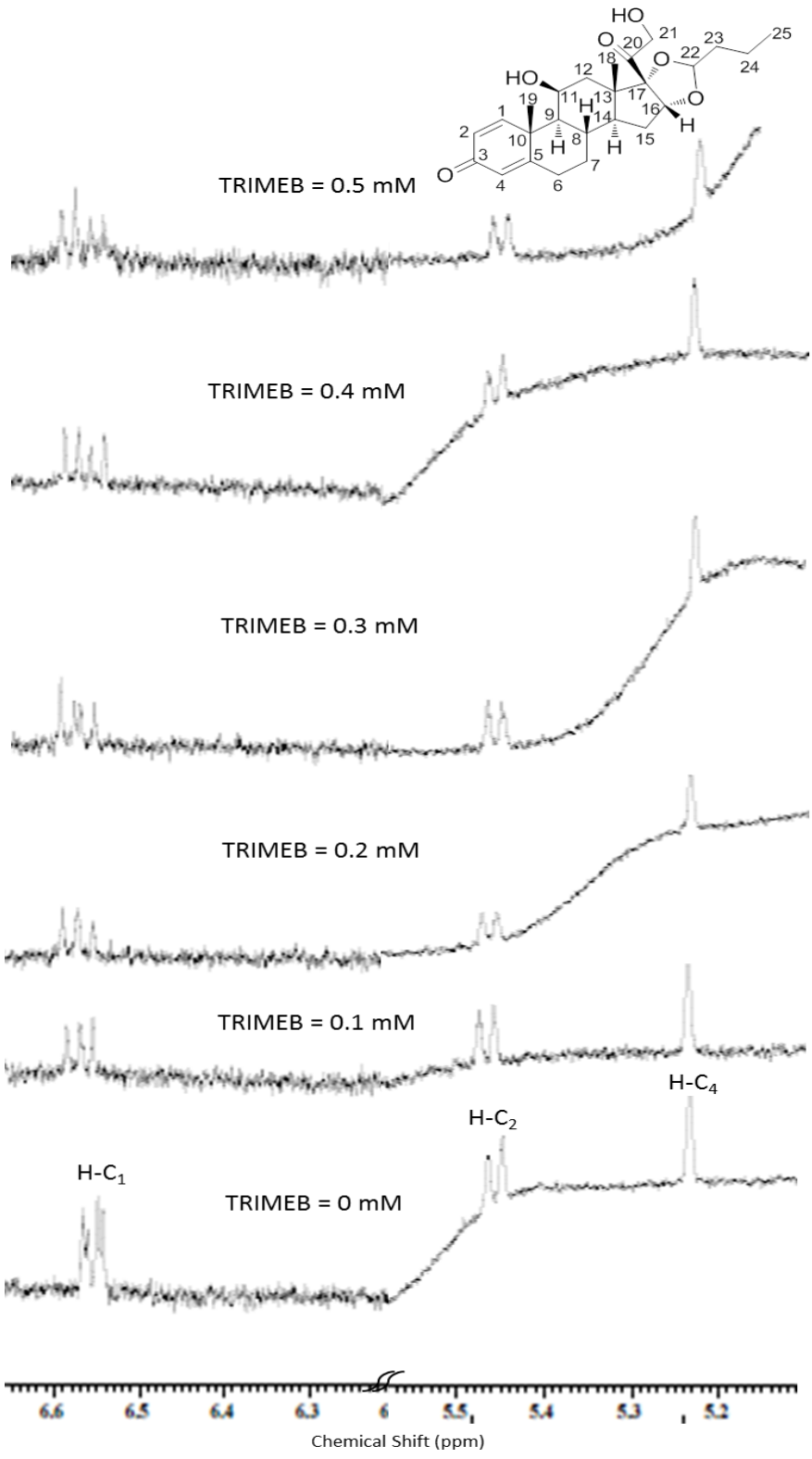

Figure 5.5: Budesonide (0.0875 mM) chemical shift in low field region (5.1-6.7 ppm) with the addition of TRIMEB at 0, 0.1, 0.2, 0.3, 0.4 and 0.5 mM in HPFP.

These results demonstrate that some protons display only small shifts with 1 mM TRIMEB concentration. A second series of experiments was performed with a more concentrated solution of TRIMEB (4 mM) in order to enhance the chemical shift displacements observed. It has been noted that the resonance at 0.34 ppm chemical shift appears as a singlet at 0.4 mM TRIMEB concentration, which is consistent with that obtained in the last experiment where one peak appeared at around 0.34 ppm chemical shift (at 0.4 and 0.5 mM of TRIMEB). The peak was split into two peaks; one showing no significant shift with increasing CD concentration, the second moving significantly to 0.44 ppm at 2 mM TRIMEB concentration. The first one (0.34 ppm chemical shift) could be assigned to the H-C_{18} peak of the *S*-enantiomer of BUD whereas the latter could be related to the H-C_{18} peak of *R*-enantiomer of BUD. Other peaks in the high field region such as H-C_{25} and H-C_{19} showed no shift, however, the peak shape changed where H-C_{25} was split into many peaks whereas the H-C_{19} resonance that showed a partial split initially was fully split into two distinctive peaks at 2 mM TRIMEB concentration (Figure 5.6).

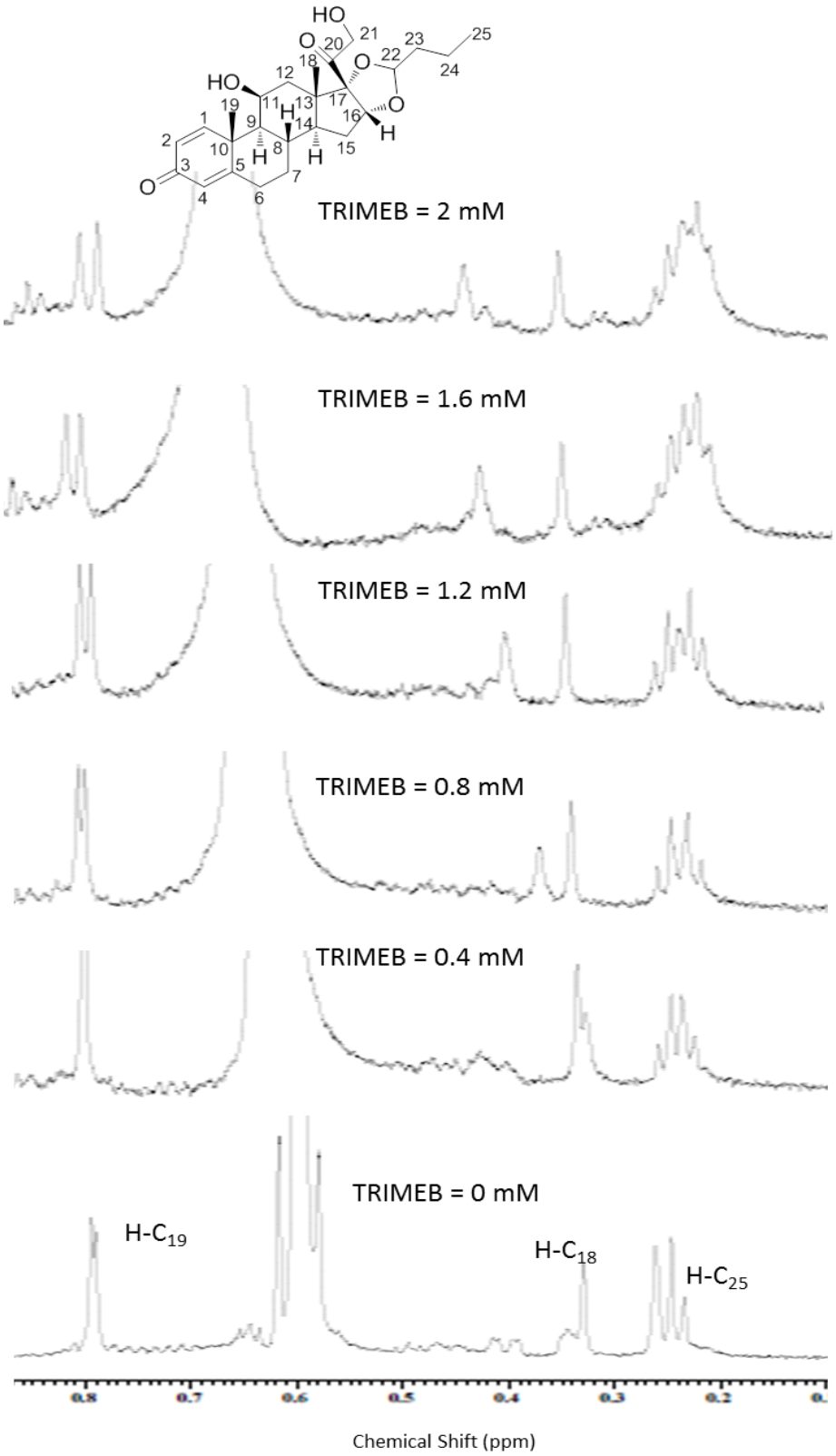

Figure 5.6: Budesonide (0.0875 mM) chemical shift in high field region (0.1-0.9 ppm) with the addition of TRIMEB at 0, 0.4, 0.8, 1.2, 1.6 and 2 mM in HPFP.

In the low field region, a significant downfield shift occurred for the H-C_1 proton of the quinone ring and the peak was split into four peaks as the concentration of TRIMEB was increased. A slight upfield shift for the H-C_4 proton with partial

splitting into two peaks at higher TRIMEB concentration (1.6 and 2 mM) was observed, with no significant shift for the H-C_2 proton of the quinone ring. The spectra of the complexed BUD in the low field region are shown in (Figure 5.7).

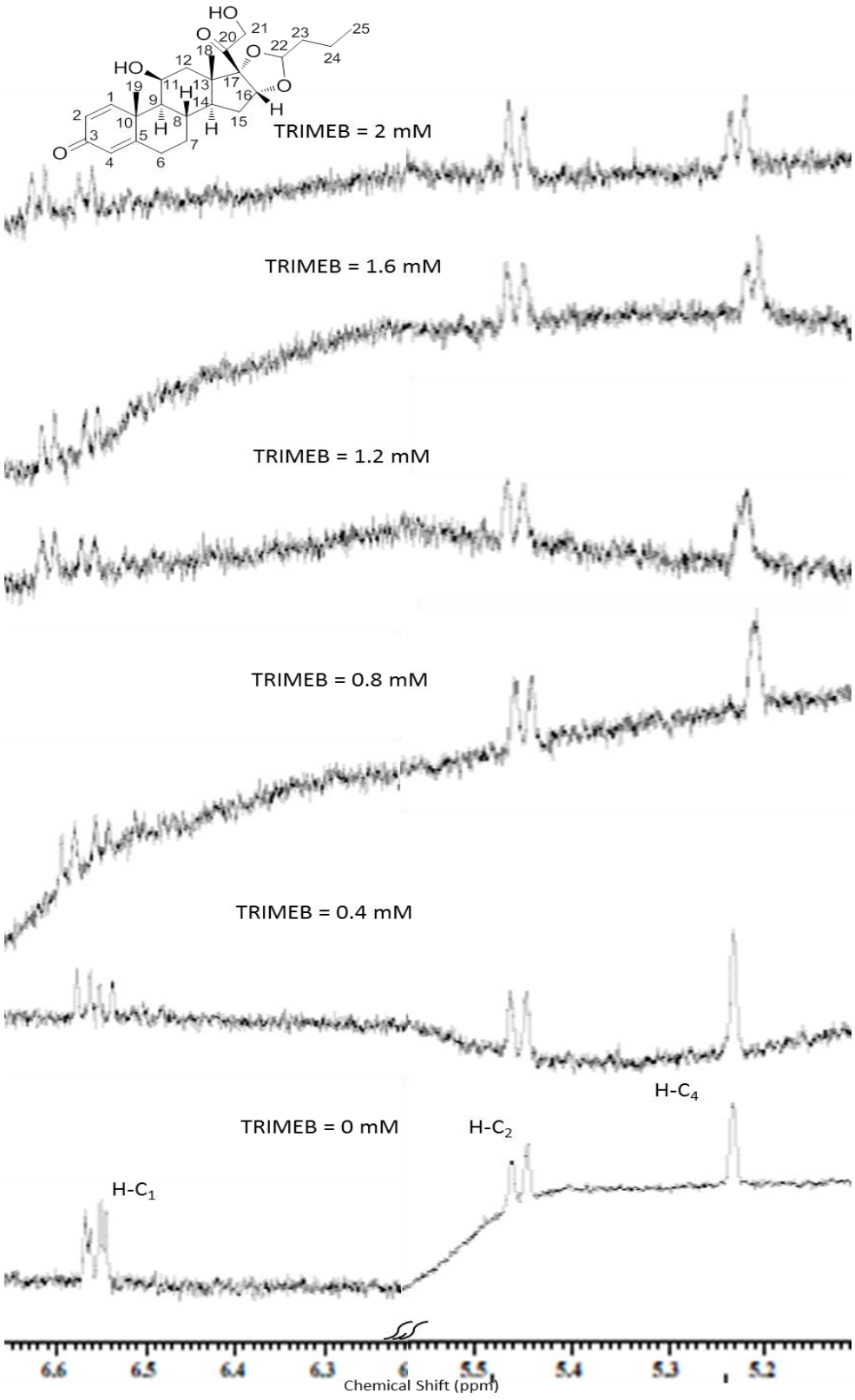

Figure 5.7: Budesonide (0.0875 mM) chemical shift in low field region (5.1-6.7 ppm) with the addition of TRIMEB at 0, 0.4, 0.8, 1.2, 1.6 and 2 mM in HPFP.

5.2.1 (22-*R*)-budesonide (pure enantiomer) with TRIMEB

The experiments performed to study the complexation between BUD and TRIMEB (4 mM) in HPFP (Section 5.2) showed two peaks appearing at *ca.* 0.34 and 0.44 ppm chemical shift that displayed a significant displacement on addition of TRIMEB. The same experiment as preformed on racemic BUD was repeated with a sample of pure *R*-enantiomer of BUD (Section 2.3.5) in order to unequivocally assign the two displaced peaks of H-C_{18} proton to the *R*- and *S*-enantiomers of BUD. It has been shown that the peak at 0.34 ppm (annotated with a star in Figure 5.8) appears as a singlet at 0.4 mM TRIMEB concentration and is shifting significantly to 0.44 ppm at 2 mM TRIMEB concentration. The peak at 0.3354 ppm of the H-C_{18} peak of the *S*-enantiomer of BUD was not observed in the spectrum of pure *R*-enantiomer. This was consistent with data obtained in the previous experiment of the racemic BUD (Section 5.2) where the singlet peak in the pure *R*-enantiomer spectrum matched the moving peak at 0.44 ppm at 2 mM (annotated with star in Figure 5.9) in the racemic BUD confirming the assignment of the H-C_{18} peak to the *R*-enantiomer of BUD. The peak displaying no shift at 0.34 ppm (annotated with a dot in Figure 5.9) in the spectrum of racemic BUD is now assigned to the H-C_{18} peak of the *S*-enantiomer of BUD.

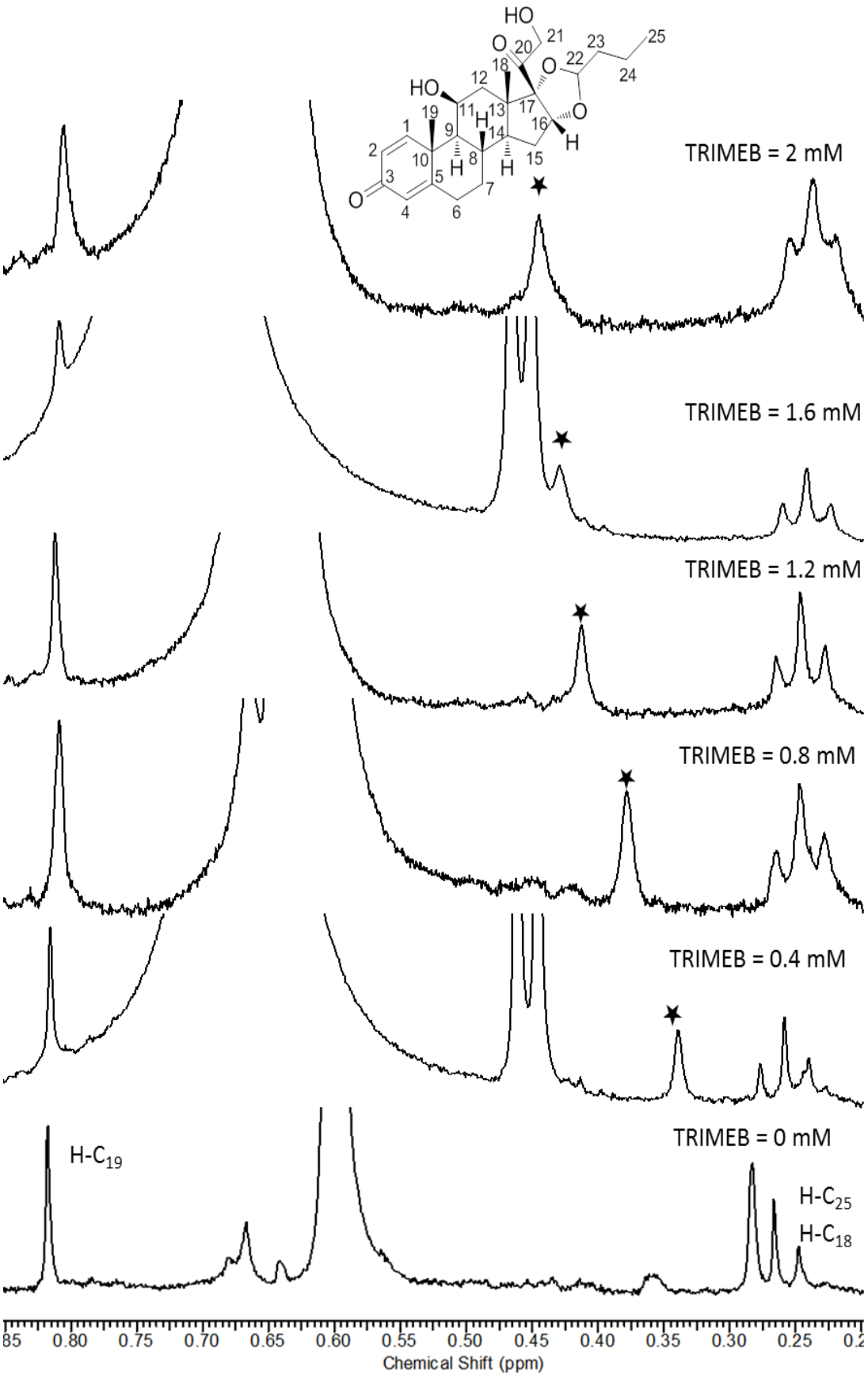

Figure 5.8: pure *R*-enantiomer of BUD (0.0875 mM) chemical shift in high field region (0.2-0.85 ppm) with the addition of TRIMEB at 0, 0.4, 0.8, 1.2, 1.6 and 2 mM in HPFP. The shifted peak annotated with star was assigned to *R*-enantiomer of BUD.

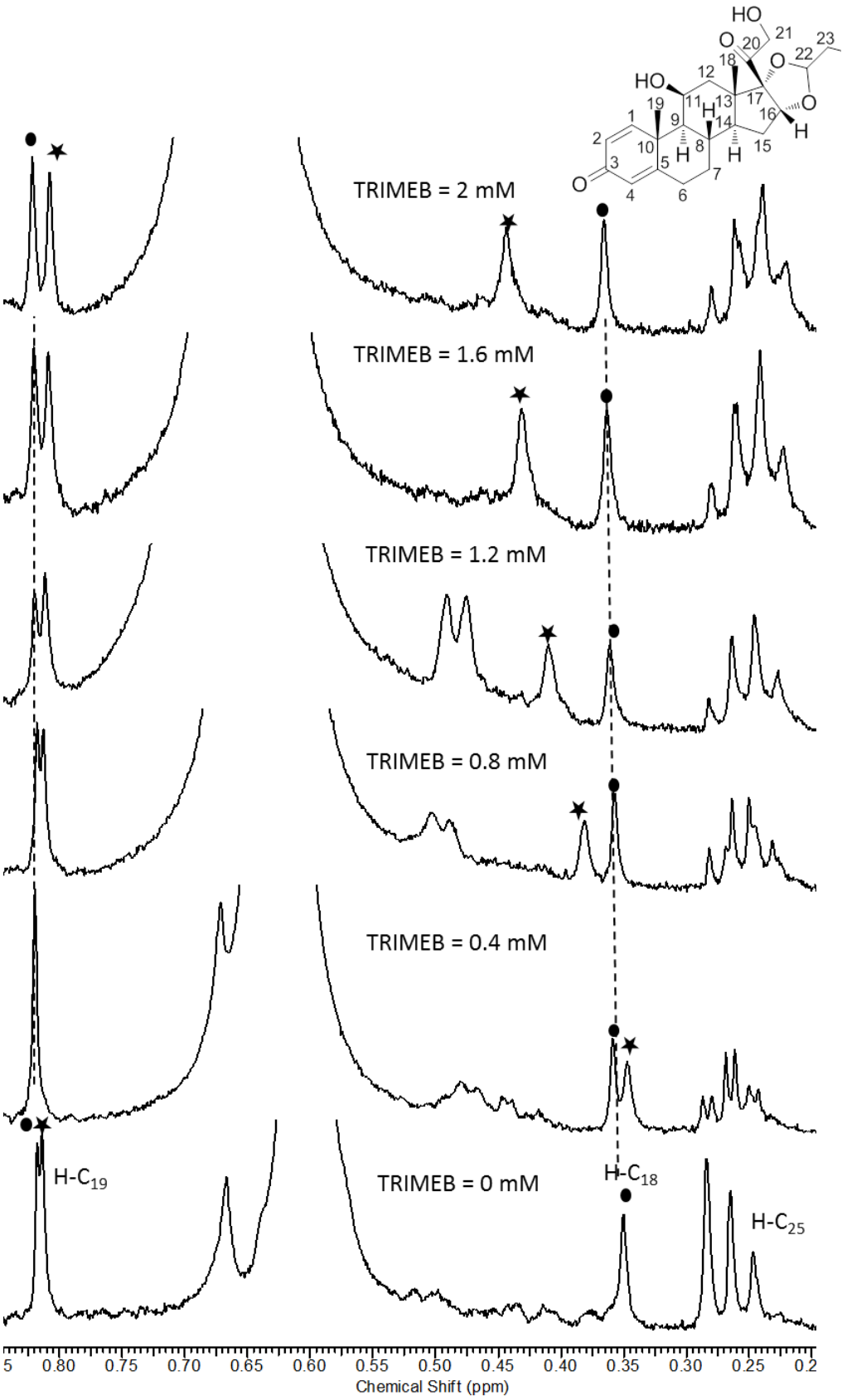

Figure 5.9: Racemic BUD (0.0875 mM) chemical shift in high field region (0.2-0.85 ppm) with the addition of TRIMEB at 0, 0.4, 0.8, 1.2, 1.6 and 2 mM in HPFP. The shifted peak annotated with star was assigned to *R*-enantiomer of BUD whereas the peak at 0.34 ppm (annotated with dot) was assigned to *S*-enantiomer of BUD

In the low field region, there was no shift observed for H-C_2 of the *R*-enantiomer whereas a small downfield shift was observed for H-C_1 at 6.5491 and 6.5666 ppm (Figure 5.10). The H-C_4 proton however showed a small upfield shift at the higher TRIMEB concentration (2 mM). The racemic BUD results showed a very small upfield shift for H-C_4 proton, and no observable shift was noted for the H-C_2 of the quinone ring. A downfield shift was observed for the H-C_1 proton of the quinone ring, and a distinct multiplicity change was noted (*J*-coupling constants increase with increasing CD concentration). Therefore, the two peaks at 6.5491 and 6.5666 ppm were related to the *R*-enantiomer of BUD whereas the other two peaks at 6.5431 and 6.5600 ppm were related to the *S*-enantiomer of BUD (Figure 5.11).

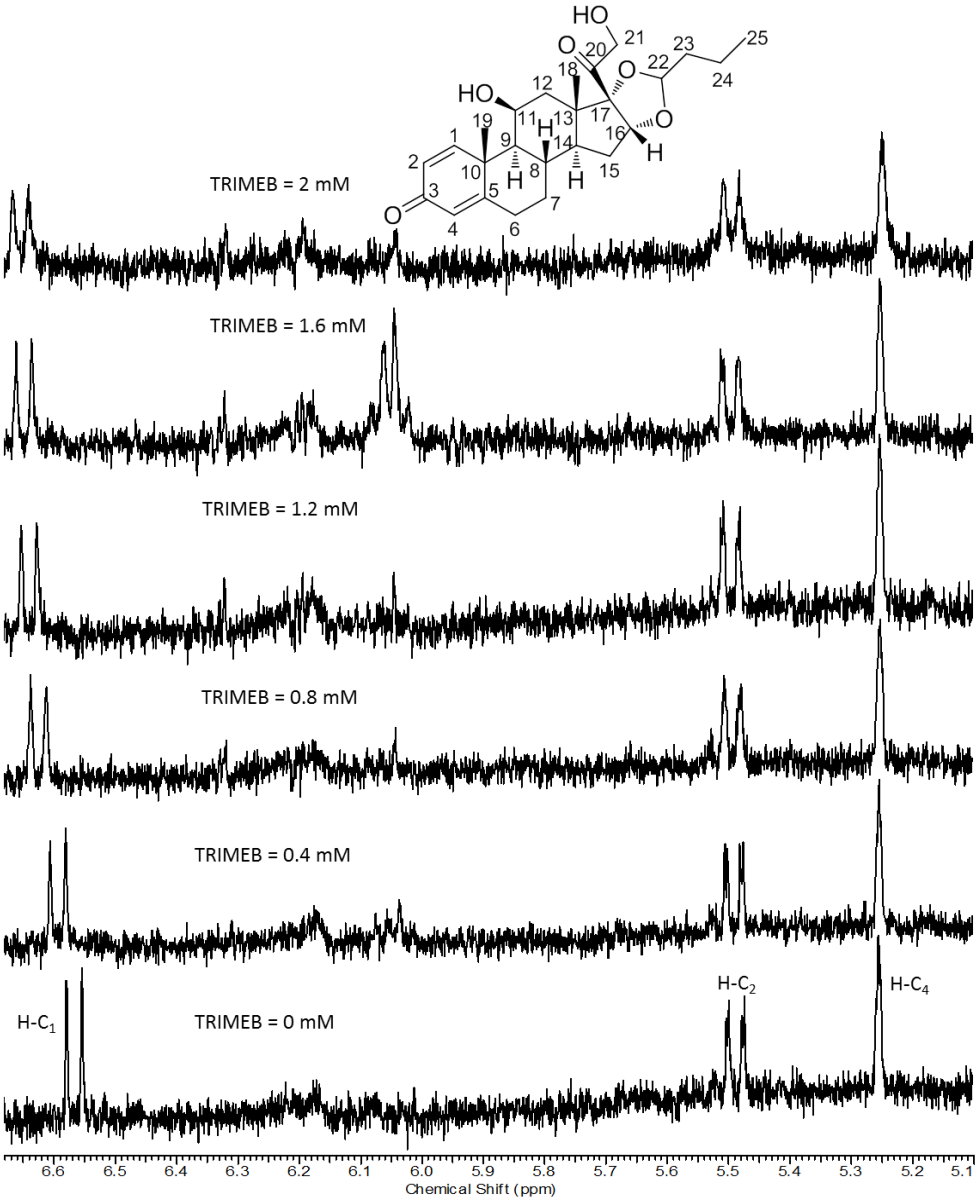

Figure 5.10: Pure *R*-enantiomer of BUD (0.0875 mM) chemical shift in low field region (5.1-6.7 ppm) with the addition of TRIMEB at 0, 0.4, 0.8, 1.2, 1.6 and 2 mM in HPFP.

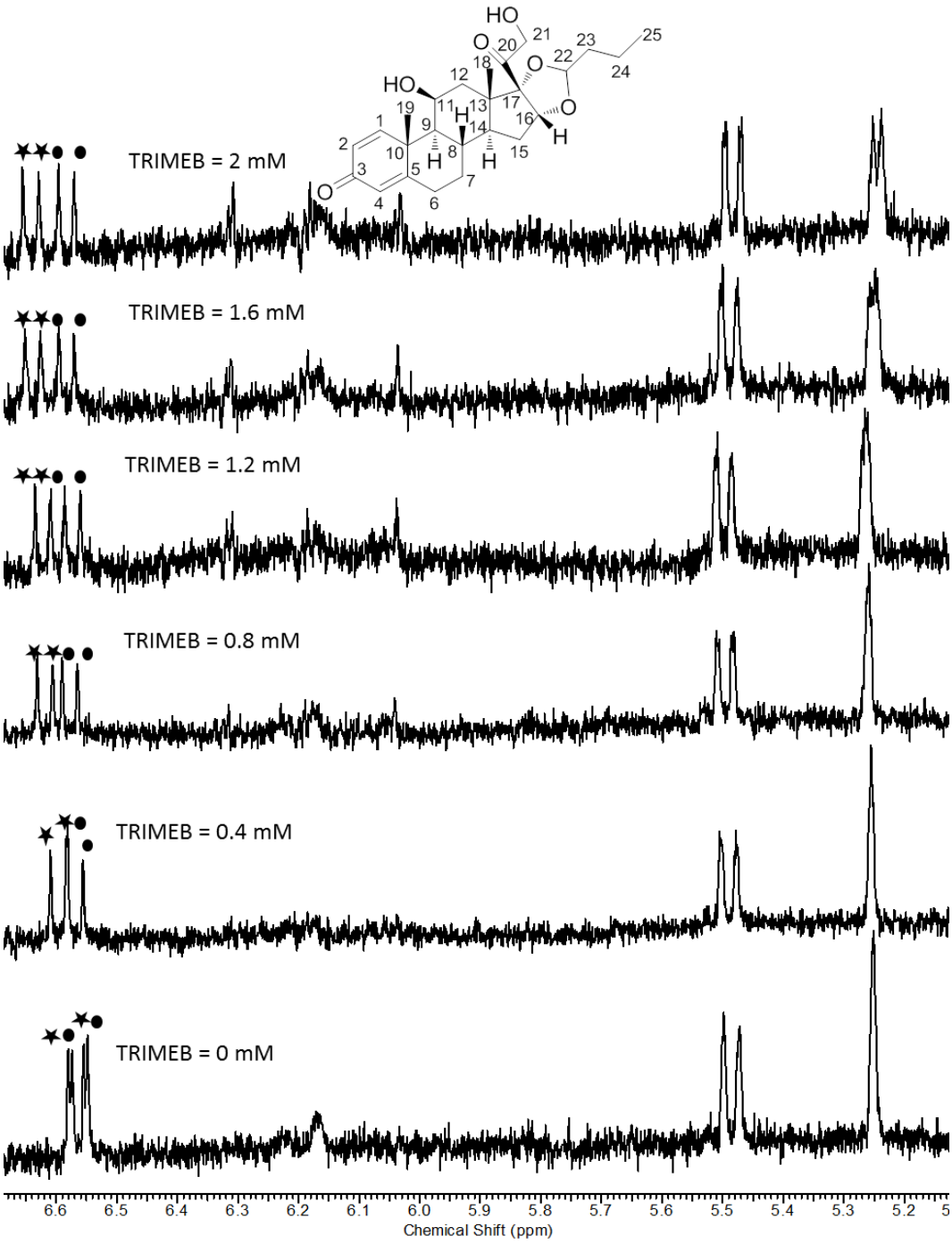

Figure 5.11: Racemic BUD (0.0875 mM) chemical shift in low field region (5.1-6.7 ppm) with the addition of TRIMEB at 0, 0.4, 0.8, 1.2, 1.6 and 2 mM in HPFP. The peaks annotated with star and dot were related to *R*- and *S*-enantiomer of BUD.

The assignment of the proton resonance shifts for the optically pure forms of BUD has allowed the stability constants for *R*- and *S*-enantiomers of BUD to be calculated using the H-C_1 proton chemical shift at 6.5491/6.5666 and 6.5431/6.5600 ppm respectively. Table 5.3 shows the results of the experiments performed on the racemic BUD, with those from the *S*- and *R*-enantiomers shown in Tables 5.4 and 5.5, with reciprocal plots for the two enantiomers shown in Figures 5.12 and 5.13.

Table 5.3: Results of the chemical shift of budesonide and TRIMEB added at 0, 0.4, 0.8, 1.2, 1.6 and 2 mM in HPFP using ^{1}H NMR.

Experiment number	Proton position (ppm)	TRIMEB concentration (mM)					
		0	0.4	0.8	1.2	1.6	2
		Chemical shift (ppm)					
1			6.5935	6.6107	6.6247	6.6344	6.6401
2	H-C_1	6.5666	6.5929	6.6103	6.6234	6.6322	6.6395
3			6.5927	6.6086	6.6240	6.6327	6.6379
	Mean		**6.5930**	**6.6099**	**6.6240**	**6.6331**	**6.6392**
	SD		**0.0004**	**0.0011**	**0.0007**	**0.0012**	**0.0011**
	% CV		**0.0063**	**0.0169**	**0.0098**	**0.0174**	**0.0171**
1			6.5653	6.5693	6.5743	6.5763	6.5803
2	H-C_1	6.5600	6.5649	6.5689	6.5727	6.5755	6.5793
3			6.5652	6.5688	6.5741	6.5760	6.5807
	Mean		**6.5651**	**6.5690**	**6.5737**	**6.5759**	**6.5801**
	SD		**0.0002**	**0.0003**	**0.0009**	**0.0004**	**0.0007**
	% CV		**0.0032**	**0.0040**	**0.0133**	**0.0061**	**0.0110**
1			6.5761	6.5946	6.6086	6.6169	6.6235
2	H-C_1	6.5491	6.5756	6.5937	6.6071	6.6145	6.6229
3			6.5758	6.5929	6.6071	6.6152	6.6236
	Mean		**6.5758**	**6.5937**	**6.6076**	**6.6155**	**6.6233**
	SD		**0.0003**	**0.0009**	**0.0009**	**0.0012**	**0.0004**
	% CV		**0.0038**	**0.0129**	**0.0131**	**0.0187**	**0.0057**
1			6.5462	6.5508	6.5568	6.5599	6.5628
2	H-C_1	6.5431	6.5461	6.5511	6.5555	6.5589	6.5622
3			6.5461	6.5499	6.5561	6.5594	6.5629
	Mean		**6.5461**	**6.5506**	**6.5561**	**6.5594**	**6.5626**
	SD		**0.0001**	**0.0006**	**0.0007**	**0.0005**	**0.0004**
	% CV		**0.0009**	**0.0095**	**0.0099**	**0.0076**	**0.0058**

Table 5.4: Results of the complexation between *R*-enantiomer of budesonide and TRIMEB added at 0.4, 0.8, 1.2, 1.6 and 2 mM in HPFP using ^{1}H NMR depending on the chemical shift differnce of H-C_1 proton 6.5666 and 6.5491 ppm.

TRIMEB (mM)	1/TRIMEB (mM^{-1})	$1/\Delta\delta_{obs}$ (6.5666 ppm)				$1/\Delta\delta_{obs}$ (6.5491 ppm)			
		1	2	3	Mean	1	2	3	Mean
0.4	2.5	37.2	38	38.3	**38**	37	37.7	37.5	**37.6**
0.8	1.3	22.7	22.9	23.8	**23.1**	22	22.4	22.8	**22.4**
1.2	0.8	17.2	17.6	17.4	**17.4**	16.8	17.2	17.2	**17.1**
1.6	0.6	14.7	15.2	15.1	**15**	14.7	15.3	15.1	**15.1**
2	0.5	13.6	13.7	14.0	**13.8**	13.4	13.6	13.4	**13.5**

Table 5.5: Results of the complexation between *S*-enantiomer of budesonide and TRIMEB added at 0.4, 0.8, 1.2, 1.6 and 2 mM in HPFP using ^{1}H NMR depending on the chemical shift differnce of H-C$_1$ proton at 6.5431 and 6.5600 ppm.

TRIMEB (mM)	1/TRIMEB (mM^{-1})	1/Δδ$_{obs}$ (6.5431 ppm)				1/Δδ$_{obs}$ (6.5600 ppm)			
		1	2	3	Mean	1	2	3	Mean
0.4	2.5	323	333	333	**330**	188.7	204	192.3	**195**
0.8	1.3	130	125	147	**134**	107.5	112	113.6	**111**
1.2	0.8	73.0	80.6	76.9	**76.9**	69.9	78.7	70.9	**73.2**
1.6	0.6	59.5	63.3	61.3	**61.4**	61.3	64.5	62.5	**62.8**
2	0.5	50.8	52.4	50.5	**61.2**	49.3	51.8	48.3	**49.8**

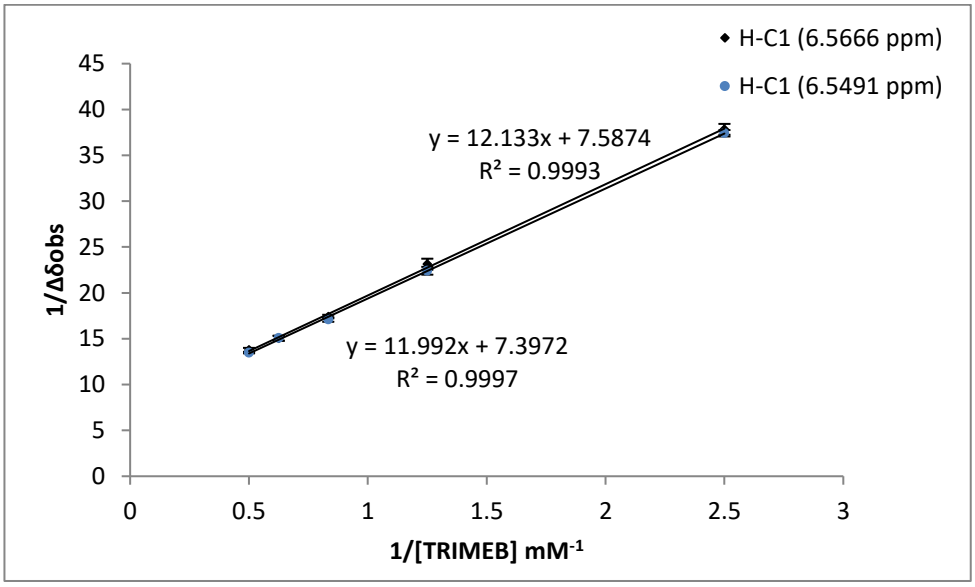

Figure 5.12: Reciprocal plot for the determination of association constant between *R*-enantiomer of BUD and TRIMEB in HPFP by ^{1}H NMR depending on the chemical shift differnce of H-C$_1$ proton at 6.5666 and 6.5491 ppm (Mean ± SD, n=3).

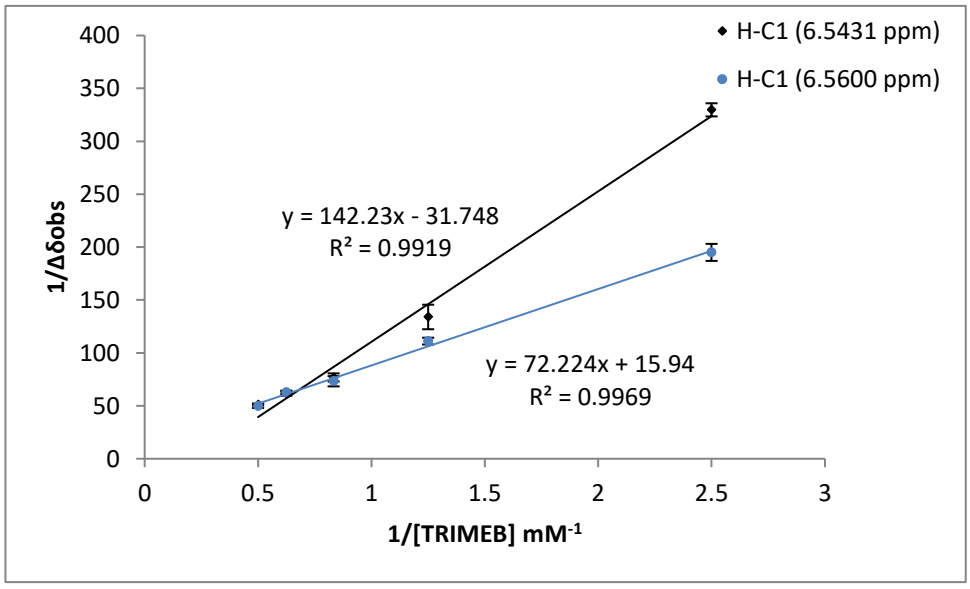

Figure 5.13: Reciprocal plot for the determination of association constant between *S*-enantiomer of BUD and TRIMEB in HPFP by ^{1}H NMR depending on the chemical shift differnce of H-C$_1$ proton at 6.5431 and 6.5600 ppm (Mean ± SD, n=3).

The reciprocal plot showed good linearity indicating that the complexation had a stoichiometry of 1:1. The mean K was found to be 621 and 222 M^{-1} for *R* and *S* enantiomers of BUD respectively as shown in Table 5.6.

Table 5.6: Results of the stability constant between *R* and *S*-enantiomers of budesonide and TRIMEB added at 0, 0.4, 0.8, 1.2, 1.6 and 2 mM in HPFP using ^{1}H NMR.

Proton NO.	BUD enantiomer	Chemical shift (ppm)	Stability constant, K (M^{-1})				SD	% CV
			1	2	3	Mean		
H-C_1	*R*	6.5666	630	624	621	**625**	4.6	0.7
		6.5491	610	617	624	**617**	7	1.1
	S	6.56	227	213	219	**220**	7	3.2
		6.5431	228	224	217	**223**	5.6	2.5

The Job's method of continuous variation was adopted (Section 2.2.3.3) to verify the stoichiometry of the complex based on the induced chemical shift changes of H-C_1 proton of BUD at 6.5666 ppm (Table 5.7). The plot is shown in Figure 5.14.

Table 5.7: Results of ^{1}H NMR analysis for the determination of stoichiometry between budesonide and TRIMEB in HPFP based on the chemical shift at H-C_1 proton of budesonide at 6.5666 ppm.

[BUD] (mM)	r	$\delta_{complex}$ (ppm)	$\Delta\delta_{obs}$ (ppm)	$\Delta\delta$[BUD]	$\Delta\delta$[BUD]*10^4
0.175	1	6.5666	0	0	0
0.1575	0.9	6.5674	0.0008	12.6×10^{-5}	1.26
0.14	0.8	6.5683	0.0017	23.8×10^{-5}	2.38
0.1225	0.7	6.5693	0.0027	33.1×10^{-5}	3.31
0.105	0.6	6.571	0.0044	46.2×10^{-5}	4.62
0.0875	0.5	6.5725	0.0059	51.6×10^{-5}	5.16
0.07	0.4	6.5735	0.0069	48.3×10^{-5}	4.83
0.0525	0.3	6.5747	0.0081	42.5×10^{-5}	4.25
0.035	0.2	6.5764	0.0098	34.3×10^{-5}	3.43
0.0175	0.1	6.5784	0.0118	20.7×10^{-5}	2.07
0	0	0	0	0	0

δ_{free} = 6.5666 ppm

The stoichiometry of the complex is shown to be 1:1, as the highest value of r was at 0.5. These data are in agreement with the titration experiments which returned a linear response when using the Hildebrand-Benesi approach.

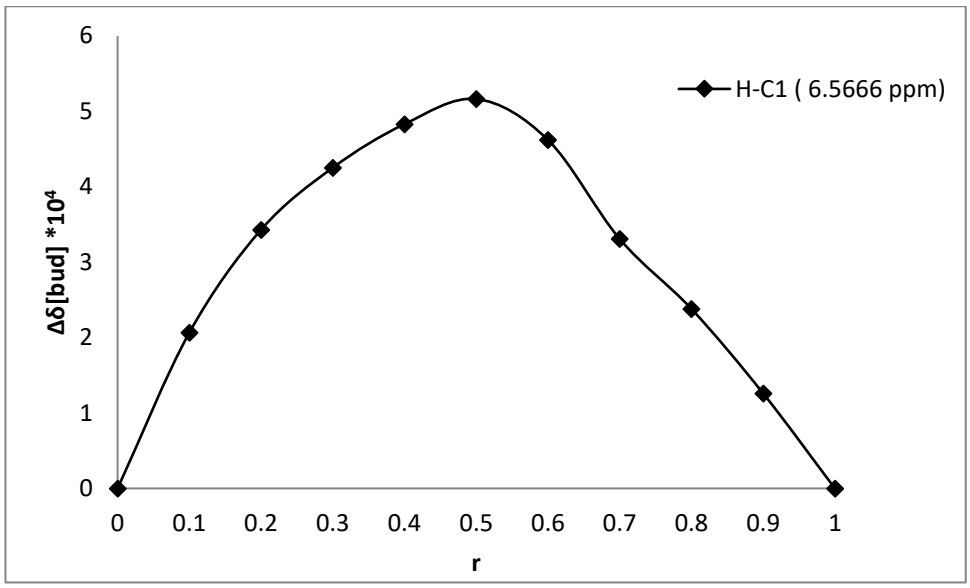

Figure 5.14: Determination of the stoichiometry of the complex between budesonide and TRIMEB in HPFP by ^{1}H NMR based on H-C_1 proton of budesonide.

5.3 Complexation study of BDP and TRIMEB

The complexation of BDP and TRIMEB in HPFP demonstrate that some protons display only very minor shifts with 1 mM TRIMEB concentration where the values were small to calculate the stability constant. The experiment was then conducted with a more concentrated solution of TRIMEB (4 mM). It has been noted that small shifts occurred for the H-C_{19} peak at 1.0206 ppm chemical shift, and no significant shifts were observed for H-C_{18} or the methyls at C_{17} and C_{21}. In addition, a minor downfield shift occurred for H-C_4 at 5.2943 ppm, with no observable shifts for the H-C_1 and H-C_2 of the quinone ring (Figures 5.15 and 5.16).

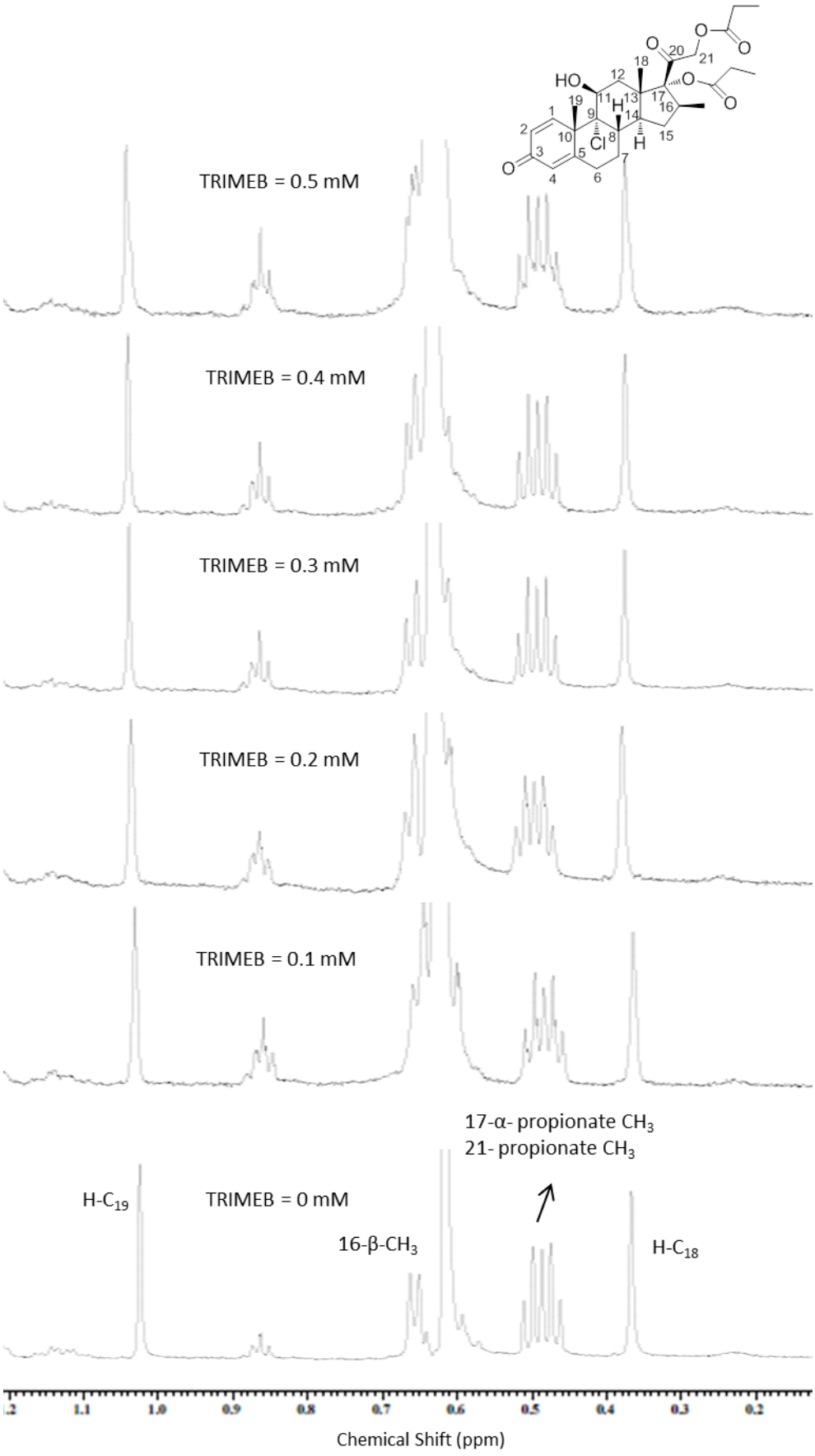

Figure 5.15: BDP (0.2 mM) chemical shift in high field region (0.1-1.2 ppm) with the addition of TRIMEB at 0, 0.4, 0.8, 1.2, 1.6 and 2 mM in HPFP.

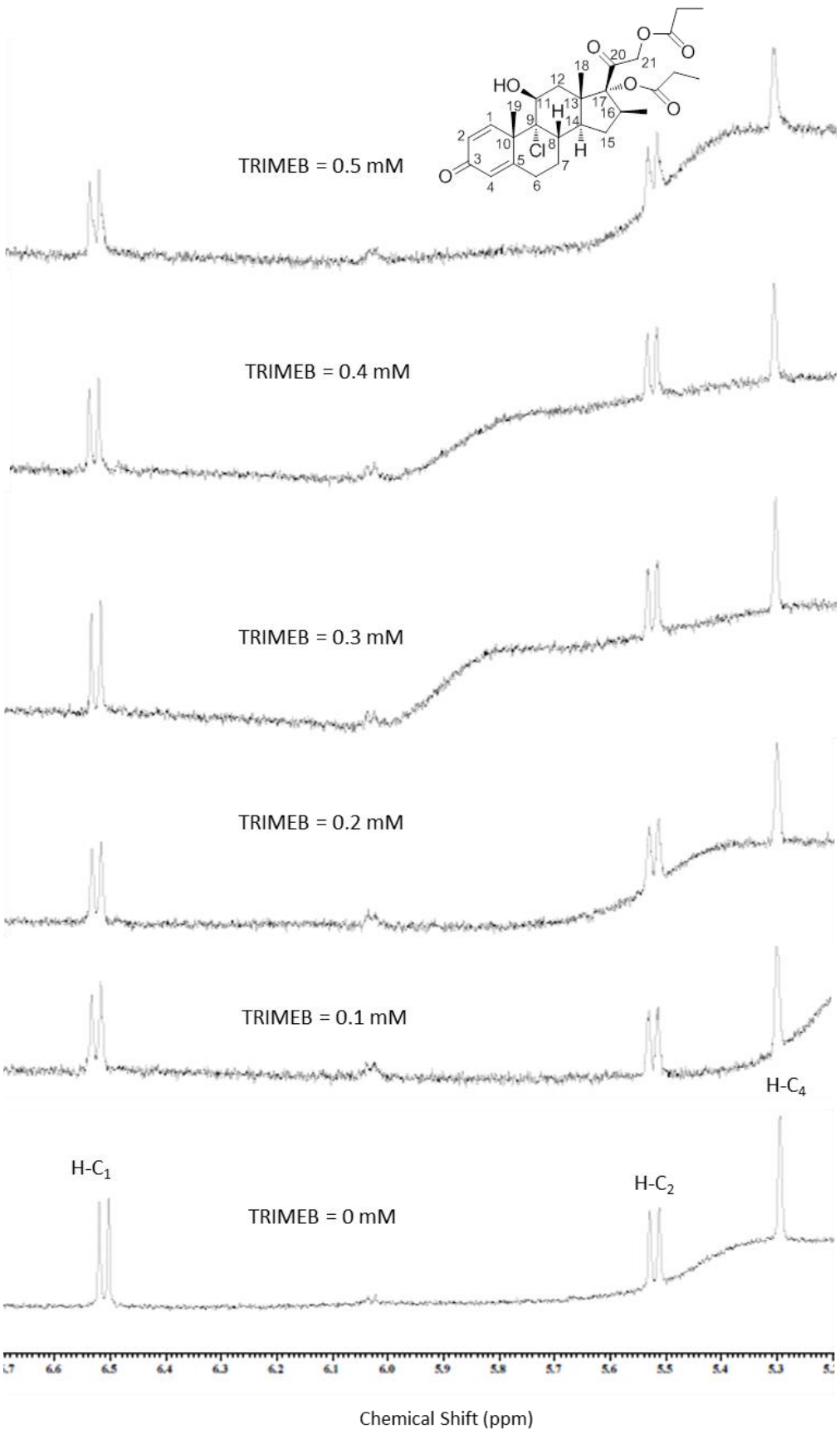

Figure 5.16: BDP (0.2 mM) chemical shift in low field region (5.2-6.7 ppm) with the addition of TRIMEB at 0, 0.4, 0.8, 1.2, 1.6 and 2 mM in HPFP.

The chemical shift differences of both H-C_{19} and H-C_4 protons at 1.0206 and 5.2943 ppm respectively were used to calculate the stability constant as these peaks displayed considerable shifts when compared to the other protons in the BDP molecule. The results of the triplicate experiments are presented in Table 5.8.

Table 5.8: Results of the chemical shift of BDP and TRIMEB added at 0, 0.4, 0.8, 1.2, 1.6 and 2 mM in HPFP using ^{1}H NMR.

Experiment number	Proton position (ppm)	TRIMEB concentration (mM)					
		0	0.4	0.8	1.2	1.6	2
		Chemical shift (ppm)					
1			1.0335	1.0439	1.0515	1.0647	1.0743
2	H-C_{19}	1.0206	1.0338	1.0451	1.0552	1.0630	1.0724
3			1.0337	1.0474	1.0546	1.0612	1.0725
	Mean		**1.0337**	**1.0455**	**1.0538**	**1.0630**	**1.0731**
	SD		**0.0002**	**0.0018**	**0.0020**	**0.0018**	**0.0011**
	% CV		**0.0148**	**0.1701**	**0.1884**	**0.1647**	**0.0996**
1			5.3123	5.3269	5.3381	5.3547	5.3689
2	H-C_4	5.2943	5.3119	5.3271	5.3376	5.3536	5.3653
3			5.3120	5.3283	5.3383	5.3524	5.3648
	Mean		**5.3121**	**5.3274**	**5.3380**	**5.3536**	**5.3663**
	SD		**0.0002**	**0.0008**	**0.0004**	**0.0012**	**0.0022**
	% CV		**0.0039**	**0.0142**	**0.0068**	**0.0215**	**0.0417**

The determination of K depending on the chemical shift differences at 1.0206 and 5.2943 ppm is presented in Table 5.9, with the Hildebrand-Benesi plots being shown in Figure 5.17.

Table 5.9: Results of the complexation between BDP and TRIMEB added at 0.4, 0.8, 1.2, 1.6 and 2 mM in HPFP using ^{1}H NMR depending on the chemical shift at 1.0206 and 5.2943 ppm.

TRIMEB (mM)	1/TRIMEB (mM^{-1})	$1/\Delta\delta_{obs}$ (1.0206 ppm)				$1/\Delta\delta_{obs}$ (5.2943 ppm)			
		1	2	3	Mean	1	2	3	Mean
0.4	2.5	77.5	75.8	76.3	**76.5**	55.6	56.8	56.5	**56.3**
0.8	1.3	42.9	40.8	37.3	**40.4**	30.7	30.5	29.4	**30.2**
1.2	0.8	32.4	28.9	29.4	**30.2**	22.8	23.1	22.7	**22.9**
1.6	0.6	22.7	23.6	24.7	**23.6**	16.6	16.9	17.2	**16.9**
2	0.5	18.6	19.3	19.3	**19.1**	13.4	14.1	14.2	**13.9**

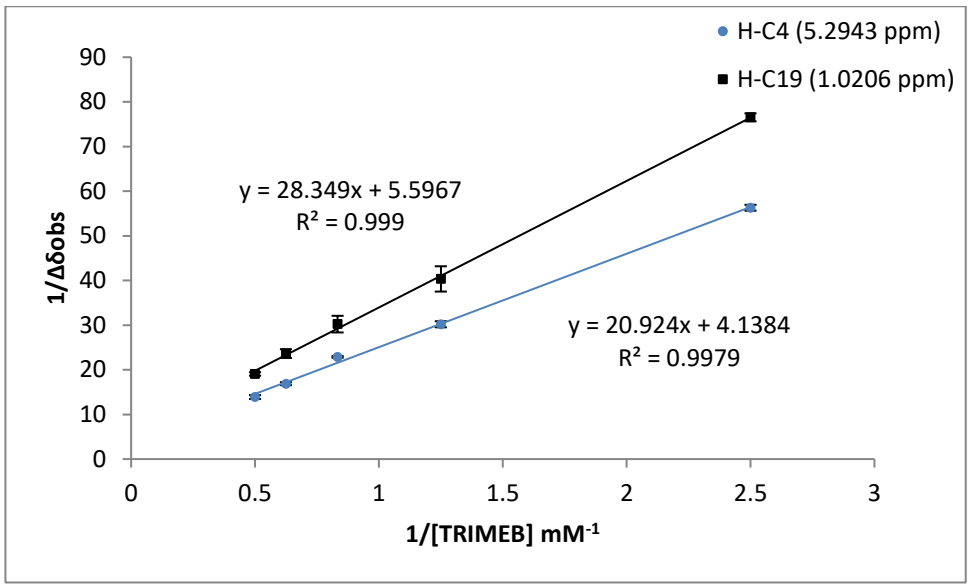

Figure 5.17: Reciprocal plot for the determination of association constant between BDP and TRIMEB in HPFP by ^{1}H NMR depending on the chemical shift at 1.0206 and 5.2943 ppm (Mean ± SD, n=3).

The reciprocal plot showed good linearity indicating that the complexation had a stoichiometry of 1:1. The mean K value was calculated and found to be 197.5 M^{-1} based on the chemical shift for H-C_4 and H-C_{19} protons (Table 5.10).

Table 5.10: Results of the stability constant between BDP and TRIMEB added at 0.4, 0.8, 1.2, 1.6 and 2 mM in HPFP using ^{1}H NMR.

Proton position	Chemical shift (ppm)	Stability constant, K (M^{-1})				SD	% CV
		1	2	3	Mean		
H-C_4	5.2943	198	196	199	**198**	1.5	0.8
H-C_{19}	1.0206	197	200	193	**197**	3.5	1.8

5.4 Complexation study of MOM and TRIMEB

The experiments of the complexation study of MOM and TRIMEB in HPFP showed that the values of the chemical shift differences with 1 mM TRIMEB concentration were too small and not reliable to do the reciprocal plot for the stability constant determination. A second series of experiments was then performed with a more concentrated solution of TRIMEB (4 mM) with the purpose of obtaining more chemical shift displacements for the MOM protons. The results showed a downfield shift occurred for H-C_{19} peak at 1.0263 ppm chemical shift, however, other peaks in the high field region were not shifted such as H-C_{18} and methyls at C_{16} (Figure 5.18).

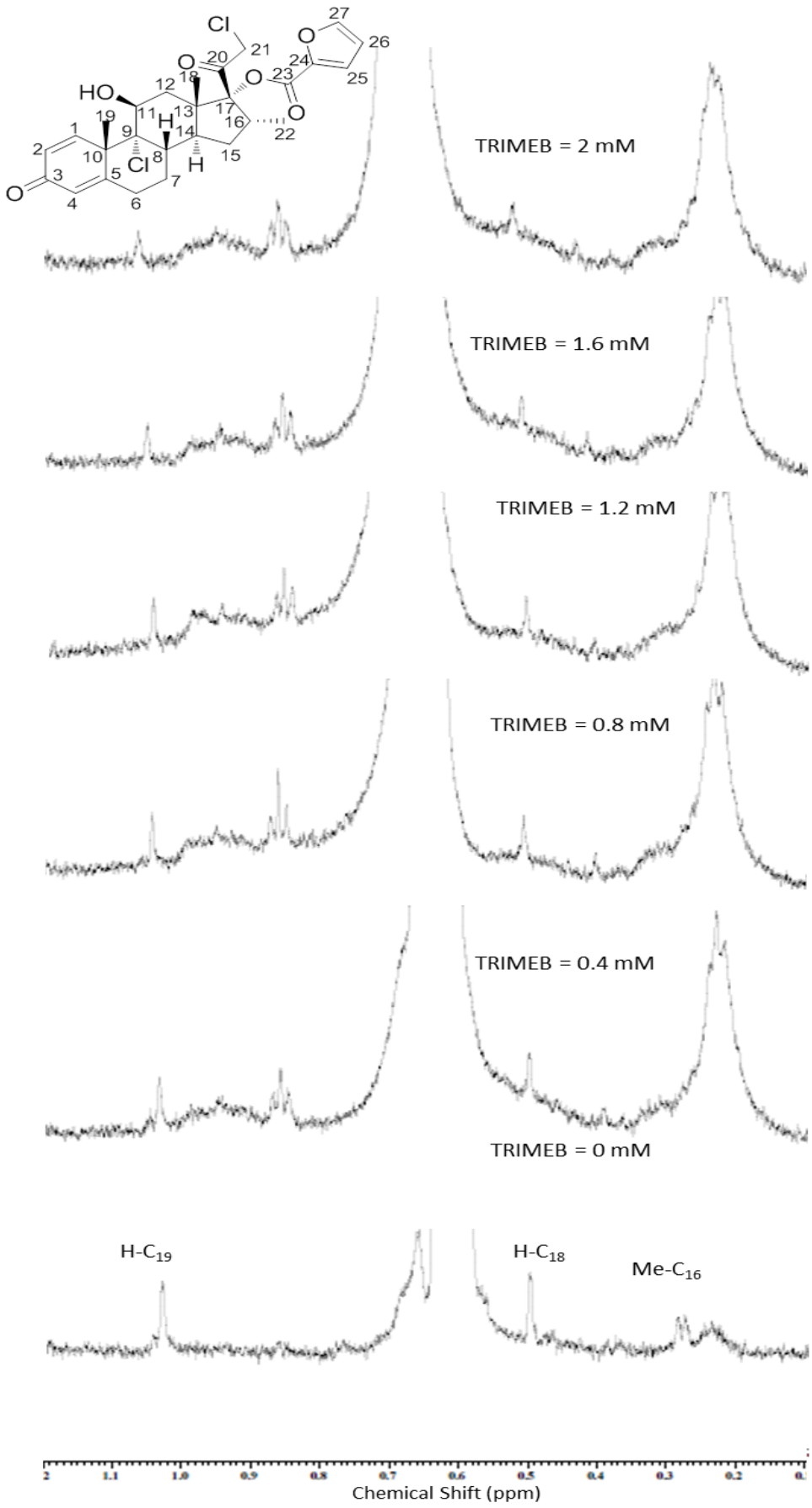

Figure 5.18: MOM (0.02 mM) chemical shift in high field region (0.1-1.2 ppm) with the addition of TRIMEB at 0, 0.4, 0.8, 1.2, 1.6 and 2 mM in HPFP.

The MOM peaks in the low field region of the complexed spectra were of low S/N ratio and therefore difficult to investigate the effect of TRIMEB on them (Figure 5.19). This was because of the low concentration of MOM in the complexed solution with CD (decreased to half, 0.02 mM) compared to the pure solution of MOM without CD and this the highest concentration that can be prepared according to its solubility in HPFP.

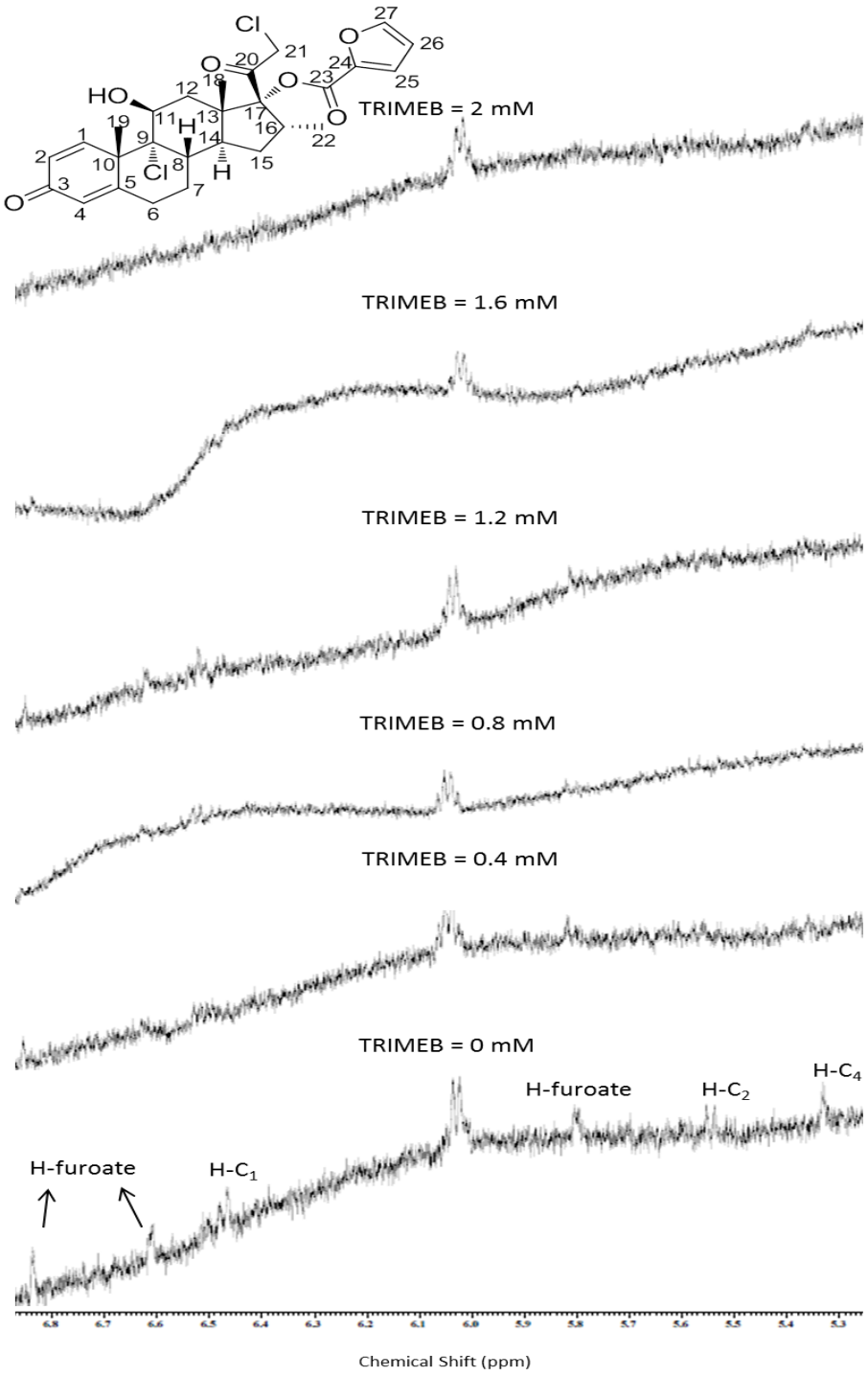

Figure 5.19: MOM (0.02 mM) chemical shift in low field region (5.2-6.9 ppm) with the addition of TRIMEB at 0, 0.4, 0.8, 1.2, 1.6 and 2 mM in HPFP.

The chemical shift displacements of H-C_{19} peak at 1.0263 ppm was used to determine the stability constant, this peak was the only one observed with considerable shift when compared to the other protons of the MOM compound. The results are presented in Table 5.11.

Table 5.11: Results of the chemical shift of MOM and TRIMEB added at 0, 0.4, 0.8, 1.2, 1.6 and 2 mM in HPFP using ^{1}H NMR.

Experiment number	Proton position (ppm)	TRIMEB concentration (mM)					
		0	0.4	0.8	1.2	1.6	2
		Chemical shift (ppm)					
1			1.0324	1.0394	1.0461	1.0557	1.0667
2	H-C_{19}	1.0263	1.0325	1.0397	1.0475	1.0549	1.0650
3			1.0323	1.0404	1.0457	1.0540	1.0655
Mean			**1.0324**	**1.0398**	**1.0464**	**1.0549**	**1.0657**
SD			**0.0001**	**0.0005**	**0.0009**	**0.0009**	**0.0009**
% CV			**0.0097**	**0.0494**	**0.0903**	**0.0806**	**0.0820**

The determination of the K based on the chemical shift displacements at 1.0263 ppm is shown in Table 5.12 with the reciprocal plot being shown in Figure 6.20.

Table 5.12: Results of the complexation between MOM and TRIMEB added at 0.4, 0.8, 1.2, 1.6 and 2 mM in HPFP using ^{1}H NMR depending on the chemical shift at 1.0263 ppm.

TRIMEB (mM)	1/TRIMEB (mM^{-1})	$1/\Delta\delta_{obs}$ (1.0263 ppm)			
		1	2	3	Mean
0.4	2.5	163.9	161.3	166.7	**164**
0.8	1.3	76.3	74.6	70.9	**74**
1.2	0.8	50.5	47.2	51.6	**49.7**
1.6	0.6	34	35	36.1	**35**
2	0.5	24.8	25.8	25.5	**25.4**

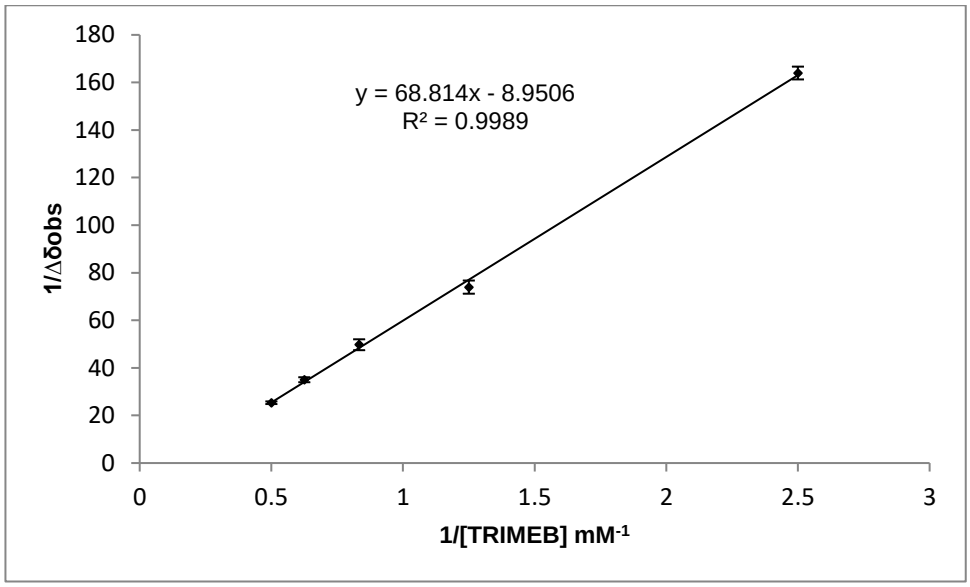

Figure 5.20: Reciprocal plot for the determination of association constant between MOM and TRIMEB in HPFP by ^{1}H NMR depending on the chemical shift at 1.0263 ppm (Mean ± SD, n=3)..

The reciprocal plot showed a linear relationship between the 1/[TRIMEB] and $1/\Delta\delta_{obs}$ which indicated the complexation had a stoichiometry of 1:1. The mean K value was calculated and found to be 130 M^{-1} (Table 5.13).

Table 5.13: Results of the stability constant between MOM and TRIMEB added at (0, 0.4, 0.8, 1.2, 1.6 and 2 mM) in HPFP using ^{1}H NMR.

Proton NO.	Chemical shift (ppm)	Stability constant, K (M^{-1})				SD	% CV
		1	2	3	Mean		
H-C_{19}	1.0263	131	125	134	**130**	4.6	3.5

5.5 Complexation study of FLU and TRIMEB

The complexation study of FLU with TRIMEB in HPFP showed that very small shifts were noted for all the FLU peaks with 1 mM TRIMEB concentration, it was difficult to apply the Hildebrand-Benesi approach to calculate the stability constant. Therefore, further experiment was performed using a concentrated solution of TRIMEB (4 mM) to display more chemical shift displacements for the FLU peaks. The results showed a downfield shift was observed for only the H-C_{19} proton at 0.8560 ppm chemical shift when the TRIMEB concentration was increased, and no observable shift was noted for the other peaks in the high field region such as methyls at C_{16} and H-C_{18} protons (Figure 5.21).

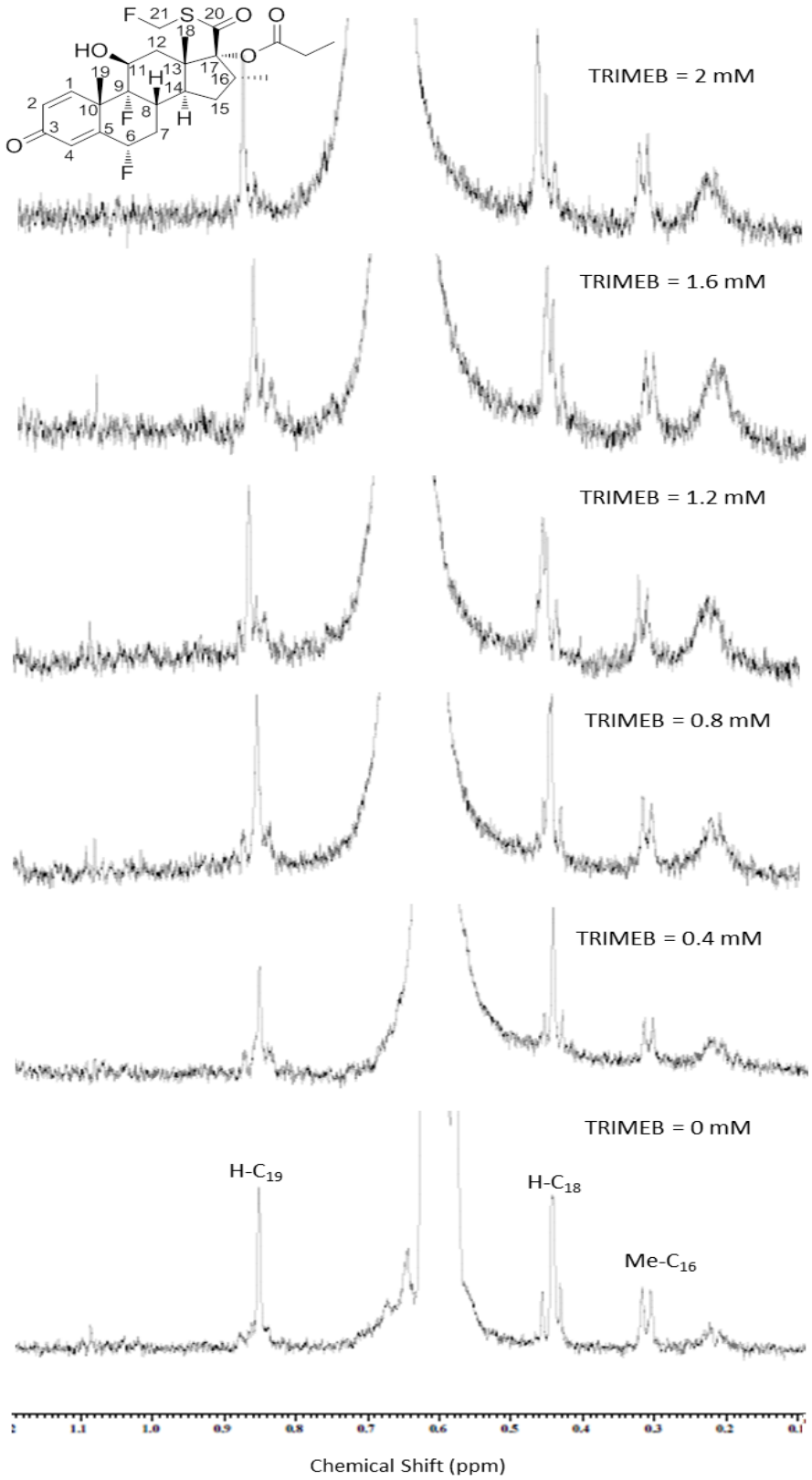

Figure 5.21: FLU (0.02 mM) chemical shift in high field region (0.1-1.2 ppm) with the addition of TRIMEB at 0, 0.4, 0.8, 1.2, 1.6 and 2 mM in HPFP.

In addition, no considerable shift was observed for the H-C_2 proton of the quinone ring at 5.64 ppm chemical shift. However, the other two protons of the quinone rings (H-C_1 and H-C_4) were not clearly observed in the complexed

spectra of FLU and displayed a low S/N ratio and therefore it was difficult to study the effect of TRIMEB on the chemical shift of those protons (Figure 5.22). This was owing to the low concentration of FLU in the complexed solution with CD (decreased to half, 0.02 mM) compared to the pure solution of FLU without CD, and this the highest concentration that can be prepared according to its solubility in HPFP.

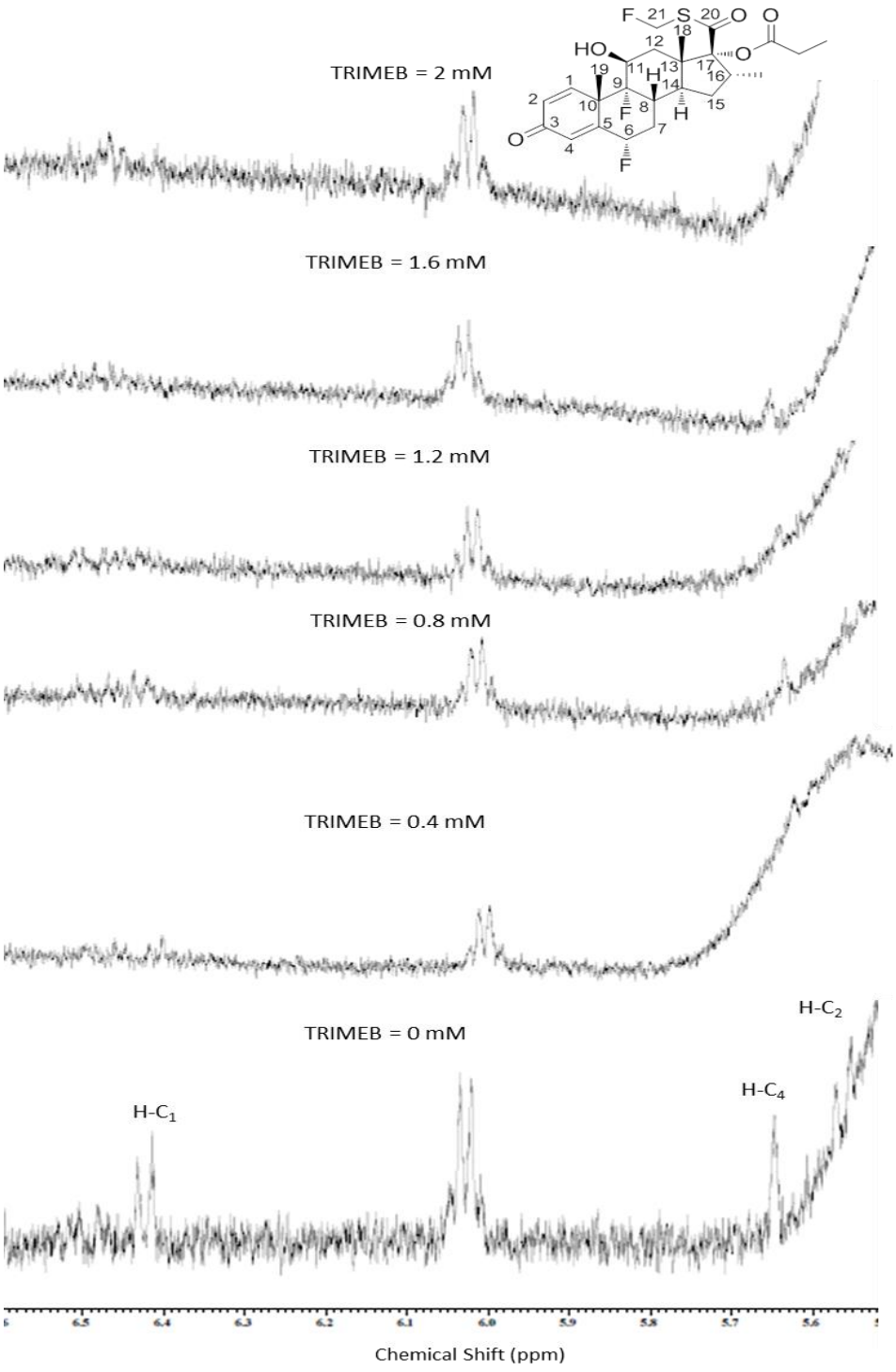

Figure 5.22: FLU (0.02 mM) chemical shift in low field region (5.5-6.6 ppm) with the addition of TRIMEB at 0, 0.4, 0.8, 1.2, 1.6 and 2 mM in HPFP.

The chemical shift displacements of the H-C_{19} proton at 0.8560 ppm are presented in Table 5.14, where they used to calculate the K as shown in Table 5.15 with reciprocal plot shown in Figure 5.23.

Table 5.14: Results of the chemical shift of FLU and TRIMEB added at 0, 0.4, 0.8, 1.2, 1.6 and 2 mM in HPFP using ^{1}H NMR.

Experiment number	Proton position (ppm)	TRIMEB concentration (mM)					
		0	0.4	0.8	1.2	1.6	2
		Chemical shift (ppm)					
1			0.8600	0.8629	0.8671	0.8708	0.8751
2	H-C_{19}	0.8560	0.8598	0.8636	0.8662	0.8696	0.8739
3			0.8599	0.8634	0.8677	0.8689	0.8739
Mean			**0.8599**	**0.8633**	**0.8670**	**0.8698**	**0.8743**
SD			**0.0001**	**0.0004**	**0.0008**	**0.0010**	**0.0007**
% CV			**0.0116**	**0.0418**	**0.0871**	**0.1105**	**0.0792**

Table 5.15: Results of the complexation between FLU and TRIMEB added at 0.4, 0.8, 1.2, 1.6 and 2 mM in HPFP using ^{1}H NMR depending on the chemical shift at 0.8560 ppm.

TRIMEB (mM)	1/TRIMEB (mM^{-1})	$1/\Delta\delta_{obs}$ (0.8560 ppm)			
		1	2	3	Mean
0.4	2.5	250	263.2	256.4	**256.5**
0.8	1.3	144.9	131.6	135.1	**137.2**
1.2	0.8	90.1	98	85.5	**91.2**
1.6	0.6	67.6	73.5	77.5	**72.9**
2	0.5	52.4	55.9	55.9	**54.7**

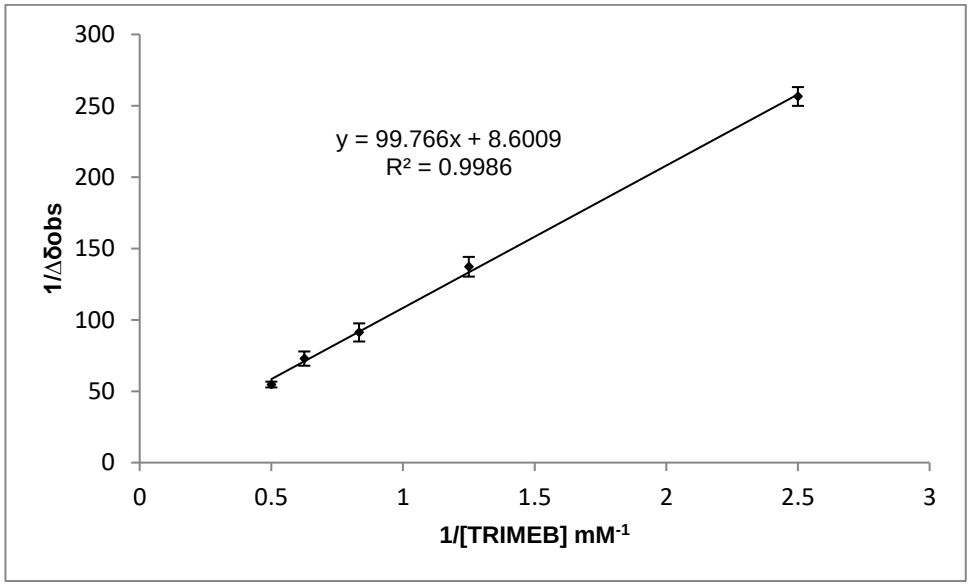

Figure 5.23: Reciprocal plot for the determination of association constant between FLU and TRIMEB in HPFP by ^{1}H NMR depending on the chemical shift at 0.8560 ppm (Mean ± SD, n=3).

The reciprocal plot showed a linear relationship which suggested the stoichiometric ratio was 1:1. The mean K value was calculated as shown in Table 5.16 and found to be 86 M^{-1}.

Table 5.16: Results of the stability constant between FLU and TRIMEB added at 0, 0.4, 0.8, 1.2, 1.6 and 2 mM in HPFP using 600 MHz ^{1}H NMR.

Proton NO.	Chemical shift (ppm)	Stability constant, K (M^{-1})				SD	% CV
		1	2	3	Mean		
H-C_{19}	0.8560	87	81	90	**86**	4.6	5.3

5.6 Complexation study of BUD and DIMEB

The study of the complexation between BUD and DIMEB was performed using the same developed method of BUD with TRIMEB. The findings demonstrated that very small shifts occurred for H-C_{18} and H-C_{19} peaks at 0.3354 and 0.7992 ppm respectively. The H-C_{25} peak was not shifted, though its multiplicity changed as the TRIMEB concentration was increased. However, the peak at 0.2667 ppm (annotated with star in Figure 5.24) experienced a very minor shift and could be attributed to the H-C_{18} peak of the *R*-enantiomer of BUD.

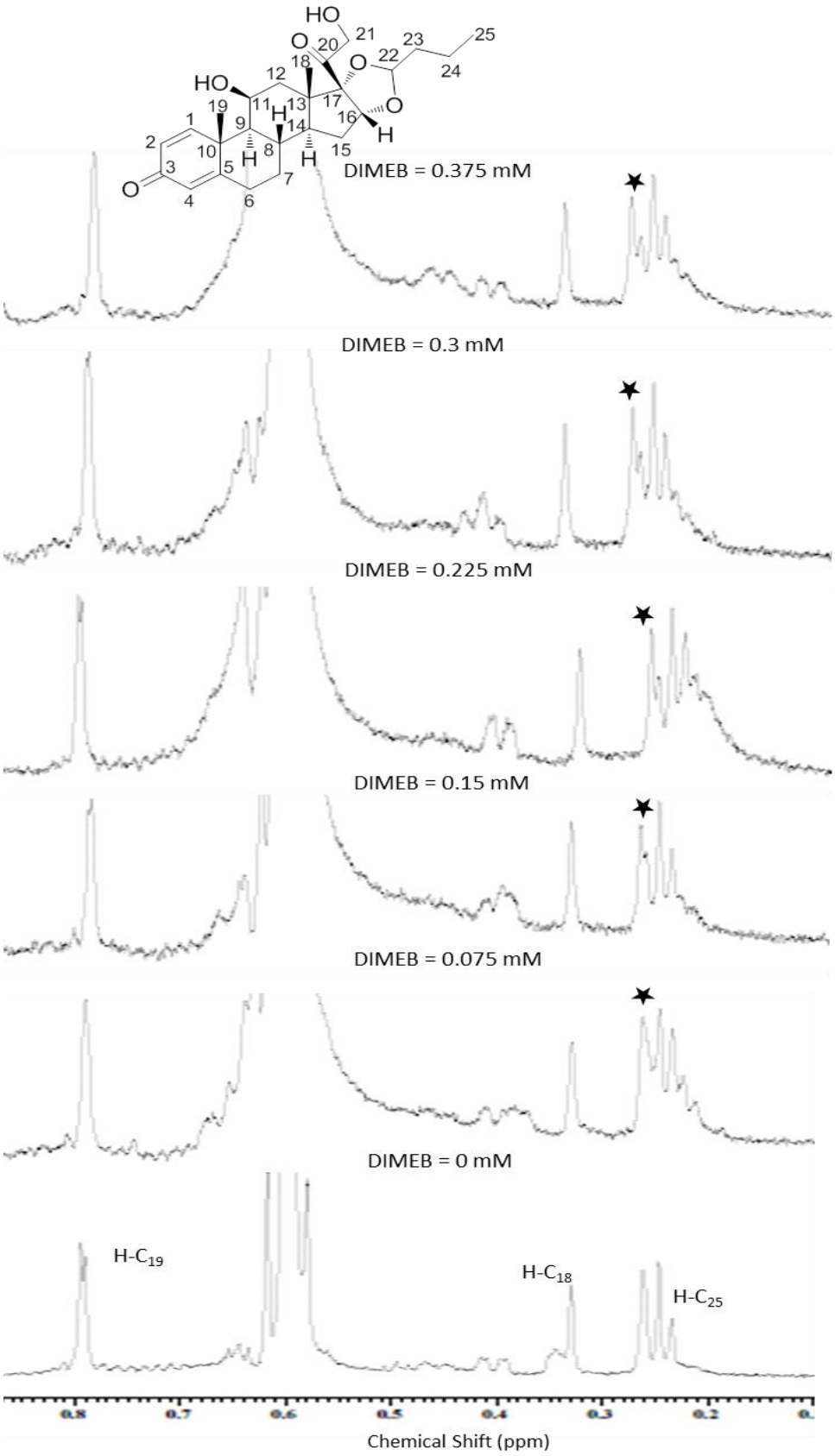

Figure 5.24: BUD (0.0875 mM) chemical shift in high field region (0.1-0.9 ppm) with the addition of DIMEB at 0, 0.075, 0.15, 0.225, 0.3 and 0.375 mM in HPFP. The peak annotated with star was related to *R*-enantiomer of BUD.

In the low field region, a slight downfield shift occurred for the H-C_1 proton of the quinone ring, as the concentration of TRIMEB was increased, and no significant shift was observed for both H-C_2 and H-C_4 protons of the quinone ring. The spectra of the complexed BUD in the low field region are shown in Figure 5.25.

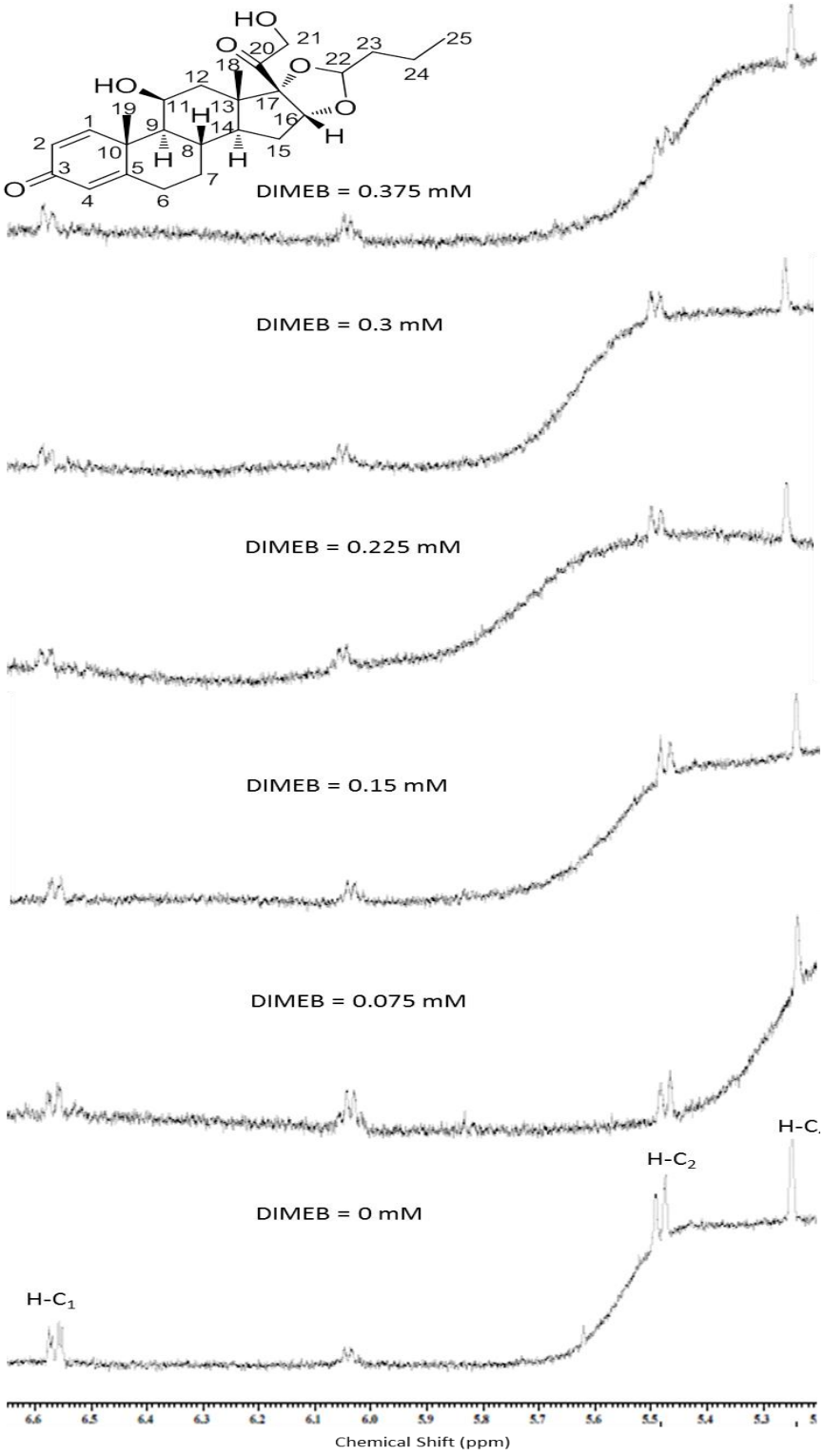

Figure 5.25: BUD (0.0875 mM) chemical shift in low field region (5.2-6.7 ppm) with the addition of DIMEB at 0, 0.075, 0.15, 0.225, 0.3 and 0.375 mM in HPFP.

The chemical shift differences of the H-C_1 proton at 6.5666 ppm are shown in Table 5.17 and the stability constant determination is presented in Table 5.18 with the reciprocal plot shown in Figure 5.26.

Table 5.17: Results of the chemical shift of budesonide and DIMEB added at 0, 0.075, 0.15, 0.225, 0.3 and 0.375 mM in HPFP using ^{1}H NMR.

Experiment number	Proton position (ppm)	DIMEB concentration (mM)					
		0	0.075	0.15	0.225	0.3	0.375
		Chemical shift (ppm)					
1			6.5694	6.5725	6.5754	6.5771	6.5829
2	H-C_1	6.5666	6.5692	6.5725	6.5741	6.5764	6.5823
3			6.5692	6.5718	6.5744	6.5763	6.5837
Mean			6.5693	6.5723	6.5746	6.5766	6.5830
SD			0.0001	0.0004	0.0007	0.0004	0.0007
% CV			0.0018	0.0061	0.0104	0.0066	0.0107

Table 5.18: Results of the complexation between budesonide and DIMEB added at 0.075, 0.15, 0.225, 0.3 and 0.375 mM in HPFP using ^{1}H NMR depending on the chemical shift at 6.5666 ppm.

DIMEB (mM)	1/DIMEB (mM^{-1})	$1/\Delta\delta_{obs}$ (6.5666 ppm)			
		1	2	3	Mean
0.075	13.3	357.1	384.6	384.6	375.5
0.15	6.7	169.5	169.5	192.3	177.1
0.225	4.4	113.6	133.3	128.2	125.1
0.3	3.3	95.2	102	103.1	100.1
0.375	2.7	61.4	63.7	58.5	61.2

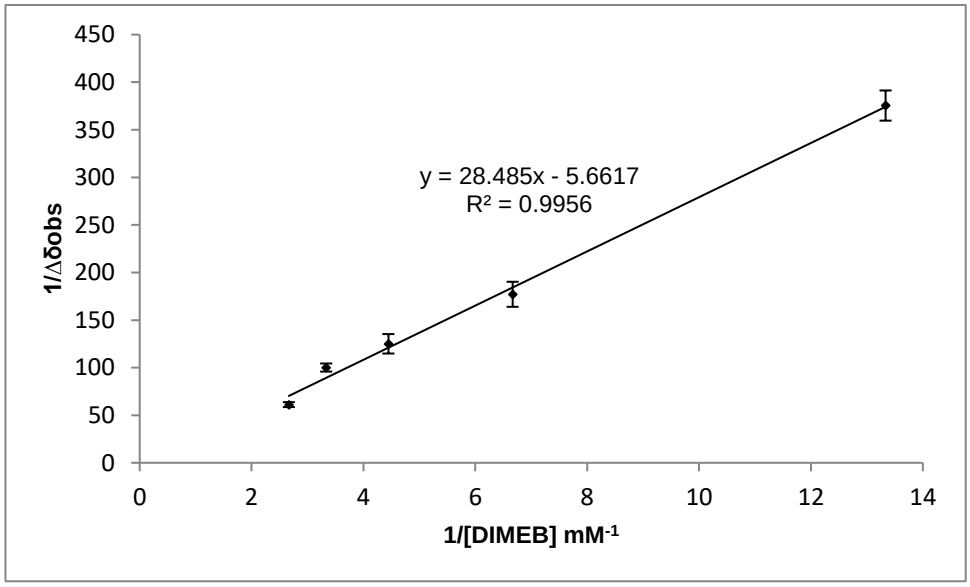

Figure 5.26: Reciprocal plot for the determination of association constant between budesonide and DIMEB in HPFP by ^{1}H NMR depending on the chemical shift at 6.5666 ppm (Mean ± SD, n=3).

The reciprocal plot showed linearity, which suggested that the stoichiometric ratio was 1:1. The mean K value was calculated as shown in Table 5.19 and found to be 199 M^{-1} based on the chemical shift difference of the H-C_1 proton.

Table 5.19: Results of the stability constant between budesonide and DIMEB added at 0, 0.075, 0.15, 0.225, 0.3 and 0.375 mM in HPFP using ^{1}H NMR.

Proton NO.	Chemical shift (ppm)	Stability constant, K (M^{-1})				SD	% CV
		1	2	3	Mean		
H-C_1	6.5666	203	194	200	**199**	4.6	2.3

The stoichiometry of the complex was confirmed by Job's diagram as described in Section 2.2.3.3, based on the chemical shift changes of H-C_1 proton of BUD at 6.5666 and 6.5600 ppm (Tables 5.20 and 5.21).

Table 5.20: Results of ^{1}H NMR analysis for the determination of stoichiometry between budesonide and DIMEB in HPFP based on the chemical shift at H-C_1 proton of budesonide at 6.5666 ppm.

[BUD] (mM)	r	$\delta_{complex}$ (ppm)	$\Delta\delta_{obs}$ (ppm)	$\Delta\delta$[BUD]	$\Delta\delta$[BUD]*10^4
0.175	1	6.5666	0	0	0
0.1575	0.9	6.5674	0.0008	12.6 x 10^{-5}	1.26
0.14	0.8	6.5685	0.0019	26.6 x 10^{-5}	2.66
0.1225	0.7	6.5706	0.004	49 x 10^{-5}	4.9
0.105	0.6	6.573	0.0064	67.2 x 10^{-5}	6.72
0.0875	0.5	6.5756	0.009	78.8 x 10^{-5}	7.88
0.07	0.4	6.5763	0.0097	67.9 x 10^{-5}	6.79
0.0525	0.3	6.5771	0.0105	55.1 x 10^{-5}	5.51
0.035	0.2	6.5791	0.0125	43.8 x 10^{-5}	4.38
0.0175	0.1	6.5814	0.0148	25.9 x 10^{-5}	2.59
0	0	0	0	0	0

δ_{free} = 6.5666 ppm

Table 5.21: Results of ^{1}H NMR analysis for the determination of stoichiometry between budesonide and DIMEB in HPFP based on the chemical shift at H-C_1 proton of budesonide at 6.5600 ppm.

[BUD] (mM)	r	$\delta_{complex}$ (ppm)	$\Delta\delta_{obs}$ (ppm)	$\Delta\delta$[BUD]	$\Delta\delta$[BUD]*10^4
0.175	1	6.5600	0	0	0
0.1575	0.9	6.5617	0.0017	26.8 x 10^{-5}	2.68
0.14	0.8	6.5636	0.0036	50.4 x 10^{-5}	5.04
0.1225	0.7	6.566	0.006	73.5 x 10^{-5}	7.35
0.105	0.6	6.5683	0.0083	87.2 x 10^{-5}	8.72
0.0875	0.5	6.5714	0.0114	99.8 x 10^{-5}	9.98
0.07	0.4	6.5733	0.0133	93.1 x 10^{-5}	9.31
0.0525	0.3	6.5751	0.0151	79.3 x 10^{-5}	7.93
0.035	0.2	6.5768	0.0168	58.8 x 10^{-5}	5.88
0.0175	0.1	6.5791	0.0191	33.4 x 10^{-5}	3.34
0	0	0	0	0	0

δ_{free} = 6.5600 ppm

The continuous variation plot confirmed the 1:1 stoichiometry as the maximum was at r = 0.5 (Figure 5.27). These data are in agreement to those obtained from the titration experiments which followed a linear trend when using the Hildebrand-Benesi approach.

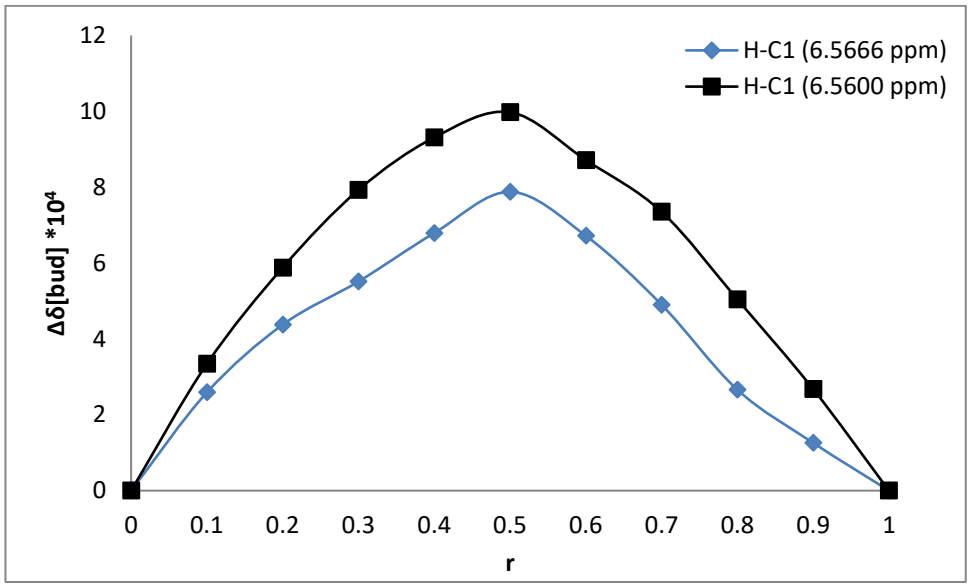

Figure 5.27: Determination of the stoichiometry of the complex between budesonide and DIMEB in HPFP by ^{1}H NMR based on H-C_1 proton of budesonide.

5.7 Complexation study of BDP and DIMEB

The study of the complexation between BUD and DIMEB was performed using the same previous method to study the complexation of BDP with TRIMEB. The findings demonstrated that very minor shift was observed for only H-C_{19} peak at 1.0206 ppm, other peaks in the high field region such as H-C_{18} and methyls at C_{17} and C_{21} were not shifted (Figure 5.28).

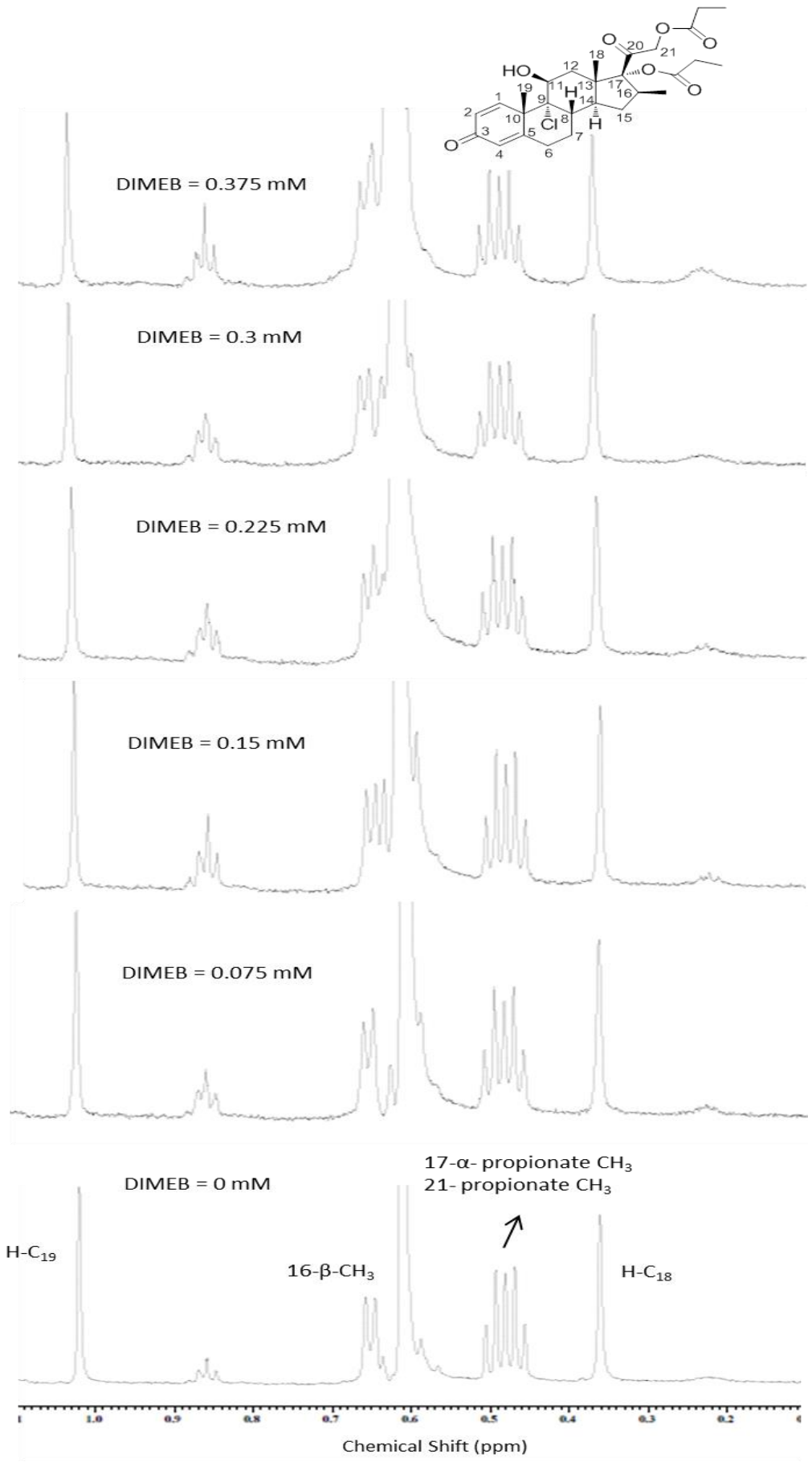

Figure 5.28: BDP (0.2 mM) chemical shift in high field region (0.1-1.1 ppm) with the addition of DIMEB at 0, 0.075, 0.15, 0.225, 0.3 and 0.375 mM in HPFP.

In addition, a slight downfield shift was observed for the H-C_4 proton at 5.2943 ppm of the quinone ring, as the concentration of TRIMEB was increased, and no observable shift was noted for both H-C_1 and H-C_2 protons of the quinone ring. The spectra of the complexed BDP in the low field region are shown in Figure 5.29.

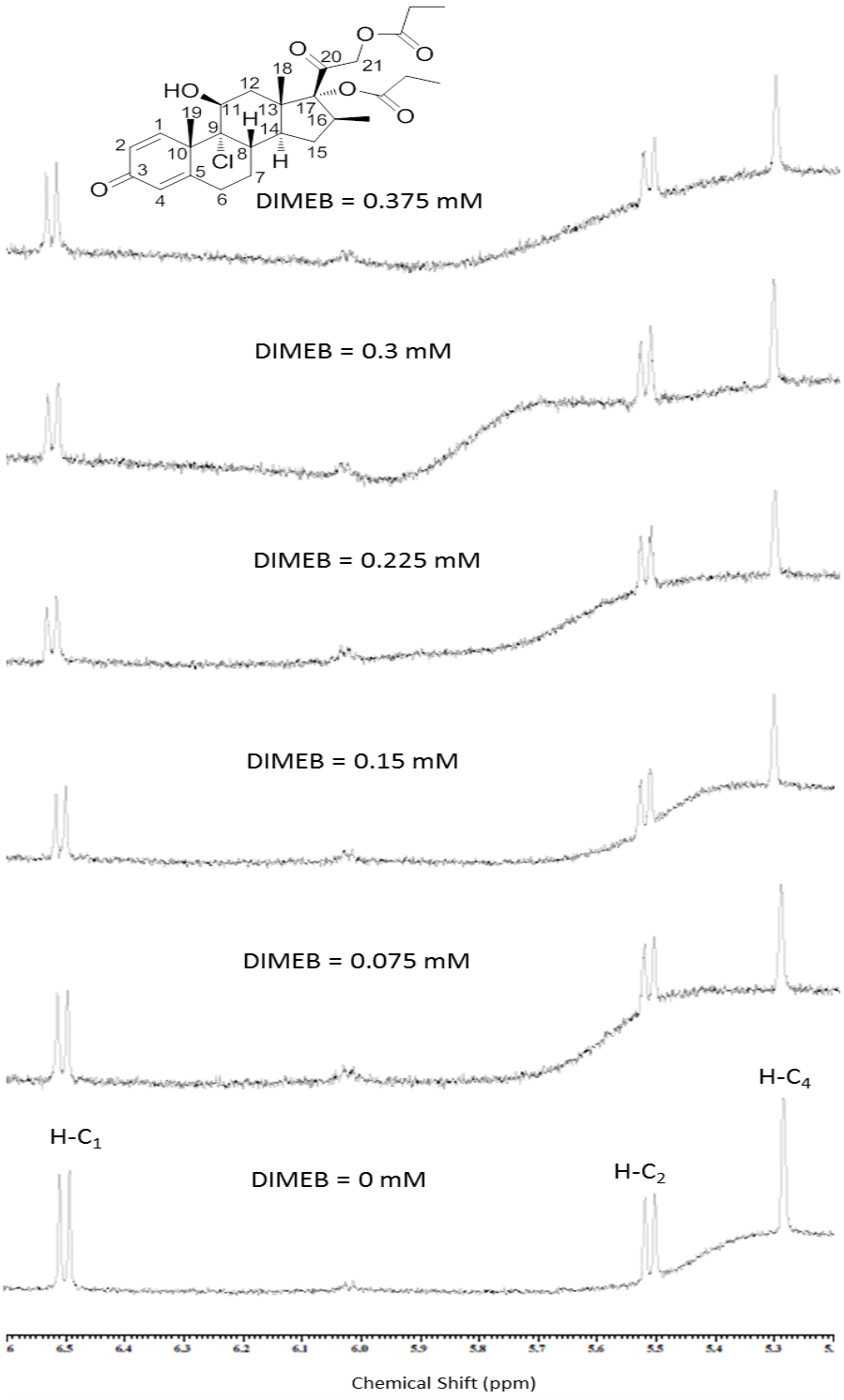

Figure 5.29: BDP (0.2 mM) chemical shift in low field region (5.2-6.6 ppm) with the addition of DIMEB at 0, 0.075, 0.15, 0.225, 0.3 and 0.375 mM in HPFP.

The chemical shift differences of the H-C_4 proton at 5.2943 ppm are presented in Table 5.22 and the stability constant calculations using the Hildebrand-Benesi approach are showed in Table 5.23 with reciprocal plot shown in Figure 5.30.

Table 5.22: Results of the chemical shift of BDP and DIMEB added at 0, 0.075, 0.15, 0.225, 0.3 and 0.375 mM in HPFP using ^{1}H NMR.

Experiment number	Proton position (ppm)	DIMEB concentration (mM)					
		0	0.075	0.15	0.225	0.3	0.375
		Chemical shift (ppm)					
1			5.2976	5.3015	5.3040	5.3073	5.3086
2	H-C_4	5.2943	5.2974	5.3009	5.3036	5.3067	5.3075
3			5.2973	5.3007	5.3033	5.3063	5.3070
Mean			5.2974	5.3010	5.3036	5.3068	5.3077
SD			0.0002	0.0004	0.0004	0.0005	0.0008
% CV			0.0029	0.0079	0.0066	0.0095	0.0154

Table 5.23: Results of the complexation between BDP and DIMEB added at 0.075, 0.15, 0.225, 0.3 and 0.375 mM in HPFP using ^{1}H NMR depending on the chemical shift at 5.2943 ppm.

DIMEB (mM)	1/DIMEB (mM^{-1})	$1/\Delta\delta_{obs}$ (5.2943 ppm)			
		1	2	3	Mean
0.075	13.3	303	322.6	333.3	319.7
0.15	6.7	138.9	151.5	156.3	148.9
0.225	4.4	103.1	107.5	111.1	107.2
0.3	3.3	76.9	80.7	83.3	80.3
0.375	2.7	69.9	75.8	78.7	74.8

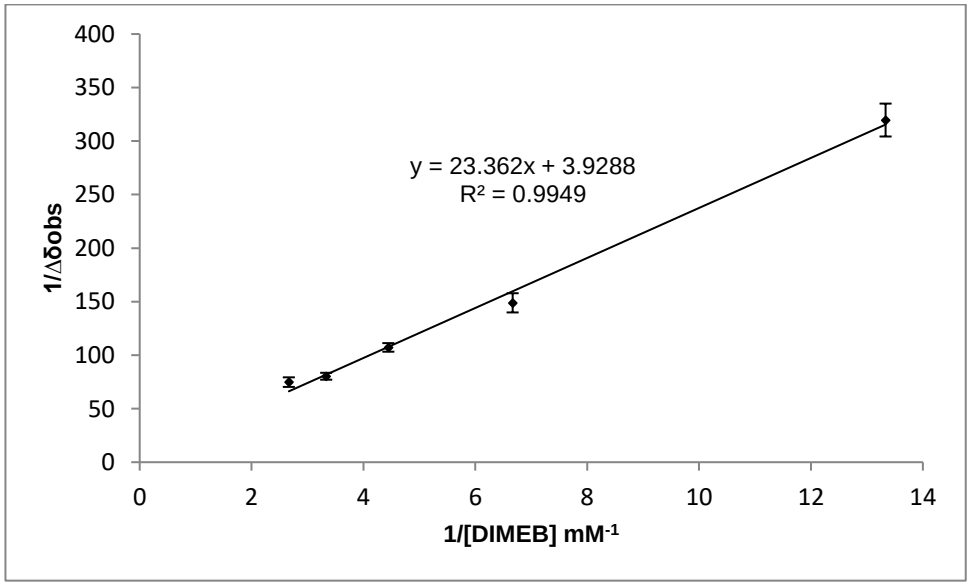

Figure 5.30: Reciprocal plot for the determination of association constant between BDP and TRIMEB in HPFP by ^{1}H NMR depending on the chemical shift at 5.2943 ppm (Mean ± SD, n=3).

The reciprocal plot showed a good linearity which indicated the stoichiometry was 1:1. The mean K value was calculated and found to be 168 M^{-1} (Table 5.24).

Table 5.24: Results of the stability constant between BDP and DIMEB added at 0.075, 0.15, 0.225, 0.3 and 0.375 mM in HPFP using ^{1}H NMR.

Proton NO.	Chemical shift (ppm)	Stability constant, K (M^{-1})				SD	% CV
		1	2	3	Mean		
H-C_4	5.2943	168	164	171	**168**	3.51	2.09

5.8 Discussion

5.8.1 Comparison between corticosteroids compounds

The complexation between the corticosteroids BUD, BDP, MOM and FLU with TRIMEB in HPFP was examined in this work. The results of the chemical shift displacements of some protons of the compounds involved in the complexation are presented in Table 5.25.

Table 5.25: A summary of the chemical shift displacements (in ppm) for BUD, BDP, MOM and FLU with 2 mM TRIMEB in HPFP related to the chemical shift of the free compounds.

Compound	Chemical shift displacements (ppm)				
	H-C_1	H-C_2	H-C_4	H-C_{18}	H-C_{19}
BUD	D** (0.07, *R*) D* (0.02, *S*)	NS	U* (0.01)	D** (0.17, *R*)	D* (0.01)
BDP	NS	NS	D* (0.07)	NS	D* (0.05)
MOM	NA	NA	NA	NS	D* (0.04)
FLU	NA	NA	NA	NS	D* (0.02)

D* = small downfield, D** = large downfield, U* = small upfield, NS = no significant shift, NA = S/N too low to interpret, *R*, *S* = enantiomers of BUD

The K values of BDP, MOM and FLU were 197.5, 130 and 86 M^{-1} respectively, which were less than that of BUD enantiomers (621 and 222 M^{-1} for *R* and *S* enantiomers respectively). The reciprocal plot of 1/[TRIMEB] versus $1/\Delta\delta_{obs}$ for the all studied corticosteroids followed a linear trend, indicating that the complexation had a stoichiometry of 1:1. The continuous variation method was then adopted to verify the stoichiometry 1:1 of the inclusion complex for BUD only (as a representative model for the other compounds) with TRIMEB. The Job's plot showed a maximum at r = 0.5 which suggests a 1:1 stoichiometry of the inclusion complex and corroborates the data obtained in the titration methods.

The complexation of all studied corticosteroids with TRIMEB in HPFP can be ranked as BUD > BDP > MOM > FLU based on the stability constant values. This might be owing to the presence of the substitution groups at C17 which are a furan ring in MOM and propionate chains in BDP and FLU structures (Figure 5.31). These groups are likely to cause steric hindrance, which hinder the entrance of BDP, FLU and MOM deeper into the TRIMEB cavity compared to BUD which does not have a bulky group at C17. Also, the presence of a Cl atom at C9 in BDP and MOM, and F atoms at C6 and C9 in FLU can cause an

extra hindrance for the compounds to enter into the TRIMEB cavity compared to the simple H atom at C9 in BUD.

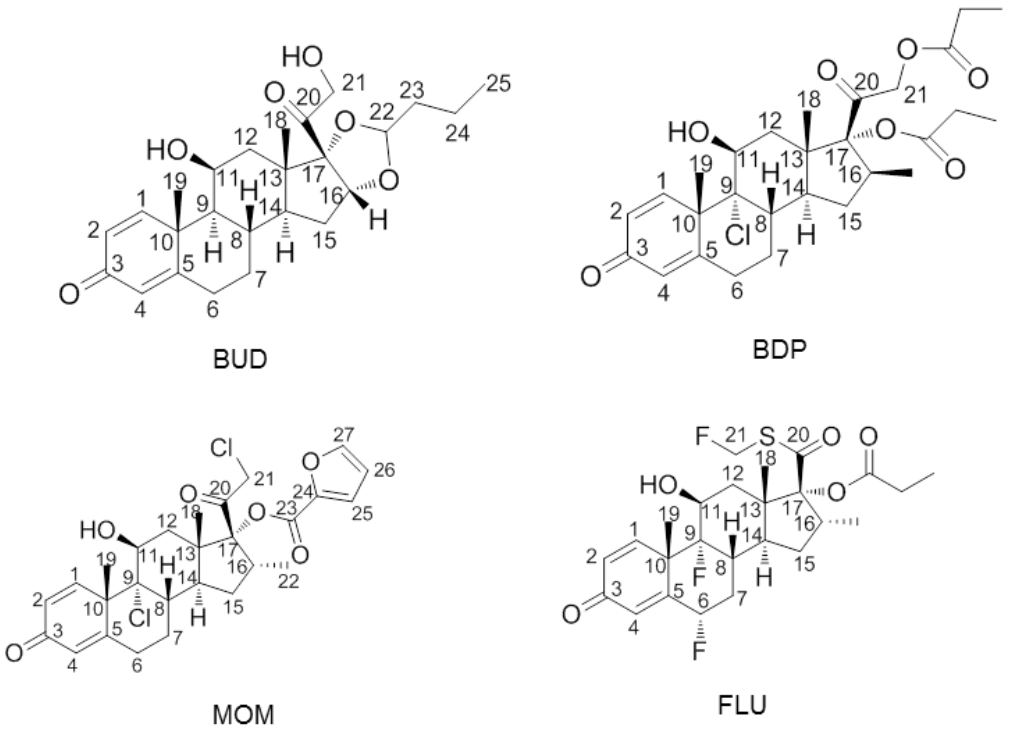

Figure 5.31: Chemical structure of BUD, BDP, MOM and FLU

A similar explanation is suggested by Larsen *et al*. who studied the complexation of 6*α*-methyl prednisolone and prednisolone with *γ*CD and *β*CD. They found that the 6*α*-methyl prednisolone prefers the *γ*CD with large cavity whereas prednisolone forms stronger complex with *β*CD of smaller cavity.[202] This might be explained by the presence of methyl group at 6 position in the structure of 6*α*-methyl prednisolone (Figure 5.32) which causes hindrance for the compound to go further into the small cavity of *β*CD compared to the prednisolone.

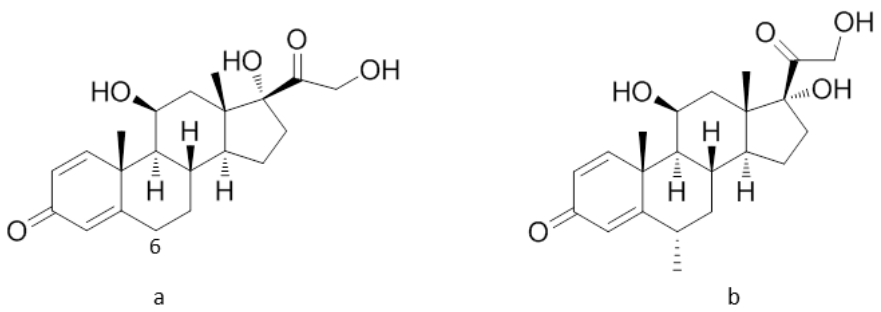

Figure 5.32: Chemical structure of (a) prednisolone and (b) 6*α*-methyl prednisolone.

5.8.2 CD type and its effect on complexation

The complexation between BUD and BDP with DIMEB in HPFP was determined and the displacements values of both complexed compounds are presented in Table 5.26 compared to the chemical shift of the pure compound.

Table 5.26: Chemical shift displacements of the BUD and BDP with 0.375 mM DIMEB compared to the chemical shift of the free compound.

Compound	Chemical shift displacements (ppm)				
	H-C_1	**H-C_2**	**H-C_4**	**H-C_{18}**	**H-C_{19}**
BUD	D* (0.02)	NS	NS	D* (0.01)	D* (0.01)
BDP	NS	NS	D* (0.01)	NS	D* (0.01)

D* = small downfield, NS = no significant shift

The small shift of some protons of both compounds suggested that both molecules partially entered into the DIMEB cavity, as it might be situated near the DIMEB rim. The small shift change of H-C_{19} proton of BUD and BDP could be attributed to the interaction of this proton with the outside surface of DIMEB.

The K values were determined for BUD and BDP with DIMEB and found to be 199 and 168 M^{-1} respectively. The results of the stability constant between BUD and DIMEB (199 M^{-1}) was less than that obtained with TRIMEB at 621 and 222 M^{-1} for both *R*- and *S*-enantiomers in HPFP. These results contradict those obtained for BUD with TRIMEB/DIMEB in D_2O, MeOD and $CDCl_3$ in which higher K values were obtained with DIMEB than with TRIMEB. The K values of BUD were 4446, 116 and 73 M^{-1} with DIMEB and 429, 91 and 64 M^{-1} with TRIMEB in D_2O, MeOD and $CDCl_3$ respectively. Zoppi *et al*. found that the affinity constant of sulfamethazine with methyl *β*CD (M*β*CD, the OH group at C2 was substituted with methyl group) was less than that with *β*CD in water (higher solubility of M*β*CD in water compared to that of *β*CD). They suggest that no hydrogen bond was formed between the guest and the substituted OH in the M*β*CD or that it could be related to the steric hindrance of the methyl group which hampers the entrance of the guest into the CD cavity.[220] It has been reported that higher CD solubility in the solvent leads to the availability of more guest molecules for the complexation. The key findings with this series of experiments is the solubility of the CD (host) in the solvent under study, drives the level of complexation observed i.e. the more soluble the host is in the given solvent, the more is available for complexation and the higher the association constant observed.[221] Our experiments have shown the strongest complexation

of BUD in D_2O was with DIMEB whereas in HPFP with TRIMEB. This could be explained by the solubility of the CD in the solvent where the water solubility of DIMEB and TRIMEB is 57 and 31 g/100 mL whereas their solubility in HPFP are 1 and 6 mg/mL (0.1 and 0.6 g/100 mL) respectively. As the CD solubility is higher in D_2O, there are more CD molecules available for complex formation. Therefore, because DIMEB solubility in water is higher than TRIMEB, with the inverse true in HPFP where TRIMEB solubility is higher than DIMEB, this leads to the availability of more CD molecules in the solution to form complexation with BUD. This might justify the stronger complexation of BUD with DIMEB in D_2O and with TRIMEB in HPFP.

5.8.3 Chiral discrimination of BUD by TRIMEB

The complexation between BUD and TRIMEB in HPFP was examined in this work. The results showed that the peak at 0.34 ppm appears as a singlet at 0.4 mM TRIMEB concentration which was then split into two peaks; the one observed at 0.34 ppm showing no significant shift with increasing CD concentration, the second moving significantly to 0.44 ppm at 2 mM TRIMEB concentration. Both peaks could be assigned to the H-C_{18} peak of the *S*-enantiomer of BUD whereas the latter could be related to the H-C_{18} peak of *R* enantiomer of BUD. Accordingly, further experiments on the pure enantiomer *R*-BUD were carried out for the purpose of full assignment of these peaks, by comparing the results to those of the racemic BUD experiments.

The results showed one singlet peak at 0.44 ppm at 2 mM TRIMEB concentration, which was consistent with the peak located at the same chemical shift in the racemic BUD spectrum (annotated with a star in Figure 5.33, b and c). This resonance could therefore be assigned to the H-C_{18} peak of the *R*-enantiomer of BUD. The peak which displayed no displacement at 0.34 ppm (annotated with a dot in Figure 5.33, b) in the spectrum of racemic BUD could be assigned to the H-C_{18} peak of the *S*-enantiomer of BUD. The H-C_{19} proton of the racemic BUD was fully split into two distinctive peaks at 2 mM TRIMEB concentration (Figure 5.33, b). However, this proton in the *R*-enantiomer appeared as singlet in the complexed form (Figure 5.33, c) suggesting that another peak appeared in the spectrum of the racemic BUD was related to the *S*-enantiomer (annotated with a dot in Figure 5.33, b).

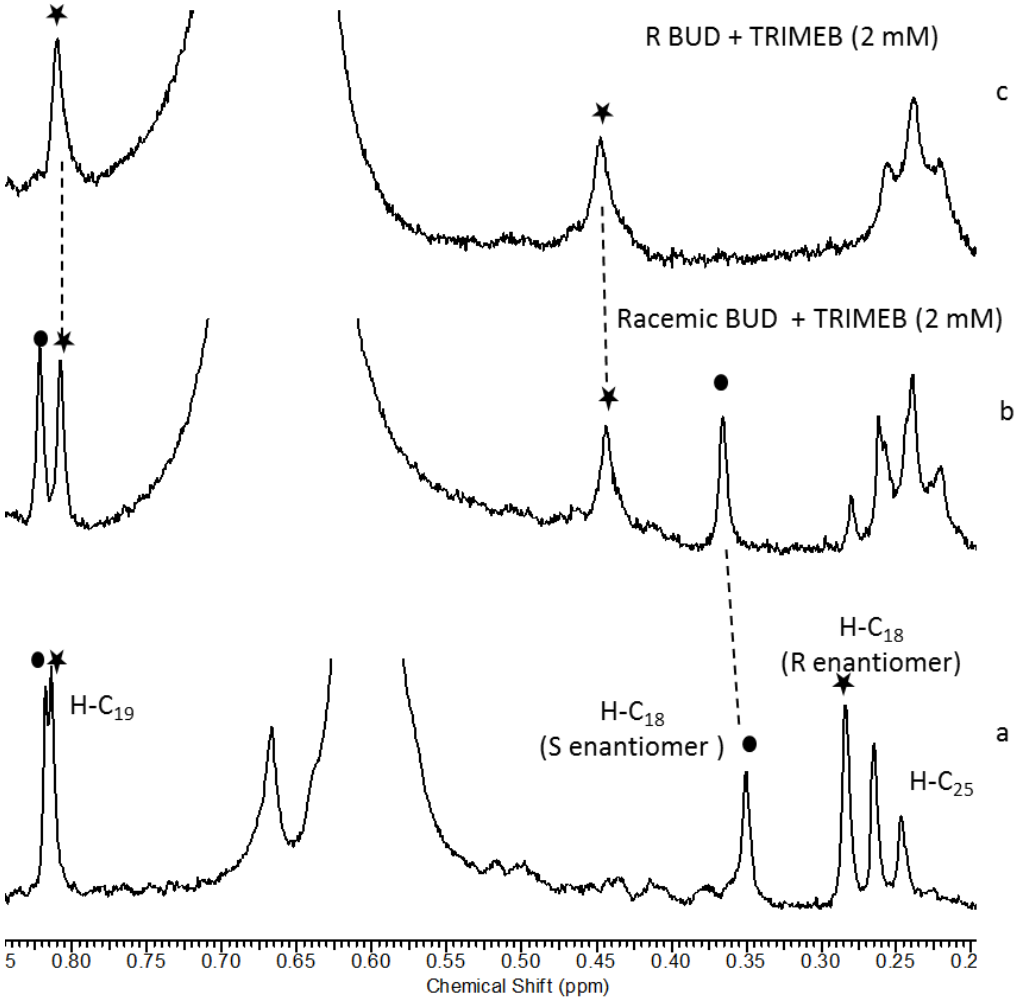

Figure 5.33: Chemical shift in high field region (0.2-0.85 ppm) of (a) pure BUD, (b) racemic and (c) pure *R*-enantiomer of BUD (0.0875 mM) with 2 mM TRIMEB in HPFP. The peaks annotated with star and dot were assigned to *R*- and *S*-enantiomer of BUD.

The H-C_4 proton of the pure *R*-enantiomer appeared as singlet peak (Figure 5.34, c) whereas in the racemic solution the signal was partially split, and showed an increase in displacement when the amount of TRIMEB was increased (Figure 5.34, b). This indicated that this peak of the racemic BUD was related to both enantiomers. No significant change was observed for H-C_2 proton of the quinone ring. A downfield shift was observed for the H-C_1 proton of the quinone ring with a multiplicity change (*J*-coupling constant increase with increasing CD concentration) for racemic BUD (Figure 5.34, b) whereas the peak was observed as doublet for *R*-enantiomer (Figure 5.34, c). Accordingly, the two peaks with the highest downfield shift in the racemic BUD spectrum were related to the *R*-enantiomer whereas the other two appear to be related to the *S*-enantiomer (annotated with a star and a dot in Figure 5.34, b respectively).

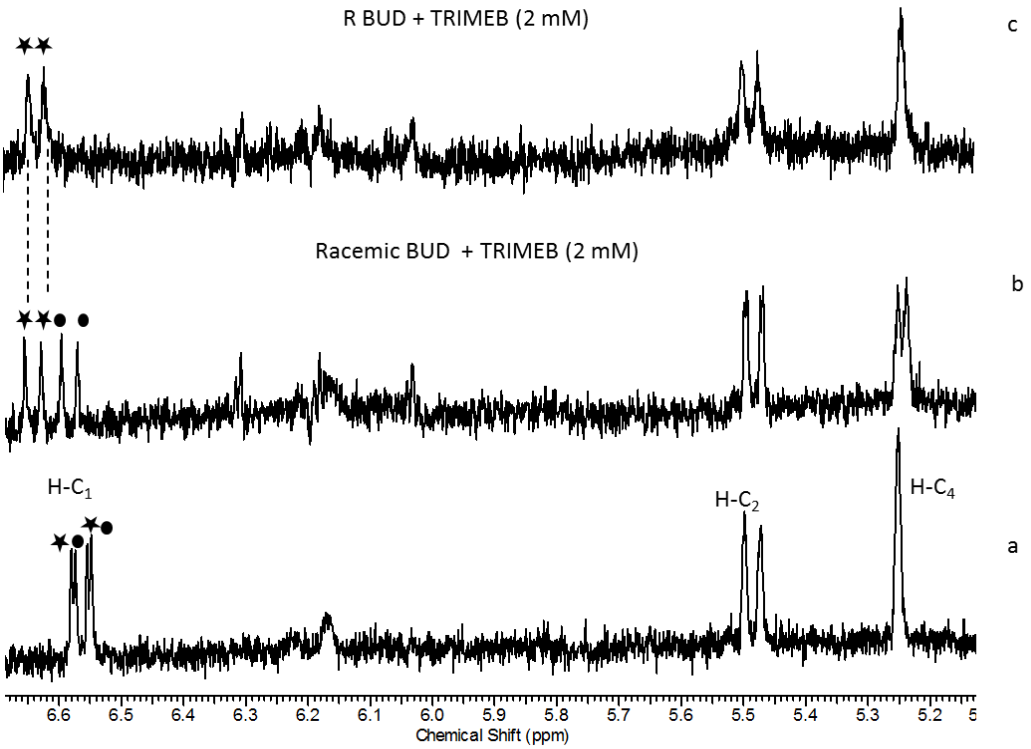

Figure 5.34: Chemical shift in low field region (5.1-6.7 ppm) of (a) pure BUD, (b) racemic and (c) pure *R*-enantiomer of BUD (0.0875 mM) with 2 mM TRIMEB in HPFP. The peaks annotated with star and dot were assigned to *R*- and *S*-enantiomer of BUD.

The downfield shift of H-C_1 proton of both *R* and *S*-enantiomers and only H-C_{18} proton for *R*-enantiomer may account for the structure rearrangement and conformational changes of guest (BUD) molecule after the complexation[200] and also to the change in the local polarity[214] or a deshielding effect resulting from van der Waals interaction with the carbohydrate chains.[213] It may also be due to the interaction of these protons (H-C_1 and H-C_{18}) with the hydrophilic, external region of the TRIMEB.[201] Consequently, it could be expected that these protons were located at a large distance from the oxygen compared to the hydrogen atom. The small upfield shift observed for the H-C_4 proton of both enantiomers could be ascribed to the conformational changes resulting from the complexation and from the shielding effect of the oxygen atoms (rich in π electron) located on the inner surface of the CD cavity. This could suggest that this proton was located close to the oxygen atom in the CD cavity.[155,201,213] This leads us to suggest that both enantiomers of BUD formed a complex by taking the position where only H-C_4 proton of the quinone ring (experienced upfield shift) entered and interacted with the oxygen atom located on the inner surface of TRIMEB.

The small shift observed resulted from partial entrance of the quinone ring into the TRIMEB cavity, with the other H-C_1 and H-C_2 protons of the quinone ring were situated outside the cavity. The downfield shift of the H-C_1 proton could be accounted for by its interaction with the methoxyl oxygen of TRIMEB. However, the shift change of H-C_1 proton of the pure *R*-enantiomer was larger than *S*-enantiomer, suggesting that it was closer to the methoxyl oxygen atoms compared to *S*-enantiomer. The spatial structure of the *R*-enantiomer made the H-C_{18} proton interact with the oxygen atom of the TRIMEB more significantly than that in the *S*-enantiomer, where the H-C_{18} proton was situated away from the TRIMEB cavity. A more downfield shift of both H-C_1 and H-C_{18} protons of *R*-enantiomer led to the stronger complexation with TRIMEB compared to *S*-enantiomer in which a smaller downfield shift of the H-C_1 proton was observed with no shift for H-C_{18} proton. In conclusion, both enantiomers formed complexation with TRIMEB in which only the H-C_4 proton was inside the cavity, the H-C_1 is thought to be outside, but near the cavity. The downfield shift of the H-C_{18} proton of *R*-enantiomer was due to its different spatial structure which could cause this proton to be closer to the oxygen atom of the TRIMEB cavity, when compared to the *S*-enantiomer.

The K values of *R*- and *S*-enantiomers were 621 and 222 M^{-1} respectively, this was in agreement with the experimental results of the NMR titration, where the *R*-enantiomer displayed the largest chemical shift changes and thus demonstrates that a stronger complexation occurs in *R* when compared to the *S*-enantiomer, and shows that TRIMEB displays chiral discrimination. From this preliminary analysis, TRIMEB can be chosen as a chiral selector for BUD, the CDs in general can be used as chiral solvating agents (CSAs) and can cause enantiomeric discrimination by two main mechanisms. Firstly, the complexes of the enantiomer pairs with the CD as CSA are diastereomers and thus display different chemical shifts. The second is the difference in the association constants of the two enantiomers with the CD as one of the enantiomers preferentially binds with the CD, with the time-averaged solvation of both of them being different.[222] The enantiomers interact with the chiral solvating agent through hydrogen bonding, π stacking and dipole–dipole interactions and are thus able to form diastereomers with the CD, which can be detected by NMR.[223]

6 Development of Cyclodextrin-Functionalised Metal Nanoparticles as Receptors for as Surface Enhanced Raman Spectroscopy of Corticosteroids

The steroid binding properties of CD systems offers a potential application in selective identification agents. In a pharmacological context steroid species may be present in a complicated array of species and creating a sensitive and selective probe for these compounds for direct application (overcoming the need for extraction and/or separation processes) would be highly desirable. This chapter addresses the development of selective Raman spectroscopic probes for the corticosteroid utilising the Surface Enhanced Raman Spectroscopy (SERS).

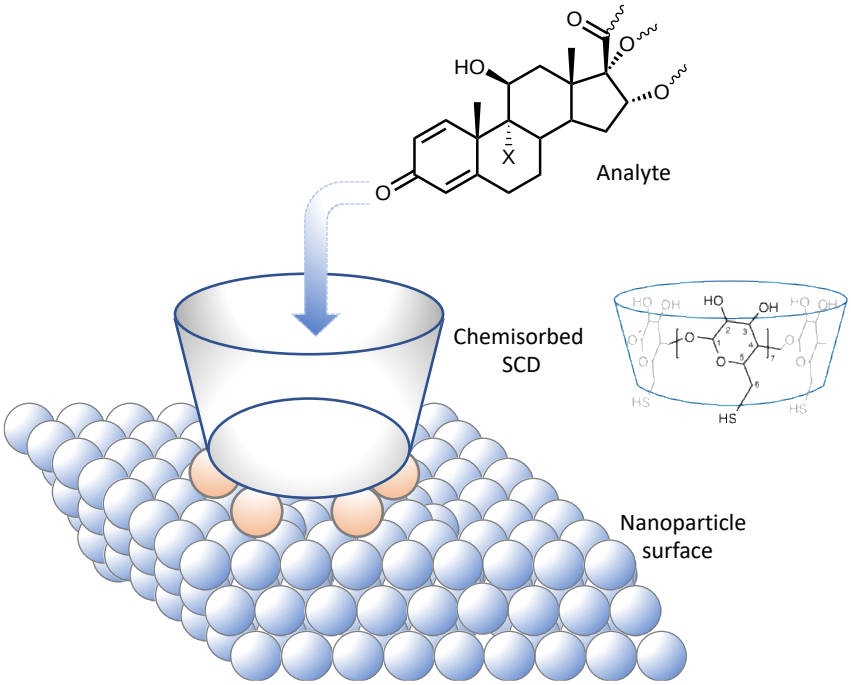

Figure 6.1: Schematic view of the design of selective SERS substrates through functionalisation of metal nanoparticle surfaces with per-6-thio-β-cyclodextrin.

The chosen strategy for development of these materials involves replacement of primary hydroxyl groups at the narrower rim of β-cyclodextrin (C6) with thiol groups to tether the CD host to the metal nanoparticle surface. It is anticipated that this will provide a means to orientate the steroid at the metal nanoparticle surface and allow selective enhancement of appropriate Raman signals.

The thiolated-cyclodextrin was prepared in two steps from β-cyclodextrin following the method described by Rojas *et al.*[167] (Figure 6.2). Characterisation data corresponded with the published values.

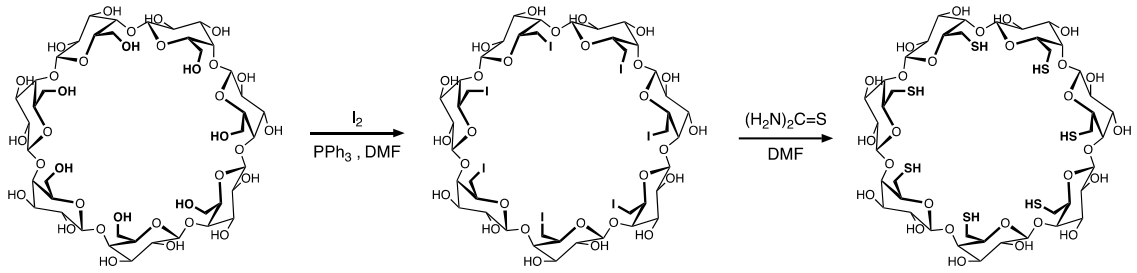

Figure 6.2: The synthesis of per-6-thio-β-cyclodextrin.[167]

6.1 Characterisation of the Silver and Gold Nanoparticle Formulations

Silver nanoparticle formulations (Ag-NP) were prepared by borohydride reduction of silver nitrate in aqueous solution.[168] Gold nanoparticles were prepared in a two-step process:[169] seed solutions were prepared from *aqu.* chloroauric acid ($HAuCl_4$) by citrate reduction and these seed were then added to an aqueous solution of $HAuCl_4$ followed by sodium citrate. In each case, solutions were centrifuged to homogenise the nanoparticle content. In the following sections, typical characterisation data for these NP formulations are discussed.

6.1.1 Plasmon resonance

The optical activity of the metal nanoparticles is a result of their surface plasmon resonance.[224] UV-Vis spectroscopy is an established technique used to identify the formation and infer the shape of the metal nanopartciles.[225] The absorption spectra for both Au- and Ag-NP formulations were recorded in the range of 300-900 nm. The Ag-NP formulation showed a single intense peak (λ_{max}) at 397 nm which is characteristic of the surface plasmon resonance Ag-NPs[226,227] corresponding with a yellow colouration of the sol (Figure 6.3).

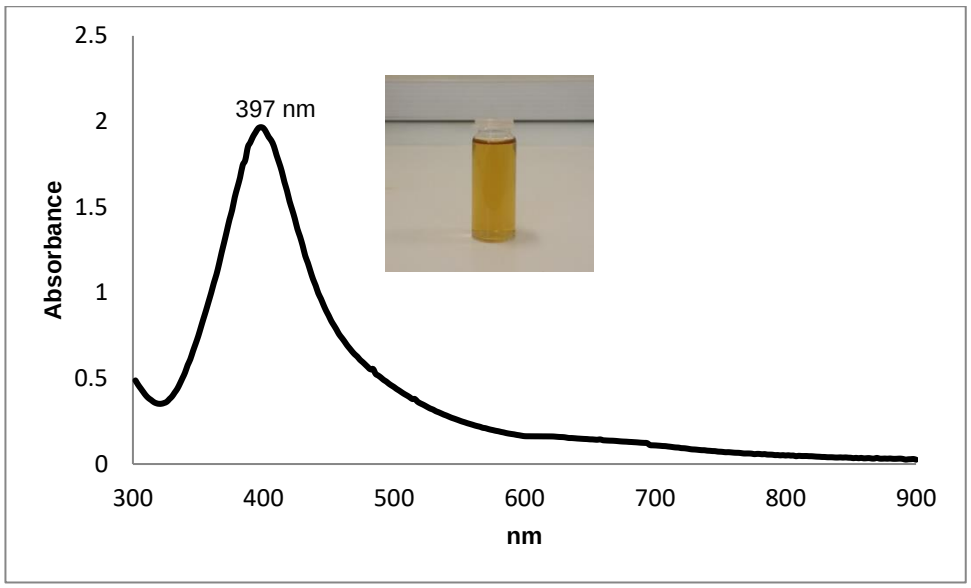

Figure 6.3: UV-Vis absorption spectrum of Ag-NP formulation (λ_{max} = 397 nm).

For the Au-NP formulations, the UV-Vis spectrum again showed a single intense peak (λ_{max}) at 520 nm for seed samples and at 532 nm for the final Au-NP formulations. These are typical of the surface plasmon resonance bands of Au-NPs.[226,227] The bathochromic shift from 520 to 532 nm at the second stage of production can be attributed to the increase in size of the Au-NPs and corresponds with the change of the colour from red to purple in the sol (Figure 6.4).

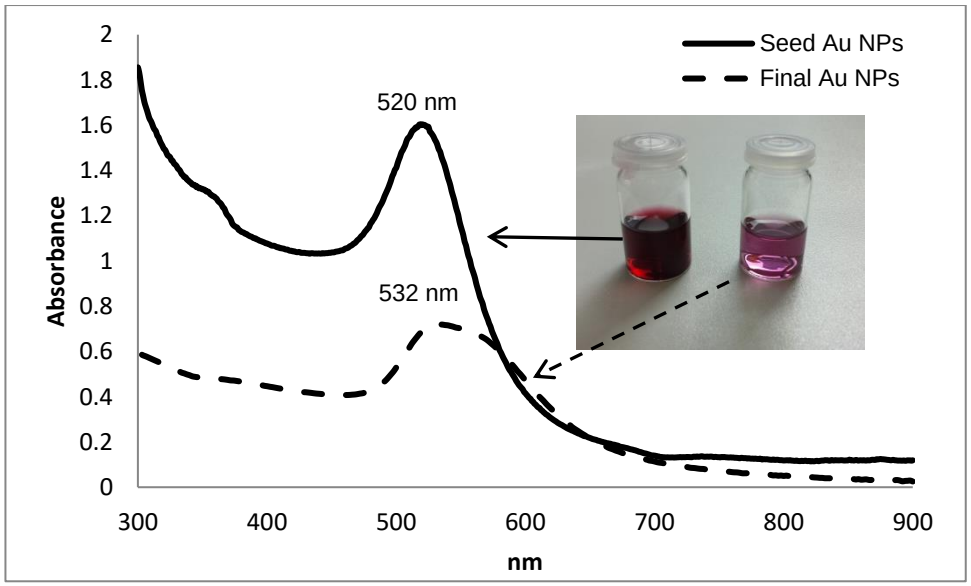

Figure 6.4: UV-Vis absorption spectra of seed (solid line, λ_{max} = 520 nm) and final (dashed line, λ_{max} = 532 nm) Au-NP formulations showing the bathochromic shift of the final formulation consistent with its larger particle size.

In addition, the presence of single surface plasmon resonance bands with relatively narrow bandwidths is consistent with the presence of isometric (essentially spherical) particles formation in both Ag- and Au-NP formulations.[227,228]

6.1.2 Particle analysis: Dynamic Light scattering

Dynamic light scattering (DLS) experiments were conducted for each final Au- and Ag-NP formulation to evaluate the particle dimensions and their distribution. The technique characterises the colloidal dispersion size by exploiting the illumination of particles solution that undergo Brownian motion by a laser beam. The time-dependent fluctuations in the scattered light intensity are analysed by autocorrelation to yield particle dimensions that correlate with the hydrodynamic radius that includes the immobilised solvent sheath associated with each particle.[229]

Uncentrifuged and centrifuged Ag-NP formulations were studied. Intensity plot (Figure 6.5) show a dominant maximum at *ca.* 59 nm and a smaller peak at 5 nm that is attributed to an artefact from the rotation motion of anisometric NPs, a common observation with this technique.[230] The indicated particle size is considerably larger than that given with TEM but this can be attributed to the measurement of the hydrodynamic radius by DLS (*i.e.* particle plus any immobilised solvent sheath). After centrifugation, the average particle size was increased to be 183 nm due to agglomeration of the nanoparticles; a narrowing of the peak-width is noticeable that suggested the narrowing of the size distribution.

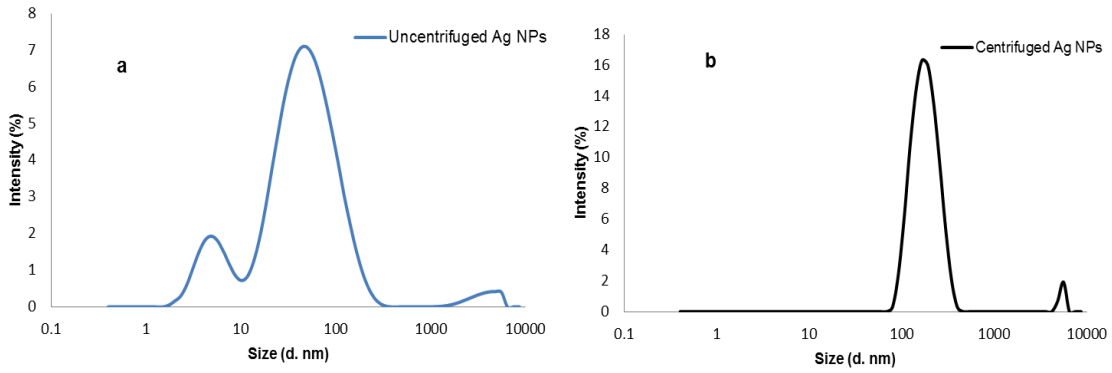

Figure 6.5: Particle size of (a) uncentrifuged and (b) centrifuged Ag-NPs from DLS.

After treatment of both uncentrifuged and centrifuged Ag NPs with per-6-thio-β-cyclodextrin (SCD) to form the functionalised Ag-SCD-NPs peak maxima moved to larger particle size. It has been shown that the indicated particle size for the uncentrifuged Ag NPs increased in each case: 65 *vs.* 59 nm for uncentrifuged formulation and 189 *vs.* 183 nm in the centrifuged system (Figure 6.6). This increase, clearly larger than the width of the SCD molecule itself, does result from the presence of the chemisorbed SCD. Structuring of the aqueous solvent sheath around the nanoparticles is likely to result from to hydrogen bonding networks involving the hydroxyls of the upper rim (C3,4) of SCD.

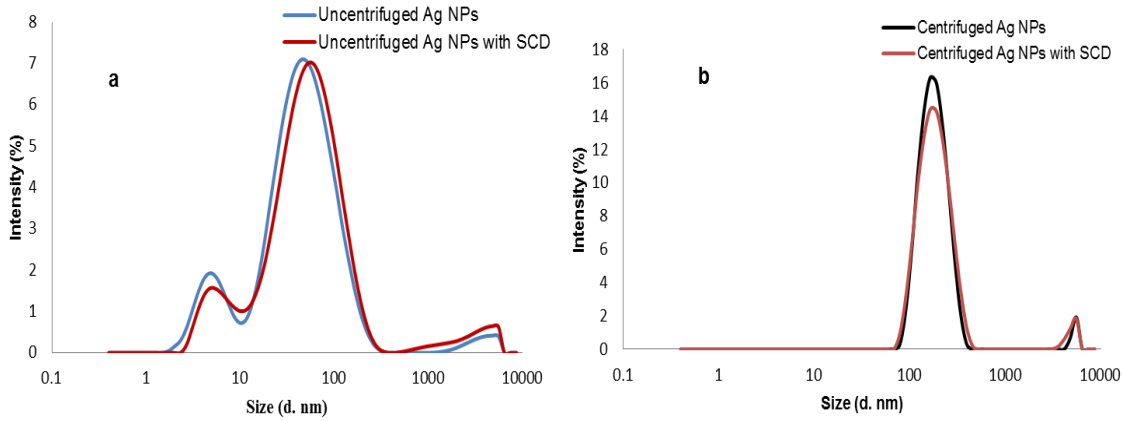

Figure 6.6: Particle size of (a) uncentrifuged Ag-NPs without and with SCD and (b) centrifuged Ag-NPs without and with SCD from DLS.

DLS plots for seed and final Au-NPs (Figure 6.7) show feature that broadly correspond with the Ag-NP analogues. Peak maxima indicate mean particle dimensions of 32 nm for the seed Au-NPs *vs*. 55 nm for the final large Au-NP formulation. Again, artefacts are present in the DLS trace: at 1 and 5 nm for seed and large Au NPs solutions and attributable to rotation motion of anisometric.[230] When the Au NPs solution was centrifuged, the average particle size increased to be 192 nm consistent with significant to agglomeration of the nanoparticles.

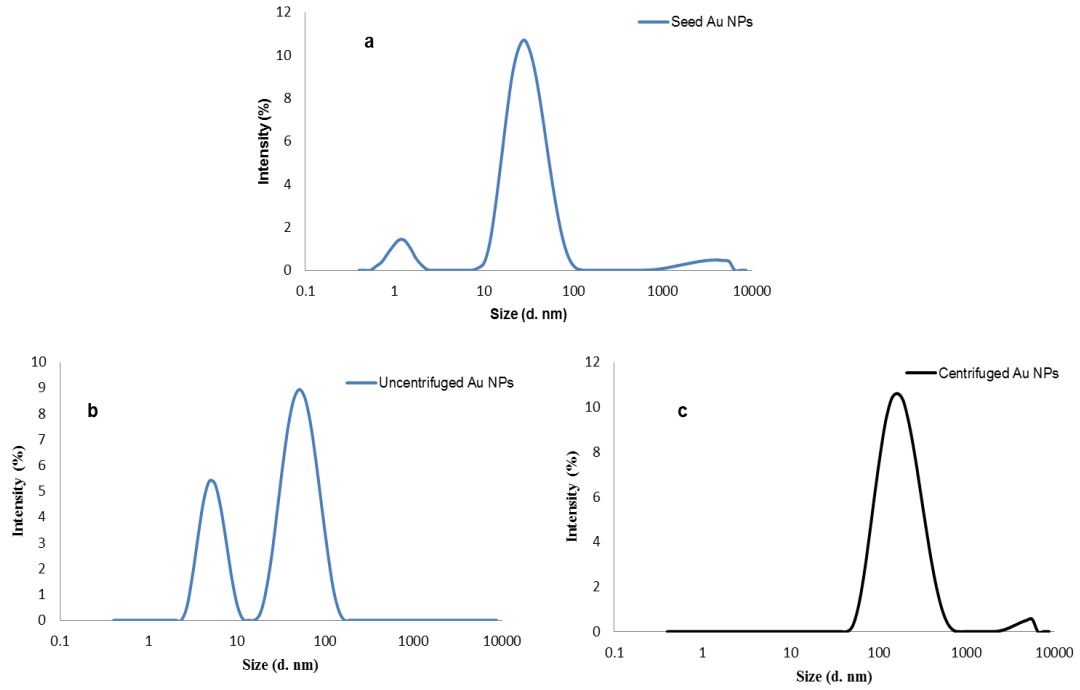

Figure 6.7: Particle size of (a) seed Au-NPs, (b) uncentrifuged and (c) centrifuged final Au-NPs from DLS.

On mixing with SCD to form SCD-Au NPs significant increases in particle dimension were observed (Figure 6.8): 59 nm *vs.* 55 for the uncentrifuged Au-NPs with SCD and 195 nm *vs*. 192 in the centrifuged cases. Again this is attributed to the structuring influence of the absorbed SCD at the surface indicated that SCD formed a little zone around the NPs.

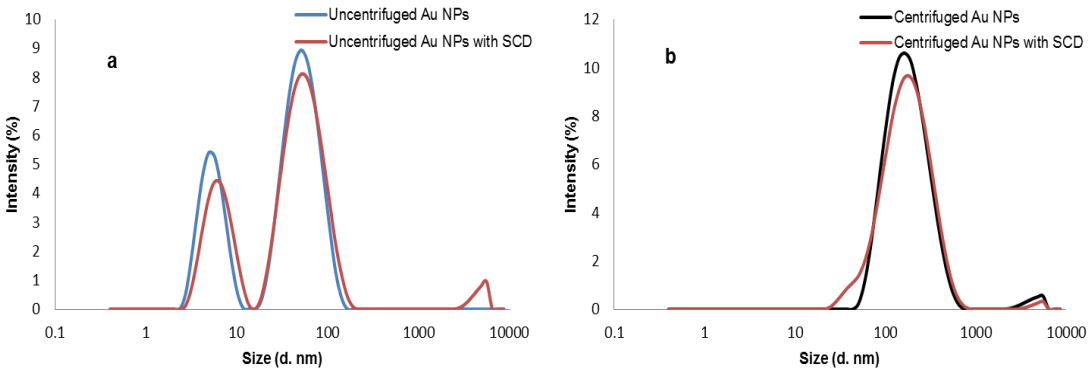

Figure 6.8: Particle size of (a) uncentrifuged Au-NPs without and with SCD and (b) centrifuged Au-NPs without and with SCD from DLS.

6.1.3 Particle analysis: Transmission Electron Microscopy.

The morphology and the particle size of the Ag-NP formulations were studied by Transmission Electron Microscopy (TEM). Visual inspection of the images indicates that the particles are largely spherical in shape (Figure 6.9, a) although some exhibit less regular shape (Figure 6.9, b). A size-distribution histogram derived from the images shows a relatively normal distribution of sizes giving an average particle size of 21 ± 7.5 nm (Figure 6.9, c). After centrifugation, agglomeration of the particles is clearly apparent in the images with intense black mass (Figure 6.9, d) corresponding to materials stacked upon itself while in other areas, particles form ribbons of material though association (Figure 6.9, e). Within these agglomerations, however, discrete largely spherical Ag-NPs are apparent and it is clear that the association caused by centrifugation has not resulted in the fusion of particles. Clearly, the images are consistent with the observations from bulk DLS measurements but provide additional information that in the massed materials, Ag-NP structures appear to remain.

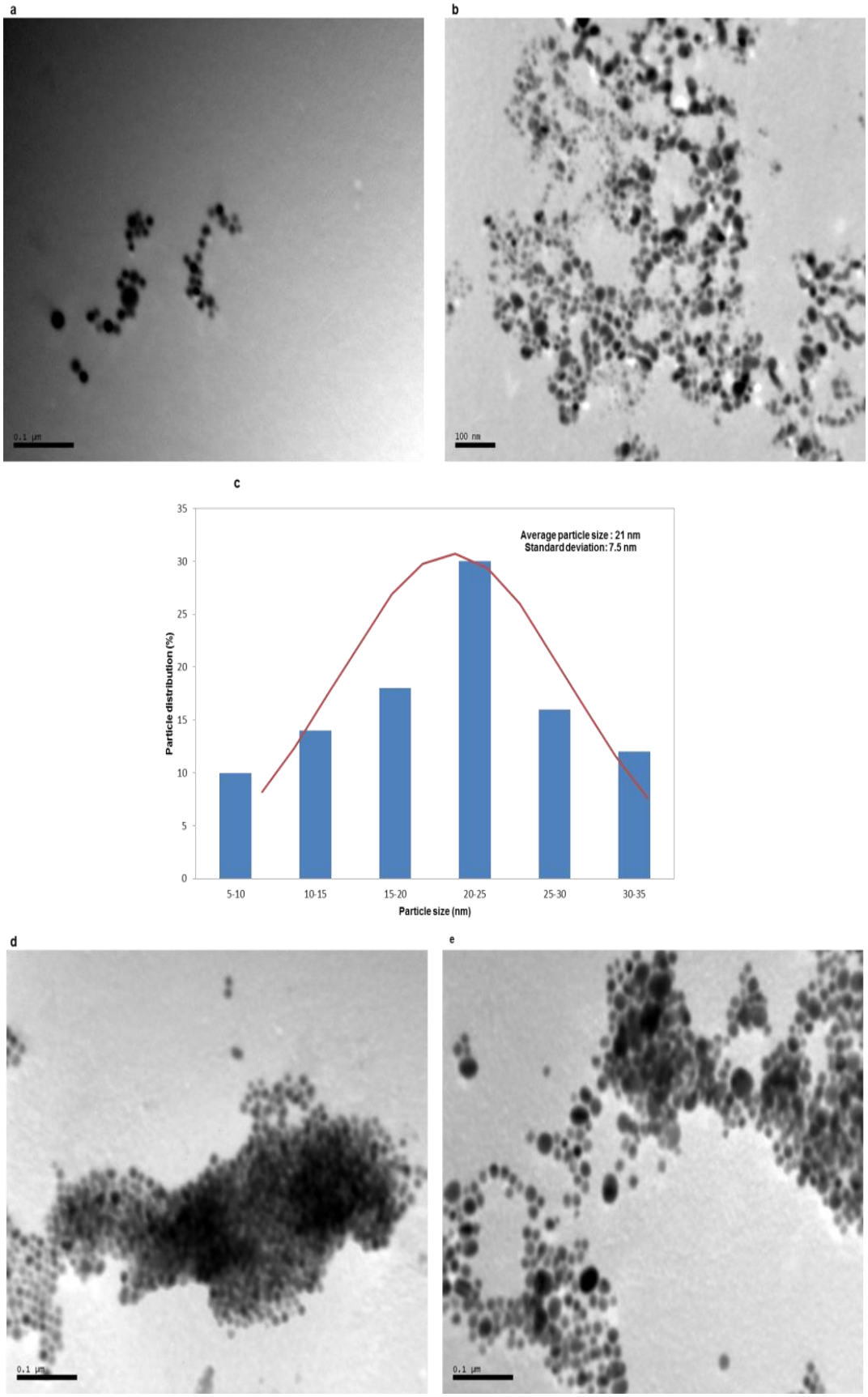

Figure 6.9: TEM images of Ag-NP formulations: (a),(b) two images for the same non-centrifuged sample; (c) the size distribution histogram of non-centrifuged material; (d),(e) two images for the same centrifuged sample showing the agglomeration of particles.

When the uncentrifuged and centrifuged Ag-NPs were mixed with SCD, the TEM images (Figure 6.10) were similar to those described above. Notably, the particulates showed a light grey layer around the nanoparticles which can be attributed to the SCD and is consistent with the presence of the lighter elements (carbon and oxygen) that constitute the SCD structure. Using analogous 3D electron tomography, Andrate *et al*.[231] identified evidence corresponding with a layer of *β*CD around Ag-NPs.

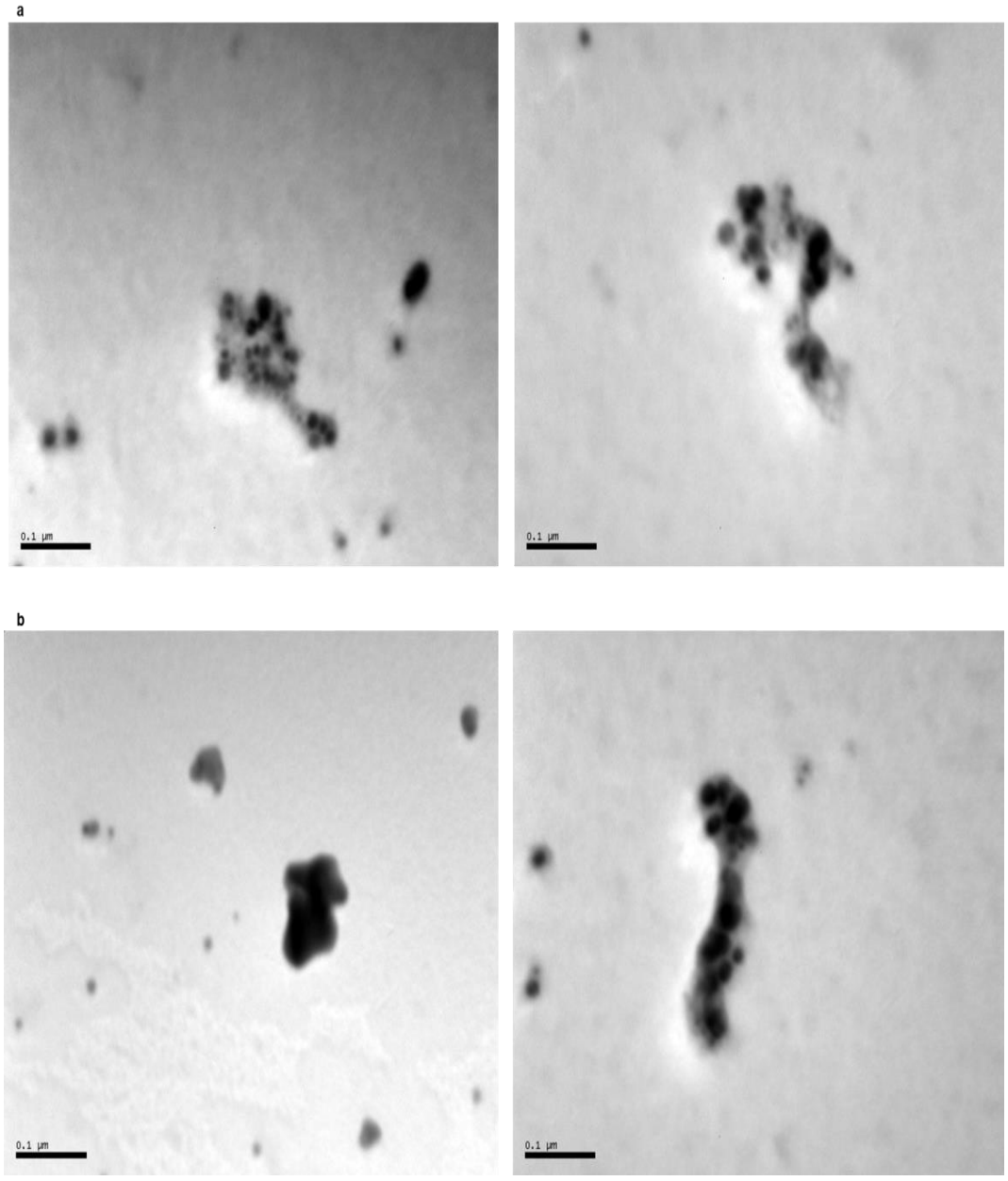

Figure 6.10: TEM different images of SCD-Ag-NP prepared with the same sample of (a) non-centrifuged Ag-NP and (b) centrifuged Ag-NP.

Similar investigation of Au-NP formulations yielded corresponding observations. Images of the Au-NP formulation indicated that the NPs were spherical in shape with some association into chains (Figure 6.11, a). Analysis of particle sizes derived from the images shows a relatively narrow size distribution: the average particle size was determined to be 18 ± 3.4 nm (Figure 6.11, b).

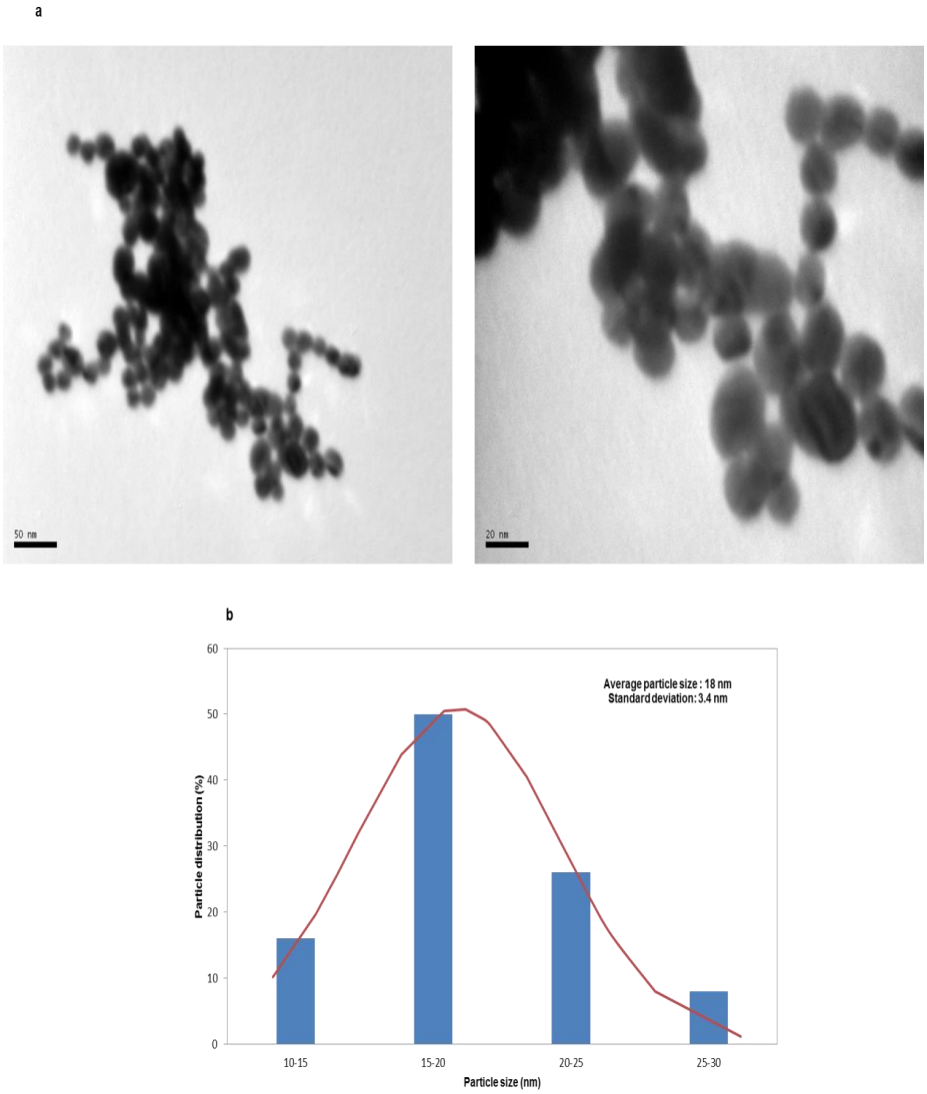

Figure 6.11: TEM analysis of seed Au-NPs: (a) TEM images showing largely spherical nanoparticles loosely associated in chains; (b) a size distribution histogram

TEM images of the final Au-NP formulations showed that the particles were of mixture of spherical and oval shapes, again loosely associated into chain structures (Figure 6.12, a). The size distribution histogram (Figure 6.12, b) reflects a rather wider particle size distribution and, while the average particle size was 36 ± 7.1 nm, the relatively large standard deviation points to a rather

greater irregularity of particle shape. After centrifugation, Au-NPs showed the expected agglomeration although discrete particulates of similar dimension to the parent formulation were apparent (Figure 6.12, c).

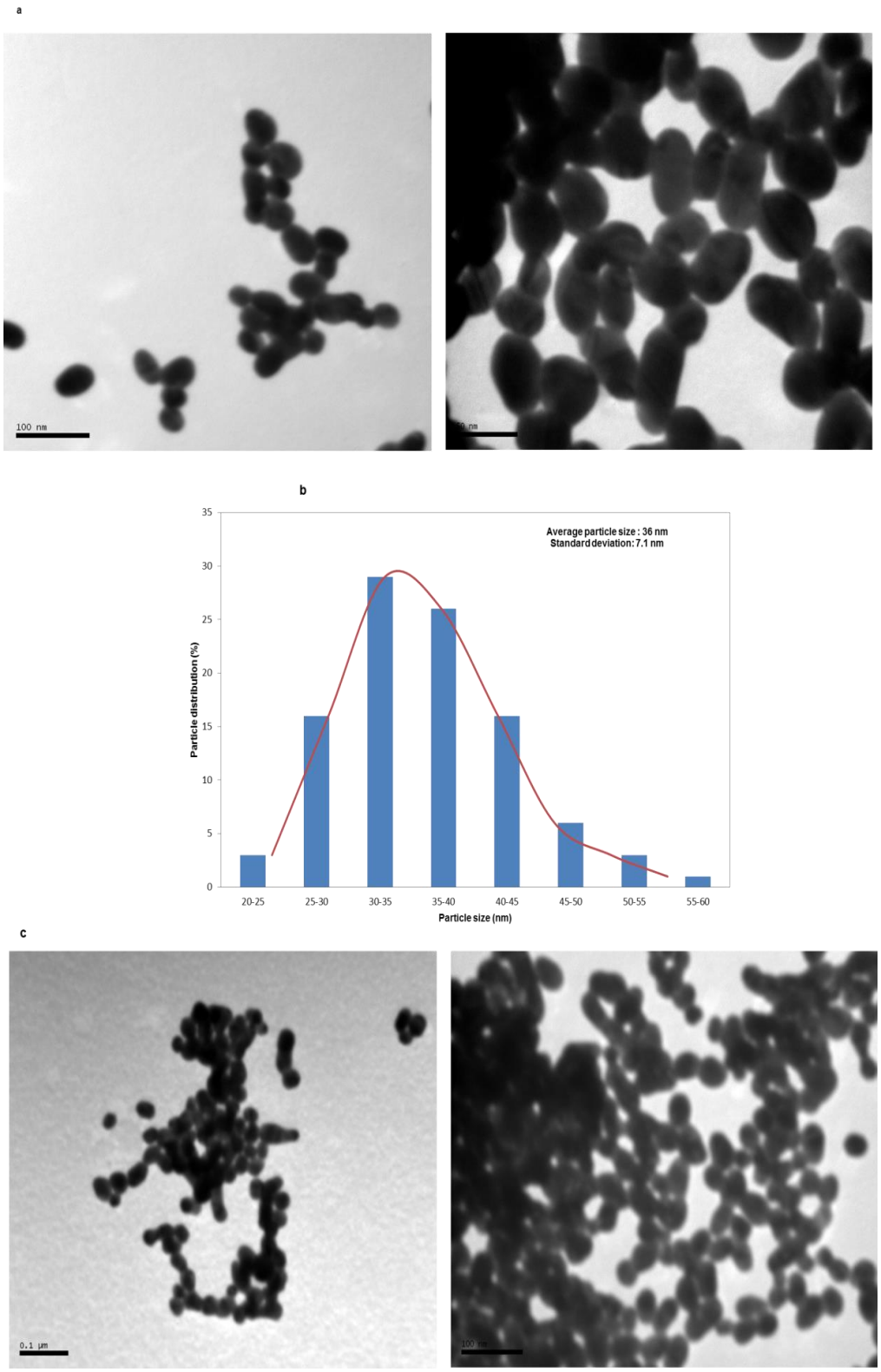

Figure 6.12: TEM analysis of final Au-NP formulations: (a) two images of the same non-centrifuged Au NPs solution showing both spherical and ellipsoidal particles; (b) size distribution histogram of particle sizes; (c) two images of the same centrifuged product showing loose associate of spherical and ellipsoidal NPs.

Again, when the uncentrifuged and centrifuged Au-NPs were mixed with SCD, the TEM images (Figure 6.13) showed a light diffuse layer around the nanoparticles as observed for Ag-NPs. This is attributed to the attachment of SCD to the NPs and it generates a more diffuse image because of the light atoms (oxygen and carbon) that constitute the SCD structure.

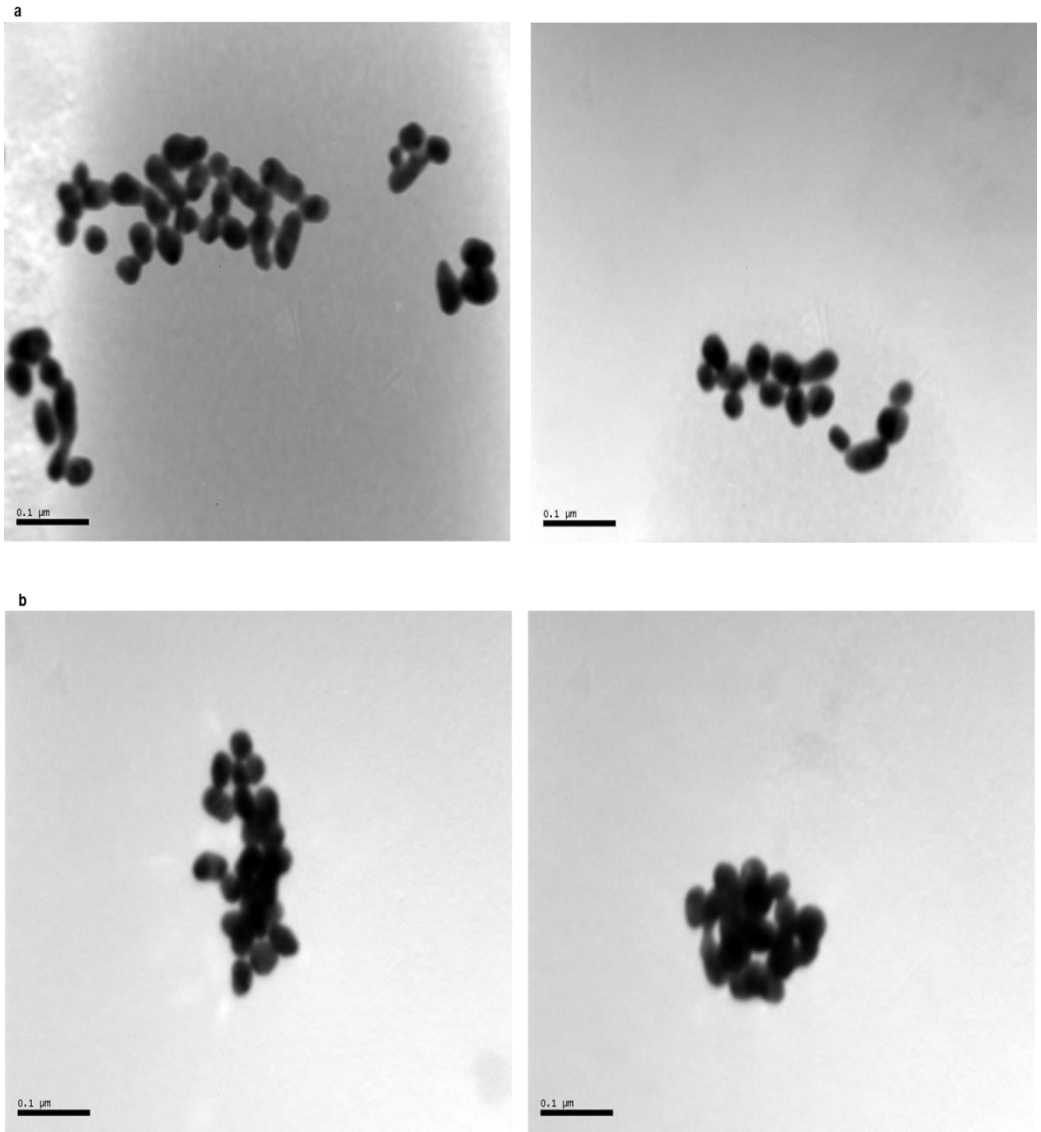

Figure 6.13: TEM different images of the same sample of (a) non-centrifuged SCD-Au-NP and (b) centrifuged SCD-Au-NP

6.1.4 Concentrations of Nanoparticles

The discontinuous nature of the silver and gold sols formed, means that direct evaluation of the amount of metal in the products can be presented in several ways. The average number of Ag/Au atoms per nanoparticle (*N*) can be estimated by using the average core diameters of the particles (*D*, nm) obtained from TEM analysis. By assuming spherical particles and a uniform face-centered cubic packing, the average number of Ag/Au atoms (*N*) per nanoparticle be calculated:

$$N = \frac{\pi \rho D^3}{6M} N_A$$

where ρ is the density of the face-centred cubic crystal [Ag (10.5 g cm^{-3}) or Au (19.3 g cm^{-3})], *M* is the atomic mass of Ag (107.86 g) or Au (196.96 g), and N_A is the Avogadro's number. This yields $N = 30.88\ D^3$ for Au-NPs and $N = 30.68\ D^3$ for Ag-NPs. Metal concentrations in the final formulations were determined by ICP-OES after digestion with concentrated nitric acid. Further detail is provided in Appendix A1.

Table 6.1: Calculation of the % NP yield for prepared Ag and Au-NP.

Formulation		D^a /nm	N^b	$[M]_{initial}{}^c$ /ppm	$[M]_{final}{}^d$ /ppm	% NP yield[e]
Ag-NP	non-centrifuged	21	2.84 x 10^5	26.97	22.22	79
	centrifuged				17.36	64
Au-NP (seed)		18	1.80 x 10^5			
Au-NP (final)	non-centrifuged	36	14.40 x 10^5	37.47	29.55	87
	centrifuged				26.90	78

[a] Mean core diameter (TEM); [b] Number of atoms per nanoparticle; [c] initial metal salt concentration; [d] final metal concentration (ICP-OES); [e] based on 100% reduction of salts.

6.2 Raman Spectroscopic Study of Selected Corticosteroids

In order to evaluate the influence of immobilised SCD on the SERS signals from metal nanoparticle substrates, the selected corticosteroids (CSs) (Figure 6.14) were studied with Raman spectroscopy at 633 nm. A relatively detailed spectral assignment exercise, based on established studies of budesonide and fluticasone,[232,233] was undertaken to correlate spectral regions with molecular features of the CSs species. In this way, it was anticipated that intensity

changes in SERS spectra for both naked and decorated NPs could be correlated to molecular interactions with the nanoparticle surfaces.

Inspection of the structures of the corticosteroids shows several common functional features that might be expected to show similar Raman signals: the A-ring is an unsaturated dien-one system with a carbonyl substituent at C3; C10 and C13 are methyl substituted and C11 has a hydroxyl substituent. Structural diversity is shown at C9 where MOM, BCL and BDP have chloro-substituents and FLU features a fluoro-substituent. A second fluoro-substituent at C6 in FLU contrasts with the unsubstituted methylenes in the other CSs. At C16, all apart from BUD are methyl substituted – in BUD the ether oxygen forms part of the 1,3-dioxalane 5-membered ring. Above the steroid plane a range of functional groups substitute the carbonyl at C17: CH_2OH for BUD and BCL; CH_2Cl for MOM; a propionate ester (O_2CPr) for BDP. Below the ring plane at C17, the hydroxyl is unsubstituted in BCL but is esterified with propionate in BDP and FLU, and with 2-furanylcarboxylate in MOM. In BUD, the oxygen at C17 forms part of 1,3-dioxalane ring.

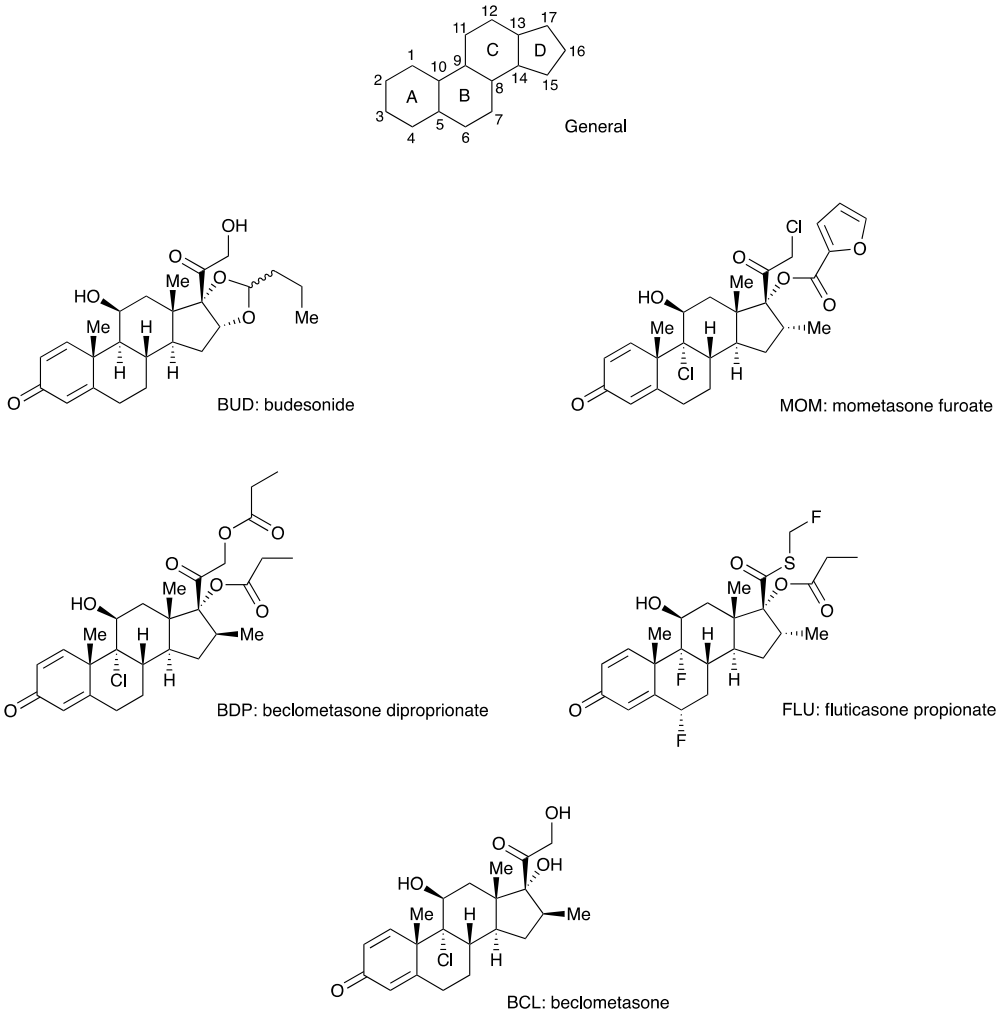

Figure 6.14: The general ring numbering scheme for the steroid ring framework and the corticosteroids selected for Raman spectroscopy studies.

With the exception of BCL, each of the CS compounds gave good quality Raman spectra at 633 nm (Figure 6.15). It is not immediately obvious, given the structural similarity to other CSs, why the BCL spectrum was swamped by a fluorescent background - only features at *ca*. 2986, 2953, 2906 cm^{-1} (corresponding with aliphatic C-H stretching modes) and 1658, 1619, 1601 cm^{-1} (corresponding with dien-one ring stretching modes) were apparent above background. For the other spectra, detailed assignments are presented in Table 6.2.

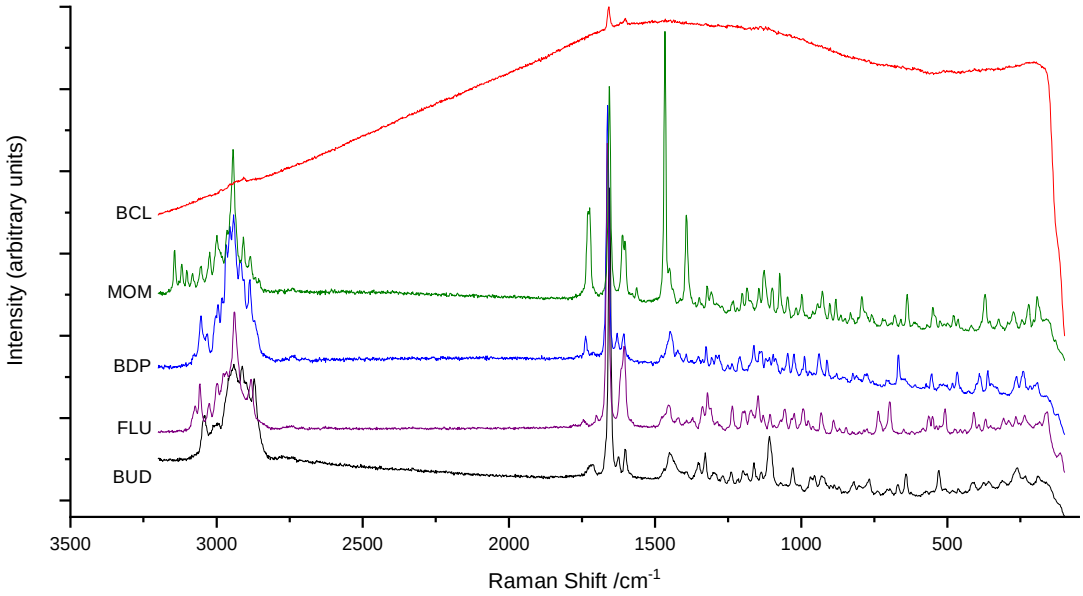

Figure 6.15: Offset Raman Spectra for selected corticosteroids (BUD = budesonide, FLU = fluticasone proprionate, BDP = beclomethasone dipropionate, MOM = mometasone furoate, BCL = beclomethasone).

Table 6.2: Assignment of the Raman peaks of the Raman spectra of budesonide (BUD), fluticasone propionate (FLU), beclomethasone dipropionate (BDP) and mometasone furoate (MOM).

Assignment	Raman peaks (cm^{-1})			
	BUD	**BDP**	**FLU**	**MOM**
3200-2800 cm^{-1}				
ν(C-H) furan	–	–	–	3143, 3118, 3099
ν(C=C-H) dienone	3041	3076, 3053, 3032	3073, 3057, 3024	3084, 3054, 3023
$\nu_{as}(CH_3)$	2998	3002, 2994	2997	2998
$\nu_{as}(CH_2)$, $\nu_{as}(CH_3)$	2969sh	2967	2976, 2966	2963
$\nu_{as}(CH_2)$	2941,	2954, 2941	2939	2943
$\nu_{s}(CH_3)$	2900	2906	2891sh	2907
$\nu_{s}(CH_2)$	2911, 2872	2919, 2889	2882	2883
1780-1550 cm^{-1}				
ν(C=O) propionate	–	1737	1743	–
ν(C=O) furanyl	–	–	–	1728
ν(C=O) thioester	–	–	1700	–
ν(C=O) dienone	1721, 1714	–	–	1724
ν(C=C) dienone	1657	1662	1662	1656
ν_{as}(C=O, C=C) dienone	1627, 1603	1629,1606	1616, 1605	1611, 1603
ν_{as}(C=O, C=C) furan	–	–	–	1562
1500-1380 cm^{-1}				
ν(C=C-C=C) furan	–	–	–	1466
$\delta(CH_3)$, $\delta(CH_2)$	1471, 1452	1448, 1421	1454, 1420	1450, 1438
ν(C-C) furan	–	–	–	1392
$\delta(CH_3)$	1393	1393	1389, 1373	1392

Table 6.2 cont. Assignment of the Raman spectra of the BUD, BDP, FLU and MOM

Assignment	Raman peaks (cm^{-1})			
	BUD	**BDP**	**FLU**	**MOM**
1380-1000 cm^{-1}				
δ_{as}(C-OH)	1352, 1329	1351, 1325, 1305	1342, 1320, 1307	1348, 1321, 1306
δ_{s}(C-OH)	1298, 1269	1292, 1281	1286	1270
ν(C-O), δ_{as}(CH), δ_{as}(CCH)	1240, 1199	1251, 1235, 1209	1235, 1198	1232, 1201
ν(C-O) furanyl	–	–	–	1219
δ_{s}(CH), δ_{s}(CCH), ν(C-CH_3)	1162	1162	1172	1184
ν(C-O) propionate	–	1150, 1138	–	–
δ(C-H) in-plane bending	1138, 1110	1135	1147, 1106	1144, 1126, 1098
ν(C-O) furanyl	–	–	–	1073
ν(C-OH)	1030	1046	1056	1044
ν(O=C-**O-C**)	–	1025	1024	1016
ν(F-C-S)	–	–	1024	–
< 1000 cm^{-1}				
τ(CH_3)	968, 956, 931	988, 939, 912	993, 970, 953, 931	997, 927, 901
ν(C-O-C=O) stretching	–	823	888, 845	829
δ(C-H)	820			
δ(C-C)	767	773	774	792, 757
δ(C-F)			737, 693	–
ν(C-S) stretching	–	–	650, 623	–
δ(ring)	670,642, 530, 416	667, 553, 466	697, 563, 551, 508, 408	677, 659, 637, 549, 477
τ(CH_3) torsional mode	–	–	262, 233	273, 221

Raman spectra of the CSs were considered in several spectral regions. Assignments were achieved with reference by comparison with *ab initio* vibrational modelling studies of budesonide[232] and fluticasone propionate[233] and supported by reference to characteristic functional group frequencies.[234]

6.2.1 Spectral Region 3200-2800 cm^{-1}

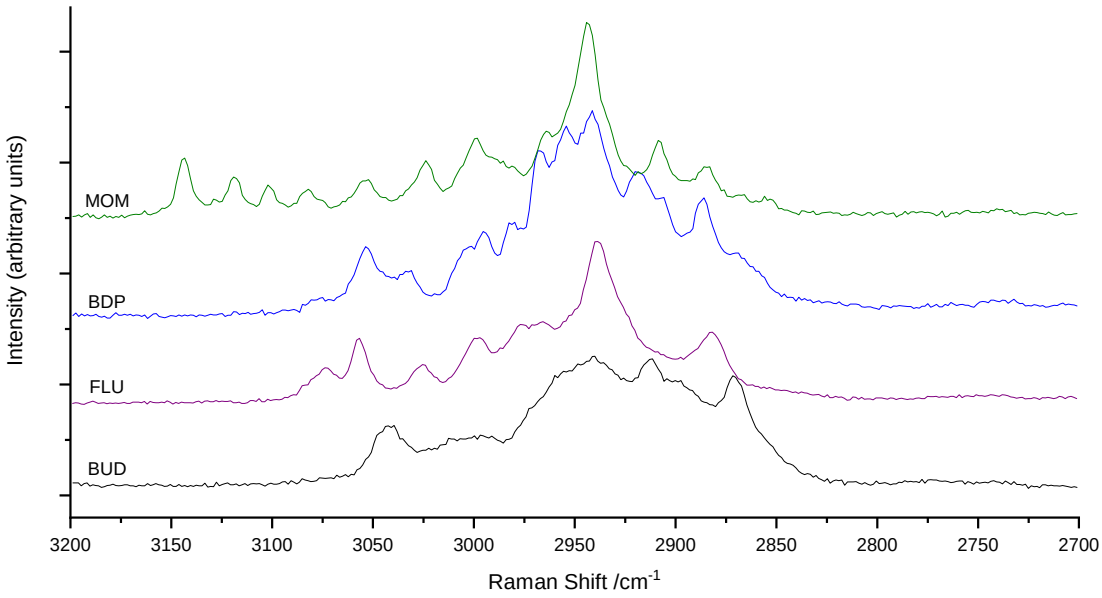

Figure 6.16: Raman spectra of selected corticosteroids (BUD = budesonide, FLU = fluticasone proprionate, BDP = beclomethasone dipropionate, MOM = mometasone furoate} in the region 3200-2700 cm^{-1}.

Bands in this region of the spectra correspond with carbon-hydrogen stretching modes. Bands above 3100 cm^{-1} appear only for MOM and correspond with the furan C-H stretching modes of the furoate ester.[235] All CSs studied show one or more bands *ca.* 3050 cm^{-1}, attributed to the C-H stretching modes of the dienone A-ring of steroid framework. Below this, asymmetric stretching modes of aliphatic methylene and methyl groups appear while at lower ranges the corresponding symmetric modes are apparent. These originate with ester and dioaxalane substituents of the D ring along with the saturated BCD rings of the steroid framework.

6.2.2 Region 1780-1550 cm^{-1}

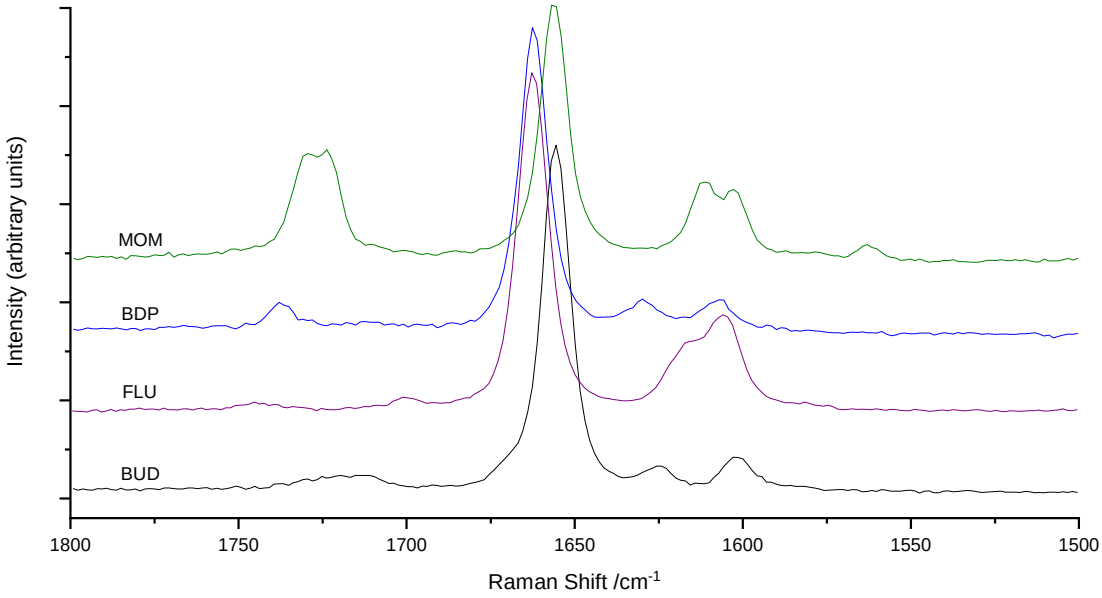

Figure 6.17: Raman spectra of selected corticosteroids (BUD = budesonide, FLU = fluticasone proprionate, BDP = beclomethasone dipropionate, MOM = mometasone furoate} in the region 1800-1500 cm^{-1}.

Bands in this region of the spectra can be attributed to stretching modes of unsaturated (C=O and C=C) functions in the species. Towards the higher wavenumbers, bands attributable to the carbonyl stretching modes of the ester substituents of the D ring are apparent. Below this, the important spectral modes of the dienone A-ring are assigned. Weak to absent features at *ca.* 1720 cm^{-1}, correspond with the isolated C=O stretching mode of the dienone – the weak intensity of this mode is consistent with Raman selection rules and has been noted in these systems previously.[232,233] In contrast, the C=C stretching modes of the dienone create amongst the strongest features each spectrum with bands at *ca.* 1660 cm^{-1}. Coupling of modes of C=C and C=O modes gives rise to two further bands of medium intensity around in the ranges 1627-1611 and 1606-1603 cm^{-1}. The significant variation in position of the higher wavenumber of these modes may indicate some associations in the solid state. The expected effects of electronegative substituents at C6 and C9 in FLU, BDP and MOM show no clear pattern - while MOM and FLU show closest similarity, the 9-chloro-substituted BDP is similar to BUD. The only remaining feature in this region, a weak-to-medium intensity band at 1562 cm^{-1}, is unique to MOM and can be assigned to the coupling of C=C and C=O modes of its furoyl ester.

6.2.3 Region 1500-100 cm^{-1}

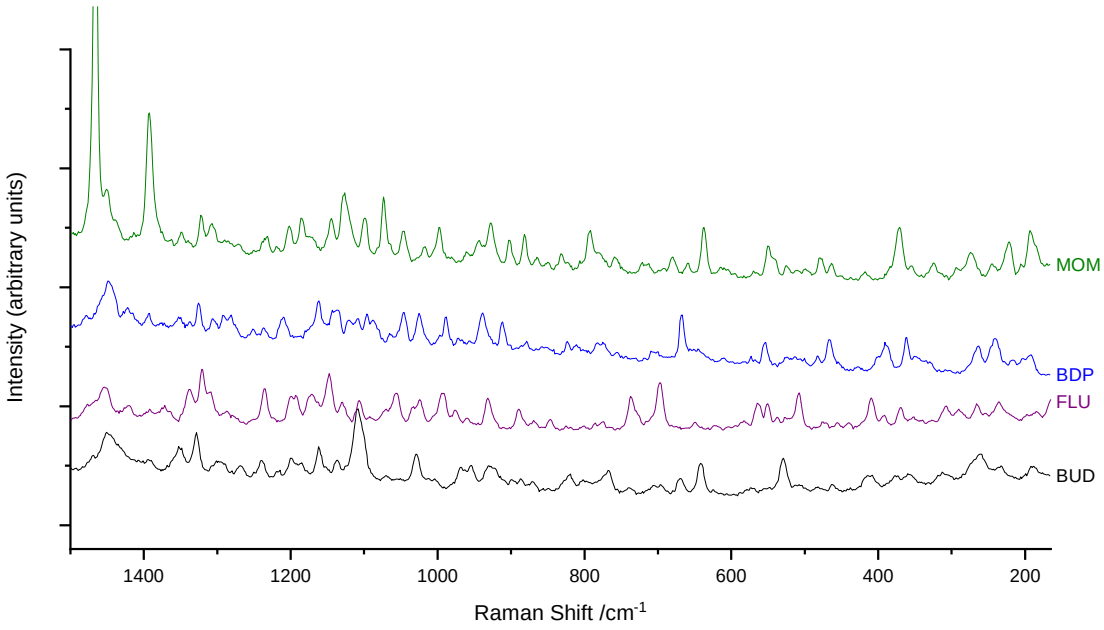

Figure 6.18: Raman spectra of selected corticosteroids (BUD = budesonide, FLU = fluticasone propionate, BDP = beclomethasone dipropionate, MOM = mometasone furoate) in the region 1450-165 cm^{-1}.

Between 1450-1380 cm^{-1}, MOM shows strong bands associated with coupled double- and single-bond stretching modes in the 5-membered ring (1466 and 1392 cm^{-1}). Aside from these features, this region between 1500 and 1380 cm^{-1} is dominated by stretching and deformation modes of saturated carbons predominantly from the steroid framework although contributions from the aliphatic esters appended to C17 of BUD, BDP and FLU are also present. Below 1380 cm^{-1}, a complex set of bands correspond with carbon-oxygen modes including the secondary hydroxyls at C11 and the C-O bonds of ester and dioxalane substituents at the D-ring. Below 1000 cm^{-1}, the bands can be attributed to methyl torsion modes (*ca*. 950 cm^{-1}) alongside an array of in- and out-of-plane deformations of aliphatic hydrocarbons. Deformation of the saturated carbon ring of the steroid framework is assigned to an array of modes *ca.* 650 cm^{-1}. In summary, portions of this spectral region can potentially be utilised for non-group specific molecular regions: 1500-1380 cm^{-1} for C/D rings of the steroid and the D-ring substituents; indicators: 1380-1000 cm^{-1} for D-ring substituents and *ca*. 650 cm^{-1} for steroid framework.

6.3 Raman Spectroscopic Study of *per*-6-thio-*β*-cyclodextrin (SCD)

SCD was analysed by Raman spectroscopy at 633 nm and, in common with other polysaccharides, these studies indicates that the cyclodextrin has a relatively low Raman cross-section and hence the resulting spectrum was of low relative intensity. It was only after a relatively large number of co-additions of the spectrum that a spectrum of suitable quality for assignment was obtained (Figure 6.19). While the spectrum showed an elevated background, peaks were clearly discernible and relatively well resolved.

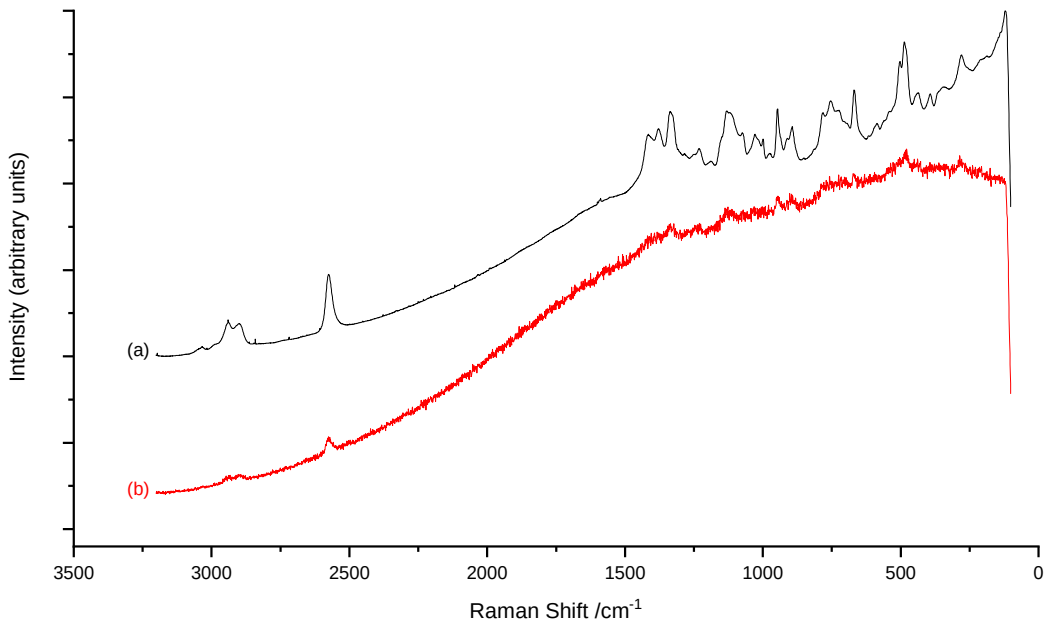

Figure 6.19: Raman spectrum of SCD collected using 633 nm excitation, 50x objective, 100% laser power, 10 s exposure time: (a) 856 accumulations; (b) 10 accumulations.

The assignment of the SCD was made with reference to the assignment *β*CD[236] (Table 6.3). The spectra of the two cyclodextrins are similar but, as might be expected, some peaks are shifted on replacement of the hydroxyl at C6 of the *β*CD with thiol. Importantly, the appearance of the band at 2575 and 668 cm^{-1} in SCD is consistent with the thiol substitution.[237] Asymmetric and symmetric stretching vibrations of the substituted-C6 methylene are shifted from *β*CD with the presence of the sulfur[238] as are bands at *ca.* 1340 and *ca.* 1240 cm^{-1} where the coupled vibrational modes include CH_2SH vibration vs CH_2OH in *β*CD. The weak scattering of SCD is a potential advantage in this application as its background spectrum is unlikely to interfere with the analyte.

Table 6.3: Assignment of SCD Raman spectrum on the basis of the *β*CD assignment.

*β*CD Raman peak (cm^{-1})	SCD Raman peak (cm^{-1})	Assignment
2942	2939	$\nu_{as}(CH_2)$
2910	2899	$\nu_s(CH_2)$,
---	2575	ν(SH)
1415	1415	δ(OCH), δ(CCH)
1390	1376	δ(OCH), δ(CCH), δ(COH)
1340	1336	δ(CCH), δ(COH), δ(HCH) + CH_2SH vibration
1250	1231	δ(OCH), δ(COH), δ(CCH) + CH_2SH vibration
1130	1130	Pyranose ring vibration mode + ν_{as}(C-O-C)
1080	1074	ν(CO) + δ(COH) bending mode + ν(CC)
1050	1028	ν(CO), ν(CC)
1010	999	ν(CC), δ(OCH, δ(CCH), δ(CCO)
950	946	Skeletal vibration (α-1,4 linkage)
850	893	ν(CO) and ν(CC) stretching, δ(CCH) mode of the anomeric vibration
---	668	ν(C-S) stretching
580	585	Skeletal vibration involving α-1,4 linkage
480	486	Skeletal vibration involving α-1,4 linkage

6.4 Raman Spectroscopic Studies of SCD-Ag-NP and SCD-Au-NP

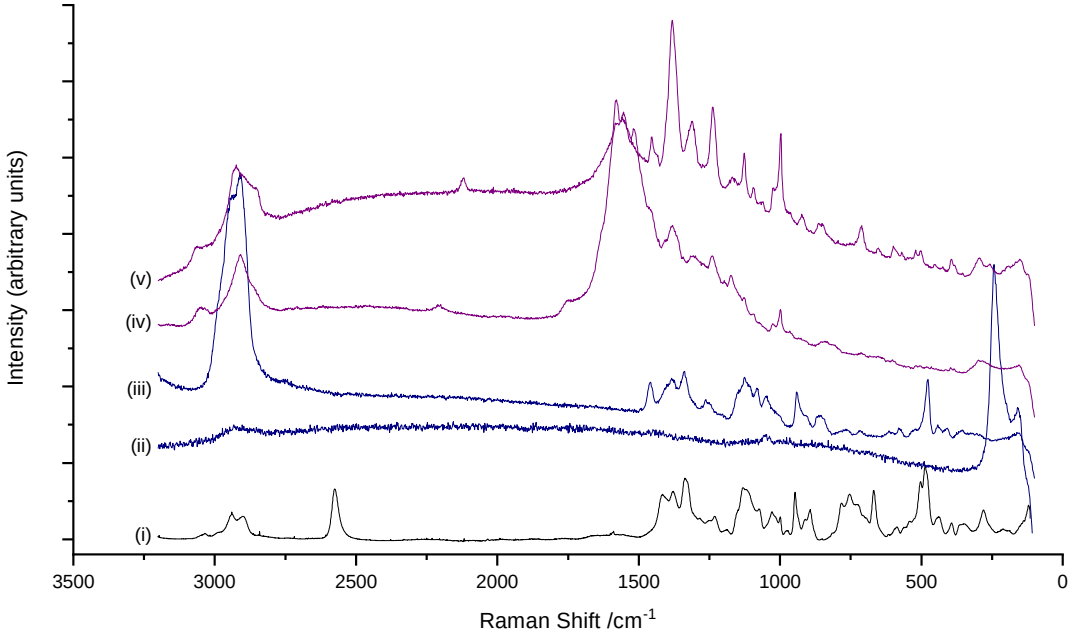

Figure 6.20: Raman spectrum of metal SCD-M-NP formulations compared to reference spectrum of SCD: (i) the SCD reference spectrum (after background removal), (ii) uncentrifuged Ag-NP after treatment with SCD, (iii) centrifuged Ag-NP after treatment with SCD, (iv) uncentrifuged Au-NP after treatment with SCD, (v) centrifuged Au-NP after treatment with SCD.

The metal NP formulations were prepared with and without centrifugation. The RS spectrum of dried drops of these materials on an aluminium foil substrate gave no significant Raman responses. The spectra obtained after these materials were mixed with SCD and analysed are given in Figure 6.20. For the Ag-NP formulation, no features from the SCD were discernible with the non-centrifuged formulation; in contrast, the centrifuged formulation gives a clear spectrum that corresponds closely with SCD reference spectrum. Notably in this case, the SH stretch at *ca.* 2575 cm^{-1} is absent in the SCD-Ag-NP system and the methylene symmetric and asymmetric stretching modes (centred around 2900 cm^{-1}) are considerably enhanced in relative intensity. These factors are consistent with the expected chemisorption of the SCD to the nanoparticle *via* the 6-CH_2SH deprotonation. No significant features relating to direct S-Ag vibration were discernible in the spectrum but features of these types can be broad and difficult to resolve in some cases.[239,240]

Both uncentrifuged and centrifuged Au-NP formulations give a discernible Raman spectrum. These are essentially similar but spectral quality and overall signal intensity is enhanced with the centrifuged formulation. Notable spectral

features are again consistent with chemisorption of SCD to the metal NP surface: the correspondence of the spectrum with SCD, the absence of thiol stretching mode and the relative enhancement of methylene stretching regions in the spectrum. In addition, there are some broad features in the region 150-200 cm^{-1} that are consistent with Au-S vibrational modes.[241] The origin of other features that appear in the SCD-Au-NP are less clear. Broad features across the range 1600-1000 cm^{-1} have been observed as an instrument artefact with the 20x objective lens used for these studies and the 180° light path to a foil substrate may have amplified this effect on these occasions. It is reasonable to conclude that the chemisorbed SCD metal nanoparticles have been prepared though these processes. The increased enhancement of signals with the centrifuged formulations is consistent with the agglomeration observed with TEM and DLS in these systems and the consequent creation of 'hot-spots' for SERS enhancement at the junctions between nanoparticles.[242]

6.5 Raman Spectroscopic Studies of Budesonide with Metal Nanoparticles

6.5.1 BUD with Ag-NP

To test the possible enhancement of the Raman spectrum of BUD, a drop of a mixture of BUD and the appropriate Ag-NP formulation was placed on a foil covered glass slide. In each case, a spectrum was obtained from the dried materials (Figure 6.21).

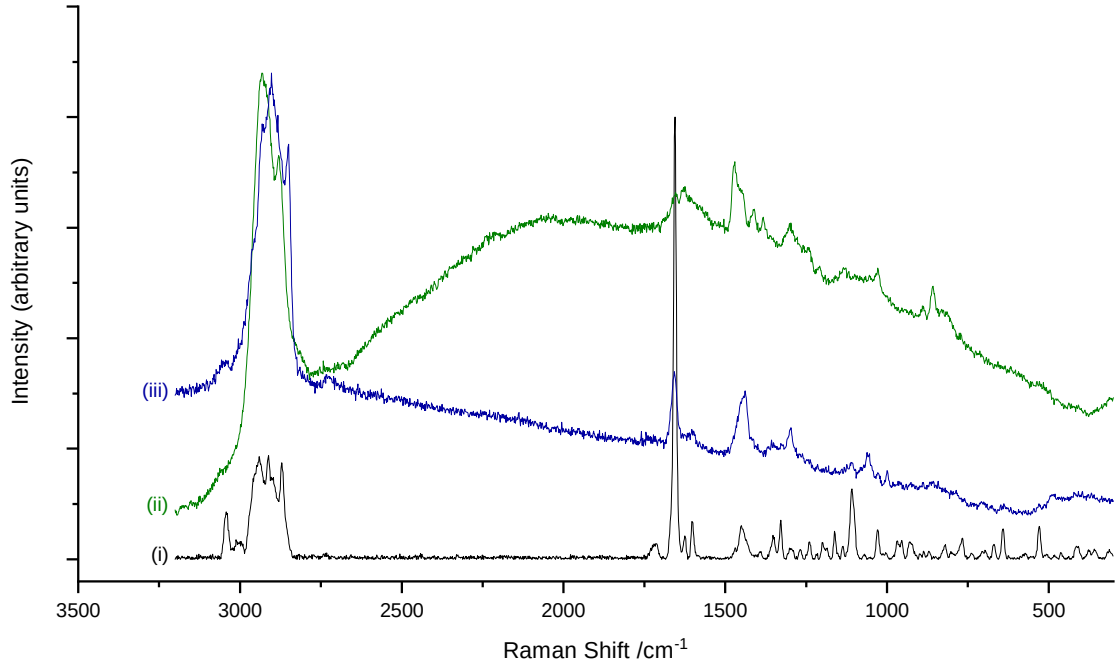

Figure 6.21: Raman spectra of budesonide (BUD) after mixing with Ag-NP formulations: (i) BUD reference spectrum (after background removal), (ii) BUD with uncentrifuged Ag-NP (iii) BUD with centrifuged Ag-NP.

The SERS spectrum in each case, is dominated by the strong bands in the high frequency spectral region (3200-2800 cm^{-1}): it appears that specifically $\nu_{as}(CH_2)$ and $\nu_s(CH_2)$ at 2931 and 2880 cm^{-1} respectively dominate the enhancement on interaction with the Ag-NP centrifuged formulation and, while these modes also appear enhanced in the non-centrifuged sample, peaks in this envelope appear to correspond to $\nu_{as}(CH_3)$ at 2903 cm^{-1} and a lower frequency $\nu_s(CH_2)$ mode at 2851 cm^{-1} (ascribed to ester methylene). In contrast, the relative intensity of the dienone (ring A) bands appears to be significantly reduced in the spectra. The ν(C=C) dienone band at *ca.* 1655 cm^{-1} still forms the most noticeable band in this region. In the non-centrifuged formulation however, other enone features [e.g. the coupled ν_{as}(C=O, C=C) at *ca.* 1627, 1603 cm^{-1} are of similar intensity although significantly broadened.

In the 1500-1380 cm^{-1} region, the C-C modes are relatively enhanced compared to the reference spectrum. Again, the spectral envelope differs between formulations: the peak maximum is at 1470 cm^{-1} [$\delta(CH_2]$ for non-centrifuged sample and at 1440 cm^{-1} [$\delta(CH_3)$], for centrifuged samples and this appears to be consistent with relative enhancements of the C-H modes.

In the 1380-1000 cm^{-1} region, the band at *ca.* 1300 cm^{-1} and *ca.* 1026 cm^{-1} appears in each sample while the 1056 cm^{-1} band is enhanced only in the centrifuged formulation. In contrast, bands at 889, 857 cm^{-1} [ν(C-O-C)] are significant only in the non-centrifuged example. The broader bands observed in the non-centrifuged examples, potentially correlates to a wider range of analyte-surface interactions. The non-centrifuged Ag-NP formulation has greater polydispersity (Figure 6.5), and this potentially leads to a greater diversity of sites with SERS 'hot-spots' and hence micro-environments for BUD functions.

Viewed overall, it appears that significant SERS enhancements are associated with the 1500-1380 cm^{-1} region, corresponding to C- and D-ring and the D-ring oxalane substituents and portions of the 1380-1000 cm^{-1} region associated with the ether modes of the dioxalane (*ca*. 1300 and 1050 cm^{-1}). Deformation modes of the steroid framework (*ca*. 650 cm^{-1}) are noticeably absent and therefore, taken together, these observations indicate that the D-ring / D-ring substituent experience the greatest enhancements with the Ag-NP formulation. Consistent with this, and the most noticeable change in the spectra, is the significant reduction in the relative intensity of the A-ring bands, particularly the ν(C=C) dienone at 1657 cm^{-1}. Therefore, it is inferred that the BUD interacts with the naked Ag-NP predominantly through the D-ring / D-ring substituents (Figure 6.22).

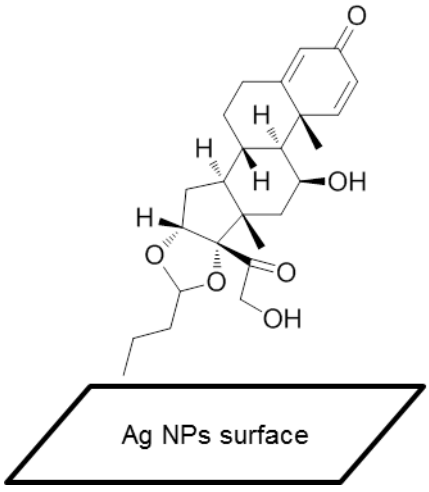

Figure 6.22: Predicted interaction of Bud with naked Ag NPs

Studies with the SCD-Ag-NP formulations yielded noticeably different enhancement of spectral regions than the naked Ag-NP (Figure 6.23). The centrifuged SCD-Ag formulation gave a significantly weaker spectrum (*ca.* two orders of magnitude than the uncentrifuged sample). The origin of this is unclear although centrifugation has been observed to affect SERS studies with SCD-decorated Au-NP.[243] Consequently, uncentrifuged Ag-NP and SCD-Ag-NP formulation provides the clearest comparison of the effect of surface-functionalisation on the SERS spectra of BUD (Figure 6.23).

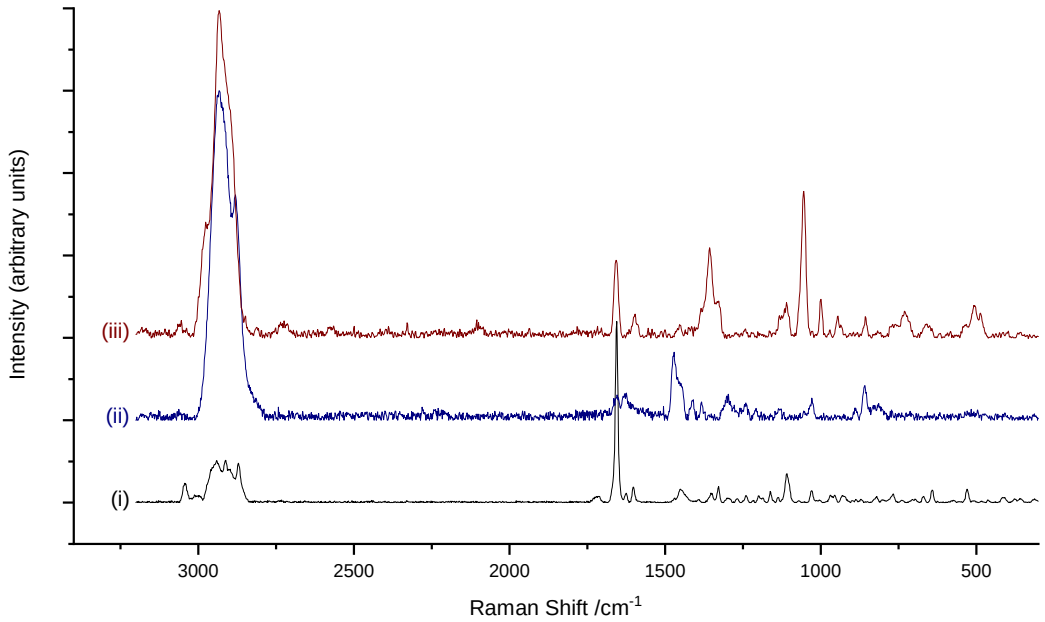

Figure 6.23: Baseline-subtracted Raman spectra of budesonide (BUD) after mixing with Ag-NP formulations (after baseline removal) showing the different enhancements for naked and SCD-functionalised Ag-NP: (i) BUD reference spectrum, (ii) BUD with uncentrifuged Ag-NP (iii) BUD with uncentrifuged Ag-SCD-NP.

In the 3200-2800 cm^{-1} region, the envelope with the SCD-Ag formulation is relatively less intense than that of the BUD with naked Ag-NP. The ν(C=C-H) modes from the steroid A-ring (dienone) at *ca.* 3050 cm^{-1} and the $\nu_{as}(CH_3)$ mode at *ca.* 2980 cm^{-1} (from methyl A-ring substituent at C10) are clearly discernible. The $\nu_s(CH_2)$ 'shoulder' in the naked Ag-NP at *ca*. 2880 cm^{-1} is absent with the SCD-Ag-NP.

In the 1780-1550 cm^{-1} region, spectral features associated with BUD's dienone A-ring are relatively enhanced with the SCD-Ag-NP and ν(C=C) dienone at 1657 cm^{-1} forms the most intense feature in this region. Interestingly, the ν_{as}(C=O, C=C) dienone mode at *ca.* 1600 cm^{-1} appears enhanced while the

other of these coupled enone modes at *ca.* 1627 cm^{-1} is absent – the opposite relative intensities are observed with the naked Ag-NP.

Remarkably, between 1500 and 1380 cm^{-1} few significant features in the spectrum with the SCD-Ag-NPs in contrast to the naked Ag-NPs where this region is significantly enhanced. The sole, relatively weak feature at *ca.* 1450 cm^{-1} can be attributed to $\delta(CH_3)$ at C10.

In the region 1380-1000 cm^{-1}, bands corresponding to δ_{as}(C-OH) at 1358 and 1328 cm^{-1} are strongly enhanced (particularly for the 1358 band) as is the ν(C-OH) band at 1056 cm^{-1}. Each of these features can be attributed to the C11 hydroxyl, and again are very weak or absent in the corresponding spectrum obtained with naked Ag-NP. Similarly, the torsional $\tau(CH_3)$ mode at *ca.* 947 cm^{-1} (attributable to C10 methyl) is enhanced with SCD-Ag-NP (and absent with naked Ag-NP) as are the various ring vibration modes between 700 and 480 cm^{-1}.

These observations lead to the conclusion that decorating the Ag-NP with SCD has reversed the approach of the CS to the Ag surface and, consistent with BUD-CD binding studies, the coordination of the A-ring into the CD cavity, orientating the C=O of the enone towards lower rim and closer to the metal surface (Figure 6.24). This is the first observation that decorating the nanoparticle surface with a 'receptor' can reorient the molecular species to reverse selective SERS enhancement.

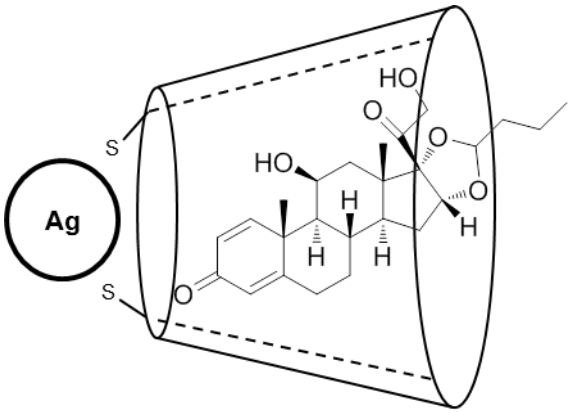

Figure 6.24: Predicted interaction of BUD with Ag-SCD NPs

6.5.2 BUD with Au-NP

With the Au-NP systems, the centrifuged formulations gave the most interesting results with all the CSs. In the non-centrifuged systems, no significant enhancement was observed on addition of the CS analyte to the solution. The spectra of SCD-Au-NP and naked Au-NP (after centrifugation) are shown with BUD in Figure 6.25.

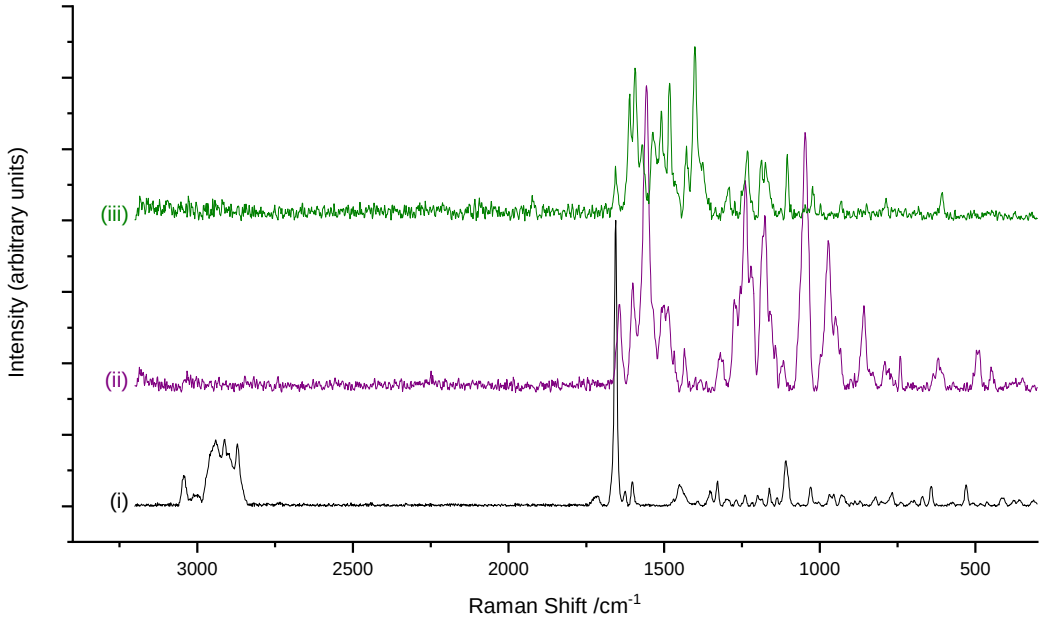

Figure 6.25: Baseline-subtracted Raman spectra of budesonide (BUD) after mixing with Au-NP formulations (after baseline removal) showing the different enhancements for naked and SCD-functionalised Au-NP: (i) BUD reference spectrum, (ii) BUD with centrifuged Au-NP (iii) BUD with centrifuged SCD-Au-NP.

Studies with Au-NP formulations and BUD gave quality spectra when the Au-NP formulation was centrifuged in advance. The study produced results that are broadly similar with the Ag-NP observations although the spectra are considerably more complicated, indicating that the regioselectivity of enhancement is lower in these systems. Additionally, it is noticeable that the overall enhancement intensity was greater with the Ag formulations and, while there are several factors influencing the sensitivity of SERS plasmon response[244] such an observation is not uncommon in comparable systems.

Neither Au-NP formulations generates any significant enhancements in the 3200-2800 cm^{-1} region of the spectrum and in the region 1780-1550 cm^{-1}, several modes of the A-ring vibrations are enhanced although those directly attributable to the A-ring, bands at *ca.* 1660, 1610 and 1590 cm^{-1} [ν(C=C)

dienone and ν_{as}(C=O, C=C) dienone] are relatively enhanced in the SCD-Au-NP formulation. The strongest enhancement for BUD by the naked Au-NP is at *ca.* 1560 cm^{-1}, which might be attributed to a modified, coupled enone [ν(C=O, C=C)] and clearly the array of enhancements here are consistent with significant A-ring interaction with un-modified Au-NP surface.

Again, while the spectral envelopes are different in the 1500-1380 cm^{-1} region, both Au-NP and SCD-Au-NP appear to enhance interactions with aliphatic carbon bonds in the structures, although, clearly with SCD-Au, these can potentially arise from enhancement of SCD itself on the NP surface (Section 6.4). The remaining significant difference between the systems is observed with bands at *ca.* 1040 and 950 cm^{-1} that appear to be exclusively enhanced in the naked NP system. These are ascribed to ν(C-O-C) and $\tau(CH_3)$ modes of the dioxalane D-ring substituent and are notable absent with the decorated Au-NP.

These observations appear to indicate that the naked nano-particle has multiple sites for interaction with BUD and both A-ring and D-ring extremities of the CS appear to interact with the surface. In contrast, functionalisation of the SCD-Au-NP surface again appears to act to orientate the A-ring functions of BUD towards the NP surface and consistent with this is the absence of significant signals attributable to dioxalane D-ring substituent. By implication this is inferred to be orientated away from the NP surface. However, it is important to note that with SCD-Au-NP, the potential interference from aliphatic modes of the SCD can complicate the interpretation, in contrast to the SCD-Ag-NP system.

6.6 Raman Spectroscopic Studies of Beclometasone Dipropionate with Metal Nanoparticles

Studies with BDP yielded enhanced spectra with most formulations with the exception of SCD-NP prepared with non-centrifuged substrates. The spectra of BDP with the corresponding Ag- and Au-materials are broadly similar (Figure 6.26) and therefore will be discussed together.

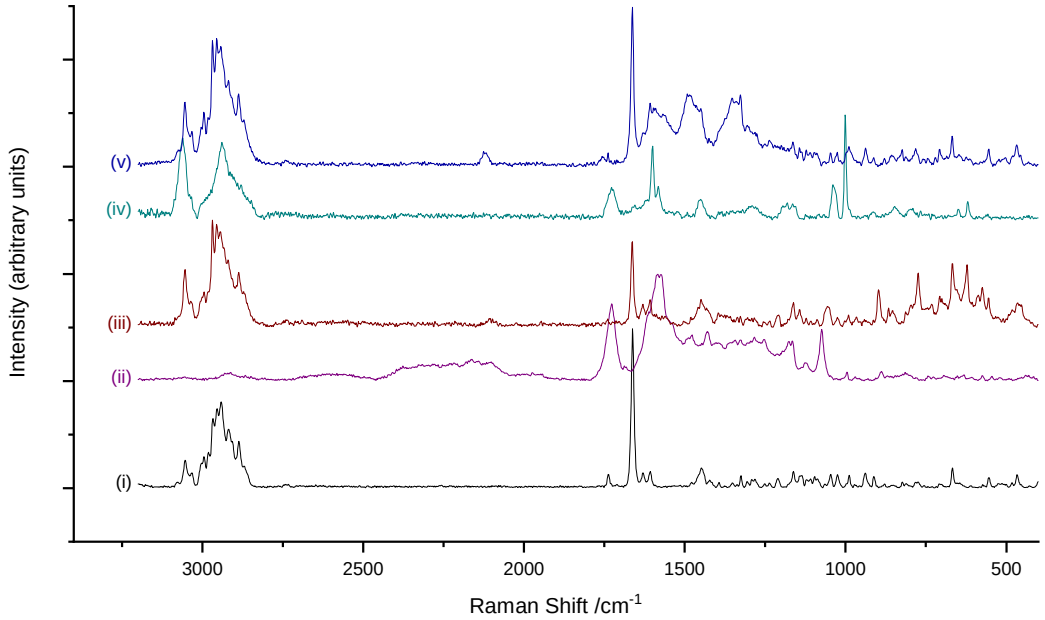

Figure 6.26: Baseline-subtracted Raman spectra of beclomethasone dipropionate (BDP) after mixing with metal-NP formulations (after baseline removal) showing the different enhancements for naked and SCD-functionalised particles: (i) BDP reference spectrum, (ii) BDP with centrifuged Ag-NP (iii) BDP with centrifuged SCD-Ag-NP, (iv) BDP with centrifuged Au-NP, (v) BDP with centrifuged SCD-Au-NP.

The interaction of BDP with naked Ag- and Au-NP leads to similar gross features in the spectra with the exception of the 3200-2800 cm^{-1} region where the Au-NP system showed significant enhancement. Most noticeably, in the region 1780-1550 cm^{-1}, bands at *ca.* 1728 cm^{-1} appear strongly enhanced. These are a little shifted from the parent ν(C=O) propionate, perhaps though reduction of bond order from charge-dipole interaction with the metal surface. The alternative assignment to ν(C=O) dienone, while closer to the frequency of this mode in the parent species, seems less likely as no significant peaks in the spectrum correspond with the accompanying ν(C=C) dienone (observed throughout these studies to be significantly a more intense feature in the

spectra) and it seems unlikely that the C=O would be exclusively enhanced through a surface interaction.

Broad features *ca.* 1580 cm^{-1} in the BDP Ag-NP, resolve to two significant bands with Au-NP at 1600 and 1584 cm^{-1} and similarly the complicated set of peaks in the 1500-1380 cm^{-1} region for the BDP Ag-NP spectrum, simplifies in the Au-NP system to the band at *ca.* 1450 cm^{-1}, due to $\delta(CH_3)$ and $\delta(CH_2)$ vibrations. Bands at *ca.* 1100, 1070 and 1040 cm^{-1}, are can be attributed to ν(C-O) and ν(C-O-C) of propionate. Taken together, these observations are indicate a consistent enhancement of bands associated with the propionate D-ring substituents indicating with a significant orientation of molecule with respect to the M-NP surface (Figure 6.27, a).

In contrast, the SCD-M-NP materials appear to orientate the molecule in the opposite direction. Inclusion of the molecule in the SCD host orientates the A-ring functions towards the metal surface (Figure 6.27, b). Key evidence for this again lies with the significant relative enhancement of the band at *ca.* 1660 cm^{-1}, due to ν(C=C) dienone, that is virtually absent in the spectra with the naked NP formulation. Other bands associated with the A-ring, coupled ν_{as}(C=O, C=C) modes at *ca.* 1630 and 1600 cm^{-1} are present in each spectrum and particularly well resolved in the SCD-Ag-NP. The relatively well resolved spectra with the SCD-functionalised NPs again points to specificity in the analyte to M-NP interaction and the proposed model is clearly consistent with the structural features inferred from NMR studies.

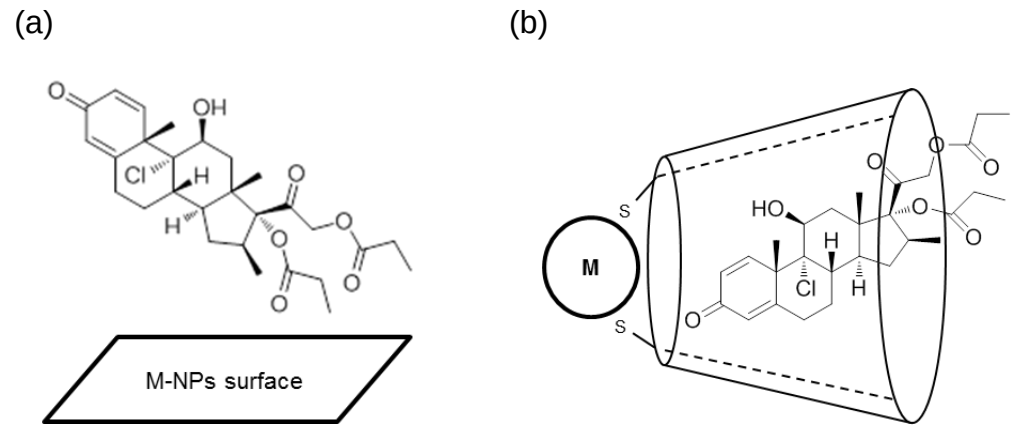

Figure 6.27: Predicted interaction of BDP with metal NPs in (a) naked metal NP and (b) SCD-functionalised NPs.

6.7 Raman Spectroscopic Studies of Fluticasone Propionate and Mometasone Furoate with Metal Nanoparticles

Both FLU and MOM yielded similar SERS behaviour with metal nanoparticle formulations: neither gave significant signals with SCD-functionalised Ag-NP and Au-NP and so therefore only centrifuged samples are compared here (Figure 6.28 for FLU and 6.29 for MOM).

With naked Ag-NPs, significant enhancements are observed in the 3200-2800 cm^{-1} regions of the FLU and MOM spectra. With FLU, this region is well-resolved and bands corresponding with asymmetric/symmetric methyl and methylene stretching modes (2987, 2963 and 2934, 2874 cm^{-1}) give the most intense bands of the spectrum. With MOM, this region is less well resolved although the strong, the relatively broad feature centred at *ca.* 2920 cm^{-1} has sufficient structure to suggest it comprises overlapped bands from similar asymmetric/symmetric methyl and methylene stretching modes. Importantly for MOM, there is no evidence of ν(C-H) furan although a small peak at *ca.* 3050 cm^{-1} is consistent with ν(C=C-H) from the steroid Ring A.

In the 1780-1550 cm^{-1} regions, bands associated with the Band A dienone stretching modes, especially the ν(C=C) dienone that dominates the free CSs, are present but as very weak features. In FLU, aside from the thioester band at *ca.* 1712 cm^{-1} and the weak band corresponding with the ν(C=C) dienone mode, no other features are present in this region. In MOM, the principal features in this region correspond with the furanyl substituent of Ring D. The ν(C=O) furanyl mode may be attributed to bands at *ca.* 1750 and 1695 cm^{-1}, but the strongest features that emerge from a broad spectral envelope are bands at *ca.* 1608 cm^{-1} and *ca.* 1560 cm^{-1}. These may originate with correspond with coupled ν(C=O, C=C) furan modes, possibly from symmetric and asymmetric vibrations of the ring and the enhancement of the former is notable, as it is possibly obscured in the spectrum of the pure material. In the remaining regions of each spectrum, the features are largely attributable to methyl and methylene deformation modes or to ester ν(C-O) modes.

Broadly similar enhancement patterns are apparent for the Au-NPs and can be concluded that the species appear to interact most strongly with the metal nanoparticle through the Band D substituents.

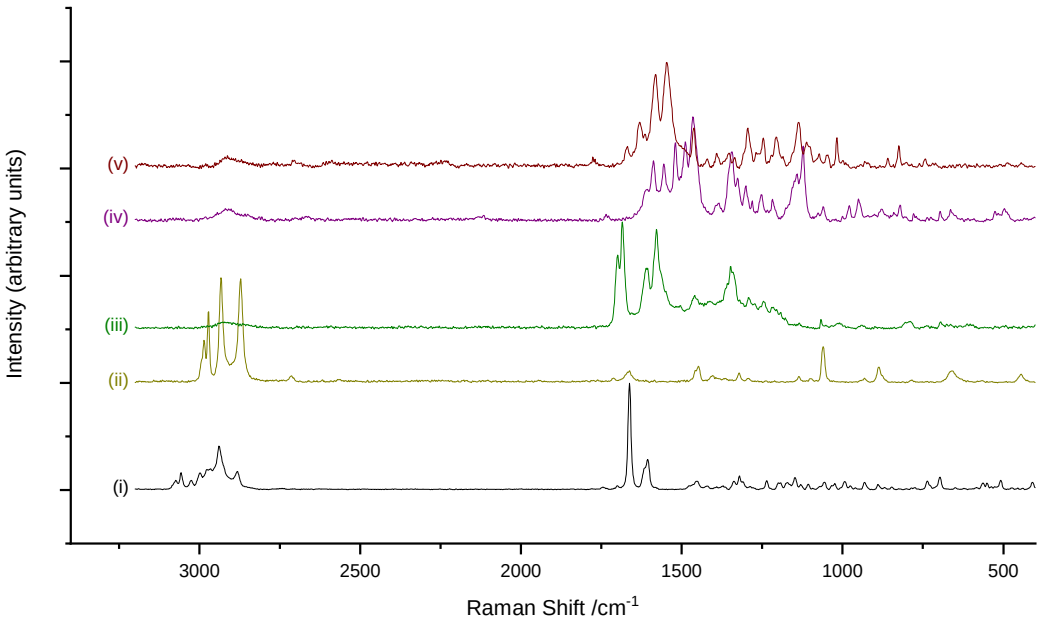

Figure 6.28: Baseline-subtracted Raman spectra of fluticasone propionate (FLU) after mixing with metal-NP formulations showing the different enhancements for naked and SCD-functionalised particles: (i) FLU reference spectrum, (ii) FLU with Ag-NP (iii) FLU with SCD-Ag-NP, (iv) FLU with Au-NP, (v) FLU with SCD-Au-NP.

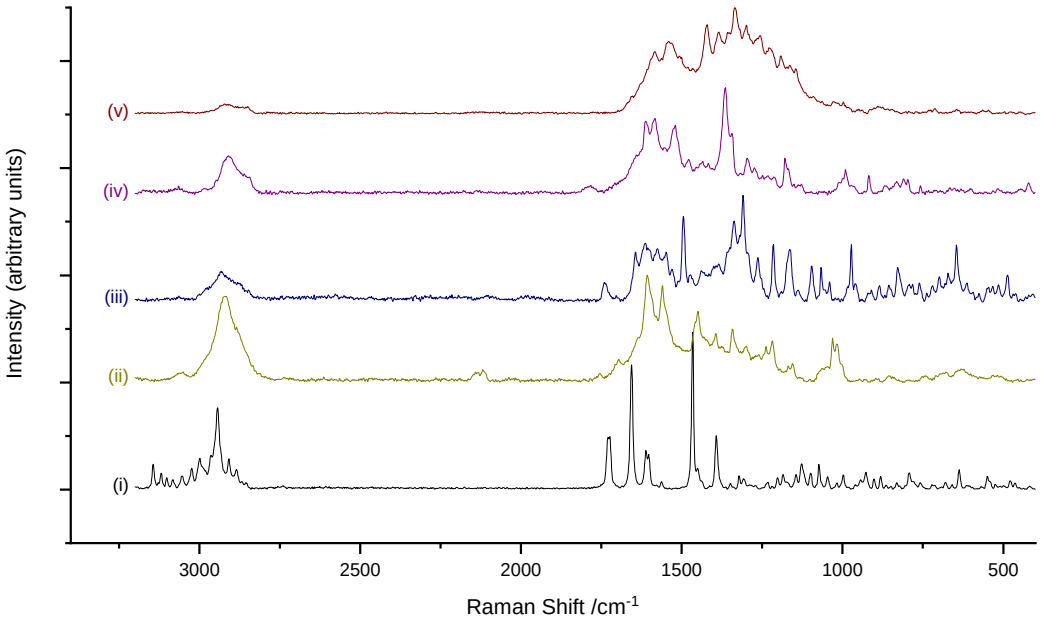

Figure 6.29: Baseline-subtracted Raman spectra of mometasone furoate (MOM) after mixing with metal-NP formulations showing the different enhancements for naked and SCD-functionalised particles: (i) MOM reference spectrum, (ii) MOM with Ag-NP (iii) MOM with SCD-Ag-NP, (iv) MOM with Au-NP, (v) MOM with SCD-Au-NP.

Comparison of the spectra arising from the SCD-functionalised metal nanoparticles present a rather less clear picture, compared to the other CSs (BUD and BDP). While enhancements of dienone functions through interaction

with SCD-Ag in particular are clearly apparent in the spectra (corresponding with the binding modes proposed for these species that, other modes also appear enhanced. Notably in the FLU SCD-Ag-NP system, the strongest enhancements occur for bands at *ca.* 1690 cm^{-1} that correspond with the fluoro-thioether moiety. It is not inconceivable that alternative SCD-CS interactions may occur with these systems and the spectra correspond with a range of direct and SCD-mediated interactions. This is clearly consistent with the lower binding affinity that FLU and MOM display for SCD (possibly related to their bulkier Ring D substituents) and would correspond with the more complex spectra seen with these systems. In summary, it can be concluded that MOM and FLU interact most strongly with the naked metal NPs through the Ring D substituents (offering little enhancement of Ring A modes). However, in the decorated systems, the picture is more complicated and, while enhancements that correspond with the SCD hosting the CSs and thereby facilitating the approach of Ring A to the NP surface are observed, strong enhancements of other molecular functions (*e.g.* fluorothioester in FLU) must arise from alternative CS…SCD-M-NP interaction. The non-selectivity of interaction is consistent with lower binding affinities for MOM and FLU.

7 Conclusion

7.1 NMR Studies

The work conducted in this thesis has established a developed method allowing us to study the physical chemistry of corticosteroid-CD complexation for the purpose of controlling the solubility and the stability of pMDI inhaler devices. The method was applied to investigate the complexation of BUD in a range of solvents with different polarities which was applied further to study the complexation of different corticosteroids; BUD, BDP, FLU and MOM with the derivatised CDs TRIMEB and DIMEB in HPFP using NMR.

Spectroscopic methods have been developed to study host:guest interactions of BUD : *β*CD/TRIMEB complexes in a mixture of EtOH/H_2O and in water and also for better comprehensive understanding of the stability constant and stoichiometry determination. The results showed a higher complexation (larger association constant) of BUD with both *β*CD and TRIMEB occurred in H_2O compared to the co-solvent system of EtOH/H_2O, where the K values were found to be 205 and 138 M^{-1} with TRIMEB and 94 and 72 M^{-1} with *β*CD in H_2O and EtOH/ H_2O mixture respectively. This is attributed to the polarity of BUD and its solubility in the solvent where BUD as a non-polar guest prefers to be more solvated in EtOH and thus reduces the driving force towards the CD cavity which is more polar in nature than the bulk solvent. This leads to the partial existence of BUD outside the cavity and thus a formation of weak complexation. However, in aqueous solution, BUD was driven into the CD cavity with a reduced polarity compared to the bulk solvent and leads to the formation of stronger complexation.

NMR methods have been used to study BUD:CDs (DIMEB/TRIMEB) in a range of different polarity solvents (CD_3CN, MeOD, $CDCl_3$ and D_2O). However, the complexation between BUD and *β*CD was not assessed in the organic solvents due to its limited solubility. The K values of the complexation of BUD with DIMEB were 116 and 73 M^{-1} and with TRIMEB were 91 and 64 M^{-1} in MeOD and $CDCl_3$ respectively. No complexation was formed in CD_3CN.The complexation in D_2O was the strongest observed of all the solvents assessed with the highest K value obtained with DIMEB followed by *β*CD and the lowest value with TRIMEB, where the values were 4446, 1129 and 429 M^{-1}

respectively. The forming of the strong complexation in different solvents assessed can be summarised as D_2O > MeOD > $CDCl_3$ > CD_3CN. No complexation was formed in CD_3CN which is ascribed to the similarity in the polarity of the solvent to the interior cavity of the CD. There is therefore no drive for the BUD to enter the CD cavity and form a complex. BUD as a nonpolar guest preferred the CD cavity of less polarity compared to bulk water, and as a result the strongest complexation was formed in the aqueous environment. In the presence of MeOD and $CDCl_3$ solvents, the CD cavity is more polar than the bulk solvent and thus the driving force towards the CD cavity entrance is reduced as BUD is relatively soluble in both solvents. It shows a preference therefore for being located outside the cavity (solvated in the bulk solvent) over interacting with the CD. Hence, a lower association constant is observed with MeOD and $CDCl_3$ when compared to water. The reciprocal plot of the titration experiments showed good linearity and the continuous variation approach showed a maximum at r = 0.5, confirming the complex had a stoichiometry of 1:1.

The effect of CD type on the complexation was studied utilising three different types of CDs; (i) *β*CD, (ii) DIMEB and (iii) TRIMEB with BUD. The results are summarised in Table 7.1.

Table 7.1: A summary of the chemical shift displacements observed (in ppm) for BUD with 2 mM *β*CD, DIMEB and TRIMEB in D_2O related to the chemical shift of free BUD.

CD type	Chemical shift displacements (ppm)				
	H-C_1	H-C_2	H-C_4	H-C_{18}	H-C_{19}
*β*CD	D* (0.01)	U** (0.07)	U** (0.03)	D* (0.05)	D** (0.12, 0.16)
DIMEB	U** (0.06)	U** (0.11)	U** (0.06)	D* (0.03)	D** (0.11)
TRIMEB	NS	D* (0.01)	U* (0.02)	NS	D* (0.04)

D* = small downfield, D** = large downfield, U* = small upfield, U** = large upfield, NS = no significant shift.

The complexation of BUD with *β*CD and DIMEB in D_2O caused downfield shift changes for the H-C_{18} and H-C_{19} protons and upfield chemical shift changes of the quinone ring protons (H-C_1, H-C_2 and H-C_4), with the exception of H-C_1 proton where it was observed with downfield shift in the complexation with *β*CD. This suggested that entrance of the quinone ring of BUD into DIMEB cavity is deeper than that of BUD in *β*CD where we anticipate the H-C_1 proton (exhibiting a downfield shift) is located outside or near the cavity. These observations are consistent with the higher association constant derived for the complex with

BUD-DIMEB compared to BUD-*β*CD. The chemical shift differences observed in the quinone ring (with the exception of H-C_1 proton) with *β*CD could be attributed to the shielding effect of the hydrophobic CD cavity: suggesting these protons are closer in proximity to the oxygen atoms located on the inner side of the cavity. Both H-C_{18} and H-C_{19} with downfield shift were supposed to be outside the *β*CD and DIMEB cavities and interacted with the external surfaces of the CD and they were situated far from the oxygen atom inside the CD cavity. The H-C_{19} was expected to be closer to the CD cavity than H-C_{18} and this explained the large chemical shift differences observed with the former proton.

In the complexation with TRIMEB, the quinone ring of BUD enters partially into the CD cavity where only H-C_4 proton of the quinone ring (experienced upfield shift) was located in the TRIMEB cavity. The H-C_2 proton of the quinone ring and H-C_{19} proton were located outside the cavity as they were observed to have a downfield shift. As the quinone ring partially entered the TRIMEB cavity, therefore, the H-C_{18} proton (with no chemical shift differences) was situated far from the cavity compared to the same proton in the complexation with *β*CD and DIMEB. The larger chemical shift differences resulted in the stronger complexation and thus show a higher value for the stability constant. Accordingly, it can be concluded that both DIMEB and *β*CD cavities were suitable in size to accommodate and interact with BUD to form stronger complexation with a better geometric fitting compared to the weaker complexation with TRIMEB. The predicted interaction of BUD with the three types of CDs has shown in Figure 7.1.

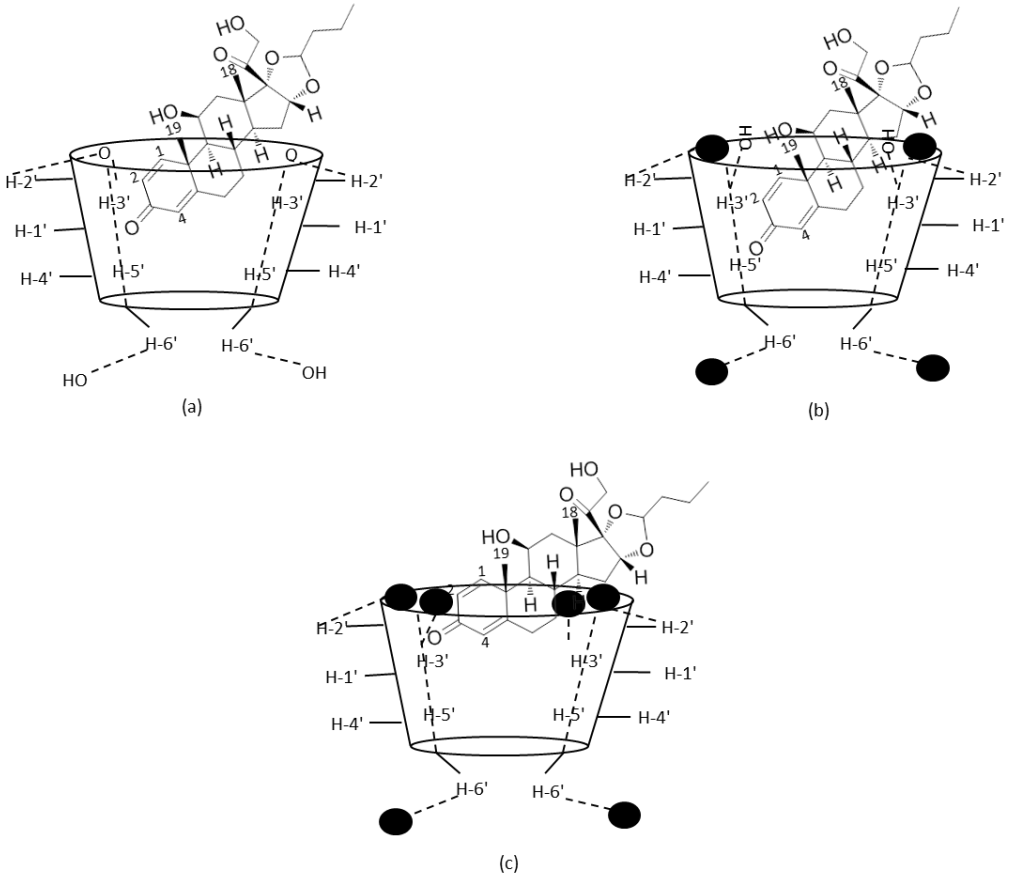

Figure 7.1: Inclusion complex of the budesonide and (a) *β*CD, (b) DIMEB and (c) TRIMEB. The black balls represent the methoxyl groups in the DIMEB and TRIMEB molecules.

The developed NMR method was then applied to study the complexation between different corticosteroids (BUD, BDP, MOM and FLU) with the derivatised CD (DIMEB and TRIMEB) in the fluorinated solvent system HPFP (of the type used in pMDIs). The results of the chemical shift displacements of the key protons of the compounds involved in the complexations studied with TRIMEB are presented in Table 7.2.

Table 7.2: A summary of the chemical shift displacements (in ppm) for BUD, BDP, MOM and FLU with 2 mM TRIMEB in HPFP related to the chemical shift of the free compounds.

Compound	Chemical shift displacements (ppm)				
	H-C_1	H-C_2	H-C_4	H-C_{18}	H-C_{19}
BUD	D** (0.07, *R*) D* (0.02, *S*)	NS	U* (0.01)	D** (0.17, *R*)	D* (0.01)
BDP	NS	NS	D* (0.07)	NS	D* (0.05)
MOM	NA	NA	NA	NS	D* (0.04)
FLU	NA	NA	NA	NS	D* (0.02)

D* = small downfield, D** = large downfield, U* = small upfield, NS = no significant shift, NA = S/N too low to interpret, *R*, *S* = enantiomers of BUD

The results showed the strongest complexation was with BUD among all the investigated corticosteroids, followed by BDP and MOM, with the weakest complexation observed with FLU based on the stability constant values. The K values of BDP, MOM and FLU were 197.5, 130 and 86 M^{-1} respectively, whereas the K values of BUD enantiomers were 621 and 222 M^{-1} for *R* and *S* enantiomers respectively.

The complexation of BUD with TRIMEB showed a downfield shift for the H-C_1 proton of the quinone ring and a very small upfield shift occurred for H-C_4, with no shift observed for the H-C_2 proton. A significant downfield shift was observed for H-C_{18} whereas the H-C_{19} resonance was observed with very small downfield shift and was fully split into two distinctive peaks at higher TRIMEB concentrations. The complexation of BDP showed minor downfield shift differences for the H-C_4 proton whereas the H-C_{19} proton was observed to show a downfield shift (no shift was noted for the other protons). Both MOM and FLU showed only a small downfield shift for the H-C_{19} proton in their complexation with TRIMEB. However, the other protons in the low field region were not clearly observed in the complexed spectra of both compounds as they displayed a low S/N ratio and therefore it was difficult to investigate the effect of TRIMEB on the chemical shift of those protons. The reciprocal plot of the titration experiments for the all studied corticosteroids followed a linear trend, demonstrating that the stoichiometric ration of the complexation was 1:1. The continuous variation method was also applied to confirm the 1:1 stoichiometry of the inclusion complex of BUD with TRIMEB. The Job's plot showed a maximum at r = 0.5 which suggests a 1:1 stoichiometry of the complexation and supports the data obtained in the titration experiments using Hildebrand-Benesi approach.

The complexation was also investigated in HPFP between BUD, BDP and DIMEB and the findings were similar to those obtained with TRIMEB in that the strongest complexation was observed with BUD. The chemical shift displacements of some quinone ring protons of BUD and BDP with TRIMEB and DIMEB in HPFP suggested the formation of the inclusion complex was similar to those observed in the other solvent systems, with the quinone ring entering both CD cavities. However, it difficult to estimate the mechanism of the interaction of MOM and FLU with TRIMEB as the quinone ring protons did not appear in the spectra of both compounds due to low S/N ratio for those protons.

The strongest complexation was achieved with BUD compared to the other corticosteroids studied. We propose that this is due to the presence of the substitution groups such as a furan ring at C17 in MOM and the propionate chains in BDP and FLU structures. These groups are expected to cause steric hindrance, which impede the deeper inclusion of BDP, FLU and MOM into the TRIMEB cavity when compared to BUD. Further, an extra hindrance results from the presence of halogenated atoms such as a Cl at C9 in BDP and MOM, and F at C6 and C9 in FLU which hamper the entrance of these compounds into the TRIMEB cavity compared to the H atom at C9 in the BUD molecule.

Further work was carried out on the pure enantiomer of BUD (*R*-BUD) in order to assign the peaks in the complexed BUD spectra correctly by relating to both enantiomers of BUD. The findings showed the splitting peaks of the H-C_{18} proton were related to the *R* and *S*-enantiomers of BUD. The resonance that showed a chemical shift displacement during the NMR titration was shown to be the *R*-enantiomer, with the *S*-form showing no displacement. The H-C_{19} proton of the *R*-enantiomer appeared as singlet in the complexed form whereas it was fully split into two distinctive peaks in the racemic mixture of BUD at high TRIMEB concentration indicating that another peak appeared in the spectrum of the racemic BUD was assigned to the *S*-enantiomer. The same results were obtained with H-C_4 proton where in the pure *R*-enantiomer it appeared as singlet peak whereas it partially split in the racemic solution suggesting that this peak in the racemic BUD spectra was related to both enantiomers. The H-C_1 proton of the quinone ring was observed to display a downfield shift, with a concurrent multiplicity change as the TRIMEB concentration was increased. The originally observed doublet (*R*-enantiomer) was split into four peaks, therefore, the two peaks with the highest downfield shift in the racemic BUD spectrum were assigned to the *R*-enantiomer whereas the other two peaks were related to the *S*-enantiomer.

The studies presented in this thesis have shown the formation of the strongest host:guest complex of BUD was with DIMEB in D_2O whereas it was with TRIMEB in HPFP. This is explained by the solubility of the host in the solvent as its solubility controls the strength of the complexation i.e. with higher CD solubility, more molecules are solvated in the solution and are available for the complexation with the guest molecules; hence a higher association constant is

observed. The water solubility of DIMEB and TRIMEB is 57 and 31 g/100 mL whereas their solubility in HPFP is 1 and 6 mg/mL (0.1 and 0.6 g/100 mL) respectively. In aqueous solution, DIMEB solubility is higher than TRIMEB; i.e. more DIMEB molecules are available to interact with the BUD in the system and thus more BUD molecules are engaged in the complexation. This results in more significant chemical shift displacements in the NMR performed and in turn a high stability constant is observed. The converse is true in the case of HPFP where the solubility of TRIMEB is higher than DIMEB. Therefore, more TRIMEB molecules in the solution are available to form complexation with BUD than with the DIMEB system and explains why the strongest complexation observed in D_2O is with BUD and DIMEB, and in HPFP is with the TRIMEB system.

The methods developed and applied to the study of corticosteroids and CD have allowed us to probe the interactions with significant detail. We have derived numerical values for the systems studied to make direct comparison between corticosteroids of different functionality, CD with different derivatisations and solvents of different polarity. We have been able to postulate the 'structure' of the complexes formed through the observations made of the chemical shift displacements in the NMR titrations performed and have, for the first time, studied these interactions in fluorinated solvent systems of the type used in pMDI based medications. The significance of the differences observed in the systems studied underpins the importance of being able to study these systems *in-situ* and provides extremely useful data for people looking to control solubility in fluorinated solvent media.

7.2 SERS Studies

As discussed in Section 7.1, the NMR methods employed have allowed us to establish the thermodynamics of binding with (relatively) polar solvents and have found that the association constants rank as BUD > BDP > MOM > FLU, showing a loose (inverse) correlation with steric bulk of D-ring substituents. We have established detailed structural information on the host-guest interaction and demonstrated in each case, the enone functionality of the A-ring inserts into guest cavity.

7.2.1 Conventional Raman Spectroscopic Studies of Corticosteroids

A detailed study of CSs with Raman for MOM and BDP has been undertaken for the first time. We have established a strategy that broadly correlates spectral regions to regions of the molecular structure in order to establish regioselectivity of SERS interaction. This strategy was required as complex spectra have significant overlaps and isolated, discrete spectral bands are unlikely to be available. The following relationships between molecular regions and spectral ranges were established: 1780-1550 cm^{-1} correlates with CS A-ring and specific D-ring substituent modes (*e.g*. ester carbonyls); 1500-1380 cm^{-1} correlates with C- and D-rings and to the D-ring substituents for this set of species; 1380-1000 cm^{-1} correlated to D-ring substituents (particularly ester functions) although certain specific bands could be used to probe the hydroxyl substituents on the steroid framework [*e.g.* δ_{as}/δ_{s}(C-OH)]; below 1000 cm^{-1}, an array of bands was correlated with vibrations of the steroid framework in addition to a number of indicative D-ring substituent bands.

7.2.2 Nanoparticle Synthesis and Characterisation

We have developed the methodologies to prepare metal nanoparticle formulations and load the surface with SCD. TEM observations ('sulfur halo') and marginal changes in particle size indicated that the metal nanoparticle surface had been functionalised with SCD. The potential importance of centrifugation was identified. The synthetic step was shown to reduce polydispersity and this appeared to correlate with enhanced SERS performance (especially with Au-NP and SCD-NP).

7.2.3 SERS with CSs

Significant enhancements were observed with all systems, with increases in intensity of the order of 10^3-10^4 routinely observed using short exposures and minimal co-additions. Generally, with the naked metal nanoparticles, regiospecific enhancements were observed that correlated to steroid D-ring substituents. It is expected that the enhancement relates to the proximity (and appropriate orientation) of these molecular regions to the NP surface (with its partial charge). These correlate with more polar regions of the molecule (consistent with NMR studies where the D-ring is shown have an affinity with the solvent medium (aqueous), leading to A-ring insertion to the (relatively)

apolar CD cavity). Ag-NPs have been observed to be generally more active and more regio-selective than Au-NP.

7.2.4 SERS with SCD-M-NP

In these studies, 'selective' SERS has been demonstrated for the first time. The studies indicate that surface functionalisation of the metal NP with CD moieties orientates different regions of the molecular species to interact with the metal surface – in all cases, enhancement has been observed in several (correlated) spectral regions. Silver NP formulations appeared to be more active than gold with most systems and, in many cases, led to better resolved spectra. A link between spectral resolution with the SERS microenvironment was inferred. The potential importance of creating homogenous metal NPs (e.g. through control of centrifugation steps in preparation) may be the topic for future development of these systems. In some cases, SCD-Au-NP formulations showed enhancement for bands from SCD host. While not desirable because of the potential interference, the SCD vibrations cover a relatively small spectral window and, in particular, obscured only the 1500-1380 cm^{-1} regions. In the cases where these effects were experience, other spectral regions could be used to give diagnostic information. Interestingly, the SCD-Ag-NP formulations showed no interference of this type. Regioselectivity appears to follow binding affinity for Ag: BUD~BDP > FLU~MOM. In the latter group, spectral complexity indicates greater diversity of enhancement possibly indicating different structural units interacting the metal-N centre.

8 Further work

The work in this thesis can be extended in a number of different directions. The NMR methods developed could be used to study the SCD systems employed in the SERS study to derive binding constants and formalise the stoichiometry of the systems, complementing the data obtained from the SERS study well. Additional thermodynamic data is relatively easily obtainable on all the systems studied, with some simple modifications to the NMR approaches used. Variable temperature work could be performed to derive van't Hoff plots allowing extraction of data to further understand enthalpic vs. entropic control of the systems studied with the different CD, solvent and ICS combinations.

The methodology summarised in this work also form the basis for transfer to investigate the complexation in HFAs 134a and 227 commonly used as propellants in pMDI products. Being gaseous at STP, most analytical approaches are cumbersome and difficult to implement for such systems. As the NMR setup used can be easily modified to incorporate a cap capable of holding the tube at pressure, HFAs 134a and 227 can be studied under the conditions present in a pMDI canister *i.e*. as liquids at room temperature.

Furthermore, other compounds of significance in inhalational therapies such as β_2 agonists (salbutamol, terbutaline, salmeterol and formoterol) could be assessed for their behaviour with CDs in these HFA solvents to interrogate any complexation exhibited and establish a greater understanding of formulation characteristics of inhaled drugs *in-situ* and develop more efficacious treatments.

The SERS studies reported have provided a fundamental insight into the SCD-Au and SCD-Ag systems and their interaction with ICS compounds. Work to study the relative quantification of regions to quantify the enhancements observed would be of benefit, leading to the possibility of quantifying the loading of SCDs. Further work to characterise the SCD and how this is oriented on the surface of the NPs would be of great value.

9 References

1. Grossman J. The evolution of inhaler technology. *The Journal of asthma : official journal of the Association for the Care of Asthma.* 1994;31(1):55-64.
2. Labiris NR, Dolovich MB. Pulmonary drug delivery. Part I: physiological factors affecting therapeutic effectiveness of aerosolized medications. *British journal of clinical pharmacology.* 2003;56(6):588-599.
3. Hoppentocht M, Hagedoorn P, Frijlink HW, de Boer AH. Technological and practical challenges of dry powder inhalers and formulations. *Advanced drug delivery reviews.* 2014.
4. Patton JS, Byron PR. Inhaling medicines: delivering drugs to the body through the lungs. *Nature reviews Drug discovery.* 2007;6(1):67-74.
5. Dolovich MB, Dhand R. Aerosol drug delivery: developments in device design and clinical use. *Lancet.* 2011;377(9770):1032-1045.
6. Keith IM, Olson EB, Jr., Wilson NM, Jefcoate CR. Immunological identification and effects of 3-methylcholanthrene and phenobarbital on rat pulmonary cytochrome P-450. *Cancer research.* 1987;47(7):1878-1882.
7. Ji CM, Cardoso WV, Gebremichael A, et al. Pulmonary cytochrome P-450 monooxygenase system and Clara cell differentiation in rats. *The American journal of physiology.* 1995;269(3 Pt 1):L394-402.
8. Yang MY, Chan JGY, Chan H. Pulmonary drug delivery by powder aerosols. *Journal of controlled release.* 2014:1-13.
9. Welbanks L. Compendium of pharmaceuticals and specialties. In. 35 ed: Ontario: Canadian Pharmacists Association; 2000.
10. Ritchie TJ, Luscombe CN, Macdonald SJ. Analysis of the calculated physicochemical properties of respiratory drugs: can we design for inhaled drugs yet? *Journal of chemical information and modeling.* 2009;49(4):1025-1032.
11. Bell JH, Hartley PS, Cox JS. Dry powder aerosols. I. A new powder inhalation device. *Journal of pharmaceutical sciences.* 1971;60(10):1559-1564.
12. Geller DE, Weers J, Heuerding S. Development of an inhaled dry-powder formulation of tobramycin using PulmoSphere technology. *Journal of aerosol medicine and pulmonary drug delivery.* 2011;24(4):175-182.
13. Global Strategy for the Diagnosis, Management and Prevention of Chronic Obstructive Pulmonary Disease, Global Initiative for Chronic Obstructive Lung Disease (GOLD), www.goldcopd.org. 2014. Accessed 12-07-2014.
14. Chapman KR, Tashkin DP, Pye DJ. Gender bias in the diagnosis of COPD. *Chest.* 2001;119(6):1691-1695.
15. Chronic obstructive pulmonary disease, Management of chronic obstructive pulmonary disease in adults in primary and secondary care (partial update), National Institute for Health and Clinical Excellence (NHS). www.nice.org.uk. 2010.
16. Barnes PJ. New treatments for COPD. *Nature reviews Drug discovery.* 2002;1(6):437-446.
17. Bousquet J, Khaltaev AN. Global surveillance, prevention and control of chronic respiratory diseases: a comprehensive approach. Global Alliance against Chronic Respiratory Diseases. *Geneva: World Health Organization.* 2007.
18. Olaguibel JM, Quirce S, Julia B, et al. Measurement of asthma control according to Global Initiative for Asthma guidelines: a comparison with the Asthma Control Questionnaire. *Respiratory research.* 2012;13:50.
19. Global Strategy for Asthma Management and Prevention, Global Initiative for asthma (GINA), 2014,www.ginasthma.org.
20. Bousquet J, Kiley J, Bateman E, Viegi G, Cruz AA. Prioritised research agenda for prevention and control of chronic respiratory diseases. . *Eur Respir J* 2010;36:995-1001.

21. Shapiro SD. Animal models for COPD. *Chest.* 2000;117(5 Suppl 1):223S-227S.
22. Barnes PJ. *Asthma and COPD : basic mechanisms and clinical management.* 2nd ed. ed. Amsterdam ; London: Academic; 2009.
23. Mason JR, et al. *Murray and Nadel's textbook of respiratory medicine.* 5th ed ed. Philadelphia, PA: Saunders/Elsevier; 2010.
24. Chung KF, Wenzel SE, Brozek JL, et al. International ERS/ATS guidelines on definition, evaluation and treatment of severe asthma. *Eur Respir J.* 2014;43(2):343-373.
25. Keatings VM, Collins PD, Scott DM, Barnes PJ. Differences in interleukin-8 and tumor necrosis factor-alpha in induced sputum from patients with chronic obstructive pulmonary disease or asthma. *American journal of respiratory and critical care medicine.* 1996;153(2):530-534.
26. de Boer WI, Yao H, Rahman I. Future therapeutic treatment of COPD: Struggle between oxidants and cytokines. *International Journal of COPD.* 2007;2(3):205-228.
27. Rennard SI. Treatment of stable chronic obstructive pulmonary disease. *Lancet.* 2004;364(9436):791-802.
28. Wouters EF. Management of severe COPD. *Lancet.* 2004;364(9437):883-895.
29. Evans DJ, et al. A comparison of low-dose inhaled budesonide plus theophylline and high-dose inhaled budesonide for moderate asthma. *The New England Journal of Medicine.* 1997;337(20):1412-1418.
30. Tinkelman DG, et al. Aerosol beclomethasone dipropionate compared with theophylline as primary treatment of chronic, mild to moderately severe asthma in children. *Pediatrics.* 1993;92(1):64-77.
31. Montuschi P. Pharmacological treatment of chronic obstructive pulmonary disease. *International Journal of COPD.* 2006;1(4):409-423.
32. Johnston SL, et al. Community study of role of viral infections in exacerbations of asthma in 9–11 year old children. *BMJ.* 1995;13(310):1225–1229.
33. Bueving HJ, Bernsen RM, de Jongste JC, et al. Influenza vaccination in children with asthma: randomized double-blind placebo-controlled trial. *American journal of respiratory and critical care medicine.* 2004;169(4):488-493.
34. Nicholson KG, R. Snacken, and A.M. Palache. Influenza immunization policies in Europe and the United States. *Vaccine.* 1995;13(4):365-369.
35. Tata LJ, et al. Does influenza vaccination increase consultations, corticosteroid prescriptions, or exacerbations in subjects with asthma or chronic obstructive pulmonary disease? *Thorax.* 2003;58(10):835-839.
36. Rothbarth PH, Kempen BM, Sprenger MJ. Sense and nonsense of influenza vaccination in asthma and chronic obstructive pulmonary disease. *American journal of respiratory and critical care medicine.* 1995;151(5):1682-1685; discussion 1685-1686.
37. Alton EW, Boushey HA, Garn H, et al. Clinical expert panel on monitoring potential lung toxicity of inhaled oligonucleotides: consensus points and recommendations. *Nucleic acid therapeutics.* 2012;22(4):246-254.
38. Ferrari N, Seguin R, Renzi P. Oligonucleotides: a multi-targeted approach for the treatment of respiratory diseases. *Future medicinal chemistry.* 2011;3(13):1647-1662.
39. Rahman I. Antioxidant therapies in COPD. *International journal of chronic obstructive pulmonary disease.* 2006;1(1):15-29.
40. Rahman I. Pharmacological antioxidant strategies as therapeutic interventions for COPD. *Biochimica et Biophysica Acta.* 2012;1822(5):714-728.
41. Shaheen SO, Sterne JA, Thompson RL, Songhurst CE, Margetts BM, Burney PG. Dietary antioxidants and asthma in adults: population-based case-control study. *American journal of respiratory and critical care medicine.* 2001;164(10 Pt 1):1823-1828.
42. Patel BD, Welch AA, Bingham SA, et al. Dietary antioxidants and asthma in adults. *Thorax.* 2006;61(5):388-393.

43. Matera MG, L. Calzetta, and M. Cazzola. TNF-a inhibitors in asthma and COPD: We must not throw the baby out with the bath water. *Pulm Pharmacol Ther.* 2010;23(2):121-128.
44. Berry M, et al. TNF-alpha in asthma. *Current Opinion in Pharmacology.* 2007;7(3):279-282.
45. Suissa S, P. Ernst, and M. Hudson. TNF-a antagonists and the prevention of hospitalisation for chronic obstructive pulmonary disease. *Pulmonary Pharmacology & Therapeutics.* 2008;21(1):234-238.
46. Barnes PJ, Adcock IM. How Do Corticosteroids Work in Asthma? *Ann Intern Med.* 2003;139(5):359-370.
47. Bateman ED, et al. Global strategy for asthma management and prevention: GINA executive summary. *Eur Respir J.* 2008;31(1):143–178.
48. Barnes PJ. Glucocorticosteroids: current and future directions. *British journal of pharmacology.* 2011;163(1):29-43.
49. Barnes PJ. How corticosteroids control inflammation: Quintiles Prize Lecture 2005. *British journal of pharmacology.* 2006;148(3):245-254.
50. Rowe BH, Spooner C, Ducharme FM, Bretzlaff JA, Bota GW. Early emergency department treatment of acute asthma with systemic corticosteroids. *The Cochrane database of systematic reviews.* 2001(1):CD002178.
51. Lipworth BJ, Jackson CM. Safety of inhaled and intranasal corticosteroids: lessons for the new millennium. *Drug safety : an international journal of medical toxicology and drug experience.* 2000;23(1):11-33.
52. Bandi N, Wei W, Roberts CB, Kotra LP, Kompella UB. Preparation of budesonide- and indomethacin-hydroxypropyl-beta-cyclodextrin (HPBCD) complexes using a single-step, organic-solvent-free supercritical fluid process. *European journal of pharmaceutical sciences : official journal of the European Federation for Pharmaceutical Sciences.* 2004;23(2):159-168.
53. Rubin BK. Air and soul: the science and application of aerosol therapy. *Respiratory care.* 2010;55(7):911-921.
54. O'Callaghan C, Barry PW. The science of nebulised drug delivery. *Thorax.* 1997;52 Suppl 2:S31-44.
55. Hess DR. Aerosol delivery devices in the treatment of asthma. *Respiratory care.* 2008;53(6):699-723; discussion 723-695.
56. Talasila GKM, Mukkala BVP, Vattikuri S. Formulation and evaluation of CFC free inhalers for beclomethasone dipropionate *Brazilian Journal of Pharmaceutical Sciences.* 2013;49(2):221-231.
57. Newman SP. Principles of Metered-Dose Inhaler Design. *Respiratory care.* 2005;50(9):1177-1190.
58. Zhou QT, Tang P, Leung SS, Chan JG, Chan HK. Emerging inhalation aerosol devices and strategies: Where are we headed? *Advanced drug delivery reviews.* 2014.
59. Khale A, Bajaj A. Formulation and development of metered dose inhalations of salbutamol in solution form. *Indian journal of pharmaceutical sciences.* 2011;73(5):543-549.
60. O'Byrne PM. Clinical comparisons of inhaler systems: what are the important aspects? *Journal of aerosol medicine : the official journal of the International Society for Aerosols in Medicine.* 1995;8 Suppl 3:S39-46; discussion S47.
61. Chrystyn H. The Diskus: a review of its position among dry powder inhaler devices. *International journal of clinical practice.* 2007;61(6):1022-1036.
62. Telko MJ, Hickey AJ. Dry powder inhaler formulation. *Respiratory care.* 2005;50(9):1209-1227.
63. Maggi L, Bruni R, Conte U. Influence of the moisture on the performance of a new dry powder inhaler. *International journal of pharmaceutics.* 1999;177(1):83-91.

64. Melani AS, Zanchetta D, Barbato N, et al. Inhalation technique and variables associated with misuse of conventional metered-dose inhalers and newer dry powder inhalers in experienced adults. *Annals of allergy, asthma & immunology : official publication of the American College of Allergy, Asthma, & Immunology.* 2004;93(5):439-446.
65. Frijlink HW, De Boer AH. Drug powder inhalers for pulmonary dug delivery. *Expert Opin Drug Deliv.* 2004;1(1).
66. Leach CL. The CFC to HFA transition and its impact on pulmonary drug development. *Respiratory care.* 2005;50(9):1201-1208.
67. Forte R, Dibble C. The role of international environmental agreements in metered-dose inhaler technology changes. *The Journal of Allergy and Clinical Immunology.* 1999;104(6):s217-s220.
68. Ibiapina CC, Cruz ÁA, Camargos PAM. Hydrofluoroalkane as a propellant for pressurized metered-dose inhalers: history, pulmonary deposition, pharmacokinetics, efficacy and safety. *Jornal de Pediatria.* 2004;80(6):441-446.
69. Leach CL, Davidson PJ, Boudreau RJ. Improved airway targeting with the CFC-free HFA-beclomethasone metered-dose inhaler compared with CFC-beclomethasone. *Eur Respir J.* 1998;12(6):1346-1353.
70. Cheng YS, Fu CS, Yazzie D, Zhou Y. Respiratory deposition patterns of salbutamol pMDI with CFC and HFA-134a formulations in a human airway replica. *Journal of aerosol medicine : the official journal of the International Society for Aerosols in Medicine.* 2001;14(2):255-266.
71. Smyth HDC. The influence of formulation variables on the performance of alternative propellant-driven metered dose inhalers. *Advanced Drug Delivery Reviews.* 2003;55(7):807-828.
72. Smith IJ. The challenge of reformulation. *Journal of aerosol medicine : the official journal of the International Society for Aerosols in Medicine.* 1995;8 Suppl 1:S19-27.
73. Brambilla G, Ganderton D, Garzia R, Lewis D, Meakin B, Ventura P. Modulation of aerosol clouds produced by pressurised inhalation aerosols. *International journal of pharmaceutics.* 1999;186(1):53-61.
74. Ibiapina CC, A.A. Cruz, and P.A.M. Camargos. Hydrofluoroalkane as a propellant for pressurized metered-dose inhalers: history, pulmonary deposition, pharmacokinetics, efficacy and safety. *Jornal de Pediatria.* 2004;80(6):441-446.
75. Ganderton D, Lewis D, Davies R, Meakin B, Brambilla G, Church T. Modulite: a means of designing the aerosols generated by pressurized metered dose inhalers. *Respiratory medicine.* 2002;96 Suppl D:S3-8.
76. Savjani KT, Gajjar AK, Savjani JK. Drug solubility: importance and enhancement techniques. *ISRN pharmaceutics.* 2012;2012:195727.
77. Xu W, Ling P, Zhang T. Polymeric micelles, a promising drug delivery system to enhance bioavailability of poorly water-soluble drugs. *Journal of drug delivery.* 2013;2013:340315.
78. Kumar A, et al. Review on solubility enhancement techniques for hydrophobic drugs. *Pharmacie Globale (IJCP).* 2011;2(3):1-7.
79. Podczeck F, J.M. Newton, and M.B. James. The adhesion strength of particles of salmeterol base and a series of salmeterol salts to compacted lactose monohydrate surfaces. *J ADHES SCI TECHNOL* 1995;9(12):1547-1558.
80. Seville PC, Simons C, Taylor G, Dickinson PA. Prodrug to probe solution HFA pMDI formulation and pulmonary esterase activity. *International journal of pharmaceutics.* 2000;195(1-2):13-16.
81. Sukasame N, P. Boonme, and T. Srichana. Development of budesonide suspensions for use in an HFA pressurized metered dose inhaler. *ScienceAsia.* 2011;37:31-37.
82. Ramteke KH, S.S. Gunjal, and Y.P. Sharma. Formulation and quality control of metered dose inhaler: a review. *JPSI.* 2012;1(2):44-49.

83. Gardenhire DS. *Rau's Respiratory Care Pharmacology* 8th ed: Elsevier Health Sciences; 2012.
84. Fairhurst D, Lee RW. Aggregation, agglomeration - how to avoid aggravation when formulating particulate suspensions. *Drug Delivery Technology.* 2008;8(8):48-52.
85. Verma S, Kumar S, Gokhale R, Burgess DJ. Physical stability of nanosuspensions: investigation of the role of stabilizers on Ostwald ripening. *International journal of pharmaceutics.* 2011;406(1-2):145-152.
86. Soni S, et al. Nanosuspension: An Approach to Enhance Solubility of Drugs. *IJPI's Journal of Pharmaceutics and Cosmetology.* 2012;2(9):50-63.
87. Plaza V, Sanchis J. Medical personnel and patient skill in the use of metered dose inhalers: a multicentric study. CESEA Group. *Respiration; international review of thoracic diseases.* 1998;65(3):195-198.
88. Brindley A. The chlorofluorocarbon to hydrofluoroalkane transition: the effect on pressurized metered dose inhaler suspension stability. *The Journal of allergy and clinical immunology.* 1999;104(6):S221-226.
89. Tan Y, Yang Z, Pan X, et al. Stability and aerosolization of pressurized metered dose inhalers containing thymopentin nanoparticles produced using a bottom-up process. *International journal of pharmaceutics.* 2012;427(2):385-392.
90. Nyambura BK, Kellaway IW, Taylor KM. Insulin nanoparticles: stability and aerosolization from pressurized metered dose inhalers. *International journal of pharmaceutics.* 2009;375(1-2):114-122.
91. Dickinson PA, Howells SW, Kellaway IW. Novel nanoparticles for pulmonary drug administration. *Journal of drug targeting.* 2001;9(4):295-302.
92. Smyth HD, Hickey AJ. Multimodal particle size distributions emitted from HFA-134a solution pressurized metered-dose inhalers. *AAPS PharmSciTech.* 2003;4(3):E38.
93. Smyth HDC, Hickey AJ. *Controlled pulmonary drug delivery.* New York ; London: Springer; 2011.
94. Zhu B, Traini D, Chan HK, Young PM. The effect of ethanol on the formation and physico-chemical properties of particles generated from budesonide solution-based pressurized metered-dose inhalers. *Drug development and industrial pharmacy.* 2013;39(11):1625-1637.
95. Evans RM, Farr SJ, Armstrong NA, Chatham SM. Formulation and in vitro evaluation of pressurized inhalation aerosols containing isotropic systems of lecithin and water. *Pharmaceutical research.* 1991;8(5):629-635.
96. Saleem IY, Smyth HD. Tuning aerosol particle size distribution of metered dose inhalers using cosolvents and surfactants. *BioMed research international.* 2013;2013:574310.
97. Nalluri BN, Chowdary KP, Murthy KV, Hayman AR, Becket G. Physicochemical characterization and dissolution properties of nimesulide-cyclodextrin binary systems. *AAPS PharmSciTech.* 2003;4(1):E2.
98. Gonda I. Development of a systematic theory of suspension inhalation aerosols-I. A framework to study the effects of aggregation on the aerodynamic behaviour of drug particles. *Int J Pharm.* 1985;27:99-116.
99. Stein SW. Estimating the number of droplets and drug particles emitted from MDIs. *AAPS PharmSciTech.* 2008;9(1):112-115.
100. Stein SW, Sheth P, Myrdal PB. A model for predicting size distributions delivered from pMDIs with suspended drug. *International journal of pharmaceutics.* 2012;422(1-2):101-115.
101. Ivey JW, Lewis D, Church T, Finlay WH, Vehring R. A correlation equation for the mass median aerodynamic diameter of the aerosol emitted by solution metered dose inhalers. *International journal of pharmaceutics.* 2014;465(1-2):18-24.
102. Stein SW, Myrdal PB. A theoretical and experimental analysis of formulation and device parameters affecting solution MDI size distributions. *Journal of pharmaceutical sciences.* 2004;93(8):2158-2175.

103. Szejtli Jz. *Cyclodextrin technology.* Dordrecht: Kluwer Academic Publishers; 1988.
104. Ali SM, et al. Complexation of enalapril maleate with β-cyclodextrin: NMR spectroscopic study in solution *Quim Nova.* 2006;29(4):685-688.
105. Cramer F. *Einschlusverbindungen (Inclusion Compounds).* Berlin: Springer-Verlag; 1954.
106. Panda S, Sahu R. Inclusion complex with cyclodextrin: a boon to pharmaceutical world. *IJBPAS.* 2014;3(6):915-926.
107. Rekharsky MV, Inoue Y. Complexation Thermodynamics of Cyclodextrins. *Chemical reviews.* 1998;98(5):1875-1918.
108. Iacovino R, Caso JV, Rapuano F, et al. Physicochemical characterization and cytotoxic activity evaluation of hydroxymethylferrocene:beta-cyclodextrin inclusion complex. *Molecules.* 2012;17(5):6056-6070.
109. Saenger W, Jacob J, Gessler K, et al. Structures of the Common Cyclodextrins and Their Larger Analogues-Beyond the Doughnut. *Chemical reviews.* 1998;98(5):1787-1802.
110. Miranda JCd, Martins TEA, Veiga F, Ferraz HG. Cyclodextrins and ternary complexes: technology to improve solubility of poorly soluble drugs. *Brazilian Journal of Pharmaceutical Sciences.* 2011;47(4):665-681.
111. Jambhekar SS, Breen P. Cyclodextrins in pharmaceutical formulations II: solubilization, binding constant, and complexation efficiency. *Drug Discov Today.* 2016;21(2):363-368.
112. Kanaka Durga Devi N, Prameela Rani A, Muneer Javed M, Sai Kumar K, Kaushik J, Sowjanya V. Cyclodextrins in pharmacy- an overview. *Pharmacopore.* 2010;1(3):155-165.
113. Van Hees T, Piel G, de Hassonville SH, Evrard B, Delattre L. Determination of the free/included piroxicam ratio in cyclodextrin complexes: comparison between UV spectrophotometry and differential scanning calorimetry. *European journal of pharmaceutical sciences : official journal of the European Federation for Pharmaceutical Sciences.* 2002;15(4):347-353.
114. Lin SZ, et al. Indomethacin and cyclodextrin complexes. *International journal of pharmaceutics.* 1991;69:211-219.
115. Veiga MD, Diaz PJ, Ahsan F. Interactions of griseofulvin with cyclodextrins in solid binary systems. *Journal of pharmaceutical sciences.* 1998;87(7):891-900.
116. Moyano JR, Arias-Blanco MJ, Gines JM, et al. Nuclear magnetic resonance investigations of the inclusion complexation of gliclazide with beta-cyclodextrin. *Journal of pharmaceutical sciences.* 1997;86(1):72-75.
117. Veiga FJ, Fernandes CM, Carvalho RA, Geraldes CF. Molecular modelling and 1H-NMR: ultimate tools for the investigation of tolbutamide: beta-cyclodextrin and tolbutamide: hydroxypropyl-beta-cyclodextrin complexes. *Chemical & pharmaceutical bulletin.* 2001;49(10):1251-1256.
118. Cserhati T, Forgacs E. Inclusion complex formation of steroidal drugs with hydroxypropyl-beta-cyclodextrin studied by charge-transfer chromatography. *Journal of pharmaceutical and biomedical analysis.* 1998;18(1-2):179-185.
119. Nakanishi K, Masukawa T, Nadai T, Yoshii K, Okada S, Miyajima K. Sustained release of flufenamic acid from a drug-triacetyl-beta-cyclodextrin complex. *Biological & pharmaceutical bulletin.* 1997;20(1):66-70.
120. Siefert B, Pleyer U, Muller M, Hartmann C, Keipert S. Influence of cyclodextrins on the in vitro corneal permeability and in vivo ocular distribution of thalidomide. *Journal of ocular pharmacology and therapeutics : the official journal of the Association for Ocular Pharmacology and Therapeutics.* 1999;15(5):429-438.
121. Otero Espinar FJ, et al. Reduction in the ulceragenicity of naproxen by complexation with β-cyclodextrin. *Int J Pharm.* 1991;70:35-41.
122. Chadha R, Kashid N, Saini A. Account of analytical techniques employed for the determination of thermodynamics of inclusion complexationof drugs with cyclodextrins. *JSIR.* 2004;63(3):211-229.

123. Siegel B, Breslow R. Lyophobic binding of substrates by cyclodextrins in nonaqueous solvents. *Journal of the American Chemical Society.* 1975;97(23):6869-6870.
124. Danil de Namor AF, Traboulssi R, Lewis DFV. Host properties of cyclodextrins towards anion constituents of antigenic determinants. A thermodynamic study in water and in N,N-dimethylformamide. *Journal of the American Chemical Society.* 1990;112(23):8442-8447.
125. Kida T, Fujino Y, Miyawaki K, Kato E, Akashi M. 6-O-Modified beta-cyclodextrin enabling inclusion complex formation in nonpolar media. *Org Lett.* 2009;11(22):5282-5285.
126. Williams RO, 3rd, Liu J. Influence of formulation technique for hydroxypropyl-beta-cyclodextrin on the stability of aspirin in HFA 134a. *European journal of pharmaceutics and biopharmaceutics : official journal of Arbeitsgemeinschaft fur Pharmazeutische Verfahrenstechnik eV.* 1999;47(2):145-152.
127. Steckel H, Wehle S. A novel formulation technique for metered dose inhaler (MDI) suspensions. *International journal of pharmaceutics.* 2004;284(1-2):75-82.
128. Singh R, et al. Characterization of cyclodextrin inclusion complexes – A review. *Journal of Pharmaceutical Science and Technology.* 2010;2(3):171-183.
129. Szejtli J. Introduction and General Overview of Cyclodextrin Chemistry. *Chem Rev.* 1998;98(5):1743-1754.
130. Kanaka Durga Devi N. Cyclodextrins in pharmacy- an overview. *Pharmacopore.* 2010;1(3):1-7.
131. Rekharsky MV, Inoue Y. Complexation Thermodynamics of Cyclodextrins. *Chemical Reviews.* 1998;98(5):1875-1918.
132. Tabushi I, Kiyosuke Y, Sugimoto T, Yamamura K. Approach to the aspects of driving force of inclusion by .alpha.-cyclodextrin. *Journal of the American Chemical Society.* 1978;100(3):916-919.
133. Matsui Y. Molecular Mechanical Calculation on Cyclodextrin Inclusion Complexes. I. The Structures of α-Cyclodextrin Complexes Estimated by van der Waals Interaction Energy Calculation. *Bulletin of the Chemical Society of Japan.* 1982;55(4):1246-1249.
134. Avakyan VG, Nazarov VB, Alfimov MV, Bagatur''yants AA, Voronezheva NI. The role of intra- and intermolecular hydrogen bonds in the formation of β-cyclodextrin head-to-head and head-to-tail dimers. The results of ab initio and semiempirical quantum-chemical calculations. *Russian Chemical Bulletin.* 2001;50(2):206-216.
135. Shi J-H, Chen K, Xu Y. Characterization of the inclusion interaction between prednisolone and di-O-methyl-β-cyclodextrin: Spectroscopic methods and molecular modeling. *Journal of Molecular Liquids.* 2014;194:172-178.
136. Rekharsky MV, Inoue Y. Complexation and chiral recognition thermodynamics of 6-amino-6-deoxy-beta-cyclodextrin with anionic, cationic, and neutral chiral guests: counterbalance between van der Waals and coulombic interactions. *Journal of the American Chemical Society.* 2002;124(5):813-826.
137. Buha SM, Baxi GA, Shrivastav PS. Liquid Chromatography Study on Atenolol--Cyclodextrin Inclusion Complex. *ISRN Analytical Chemistry.* 2012;2012:1-8.
138. Park JW, Lee SY, Song HJ, Park KK. Self-inclusion behavior and circular dichroism of aliphatic chain-linked beta-cyclodextrin-viologen compounds and their reduced forms depending on the side of modification. *J Org Chem.* 2005;70(23):9505-9513.
139. Marangoci N, Mares M, Silion M, et al. Inclusion complex of a new propiconazole derivative with β-cyclodextrin: NMR, ESI-MS and preliminary pharmacological studies. *Results in pharma sciences.* 2011;1(1):27-37.
140. Mokhtar M, Adnan R. Preparation method and characterisation of inclusion complex of theophylline/beta *ESTEEM Academic Journal.* 2012;8(2):50-63.
141. Yang X, Ke W, Zi P, Liu F, Yu L. Detecting and identifying the complexation of nimodipine with hydroxypropyl-beta-cyclodextrin present in tablets by Raman spectroscopy. *Journal of pharmaceutical sciences.* 2008;97(7):2702-2719.

142. Wen J, Liu B, Yuan E, Ma Y, Zhu Y. Preparation and physicochemical properties of the complex of naringenin with hydroxypropyl-beta-cyclodextrin. *Molecules (Basel, Switzerland).* 2010;15(6):4401-4407.
143. Brewster ME, Loftsson T. Cyclodextrins as pharmaceutical solubilizers. *Advanced Drug Delivery Reviews.* 2007;59(7):645-666.
144. Loukas YL. Measurement of Molecular Association in Drug: Cyclodextrin Inclusion Complexes with Improved 1H NMR Studies. *Journal of Pharmacy and Pharmacology.* 1997;49(10):944-948.
145. Marangoci N, et al. Inclusion complex of a new propiconazole derivative with b-cyclodextrin: NMR, ESI–MS and preliminary pharmacological studies. *Results in Pharma Sciences.* 2011;1(1):27-37.
146. Upadhyay SK, Kumar G. NMR and molecular modelling studies on the interaction of fluconazole with beta-cyclodextrin. *Chemistry Central journal.* 2009;3:9.
147. Ali SM, et al. High resolution NMR spectroscopic study of complexation of hydroxyzine hydrochloride with β-cyclodextrin in aqueous solution. *Journal of the Chinese Chemical Society.* 2006;53(4):867-871.
148. Bernatowicz P, Nowakowski M, Dodziuk H, Ejchart A. Determination of association constants at moderately fast chemical exchange: Complexation of camphor enantiomers by α-cyclodextrin. *Journal of Magnetic Resonance.* 2006;181(2):304-309.
149. Schalley CA, ProQuest. *Analytical Methods in Supramolecular Chemistry.* 2nd completely rev. and enlarg ed. Weinheim, Germany: Wiley-VCH; 2012.
150. Yujuan C, Runhua L. 1H NMR titration and quantum calculation for the inclusion complexes of cis-cyclooctene, cis, cis-1, 3-cyclooctadiene and cis, cis-1, 5-cyclooctadiene with beta-cyclodextrin. *Spectrochim Acta A Mol Biomol Spectrosc.* 2009;73(4):713-718.
151. Schneider HJ, Hacket F, Rudiger V, Ikeda H. NMR Studies of Cyclodextrins and Cyclodextrin Complexes. *Chemical reviews.* 1998;98(5):1755-1786.
152. Rawat S, Jain SK. Solubility enhancement of celecoxib using beta-cyclodextrin inclusion complexes. *European journal of pharmaceutics and biopharmaceutics : official journal of Arbeitsgemeinschaft fur Pharmazeutische Verfahrenstechnik eV.* 2004;57(2):263-267.
153. Al-Rawashdeh NAF, Al-Sadeh KS, Al-Bitar MB. Inclusion Complexes of Sunscreen Agents withβ-Cyclodextrin: Spectroscopic and Molecular Modeling Studies. *Journal of Spectroscopy.* 2013;2013:1-11.
154. Saha S, Roy A, Roy K, Roy MN. Study to explore the mechanism to form inclusion complexes of β-cyclodextrin with vitamin molecules. *Scientific Reports.* 2016;6:35764.
155. Shi J-H, Zhou Y-f. Inclusion interaction of chloramphenicol and heptakis (2,6-di- O-methyl)-β-cyclodextrin: Phase solubility and spectroscopic methods. *Spectrochimica Acta Part A: Molecular and Biomolecular Spectroscopy.* 2011;83(1):570-574.
156. Aggarwal RL, Farrar LW, Diebold ED, Polla DL. Measurement of the absolute Raman scattering cross section of the 1584-cm−1band of benzenethiol and the surface-enhanced Raman scattering cross section enhancement factor for femtosecond laser-nanostructured substrates. *Journal of Raman Spectroscopy.* 2009;40(9):1331-1333.
157. Fleischmann M, Hendra PJ, McQuillan AJ. Raman spectra of pyridine adsorbed at a silver electrode. *Chemical Physics Letters.* 1974;26(2):163-166.
158. Guillot N, de la Chapelle ML. The electromagnetic effect in surface enhanced Raman scattering: Enhancement optimization using precisely controlled nanostructures. *Journal of Quantitative Spectroscopy and Radiative Transfer.* 2012;113(18):2321-2333.
159. Kedem O, Tesler AB, Vaskevich A, Rubinstein I. Sensitivity and optimization of localized surface plasmon resonance transducers. *ACS Nano.* 2011;5(2):748-760.
160. Haes AJ, Zou S, Schatz GC, Van Duyne RP. A Nanoscale Optical Biosensor: The Long Range Distance Dependence of the Localized Surface Plasmon Resonance of Noble Metal Nanoparticles. *The Journal of Physical Chemistry B.* 2004;108(1):109-116.

161. Dieringer JA, McFarland AD, Shah NC, et al. Introductory Lecture : Surface enhanced Raman spectroscopy: new materials, concepts, characterization tools, and applications. *Faraday Discuss.* 2006;132:9-26.
162. Sharma B, Frontiera RR, Henry A-I, Ringe E, Van Duyne RP. SERS: Materials, applications, and the future. *Materials Today.* 2012;15(1-2):16-25.
163. Patil JS, et al. Inclusion complex system; a novel technique to improve the solubility and bioavailability of poorly soluble drugs: A review. *International Journal of Pharmaceutical Sciences Review and Research.* 2010;2(2):29-34.
164. Menger FM, Dulany MA. Chemistry of a heptane-soluble cyclodextrin derivative. *Tetrahedron Letters.* 1985;26(3):267-270.
165. Uccello-Barretta G, Sicoli G, Balzano F, Schurig V, Salvadori P. Highly efficient NMR enantiodiscrimination of 1,1,1,3,3-pentafluoro-2-(fluoromethoxy)-3-methoxypropane, a chiral degradation product of sevoflurane, by heptakis(2,3-di-O-acetyl-6-O-tert-butyldimethylsilyl)-β-cyclodextrin. *Tetrahedron: Asymmetry.* 2006;17(17):2504-2510.
166. Rogueda PG. HPFP, a model propellant for pMDIs. *Drug development and industrial pharmacy.* 2003;29(1):39-49.
167. Rojas MT, Koeniger R, Stoddart JF, Kaifer AE. Supported Monolayers Containing Preformed Binding Sites. Synthesis and Interfacial Binding Properties of a Thiolated .beta.-Cyclodextrin Derivative. *Journal of the American Chemical Society.* 1995;117(1):336-343.
168. Soloman SD, Bahadory M, Jeyarajasingam AV, Rutkowsky SA, Boritz C, Mulfinger L. Synthesis and study of silver nanoparticles. *Journal of Chemical Education.* 2007;84(2):322.
169. Drake P, Chang H-W, Lin Y-J. The design of a peptide linker group to enhance the SERS signal intensity of an atto680 dye-nanoparticle system. *Journal of Raman Spectroscopy.* 2010;41(10):1248-1253.
170. Polovinkin V, Balandin T, Volkov O, et al. Nanoparticle surface-enhanced Raman scattering of bacteriorhodopsin stabilized by amphipol A8-35. *J Membr Biol.* 2014;247(9-10):971-980.
171. Balasubramanian SK, Yang L, Yung LY, Ong CN, Ong WY, Yu LE. Characterization, purification, and stability of gold nanoparticles. *Biomaterials.* 2010;31(34):9023-9030.
172. Johari SA, Kalbassi MR, Soltani M, Yu IJ. Toxicity comparison of colloidal silver nanoparticles in various life stages of rainbow trout (Oncorhynchus mykiss). *Iranian Journal of Fisheries Sciences.* 2013;12(1):76-95.
173. Pirnau A, Bogdan M, Floare CG. NMR Spectroscopic characterization of β-cyclodextrin inclusion complex with vanillin. *Journal of Physics.* 2009;182:1-5.
174. Lee YS, Park HJ, Jang DJ. Encapsulation of 6-Hydroxyquinoline in Heptakis(2,6-di-O-methyl)-β-cyclodextrin. *Bull Korean Chem Soc.* 2006;27(9):1450-1452.
175. Sambasevam KP, Mohamad S, Sarih NM, Ismail NA. Synthesis and Characterization of the Inclusion Complex of beta-cyclodextrin and Azomethine. *International journal of molecular sciences.* 2013;14(2):3671-3682.
176. Claridge TDW. *High-resolution NMR techniques in organic chemistry.* 1st ed. Amsterdam ; New York: Pergamon; 1999.
177. Jacobsen NE. *NMR spectroscopy explained : simplified theory, applications and examples for organic chemistry and structural biology.* Hoboken, N.J.: Wiley ; Chichester : John Wiley [distributor]; 2007.
178. NMR Consumables, Small Volume and External Referencing. *wwwwilmad-labglasscom.* [Accessed on 15-10-2014].
179. Telford R. The physical chemistry of pMDI formulations derived from hydrofluoroalkane propellants. *University of Bradford, thesis.* 2013.
180. Thalen A. Epimers of budesonide and related corticosteroids. III. Synthesis and structure elucidation by carbon-13 and proton nuclear magnetic resonance spectroscopy. *Acta pharmaceutica Suecica.* 1987;24(3):97-114.

181. Jing Z, Xuan Z, Xian J, ling X, Song Y. NMR studies on the two epimers of budesonide [Chinese paper]. *Journal of Shenyang Pharmaceutical University.* 2009;26(1):30-35.
182. Raval MK, Ramani RV, Sheth NR. Formulation and evaluation of sustained release enteric-coated pellets of budesonide for intestinal delivery. *International journal of pharmaceutical investigation.* 2013;3(4):203-211.
183. Gangurde HH, Chordiya MA, Tamizharasi S, Sivakumar T. Optimization of budesonide pH dependent coated pellets for potential colon targeted drug delivery. *Insight Pharmaceutical Sciences.* 2013;3(1):1-13.
184. Roik NV, Belyakova LA. IR spectroscopy, X-ray diffraction and thermal analysis studies of solid "β-cyclodextrin - para-aminobenzoic acid " inclusion complex. *Physics and Chemistry of Solid State.* 2011;12(1):168-173.
185. Rabadiya B, Thakkar V, Rabadiya P. Drug-excipients interaction and solubiliy enhancement study of simvastatin. *IJPRBS.* 2013;2(1):168-185.
186. Ali HR, Edwards HG, Kendrick J, Munshi T, Scowen IJ. An experimental and computational study on the epimeric contribution to the infrared spectrum of budesonide. *Drug testing and analysis.* 2010;2(9):447-451.
187. Viernstein H, Weiss-Greiler P, Wolschann P. Solubility enhancement of low soluble biologically active compounds--temperature and cosolvent dependent inclusion complexation. *Int J Pharm.* 2003;256(1-2):85-94.
188. Rungnim C, Phunpee S, Kunaseth M, et al. Co-solvation effect on the binding mode of the α-mangostin/β-cyclodextrin inclusion complex. *Beilstein journal of organic chemistry.* 2015;11(1):2306-2317.
189. Loftsson T, Jarho P, Masson M, Jarvinen T. Cyclodextrins in drug delivery. *Expert Opin Drug Deliv.* 2005;2(2):335-351.
190. Doliwa A, Santoyo S, Ygartua P. Influence of piroxicam: hydroxypropyl-beta-cyclodextrin complexation on the in vitro permeation and skin retention of piroxicam. *Skin Pharmacol Appl Skin Physiol.* 2001;14(2):97-107.
191. Boonyarattanakalin KS, Wolschann P, Lawtrakul L. Molecular dynamics of β-CD in water/co-solvent mixtures. *Journal of Inclusion Phenomena and Macrocyclic Chemistry.* 2011;70(3):279-290.
192. Boonyarattanakalin K, Viernstein H, Wolschann P, Lawtrakul L. Influence of Ethanol as a Co-Solvent in Cyclodextrin Inclusion Complexation: A Molecular Dynamics Study. *Sci Pharm.* 2015;83(2):387-399.
193. Okubo T, Kitano H, Ise N. Conductometric studies on association of cyclodextrin with colloidal electrolytes. *The Journal of Physical Chemistry.* 1976;80(24):2661-2664.
194. Martin JV, Turmine M, Letellier P, Hemery P. Study of β-cyclodextrin/dodecyltrimethylammonium bromide complex into water-isopropanol mixtures. *Electrochimica Acta.* 1995;40(17):2749-2753.
195. Smithrud DB, Diederich F. Strength of molecular complexation of apolar solutes in water and in organic solvents is predictable by linear free energy relationships: a general model for solvation effects on apolar binding. *Journal of the American Chemical Society.* 1990;112(1):339-343.
196. Nakai Y, Yamamoto K, Terada K, Horibe H. Interaction of Tri-O-methyl-[beta]-cyclodextrin with Drugs. I. Effect of Tri-O-methyl-[beta]-cyclodextrin on the Partition Coefficients of Drugs. *Chemical & Pharmaceutical Bulletin.* 1982;30(5):1796.
197. Mizutani T, Wada K, Kitagawa S. Molecular recognition of amines and amino esters by zinc porphyrin receptors: binding mechanisms and solvent effects. *The Journal of organic chemistry.* 2000;65(19):6097-6106.
198. Maitra U, Rao P, Vijay KP, Balasubramanian R, Mathew L. Solvent effect in molecular recognition: Determining binding constants in different solvents following an extraction based protocol. *Tetrahedron Letters.* 1998;39(20):3255-3258.

199. Pai N, Patil SS. Development and validation of RP-HPLC method for estimation of formoterol fumarate and budesonide in pressurised meter dose inhaler form. *Der Pharmacia Sinica.* 2013;4(4):15-25.
200. Veiga FJB, Fernandes CM, Carvalho RA, Geraldes CFGC. Molecular Modelling and 1H-NMR: Ultimate Tools for the Investigation of Tolbutamide: .BETA.-Cyclodextrin and Tolbutamide: Hydroxypropyl-.BETA.-Cyclodextrin Complexes. *Chemical and Pharmaceutical Bulletin.* 2001;49(10):1251-1256.
201. Ribeiro L, Carvalho RA, Ferreira DC, Veiga FJB. Multicomponent complex formation between vinpocetine, cyclodextrins, tartaric acid and water-soluble polymers monitored by NMR and solubility studies. *European Journal of Pharmaceutical Sciences.* 2005;24(1):1-13.
202. Larsen KL, Aachmann FL, Wimmer R, Stella VJ, Kjolner UM. Phase solubility and structure of the inclusion complexes of prednisolone and 6 alpha-methyl prednisolone with various cyclodextrins. *Journal of pharmaceutical sciences.* 2005;94(3):507-515.
203. Uekama K, Sakai A, Arimori K, Otagiri M, Saito H. Different mode of prednisolone within alpha-, beta-, and gamma-cyclodextrins in aqueous solution and in solid state. *Pharm Acta Helv.* 1985;60(4):117-121.
204. Charumanee S, Okonogi S, Sirithunyalug J, Wolschann P, Viernstein H. Effect of Cyclodextrin Types and Co-Solvent on Solubility of a Poorly Water Soluble Drug. *Sci Pharm.* 2016;84(4):694-704.
205. Green AR, Guillory JK. Heptakis(2,6-di-O-methyl)-β-cyclodextrin Complexation with the Antitumor Agent Chlorambucil. *Journal of Pharmaceutical Sciences.* 1989;78(5):427-431.
206. Cruickshank DL, Rougier NM, Vico RV, et al. Inclusion of the insecticide fenitrothion in dimethylated-β-cyclodextrin: unusual guest disorder in the solid state and efficient retardation of the hydrolysis rate of the complexed guest in alkaline solution. *Beilstein journal of organic chemistry.* 2013;9(1):106-117.
207. Wenz G. Influence of intramolecular hydrogen bonds on the binding potential of methylated beta-cyclodextrin derivatives. *Beilstein J Org Chem.* 2012;8:1890-1895.
208. Iijima T, Karube Y. The interaction of acid azo dyes with chemically modified β-cyclodextrins. *Elsevier Science Ltd.* 1998;36(4):305-311.
209. Bardelang D, Rockenbauer A, Jicsinszky L, et al. Nitroxide bound beta-cyclodextrin: is there an inclusion complex? *The Journal of organic chemistry.* 2006;71(20):7657-7667.
210. Iijima T, Karube Y. The interaction of acid azo dyes with chemically modified β-cyclodextrins. *Dyes and Pigments.* 1998;36(4):305-311.
211. Letort S, Balieu S, Erb W, Gouhier G, Estour F. Interactions of cyclodextrins and their derivatives with toxic organophosphorus compounds. *Beilstein journal of organic chemistry.* 2016;12(1):204-228.
212. Miranda JC, Martins TE, Veiga F, Ferraz HG. Cyclodextrins and ternary complexes: technology to improve solubility of poorly soluble drugs. *Brazilian Journal of Pharmaceutical Sciences.* 2011;47(4):665-681.
213. Ventura CA, Giannone I, Paolino D, Pistarà V, Corsaro A, Puglisi G. Preparation of celecoxib-dimethyl-β-cyclodextrin inclusion complex: characterization and in vitro permeation study. *European Journal of Medicinal Chemistry.* 2005;40(7):624-631.
214. Djedaïni F, Lin SZ, Perly B, Wouessidjewe D. High-Field Nuclear Magnetic Resonance Techniques for the Investigation of a β-Cyclodextrin:Indomethacin Inclusion Complex. *Journal of Pharmaceutical Sciences.* 1990;79(7):643-646.
215. Mic M, Prnu A, Bogdan M, Turcu I. Inclusion complex of benzocaine and -cyclodextrin: 1 H NMR and isothermal titration calorimetry studies. Paper presented at: Processes in Isotopes and Molecules2013.
216. Pinto LM, Fraceto LF, Santana MH, Pertinhez TA, Junior SO, de Paula E. Physico-chemical characterization of benzocaine-beta-cyclodextrin inclusion complexes. *Journal of pharmaceutical and biomedical analysis.* 2005;39(5):956-963.

217. Foe K, Cheung HT, Tattam BN, Brown KF, Seale JP. Degradation products of beclomethasone dipropionate in human plasma. *Drug Metab Dispos.* 1998;26(2):132-137.
218. Sahasranaman S, Issar M, Toth G, Horvath G, Hochhaus G. Characterization of degradation products of mometasone furoate. *Pharmazie.* 2004;59(5):367-373.
219. Bardsley B, Smith MS, Gibbon BH. Structure elucidation and spectroscopic analysis of photodegradants of the anti-rhinitis drug fluticasone furoate. *Org Biomol Chem.* 2010;8(8):1876-1880.
220. Zoppi A, Delrivo A, Aiassa V, Longhi MR. Binding of sulfamethazine to beta-cyclodextrin and methyl-beta-cyclodextrin. *AAPS PharmSciTech.* 2013;14(2):727-735.
221. Del Valle EMM. Cyclodextrins and their uses: a review. *Process Biochemistry.* 2004;39(9):1033-1046.
222. Puentes CM, Wenzel TJ. Phosphated cyclodextrins as water-soluble chiral NMR solvating agents for cationic compounds. *Beilstein Journal of Organic Chemistry.* 2017;13(1):43-53.
223. Provencher KA, Weber MA, Randall LA, Cunningham PR, Dignam CF, Wenzel TJ. Carboxymethylated cyclodextrins and their complexes with Pr(III) and Yb(III) as water-soluble chiral NMR solvating agents for cationic compounds. *Chirality.* 2010;22(3):336-NA.
224. Aussenegg F, Ditlbacher H. Plasmonen als Lichttransporter: Nanooptik. *Physik in unserer Zeit.* 2006;37(5):220-226.
225. Kelly KL, Coronado E, Zhao LL, Schatz GC. The Optical Properties of Metal Nanoparticles: The Influence of Size, Shape, and Dielectric Environment. *The Journal of Physical Chemistry B.* 2003;107(3):668-677.
226. Mishra A, Tripathy P, Ram S, Fecht HJ. Optical properties in nanofluids of gold nanoparticles in poly(vinylpyrrolidone). *J Nanosci Nanotechnol.* 2009;9(7):4342-4347.
227. Ahmad MB, Tay MY, Shameli K, Hussein MZ, Lim JJ. Green synthesis and characterization of silver/chitosan/polyethylene glycol nanocomposites without any reducing agent. *International journal of molecular sciences.* 2011;12(8):4872-4884.
228. Bac LH, Kim JS, Kim JC. Size, optical and stability properties of gold nanoparticles synthesized by electrical explosion of wire in different aqueous media. *Reviews on advanced materials science.* 2011;28(2):117-121.
229. Kaszuba M, McKnight D, Connah MT, McNeil-Watson FK, Nobbmann U. Measuring sub nanometre sizes using dynamic light scattering. *Journal of Nanoparticle Research.* 2008;10(5):823-829.
230. Khlebtsov BN, Khlebtsov NG. On the measurement of gold nanoparticle sizes by the dynamic light scattering method. *Colloid Journal.* 2011;73(1):118-127.
231. Andrade PF, de Faria AF, da Silva DS, Bonacin JA, Goncalves Mdo C. Structural and morphological investigations of beta-cyclodextrin-coated silver nanoparticles. *Colloids Surf B Biointerfaces.* 2014;118:289-297.
232. Ali HRH, Edwards HGM, Kendrick J, Munshi T, Scowen IJ. Vibrational spectroscopic study of budesonide. *Journal of Raman Spectroscopy.* 2007;38(7):903-908.
233. Ali HR, Edwards HG, Kendrick J, Scowen IJ. Vibrational spectroscopic study of fluticasone propionate. *Spectrochim Acta A Mol Biomol Spectrosc.* 2009;72(2):244-247.
234. Infrared and Raman Characteristic Group Frequencies: Tables and Charts. 3rd ed By George Socrates (The University of West London, Middlesex, U.K.). J. Wiley and Sons: Chichester. 2001. xviii + 348 pp. $185.00. ISBN: 0-471-85298-8. *Journal of the American Chemical Society.* 2002;124(8):1830-1830.
235. Kim T, Assary RS, Curtiss LA, Marshall CL, Stair PC. Vibrational properties of levulinic acid and furan derivatives: Raman spectroscopy and theoretical calculations. *Journal of Raman Spectroscopy.* 2011;42(12):2069-2076.
236. Egyed O. Spectroscopic studies on β-cyclodextrin. *Vibrational Spectroscopy.* 1990;1(2):225-227.

237. Hill W, Fallourd V, Klockow D. Investigation of the Adsorption of Gaseous Aromatic Compounds at Surfaces Coated with Heptakis(6-thio-6-deoxy)-β-cyclodextrin by Surface-Enhanced Raman Scattering. *The Journal of Physical Chemistry B.* 1999;103(22):4707-4713.
238. Gimenez IF, Anazetti MC, Melo PS, et al. Cytotoxicity on V79 and HL60 cell lines by Thiolated-beta-Cyclodextrin-Au/Violacein Nanoparticles. *J Biomed Nanotech.* 2005;1(3):1-7.
239. Bryant MA, Pemberton JE. Surface Raman scattering of self-assembled monolayers formed from 1-alkanethiols at silver [electrodes]. *Journal of the American Chemical Society.* 1991;113(10):3629-3637.
240. Joo TH, Kim MS, Kim K. Surface-enhanced Raman scattering of benzenethiol in silver sol. *Journal of Raman Spectroscopy.* 1987;18(1):57-60.
241. Varnholt B, Oulevey P, Luber S, Kumara C, Dass A, Bürgi T. Structural Information on the Au–S Interface of Thiolate-Protected Gold Clusters: A Raman Spectroscopy Study. *The Journal of Physical Chemistry C.* 2014;118(18):9604-9611.
242. Willets KA. Super-resolution imaging of SERS hot spots. *Chemical Society reviews.* 2014;43(11):3854-3864.
243. Xie Y, Wang X, Han X, et al. Selective SERS detection of each polycyclic aromatic hydrocarbon (PAH) in a mixture of five kinds of PAHs. *Journal of Raman Spectroscopy.* 2011;42(5):945-950.
244. Lee K-S, El-Sayed MA. Gold and silver nanoparticles in sensing and imaging: Sensitivity of plasmon response to size, shape, and metal composition. *Journal of Physical Chemistry B.* 2006;110(39):19220-19225.

Appendix A1

a) The average number of Ag or Au atoms per nanoparticles may be calculated based on the determination of the average core diameters of the particles (*D*, nm) using TEM analysis. Assuming a spherical and a uniform fcc (face centered, cubic) shape of the nanoparticle, the average number of Ag or Au atoms (*N*) per nanoparticle be calculated by the following equation:

$$N = \frac{\pi \rho D^3}{6M} N_A$$

Where *N* is the average number of Ag or Au atoms per nanoparticle, ρ is the density of fcc of Ag (10.5 g/cm^3) or Au (19.3 g/cm^3), *D* is the average diameter of the nanoparticles, *M* is the atomic mass of Ag (107.86 g) or Au (196.96 g), N_A is the Avogadro's number (the number of atoms per mole = 6.023×10^{23} atoms/gram-mole).

As the π, N_A, ρ and M are constant; therefore the equation is calculated to be

$N = 30.88\ D^3$ for Au, $N = 30.68\ D^3$ for Ag.

The number of the Ag or Au atoms per nanoparticles can be calculated by another method, assuming a spherical shape of the Ag/Au NPs and considering the volume ratio of Ag/Au atoms to the Ag/Au-NPs is 74.1% with the cubic structure. For Ag atom, the radius of the atom is 0.144 nm and its volume can be calculated by the following equation

$$V = \frac{4}{3}\pi r^3$$

Where the r is the radius of the Ag atom and therefore its volume is 0.0125 nm^3. The volume of Ag NPs with diameter (D) in nm is $\frac{\pi}{6}D^3$. Thus, the number of the Ag atoms in one nanoparticle is $\frac{74.1}{100} \times \frac{\pi}{6} D^3 \times \frac{1}{0.0125}$, which is can be calculated to be 31 D^3

b) The molar concentration of the Ag or Au-NPs is calculated by dividing the total number of the Ag or Au atoms (which is equal to the initial amount of the

silver or gold salt used in the first reaction) over the average number of the Ag or Au atoms per nanoparticle according to the following equation

$$C = \frac{N_{Total}}{NVN_A}$$

Where N_{Total} is the total number of Ag or Au atoms added in the first reaction, N is the average number of Ag or Au atoms per nanoparticle, V is the volume of the reaction solution in litre and N_A is the Avogadro's number.

c) The concentration of the Ag-NPs is calculated by using the $N = 30.68\ D^3$ for the calculation of the average number of Ag atoms per nanoparticle and the D was found to be 21 nm from the TEM analysis. Therefore N was equal to 2.84×10^5 nm^3.

The molarity of the Ag salt in the first reaction was 1 mM (0.001 M) and its volume was 10 mL (0.01 L) whereas the total volume of the reaction solution was 40 mL (0.04 L). Therefore, the concentration of the Ag-NPs was:

$$C = \frac{N_{Total}}{NVN_A}$$

$$C = \frac{0.001 \times 0.01 \times 6.023 \times 10^{23}}{2.84 \times 10^5 \times 0.04 \times 6.023 \times 10^{23}} = 8.8 \times 10^{-10} M = 0.88\ nM$$

The initial Ag concentration in ppm is:

$$8.8 \times 10^{-10} \times 1000 \times 2.84 \times 10^5 \times 107.86 = 26.97\ ppm$$

d) The final Ag concentration in the uncentrifuged and centrifuged Ag-NPs solutions were 10.61 and 8.68 ppm respectively and because they had been diluted to half by nitric acid, then the concentration would be 21.22 and 17.36 ppm respectively. As the initial Ag concentration was 26.97 ppm, then, the percentage of the synthesised Ag NPs was 78.7 and 64 % for uncentrifuged and centrifuged Ag-NPs solutions respectively.

e) The seed Au-NPs concentration is calculated by using the $N = 30.88\ D^3$ for the calculation of the average number of Au atoms per nanoparticle and the D

was found to be 18 nm from the TEM analysis. Therefore *N* was equal to 1.80 x 10^5 nm^3.

The molarity of the Gold(III) chloride trihydrate ($HAuCl_4$) used in the first reaction to prepare the seed particles was 1 mM (0.001 M) and its volume was 50 mL (0.05 L) whereas the total volume of the reaction solution was 55 mL (0.055 L). Therefore, the concentration of the seed Au NPs was:

$$C = \frac{0.001 \times 0.05 \times 6.023 \times 10^{23}}{1.80 \times 10^{5} \times 0.055 \times 6.023 \times 10^{23}} = 5.05 \times 10^{-9}\ M = 5\ nM$$

f) The final Au NPs concentration is calculated by using the N = 30.88 D^3 for the calculation of the average number of Au atoms per nanoparticle and the *D* was found to be 36 nm from the TEM analysis. Therefore *N* was equal to 14.40 x 10^5 nm^3.

The molarity of the $HAuCl_4$ used in the second reaction to prepare the large particles was 11 mM (11×10^{-3} M) and its volume was 0.5 mL (5×10^{-4} L). Also, the seed particles was added to this reaction with a concentration 5.05×10^{-9}M (previously determined) and at volume of 0.3 mL (3×10^{-4} L) and the total volume of the reaction solution was 32.97 mL (32.97×10^{-3} L). Therefore, the concentration of the large Au NPs was:

$$C = \frac{\left[\left(5.05 \times 10^{-9} \times 3 \times 10^{-4} \times 180 \times 10^{3}\right) + \left(11 \times 10^{-3} \times 5 \times 10^{-4}\right)\right] \times 6.023 \times 10^{23}}{14.40 \times 10^{5} \times 32.97 \times 10^{-3} \times 6.023 \times 10^{23}}$$

$$= 1.2 \times 10^{-10}\ M$$

The initial Au concentration in ppm is:

$$1.2 \times 10^{-10} \times 1000 \times 14.40 \times 10^{5} \times 196.96 = 34.47\ ppm$$

g) The final Au concentration in the uncentrifuged and centrifuged Au-NPs solutions were 29.55 and 26.90 ppm respectively. As the initial Au concentration was calculated and found to be 34.47 ppm, the percentage of the synthesised Au-NPs was 85.7 and 78 % for uncentrifuged and centrifuged Au-NPs solutions respectively.